

ADVANCED RESERVOIR CHARACTERIZATION AND EVALUATION OF CO₂ GRAVITY DRAINAGE IN THE NATURALLY FRACTURED SPRABERRY TREND AREA

Annual Report
September 1, 1997 – August 31, 1998

By
David S. Schechter
Paul McDonald

February, 1999

Work Performed Under Contract No. DE-FC22-95BC14942

New Mexico Institute of Mining & Technology
Socorro, New Mexico



National Petroleum Technology Office
U. S. DEPARTMENT OF ENERGY
Tulsa, Oklahoma

DISCLAIMER

This report was prepared as an account of work sponsored by an agency of the United States Government. Neither the United States Government nor any agency thereof, nor any of their employees, makes any warranty, expressed or implied, or assumes any legal liability or responsibility for the accuracy, completeness, or usefulness of any information, apparatus, product, or process disclosed, or represents that its use would not infringe privately owned rights. Reference herein to any specific commercial product, process, or service by trade name, trademark, manufacturer, or otherwise does not necessarily constitute or imply its endorsement, recommendation, or favoring by the United States Government or any agency thereof. The views and opinions of authors expressed herein do not necessarily state or reflect those of the United States Government.

This report has been reproduced directly from the best available copy.

Available to DOE and DOE contractors from the Office of Scientific and Technical Information, P.O. Box 62, Oak Ridge, TN 37831; prices available from (615) 576-8401.

Available to the public from the National Technical Information Service, U.S. Department of Commerce, 5285 Port Royal Rd., Springfield, VA 22161

DOE/BC/14942-7
Distribution Category UC-122

Advanced Reservoir Characterization and Evaluation of CO₂ Gravity Drainage in the Naturally
Fractured Spraberry Trend Area

By
David S. Schechter
Paul McDonald

February 1999

Work Performed Under Contract No. DE-FC22-95BC14942

Prepared for
U.S. Department of Energy
Assistant Secretary for Fossil Energy

Dan Ferguson, Technology Manager
National Petroleum Technology Office
P.O. Box 3628
Tulsa, OK 74101

Prepared by
Petroleum Recovery Research Center
New Mexico Institute of Mining and Technology
Socorro, NM 87801

CONTENTS

LIST OF TABLES	vii
TABLE OF FIGURES	vii
ABSTRACT	xi
EXECUTIVE SUMMARY	xiii
ACKNOWLEDGEMENTS	xvii
1. RESERVOIR CHARACTERIZATION	1
1.1 INTRODUCTION	1
1.1.1 References	1
1.2 CORE INTERPRETATION AND SEDIMENTOLOGICAL ANALYSIS.....	3
1.2.1 Generalized Core Description	3
1.2.1.1 Textural Lithofacies for Fine Grained Deposits	3
1.2.1.2 Textural Lithofacies for Coarse Grained Deposits	4
1.2.1.3 Lithofacies Interpretation.....	5
1.2.1.3.1 Depositional Setting for Low Energy Environment	5
1.2.1.3.2 Depositional Setting for Low Energy Environment	6
1.2.1.4 References.....	6
1.3 PETROGRAPHY AND DIAGENESIS.....	9
1.3.1 Petrography.....	9
1.3.1.1 General Textures and Mineralogy	9
1.3.1.2 Porosity.....	10
1.3.1.3 Small Scale Lithofacies – Rock Types.....	10
1.3.1.3.1 Rock Type “A”	11
1.3.1.3.2 Rock Type “B”	11
1.3.1.3.3 Rock Type “C”	11
1.3.1.3.4 Rock Type “D”	11
1.3.1.3.5 Rock Type “E”	11
1.3.1.3.6 Rock Type “F”	12
1.3.2 Diagenesis	12
1.3.2.1 Quartz and Feldspar Overgrowth, Authigenic Feldspar, and Pressure Solution.....	12
1.3.2.1.1 Authigenic Clays.....	12
1.3.2.1.2 Pyrite.....	13
1.3.2.1.3 Carbonate.....	13
1.3.2.1.4 Pore Space	13
1.3.3 Paragenesis	13
1.3.3.1 Porosity, Dissolution and Reservoir Quality Preservation	14
1.3.3.2 Hydrocarbon Emplacement.....	16
1.3.3.3 Fracture model	16
1.3.3.3.1 1U Fractures	17
1.3.3.3.2 5U Fractures	17
1.3.3.3.3 Other Fracture Sets.....	18
1.3.3.3.4 Fracturing Paragenetic Sequences.....	18
1.3.4 Discussion	19
1.3.4.1 Relationship Between Depositional Features, Mineralogy, Provenance, Pore-Filling Constituents, Pore Space and Reservoir Quality.....	19
1.3.4.2 References.....	20
1.4 PETROPHYSICS: COMBINED ROCK AND FLUID CHARACTER	27
1.4.1 Gamma Ray Log Resolution	27

1.4.2	<i>Determination of Petrophysical Properties</i>	27
1.4.2.1	Computer-Controlled Scanning Air-Minipermeameter (CCSAM).....	27
1.4.2.2	Methodology for Obtaining Petrophysical Properties.....	28
1.4.2.2.1	Permeability determination with Nitrogen Flow Through Rock Type	28
1.4.2.2.2	Helium Porosity Determination	28
1.4.2.2.3	Mercury Injection Techniques: Capillary Pressure, Pore Distribution, Pore Throat and Connectivity	29
1.4.2.3	Rock Types and Rock-Fluid Properties	29
1.4.2.3.1	Discussion of Petrophysical Properties.....	29
1.4.2.3.2	Permeability, Porosity and Water Saturation Relationships.....	30
1.4.2.3.3	Grain Density and Porosity Relationships	32
1.4.2.3.4	Capillary Pressure and Pore Throat Relationships	32
1.4.2.4	Description of Rock Types.....	32
1.4.3	<i>Summary</i>	34
1.4.4	<i>References</i>	35
2.	INVESTIGATION OF CRUDE OIL/BRINE/ROCK INTERACTION	47
2.1	EXPERIMENTAL STUDY OF CRUDE/BRINE/ROCK INTERACTION AT RESERVOIR CONDITIONS	47
2.1.1	<i>Introduction</i>	47
2.1.2	<i>Experimental Material</i>	47
2.1.3	<i>Experimental Procedures</i>	48
2.1.4	<i>Results and Discussion</i>	49
2.1.4.1	Effect of Temperature on Spontaneous Imbibition.....	49
2.1.4.2	Effect of Aging Time.....	50
2.1.4.3	Effect of Temperature on Brine Displacement.....	51
2.1.4.4	Wettability Index.....	51
2.1.4.5	Heterogeneity in Rock Properties.....	52
2.1.5	<i>Conclusions</i>	52
2.1.6	<i>References</i>	53
2.2	SPONTANEOUS IMBIBITION MODELING OF SPRABERRY CORES USING A FINITE DIFFERENCE SCHEME	69
2.2.1	<i>Introduction</i>	69
2.2.2	<i>Background</i>	69
2.2.3	<i>Experimental Data</i>	70
2.2.4	<i>Mathematical Formulation</i>	70
2.2.5	<i>Finite-Difference Scheme</i>	71
2.2.6	<i>Results and Discussions</i>	72
2.2.6.1	The Effect of Capillary Pressure	73
2.2.6.2	The Effect of Oil and Water Relative Permeabilities.....	73
2.2.6.3	The Effect of Oil and Water Viscosity.....	73
2.2.6.4	The Effect of Initial Water Saturation	74
2.2.7	<i>Conclusions</i>	74
2.2.8	<i>Nomenclature</i>	74
2.2.9	<i>References</i>	75
2.3	IMBIBITION-FLOODING MODELING OF ARTIFICIALLY FRACTURED CORE	81
2.3.1	<i>Background</i>	81
2.3.2	<i>Experimental Study</i>	82
2.3.3	<i>Numerical Model</i>	83
2.3.4	<i>Results and Discussions</i>	84
2.3.5	<i>Conclusions</i>	84
2.3.6	<i>References</i>	85

3	RESERVOIR PERFORMANCE ANALYSIS.....	93
3.1	ANALYSIS OF IMBIBITION MECHANISM IN THE NATURALLY FRACTURED SPRABERRY RESERVOIR	93
3.1.1	Introduction	93
3.1.2	Concept of Process.....	93
3.1.3	Scaling of Imbibition Data.....	94
3.1.4	Imbibition Recovery Model.....	94
3.1.5	Production Decline Model.....	96
3.1.6	Analysis of Recovery Mechanism.....	97
3.1.6.1	Recovery Based on Laboratory Scaling of Imbibition Data.....	97
3.1.6.2	Recovery Field Performance.....	98
3.1.6.2.1	Fluid Saturation.....	98
3.1.6.2.2	Displacement Efficiency ($E_{\text{displ.}}$)	98
3.1.7	Sensitivity Study of Imbibition Model	99
3.1.7.1	Reservoir Parameters.....	100
3.1.7.1.1	Matrix Permeability.....	100
3.1.7.1.2	Fracture Spacing	101
3.1.7.1.3	Production Decline.....	101
3.1.8	Conclusion.....	101
3.1.9	Nomenclature.....	102
3.1.10	Reference	102
3.2	DETERMINATION OF INPUT PARAMETERS FOR SIMULATION OF CO ₂ FLOODING	113
3.2.1	Introduction	113
3.2.2	Absolute Matrix Permeability	113
3.2.3	Relationship between Capillary Pressure and Rock Permeability.....	114
3.2.4	Analytical Determination of Swanson Parameter (S_v/P_d) _A	115
3.2.4.1	Advantages of Using Eq. (13).....	116
3.2.4.2	Application of Eq. (13) to the Spraberry Sand	117
3.2.5	Secondary Porosity	117
3.2.6	Secondary Permeability.....	118
3.2.6.1	Parallel Flow Model	118
3.2.6.2	Scaling Model	120
3.2.7	Conclusions	120
3.2.8	References	121
	Appendix A – Interrelationship between Effective On-Trend Reservoir Permeability, Matrix Permeability and Intrinsic Fracture Permeability in Naturally Fracture Reservoirs	122
3.3	NUMERICAL MODELING OF SOLID DEFORMATION AND STRESS-DEPENDENT PERMEABILITY IN NATURALLY FRACTURED RESERVOIRS	125
3.3.1	Introduction	126
3.3.2	Technical Approach	126
3.3.2.1	Dual-Porosity/Dual-Permeability Fluid Flow Model.....	126
3.3.2.2	Poroelectric Model.....	131
3.3.2.3	Initial and Boundary Conditions	132
3.3.3	Results and Discussions	133
3.3.4	Conclusions	134
3.3.5	Nomenclature.....	134
3.3.6	References	136
3.4	SIMULATED HORIZONTAL WELL PERFORMANCE IN THE NATURALLY FRACTURED SPRABERRY TREND AREA	143
3.4.1	Introduction	143
3.4.2	Horizontal Well Performance	144
3.4.3	The Effects of Water Injection on the Performance of Vertical and Horizontal Wells	145
3.4.4	Conclusions	147
3.4.5	References	148

4	INVESTIGATION OF RECOVERY MECHANISMS BY CO₂ INJECTION IN FRACTURES	
SYSTEM		155
4.1	ANALYSIS OF CO ₂ GRAVITY DRAINAGE	155
4.1.1	Introduction	155
4.1.2	Laboratory Stacked Core Experiments	155
4.1.3	Comparison and Discussion	157
4.1.4	Scaling of the Experimental Results	157
4.1.5	Current CO ₂ Gravity Drainage Laboratory Experiments	158
4.1.6	Summary	159
4.1.7	References	160
5	FIELD DEMONSTRATION PROJECT	169
5.1	DRILLING	169
5.1.1	Flood Facilities	169
5.1.2	Future Plans	169

List of Tables

TABLE 1.1-1 CORES ANALYSIS TECHNIQUES USED TO STUDY THE SPRABERRY FORMATION.....	2
TABLE 1.3-1 MINERALOGICAL AVERAGES FOR POINT COUNTS OF THIN SECTIONS FOR SIX CATEGORIES OF SMALL-SCALE LITHOFACIES, SUMMARY OF DATA FROM THREE CORES FROM DIFFERENT WELLS.....	22
TABLE 1.3-2 X-RAY DIFFRACTION DATA FOR CLAY MINERALOGY COVERING ALL LITHOLOGIC TYPES IN THE SPRABERRY FORMATION	23
TABLE 1.3-3 A SUMMARY OF THE PORE TYPES ENCOUNTERED IN SEM SAMPLES FROM THE SPRABERRY FORMATION	23
TABLE 1.4-1 SUMMARY OF GRAIN DENSITY DATA CORRELATED WITH THE MAJOR ROCK TYPES.....	43
TABLE 1.4-2 SUMMARY OF HELIUM, NITROGEN AND MERCURY INJECTION DATA FOR PLUGS OF DIFFERENT ROCK TYPES THAT FORM THE SPRABERRY FORMATION	43
TABLE 2.1-1 THE PHYSICAL PROPERTIES OF THE RESERVOIR CORE SAMPLES	55
TABLE 2.1-2 COMPOSITION OF SYNTHETIC SPRABERRY RESERVOIR BRINE	55
TABLE 2.1-3 PROPERTIES OF SPRABERRY CRUDE OIL *	56
TABLE 2.1-4 SPRABERRY CRUDE OIL COMPOSITION *	56
TABLE 2.2-1 CORE AND FLUID PROPERTIES	76
TABLE 2.3-1 CORE AND FLUID PROPERTIES	86
TABLE 2.3-2 IMBIBITION DATA FROM LABORATORY EXPERIMENT	86
TABLE 3.1-1 THE AVERAGING ABSOLUTE PERMEABILITY AND POROSITY FOR BOTH SAND UNITS (1U AND 5U) IN SPRABERRY TREND AREA RESERVOIR.....	104
TABLE 3.1-2 EVALUATION OF WATER SATURATION AND CURRENT OIL SATURATION ^(A)	104
TABLE 3.1.3 EVALUATION AND DISPLACEMENT EFFICIENCY (E_D) AND VOLUMETRIC	104
TABLE 3.1-4 RESERVOIR PARAMETERS AS INPUT DATA.....	105
TABLE 3.1-5 FRACTURING SPACING	105
TABLE 3.2-1 AIR, WATER, AND OIL PERMEABILITIES OF SPRABERRY TREND AREA RESERVOIR CORES ...	124
TABLE 3.3-1 MODEL PARAMETER EMPLOYED.....	137
TABLE 4.1-1 PHYSICAL PROPERTIES OF CORE SAMPLES USED IN THE EXPERIMENTS.....	161
TABLE 4.1-2 AVERAGE MOLECULAR WEIGHTS OF THE OIL SAMPLES PRODUCED	161
TABLE 4.1-3 CALCULATIONS OF CURRENT OIL RESERVES IN THE AREA TO BE SWEEPED BY CO ₂ IN THE E.T. O'DANIEL CO ₂ PILOT	162

Table of Figures

FIG. 1.2-1 DEPTH PROFILES SHOWING THE CORRELATION OF GAMMA RAY LOG WITH CORE DESCRIPTION FOR THE E.T. O'DANIEL 37 WELL.....	7
FIG. 1.3-1 SEM PHOTOMICROGRAPHS SHOWING DIFFERENT TYPES OF ILLITE CLAY ACCUMULATION, DOLOMITE CEMENT, AND PYRITE OCCURRENCE IN THE SPRABERRY FORMATION	24
FIG. 1.3-2 TWO X-RAY DIFFRACTOGRAMS SHOWING CLAY MINERALOGICAL COMPOSITION.....	25
FIG. 1.4-1 CORE E.T. O'DANIEL 37 – INTEGRATION OF PETROGRAPHIC AND PETROPHYSICAL DATA.....	36
FIG. 1.4-2 CROSS PLOTS ILLUSTRATE THE DIFFERENCES IN POROSITY-PERMEABILITY CORRELATION FOR SAMPLES ABOVE AND BELOW 7195 FT DEPTH FOR E.T. O'DANIEL 37 CORE	37
FIG. 1.4-3 SET OF POROSITY-PERMEABILITY CROSS PLOTS SHOWS THE LITHOLOGICAL CONTROL UPON Φ AND K. SHACKELFORD 138-A CORE.....	38
FIG. 1.4-4 SET OF CROSS-PLOTS SHOWING THE LITHOLOGICAL CONTROL UPON POROSITY AND PERMEABILITY FOR SIX LARGE-SCALE LITHOFACIES, CORE E.T. O'DANIEL 37	39
FIG. 1.4-5 COMPARISON OF FLUORESCING PAY ZONE AND NON-PAY ZONES RICHER IN CLAY CONTENT FOR SHACKELFORD 1-38A.....	40
FIG. 1.4-6 NON-FLUORESCENT ZONES ARE COMMONLY LOWER QUALITY RESERVOIRS AND NON-RESERVOIR ROCK STRONGLY AFFECTED BY PORE LINING AND PORE BRIDGING CLAYS	40
FIG. 1.4-7 POROSITY VS. WATER SATURATION FROM THE E.T. O'DANIEL 37 AND SHACKELFORD 1-38A	41
FIG. 1.4-8 GRAIN DENSITY VS. POROSITY CROSS-PLOT SUGGESTS STRONG LITHOLOGICAL CONTROLS ON RESERVOIR QUALITY	42
FIG. 1.4-9 GRAPH SHOWING SEVERAL CURVES FOR S_w AND CAPILLARY PRESSURE FROM IMBIBITION EXPERIMENTS DONE WITH CORE PLUGS FROM VARIOUS DEPTHS.....	44
FIG. 1-410 THREE CROSS-PLOTS PRESENTING MERCURY INJECTION DATA CORRELATED WITH POROSITY PERMEABILITY AND PORE THROAT RADIUS. CROSS-PLOTS SUGGEST THAT ROCK-FLUID BEHAVIOR IS LINKED TO LITHOLOGICAL VARIABILITY FOR THE SIX ROCK TYPES UNDER STUDY	45
FIG. 2.1-1 SCHEMATIC EXPERIMENTAL PROGRAM.....	57

FIG. 2.1-3 VARIATION IN DENSITY OF SYNTHETIC SPRABERRY BRINE WITH TEMPERATURE INCREASE	58
FIG. 2.1-4 VARIATION IN VISCOSITY OF SPRABERRY OIL WITH TEMPERATURE INCREASE	59
FIG. 2.1-5 VARIATION IN DENSITY OF SPRABERRY OIL WITH TEMPERATURE INCREASE	59
FIG. 2.1-6 INTERFACIAL TENSION OF SPRABERRY OIL – BRINE AT ELEVATED PRESSURE	60
FIG. 2.1-7 INTERFACIAL TENSION OF SPRABERRY OIL – BRINE AT ELEVATED TEMPERATURE	60
FIG. 2.1-8 THERMAL EXPANSION OF SPRABERRY OIL	61
FIG. 2.1-9 SPONTANEOUS IMBIBITION APPARATUS.....	61
FIG. 2.1-10 EFFECT OF ELEVATED PRESSURE ON RATE OF IMBIBITION AND RECOVERY USING BEREASANDSTONE	62
FIG. 2.1-11 EFFECT OF CHANGING TEMPERATURE ON RATE OF IMBIBITION AND RECOVERY USINGBEREA SANDSTONE	62
FIG. 2.1-12 EFFECT OF TEMPERATURE IN IMBIBITION TESTS	63
FIG. 2.1-13 EFFECT OF TEMPERATURE CHANGES ON OIL RECOVERY BY IMBIBITION.....	63
FIG. 2.1-14 OIL RECOVERY CURVE OBTAINED FROM IMBIBITION EXPERIMENT PERFORMED ATRESERVOIR TEMPERATURE.....	64
FIG. 2.1-15 EFFECT OF AGING TIME ON THE RECOVERY OF OIL BY IMBIBITION	64
FIG. 2.1-16 TOTAL RECOVERY (IMBIBITION PLUS DISPLACEMENT) VERSUS AGING TIME TO EXCLUDE THEEFFECTS OF AGING TIME ON THE RECOVERY MECHANISMS	65
FIG. 2.1-17 EFFECT OF AGING TIME ON TOTAL RECOVERY AT ELEVATED TEMPERATURES.....	65
FIG. 2.1-18 WETTABILITY INDEX TO WATER VERSUS AGING TIME FOR THE DIFFERENT EXPERIMENTTEMPERATURES	66
FIG. 2.1-19 EFFECT OF INITIAL WATER SATURATION ON OIL RECOVERY BY IMBIBITION.....	66
FIG. 2.1-20 EFFECT OF INITIAL WATER SATURATION ON TOTAL RECOVERY	67
FIG. 2.1-21 EFFECT OF PERMEABILITY ON RECOVERY BY IMBIBITION	67
FIG. 2.1-22 EFFECT OF PERMEABILITY ON TOTAL OIL RECOVERY	68
FIG. 2.2-1 IMBIBITION CAPILLARY PRESSURE OBTAINED FROM ATCHING SPONTANEOUS IMBIBITIONDATA	76
FIG. 2.2-2 MATCHING BETWEEN SPONTANEOUS-IMBIBITION EXPERIMENTS WITH NUMERICALSOLUTION	77
FIG. 2.2-3 NON-LINEAR DIFFUSION COEFFICIENT	77
FIG. 2.2-4 EFFECT ON DIFFERENT CAPILLARY PRESSURES ON OIL VOLUME RECOVERED	78
FIG. 2.2-5 EFFECT OF DIFFERENT OIL RELATIVE PERMEABILITIES ON OIL VOLUME RECOVERED.....	78
FIG. 2.2-6 EFFECT OF DIFFERENT WATER RELATIVE PERMEABILITIES ON OIL VOLUME RECOVERED	79
FIG. 2.2-7 EFFECT ON DIFFERENT OIL VISCOSITIES ON OIL VOLUME RECOVERED.....	79
FIG. 2.2-8 EFFECT ON DIFFERENT WATER VISCOSITIES ON OIL VOLUME RECOVERED.....	80
FIG. 2.2-9 EFFECT ON DIFFERENT INITIAL WATER SATURATION ON OIL VOLUME RECOVERED.....	80
FIG. 2.3-1 GRIND BLOCK MODELING REPRESENT THE CORE.....	87
FIG. 2.3-2 EXPERIMENTAL SETUP OF IMBIBITION-FLOODING	87
FIG. 2.3-3 MATCHING BETWEEN OBSERVED EXPERIMENTAL DATA AND NUMERICAL MODEL FOR WATERPRODUCTION RATE	88
FIG. 2.3-4 MATCHING BETWEEN OBSERVED EXPERIMENTAL DATA AND NUMERICAL MODEL FOR WATERPRODUCTION	88
FIG. 2.3-5 MATCHING BETWEEN OBSERVED EXPERIMENTAL DATA AND NUMERICAL MODEL FOR OILPRODUCTION RATE	89
FIG. 2.3-6 MATCHING BETWEEN OBSERVED EXPERIMENTAL DATA AND NUMERICAL MODEL FOR OILPRODUCTION	89
FIG. 2.3-7 MATCHING BETWEEN OBSERVED EXPERIMENTAL DATA AND NUMERICAL MODEL FOR OILRECOVERY	90
FIG. 2.3-8 MATCHING BETWEEN OBSERVED EXPERIMENTAL DATA AND NUMERICAL MODEL FOR WATERCUT	90
FIG. 2.3-9 CAPILLARY PRESSURE CURVE	91
FIG. 3.1-1 OIL RECOVERY CURVES OBTAINED UNDER RESERVOIR CONDITION PLOTTED USINGDIMENSIONLESS VARIABLES AND COMPARED WITH OIL RECOVERY CURVES OBTAINED UNDERAMBIENT CONDITIONS.....	106
FIG. 3.1-2 AVERAGING OF IMBIBITION CURVES USING THE ARANOFSKY EQUATION TO FIT THE IMBIBITIONEXPERIMENTAL DATA BY ADJUSTING EMPIRICAL CONSTANT λ	106
FIG. 3.1-3 POROSITY AND ABSOLUTE PERMEABILITY OF UPPER SPRABERRY 1U UNIT VERSUE DEPTH(DATA TAKEN FROM WELL SHACKLEFORD 1-38A)	107
FIG. 3.1-4 POROSITY AND ABSOLUTE PERMEABILITY OF UPPER SPABERRY 5U UNIT VERSUS DEPTH(DATA TAKEN FROM WELL E.T. O'DANIEL 37).....	107

FIG. 3.1-5 CALCULATED IMBIBITION OIL RECOVERY FOR FIVE YEARS OF WATERFLOODING FROM UPPER SPRABERRY 1U FORMATION, BASED ON SCALING OF EXPERIMENTAL DATA AND FRACTURE SPACING OF 3.79 FT	108
FIG. 3.1-6 CALCULATED IMBIBITION OIL RECOVERY FOR FIVE YEARS OF WATERFLOODING FROM UPPER SPRABERRY 5U FORMATION, BASED ON SCALING OF EXPERIMENTAL DATA AND FRACTURE SPACING OF 3.79FT	108
FIG. 3.1-7 HISTORY OF WATERFLOOD RECOVERY PROFILES FROM UPPER SPRABERRY 1U FORMATION, BASED ON SCALING OF EXPERIMENTAL DATA AND FRACTURE SPACING OF 3.79FT.....	109
FIG. 3.1-8 HISTORY OF WATERFLOOD RECOVERY PROFILES FROM UPPER SPRABERRY 5U FORMATION, BASED ON SCALING OF EXPERIMENTAL DATA AND FRACTURE SPACING OF 3.79FT	109
FIG. 3.1-9 CALCULATED IMBIBITION OIL RECOVERY FOR 40 YEARS OF WATERFLOODING FROM SPRABERRY 1U AND 5U FORMATION, BASED ON SCALING OF EXPERIMENTAL DATA AND FRACTURE SPACING OF 3.79FT	110
FIG. 3.1-10 INITIAL WATER SATURATION IN THE SPRABERRY RESERVOIR	110
FIG. 3.1-11 EFFECT OF MATRIX PERMEABILITY ON OIL RECOVERY MECHANISM.....	111
FIG. 3.1-12 EFFECT OF MATRIX PERMEABILITY ON CALCULATION OF PRODUCTION RATES.....	111
FIG. 3.1-13 EFFECT OF FRACTURE SPACING ON RECOVERY MECHANISM	112
FIG. 3.1-14 EFFECT OF MATRIX PERMEABILITY AND FRACTURE SPACING ON DECLINE RATE CONSTANT	112
FIG. 3.2-1 CURVE MATCHING OF OIL-WATER DRAINAGE CAPILLARY PRESSURE FOR A SPRABERRY CORE	124
FIG. 3.2-2 A PARALLEL-FLOW MODEL FOR SIMULATING FLUID FLOW IN NATURALLY FRACTURED RESERVOIRS	125
FIG. 3.3-1 TWO-DIMENSIONAL FRACTURE-MATRIX IDEALIZATION.....	137
FIG. 3.3-2 PERMEABILITY REDUCTION CURVE AS FUNCTION OF PORE PRESSURE OBTAINED FROM HUMBLE PILOT SIMULATION.....	138
FIG. 3.3-3 SOLID DISPLACEMENT DISTRIBUTION IN X-DIRECTION AT 20 DAYS.....	138
FIG. 3.3-4 FRACTURE PRESSURE DISTRIBUTION AT 20 DAYS	139
FIG. 3.3-5 EFFECTIVE STRESS DISTRIBUTION IN X-DIRECTION AT 20 DAYS	139
FIG. 3.3-6 REDUCTION OF EFFECTIVE FRACTURE PERMEABILITY AT THE GRIDBLOCKS IN THE X-DIRECTION INTERSECT THROUGH THE GRID BLOCK CONTAINING THE WELL	140
FIG. 3.3-7 REDUCTION OF EFFECTIVE FRACTURE PERMEABILITY AT THE GRID BLOCKS IN THE Y-DIRECTION INTERSECT THROUGH GRID BLOCK CONTAINING THE WELL	140
FIG. 3.3-8 FLOW RATE AS A FUNCTION OF BOTTOMHOLE PRESSURE FROM THE CONVENTIONAL DUAL-POROSITY SIMULATOR.....	141
FIG. 3.3-9 FLOW RATE AS A FUNCTION OF BOTTOMHOLE PRESSURE FROM THE STRESS DUAL-POROSITY SIMULATOR	141
FIG. 3.3-10 COMPARISON OF PERFORMANCE BETWEEN CONVENTIONAL AND STRESS DUAL-POROSITY SIMULATORS	142
FIG. 3.4-1 THE UNITIZED PORTION OF THE SPRABERRY TREND AREA, SHOWING THE LOCATION OF HUMBLE PILOT AREA	149
FIG. 3.4-2 THE HUMBLE WATERFLOOD TEST SHOWED THAT PRODUCTION OF THE CENTER PILOT WELL INCREASED TO OVER 250 BOPD AT THE BEGINNING OF WATERFLOOD.....	150
FIG. 3.4-3 EFFECT OF AVERAGE RESERVOIR PRESSURE ON CUMULATIVE OIL PRODUCTION (COP).....	151
FIG. 3.4-4 THE EFFECT OF A VERTICAL PRODUCTION WELL ON THE OIL PRODUCTION RATE.....	151
FIG. 3.4-5 THE EFFECT OF A HORIZONTAL PRODUCTION WELL WITH VERTICAL INJECTION WELLS ON THE OIL PRODUCTION RATE	152
FIG. 3.4-6 THE EFFECT OF VERTICAL AND HORIZONTAL PRODUCTOIN WELLS WITH HORIZONTAL INJECTION WELLS ON THE OIL PRODUCTION RATE	152
FIG. 3.4-7 THE EFFECT OF A HORIZONTAL PRODUCTION WELL WITH VERTICAL INJECTION WELLS AND DIFFERENT INJECTION SCHEMES ON CUMULATIVE OIL PRODUCTION.....	153
FIG. 3.4-8 THE EFFECT OF A HORIZONTAL PRODUCTION WELL WITH HORIZONTAL INJECTION WELLS AND DIFFERENT INJECTION SCHEMES ON CUMULATIVE OIL PRODUCTION (NOTE: THE CUMULATIVE OIL PRODUCTION IS LOWER THAN THAT SHOWN IN THE PREVIOUS FIGURE).....	153
FIG. 3.4-9 THE EFFECT OF A VERTICAL PRODUCTION WELL WITH VERTICAL AND HORIZONTAL INJECTION WELLS	154
FIG. 3.4-10 THE EFFECT OF A CYCLIC RATE OF 1:2 AND CONSTANT INJECTION RATE ON THE OIL PRODUCTION RATE	154
FIG. 4.1-1 OIL RECOVERY CURVES OBTAINED FROM FOUR CO ₂ INJECTION EXPERIMENTS USING CONTINUOUS CORES WITH DIFFERENT PERMEABILITIES AND WATER SATURATIONS.....	163
FIG. 4.1-2 SCHEMATIC ILLUSTRATING EXPERIMENTAL PROCEDURE.....	163
FIG. 4.1-3 OIL RECOVERY CURVE OBTAINED FROM A CO ₂ INJECTION EXPERIMENT USING A 0.05 MD CORE STACK WITH AN INITIAL WATER SATURATION 0.376	164

FIG. 4.1-4 COMPARISON OF OIL RECOVERY CURVES OBTAINED FROM FIVE CO ₂ INJECTION EXPERIMENTS USING CORES WITH DIFFERENT PERMEABILITIES AND WATER SATURATIONS.....	164
FIG. 4.1-5 WELL LOCATIONS IN THE E.T. O'DANIEL CO ₂ PILOT (NOT TO SCALE).....	165
FIG. 4.1-6 PREDICTING OIL RECOVERY FROM THE E.T. O'DANIEL CO ₂ PILOT AREA.....	165
FIG. 4.1-7 PREDICTING OIL PRODUCTION RATE FROM THE E.T. O'DANIEL CO ₂ PILOT AREA.....	166
FIG. 4.1-8 PREDICTING CUMULATIVE OIL PRODUCTION FROM THE E.T. O'DANIEL CO ₂ PILOT AREA.....	166
FIG. 4.1-9 SCHEMATIC OF IMBIBITION GRAVITY DRAINAGE EXPERIMENT	167

ABSTRACT

The overall goal of this project is to assess the economic feasibility of CO₂ flooding the naturally fractured Spraberry Trend Area in West Texas. This objective is being accomplished by conducting research in four areas: 1) extensive characterization of the reservoirs, 2) experimental studies of crude oil/brine/rock (COBR) interactions in the reservoirs, 3) reservoir performance analysis, and, 4) experimental investigations on CO₂ gravity drainage in Spraberry whole cores. This report provides results of the third year of the five-year project for each of the four areas including a status report of field activities leading up to injection of CO₂.

In Section 1, we have completed the reservoir characterization, which includes matrix description, and pay zone detection (from core-log integration), and fracture characterization. Much of this information is found in the 2nd Annual Technical Report. We have extended geological interpretation found in the 2nd Annual Report. This report provides a detailed analysis of petrography and diagenesis of the varying rock types. We have extended the classification of rock types and finally we have developed relationships between depositional features, petrophysical parameters and reservoir quality.

In Section 2, we have completed extensive imbibition experiments clearly indicating that the weakly water-wet behavior of the reservoir rock is responsible for poor waterflood response observed in many Spraberry fields. We have conducted a detailed investigation of both static and dynamic imbibition at reservoir temperature. We have also explored the effect of reservoir conditions on wettability determination in the Spraberry. Characterization of the crude oil/brine/rock interaction in the Spraberry matrix has been carried out based on results of laboratory experiments conducted at ambient conditions in the second year. It was found that brine imbibition rate was accelerated by elevated temperature and essentially unaffected by elevated pressure. Aging condition in oil decelerated brine imbibition while the wettability index to water was essentially unchanged. We have determined that the wettability index is approximately 0.2 at reservoir conditions, once again demonstrating the weakly water-wet nature of the Spraberry Trend Area reservoirs. Also in Section 2, we demonstrate that there is a significant difference between modeling static imbibition and dynamic imbibition experiments. Our results suggest that static imbibition tests do not reproduce the behavior characteristic of dynamic conditions that prevail in the reservoir. We have used a numerical, commercial simulator (ECLIPSE) in order to demonstrate the difference in the two experimental procedures.

In Section 3, we have made significant progress in analytical and numerical simulation of performance in Spraberry reservoirs. We have performed extensive simulations for the following phenomenon we believe are important in the Spraberry Trend Area: 1) imbibition waterflooding 2) determination of input parameters for CO₂ flooding 3) numerical modeling of solid deformation and stress dependent permeability and finally 4) simulation of horizontal well performance.

In Section 4, we have continued performing CO₂ gravity drainage experiments in Spraberry and Berea whole cores at reservoir conditions. The results of these experiments have been useful in

developing a model for free-fall gravity drainage and have validated our premise that CO₂ will recover oil from tight, unconfined Spraberry matrix. In Section 4, we provide a status report for the CO₂ gravity drainage experiments conducted at reservoir conditions.

Finally, in Section 5, we provide an update for the ongoing pilot in the E.T. O'Daniel Unit of the Spraberry Trend Area, including drilling of several new wells in the pilot pattern.

EXECUTIVE SUMMARY

The overall goal of this project is to assess the economic feasibility of CO₂ flooding the naturally fractured Spraberry Trend Area in West Texas. This objective is being accomplished by conducting research in four areas: 1) extensive characterization of the reservoirs, 2) experimental studies of crude oil/brine/rock (COBR) interactions in the reservoirs, 3) reservoir performance analysis, and, 4) experimental investigations on CO₂ gravity drainage in Spraberry whole cores. Additionally, a ten-acre field demonstration pilot project is part of this project. This report provides results of the third year of the five-year project for each of the four research areas and reports on the progress to date on the field demonstration pilot project.

Section 1 of this report is a detailed geological/petrophysical analysis of the Spraberry Trend reservoir and non-reservoir rocks in partial fulfillment of the first area of directed research. Some of the work presented in section 1 has been discussed in previous annual reports, but not as completely, detailed, and in depth as presented here. This investigation provided a rock-fluid model, which in conjunction with the fracture model developed in a parallel investigation, provides an improved characterization of the Spraberry reservoir. The extensive geological study attempts to more precisely define Spraberry rock quality based on integrating accurate mineralogical and diagenetic data with information of fluid distribution, saturation, conductivity, and capillary pressure data.

Additionally the geological study identified six small-scale lithofacies defined on thin sections, SEM, XRD, and, petrophysical measurements that comprise the subject reservoirs. The lithological variability was shown to exert control upon the different petrophysical parameters: porosity, permeability, capillary pressure, pore throat size, and water saturation. The study reviewed here provides the background to define pay zones, exploration of new horizons, determination of targets in horizontal drilling, isopach mapping, reserve estimations and input data for simulating the Spraberry Trend reservoirs. This type of analysis is important for proper reservoir management of the naturally fractured Spraberry Trend and has the potential of extension to other naturally fractured reservoirs.

Section 2 comprises the second area of experimental studies of crude oil/brine/rock (COBR) interactions in the reservoirs. We have completed extensive imbibition experiments showing the effects of temperature, pressure, and aging on the imbibition process and subsequently on oil recovery in naturally fractured reservoirs. Characterization of the COBR interaction in the Spraberry matrix has continued into the third year. The brine imbibition rate was found to accelerate at elevated temperature. However, pressure changes had little effect on imbibition. Aging of cores saturated with oil decelerated brine imbibition, resulting in reduced oil production at reservoir conditions.

Sets of coreflood experiments were also conducted on artificially fractured core at reservoir temperature and confining pressures of 500 psia. Brine was injected into the fracture and oil was produced at the other end of the fracture. The produced oil was water-free for a period of time, indicating that the imbibition rate of the rock was equal to the injection rate. A computer

simulation using the commercial software ECLIPSE™ was used to match the experimental data and determine a capillary pressure.

In addition to experimental investigations of the imbibition process of Spraberry rocks, numerical modeling was conducted. A mathematical model and 2D fully implicit numerical computer solution is presented in Section 2 to simulate the spontaneous imbibition process. The model simulates the laboratory static spontaneous imbibition experiment. The imbibition model predicts a low imbibition capillary pressure for the Spraberry core. Results also corroborate the wettability of the Spraberry as weakly water-wet. One of the purposes of developing the model was to define key parameters of the imbibition process. Sensitive key parameters for the imbibition process are capillary pressure, oil relative permeability, oil viscosity, and initial water saturation. The rate of imbibition was found not to be sensitive to water relative permeability and water viscosity.

Section 3 discusses the contribution of spontaneous imbibition to the oil recovery mechanism in the West Texas Spraberry reservoir. It has been suggested that waterflood recovery in the Spraberry reservoir is dominated by counter-current imbibition of water. The imbibition experiments conducted under reservoir conditions suggest that the recoverable oil by water imbibition is only 13% of the original oil in place. The scale-up of imbibition experimental results to field scale imbibition flooding uses several assumptions of the rate law that governs mass transfer. The developed scaling equation is then applied to evaluate scaling up from core geometry to matrix block geometry in the 1U and 5U Units of the Upper Spraberry zone. The results are in agreement with the observed 8 to 15% IOIP for 40 years of waterflooding in the Upper Spraberry sand.

Fluid saturation, waterflooding efficiency, and recovery are also reviewed in this section. Based on analysis of fluid saturation of the field, the volumetric sweep efficiency in the Spraberry reservoir is much higher than the displacement efficiency. This characteristic suggests that the waterflood failed primarily because of very poor imbibition displacement efficiency. A sensitivity study using the imbibition model showed that after 40 years of waterflooding in the Spraberry Trend a maximum oil recovery of only 13% IOIP. This shows that the imbibition mechanism has not been significantly effective in increasing oil recovery. The degree of heterogeneity in the matrix and the fracture system control the recovery during waterflooding the Spraberry.

A new approach to determine some of the input parameters for simulation of CO₂ flooding the naturally fractured Spraberry Trend Area reservoir in West Texas was also developed in Section 3. The results of this investigation demonstrate that the primary permeability, or the absolute matrix permeability, to be used in the simulator should be determined from the oil-water drainage capillary pressure curve. Although core flood data provide good estimates of matrix porosity, permeability derived from the core floods depend strongly upon the fluid type and wetting behavior of the rock in low permeability regions. The matrix permeability is estimated from water-oil capillary pressure and is more realistic for reservoir simulation. Water-oil imbibition capillary pressure should be from direct measurements or history matched as opposed to scaling from mercury injection. Mercury intrusion data fails to account for wettability and often gives an incorrect value of S_{wi} .

The secondary porosity due to natural fractures has been estimated based on the average fracture intensity and aperture. Fracture intensity and aperture were determined from horizontal coring. The secondary permeability due to natural fracture has been estimated based on a parallel flow model. The results are consistent with those derived from well test analyses and are being verified by scale-up of core flood data obtained using naturally fractured cores. The scaling model is presented in Section 3.

During the first year of this project, we analyzed the productivity behavior of Spraberry wells using a newly developed mathematical model. In the second year of this project, we modified the mathematical model with a consideration of mechanical skin due to fluid damage to the matrix permeability. In the third year of this project, the stress-sensitive permeability was studied in detail including the effect of deformation. A model coupling the solid deformation and the motion of fluid flow was developed using a fully implicit finite-difference scheme. The comparison of constant and variable permeability-porosity performances between conventional and stress sensitive dual-porosity was made. The variable permeability-porosity shows a significant reduction in the production rate as compared to constant permeability-porosity. Conventional dual-porosity with variable permeability cannot be used for high production rates in naturally fractured reservoirs.

Horizontal wells were studied using the commercial simulator ECLIPSE. During the first and second year of the project, numerical simulation of the Humble Waterflood Pilot was carried out using commercial simulators VIP and ECLIPSE. A good quality history match was achieved. The feasibility and optimization of using horizontal wells in the Humble pilot was completed in this report period. Several simulation scenarios were completed. The major conclusions are: 1) that the use of horizontal production wells could increase cumulative oil production. 2) Horizontal production wells surrounded by vertical injection well could yield higher cumulative oil production than that of horizontal injection wells 3) High water injection (greater than 500 STBWD per well) is not successful in 40-acre Spraberry fractured reservoir using vertical injection wells with constant injection scheme 4) Use of a cyclic waterflood with vertical injection wells could restore reservoir pressure and increase oil recovery in the Spraberry trend Area.

In the fourth area, we reported on several sets of CO₂ gravity drainage experiments in Spraberry and Berea whole cores at reservoir conditions. The results of these experiments have been useful in developing a model for free-fall gravity drainage and have validated our premise that CO₂ will recover oil from tight, unconfined Spraberry matrix. During this report period we completed a long-term drainage experiment of a stacked core to emulate a horizontal fracture intersecting a vertical fracture. An argument exists that matrix blocks in naturally fractured reservoirs may not be vertically continuous due to possible horizontal fractures or thin shale partings in the pay zone. This matrix discontinuity may affect gravity drainage efficiency. To address this issue, we conducted an experiment using a stack of whole cores emulating vertically discontinuous matrix blocks. The results show that the rate of recovery from a 0.05 md stacked composite core is slightly improved over that of a 0.38 md continuous core and less than the rate of recovery from a 0.01 md continuous core of similar water saturation. However, the 0.38 md continuous core had a higher water saturation that could be effecting the oil recovery rate from that core.

Additional work is needed to conclude as to whether a matrix block discontinuity significantly affects the efficiency of CO₂ gravity drainage.

To optimize the CO₂ pilot design in the E.T. O'Daniel Unit of the Spraberry Trend Area, we have scaled up our experimental results from core to field scale using our mathematical model presented in the First Annual Technical Progress Report. The results indicate that depending on the matrix permeability, water saturation and fracture intensity, significant amount of oil can be recovered from the pilot area by CO₂ flooding in a relatively short time period. Assuming a matrix air permeability of 0.9 md, water saturation of 0.45 and fracture spacing of 1.6 ft in the pilot area, the scaling model predicts incremental oil recovery of 10% within two years.

The final three years of this project involves primarily the implementation of the CO₂ pilot. Phase II of the project was initiated in January 1998. The favorable results from the four research areas have led us to conclude that CO₂ flooding is technically feasible in increasing recoverable reserves for the naturally fractured Spraberry Trend and the pilot phase of the project should be continued. The proposed design of the pilot requires drilling 16 wells. As of September 28, 1998, two of the six water injection wells and all three producers have been drilled and logged. Design of the injection facility has been completed. The remaining water injection wells, and injection facilities should be complete by the end of 1998, with water injection commencing shortly thereafter. The four CO₂ injection wells will be completed in 1999 with CO₂ injection scheduled in late 1999.

ACKNOWLEDGMENTS

The work presented in this report was financially supported by the United States Department of Energy's National Petroleum Technology Office and the following consortium of companies: Marathon Oil Co., Mobil Research and Development Corp., Pioneer Natural Resources (formerly Parker and Parsley Petroleum Co.), Petroglyph Operating Co., Texaco E&P Technology Dept., The Wiser Oil Co. and Union Pacific Resources. This support is gratefully acknowledged. Geographix Inc donated software used in reservoir characterization. Schlumberger donated ECLIPSE software used in reservoir simulation. I greatly appreciate diligent efforts from the following individuals who contributed to this project. Claudio Saleta, a Masters student in Geology, presents in Section 1 an extensive and detailed geological/petrophysical analysis of the Spraberry Trend Reservoir and non-reservoir rocks. Erwinsyah Putra, a PhD. Candidate and Yan Fidra, a Masters candidate, both Petroleum Engineering Students made significant technical contributions in extending the understanding of imbibition by experimental work, mathematical modeling, and computer simulations. Their work is reflected throughout Sections 2 and 3. Hujin Li's gravity drainage experiments are reported in Section 4.

Martha Cather performed the fracture diagenesis work and advised Claudio Saleta. Collaboration with Dr. John Lorenz from Sandia National Laboratory, who performed the fracture analysis of the horizontal core previously reported in the second annual report, has been beneficial. Other acknowledgments go to Richard Baker of Epic Consulting Ltd., Steve Melzer and Loren Stiles of UTPB-CEED, Randy Miller of Reservoirs Inc. and Lincoln Elkins. Chris Whigham and Paul McDonald continue to guide this project. Finally, thanks go to John Rogers for assembly and proof reading this document.

1 RESERVOIR CHARACTERIZATION

1.1 INTRODUCTION

One objective of this project is to develop a detailed geological characterization of the reservoir and non-reservoir rocks of the Permian upper Spraberry Formation, in West Texas. The Spraberry sandstones, widespread in the subsurface of the Permian Basin, are important targets for CO₂ enhanced recovery of oil.

The Spraberry reservoirs were discovered in 1949, and have been producing oil since then. Traditionally marginal producers, these clastic reservoirs are comprised of fine-grained sandstones and siltstones with low permeability and low-pressure that are interbedded with shaly non-reservoir rocks. The Spraberry Formation is Leonardian in age (Silver and Todd, 1969) and its occurrence is restricted to the subsurface of the Midland Basin. Although the formation is composed of three members: upper, middle, and lower; it is the upper member that is main focus of this study. The “operational units” in the upper Spraberry comprise two, crude, coarsening-upward intervals designated as the Floyd Submarine Fan (operational units 1U-4U) and the Driver Submarine Fan (operational units 5U-6U), respectively. Three cores from the Spraberry were used in this study (Table 1.1-1).

The goal of the detailed geological characterization is to integrate the results from the geologic studies with petrophysical measurements of rock-fluid properties. Most previous works on the Spraberry attempted to define reservoir targets based on strength and shape of the gamma ray (GR) deflection as criteria for determination of net pay. Isopach maps were developed based on this type of delineation of the pay zones (Tyler and Gholston, 1988; Guevara, 1988). The present study attempts to more precisely define Spraberry rock quality based on integrating accurate mineralogical and diagenetic data with information on fluid distribution, saturation, conductivity, and capillary pressure data.

This study identifies the different lithofacies that comprise the subject reservoirs, marginal reservoirs and non-reservoir rocks. Two different scales of lithofacies are observed depending on the relative dimensions of the observations or measurements. Eight large-scale lithofacies are described with simple observations of core slabs. These are defined based on the occurrence of particular sedimentary structures, textures, color and microorganisms. These types of observations are analyzed in view of the published literature related to sedimentological setting and basin model in order to delineate bases for the small-scale study of reservoir and non-reservoir rocks.

The small-scale lithofacies are referred to as Rock Type and are defined as intervals of rocks with unique pore geometry, determined mineralogical composition related to certain specific fluid flow characteristics. In order to analyze the microscopic character of rocks and the fluid flow through the porous media that form these rocks a combination of analytical techniques is used. Analysis of thin-section, SEM observations, and analysis XRD mineralogy define the rock types and reservoir and non-reservoir character, which is correlated with results from

petrophysical measurements of core plugs. The combined use of petrographic and petrophysical analysis (Table 1.1-1) serves in the creation of a sound rock-fluid model for small-scale lithofacies. This model can be used in log analysis. Geophysical well log response is correlated to the rock, pore and fluid model in order to perform more correct and efficient log interpretation in uncored wells. A rock-fluid model and log interpretation in the Spraberry Formation are necessary for definition of pay zones, exploration of new horizons, determination of targets in horizontal drilling, isopach mapping, reserve estimations and input data in simulation. For these purposes, this type of investigation is of extreme importance for proper management of the Spraberry trend area reservoirs.

1.1.1 References

1. Guevara, E. H., 1988, Geological characterization of Permian submarine fan reservoirs of the Driver waterflood Unit, Spraberry Trend, Midland Basin, Texas; BEG, UT Austin; Report of Investigation No. 172.
2. Silver, B. A., and Todd, R.G., 1969, Permian cyclic strata, northern Midland and Delaware Basins, West Texas and Southeastern New Mexico.
3. Tyler, N. and Gholston, J. C., 1988, Heterogeneous deep-sea fan reservoirs, Shackelford and Preston waterflood units, Spraberry Trend, West Texas; BEG, UT at Austin, Report of Investigation No. 171.

Table 1.1-1 Cores and analysis techniques used to study the Spraberry formation

Combined Techniques	Arthur No.5		Judkins		Shackelford 138-A		E.T. O'Daniel No.37	
	1U	5U	1U	5U	1U	5U	1U	5U
Operational Unit (sandstones)								
Core-Plug Petrophysics	---	---	X	---	X	X	X	X
Side Wall Core Plugs	---	---	---	---	X	---	---	---
Thin Sections	13	9	34	---	5	19	5	19
XRD	---	---	8	---	---	---	---	---
SEM	---	---	X	---	X	X	X	X

1.2 CORE INTERPRETATION AND SEDIMENTOLOGICAL ANALYSIS

1.2.1 Generalized Core Description

Two cores, E.T. O'Daniel 37 and Shackelford 138A, were examined in detail. Shown in Fig. 1.2-1 is the core description for E.T. O'Daniel 37 correlated to the gamma ray log. A total of eight large-scale lithologic categories were delineated by this study. These lithofacies are based on distinguishable sedimentary structures, textures, grain size, primary mineralogy, and environment as inferred from these characteristics. The following list shows the different lithofacies defined by this core analysis:

Textural Lithofacies for Fine Grained Deposits:

Lithofacies L1: Massive, silty dolostone and dolomite cemented siltstones.

Lithofacies L2: Shales.

Lithofacies L3: Thin bedded argillaceous siltstone with lenticular or convolute lamination.

Lithofacies L4: Bioturbated argillaceous coarse-grained siltstone.

Lithofacies L5: Parallel finely laminated siltstone.

Textural Lithofacies for Coarse Grained Deposits:

Lithofacies L6: Thick bedded, massive, very fine sandstones and siltstones.

Lithofacies L7: Thin bedded, massive, very fine sandstones and coarse siltstone.

Lithofacies L8: Thin bedded, graded cross-laminated, very fine sandstones and siltstones.

1.2.1.1 Textural Lithofacies for Fine Grained Deposits

Low energy deposits consist of siltstones, shaly laminated siltstones, thin layers of black shale, and silty dolostone. These are volumetrically the most abundant lithofacies comprising the upper Spraberry formation. The following lithofacies are observed in Spraberry cores:

Lithofacies L1: Massive, silty dolostone and dolomite cemented siltstones. These are dark gray to black, massive, very well indurated, silty dolomite mudstones and siltstones, which display massive or faint planar horizontal bedding. Ripple laminae and contorted bedding are rare. Dolomite occurs both as locally abundant or pervasive cement. Beds range from 1 to 3 ft thick and have sharp or scoured basal contacts or grade into underlying sandstones. Dolomite cement severely limits reservoir quality. Carbonate rocks are not very common in the analyzed cores.

Lithofacies L2: Shales. Shale beds are typically less than 2 ft thick and also grade into underlying siltstones. The shales are structureless and are only locally disrupted by small, horizontal burrows. Thin, isolated lenses of silt occur infrequently; the black color of these shales is a function of their high organic carbon content. Organics occur in association with locally

abundant pyrite; phosphatic nodules are common. Shales are relatively abundant in the Spraberry study cores.

Lithofacies L3: Thin bedded argillaceous siltstone with lenticular or convolute lamination - These rocks are medium to dark gray colored argillaceous siltstones and consist of thin (<0.5 ft) interbedded coarse siltstones and shales. They have poorly preserved lenticular lamination. The siltstones are moderately well sorted. Most of the original bedding within these rocks has been disrupted by soft sediment deformation. Convolute bedding and pillow structures are common.

Lithofacies L4: Bioturbated argillaceous coarse-grained siltstone. These rocks are gray to black in color. The rock groundmass consists of detrital clays that support scattered silt-sized grains of quartz and feldspar. Bioturbation has destroyed original sedimentary structures. The intensity of bioturbation ranges from moderate to extreme. Fossil burrows from browsing or feeding animals that leave traces generally parallel to bedding were evident in the cores. This trace fossil assemblage is indicative of deposition in deep-water (slope to basin) setting (Basan, et al., 1978).

Lithofacies L5: Parallel finely laminated siltstone. This lithofacies is characterized by alternations of light and dark colored fine laminae, each a few millimeters (generally <5mm) in thickness. Light colored laminae are quartz-rich, coarse siltstone. Dark colored laminae consist of the same silt sized detrital grains mixed with organic detritus and small amounts of argillaceous material. Commonly laminae have sharp/erosional bases. Normal graded bedding is common. Lamination is generally parallel. A few tops of finely laminated sequences are ripple laminated.

1.2.1.2 Textural Lithofacies for Coarse Grained Deposits

The very fine-grained deposits described above are widespread along the Spraberry Trend. They form a depositional continuum and encase the more localized very fine-grained "clean" sandstones and coarse siltstones. These sandstones are very fine grained and moderately to well sorted. The following coarse-grained lithofacies are observed in the cores:

Lithofacies L6: Thick bedded, massive very fine sandstones and siltstones– This lithofacies consists of light gray to light brown colored, fine grained, well-sorted sandstones to coarse grained siltstones. These sandstones occur as individual beds, 1 to 3 ft in thickness that stack vertically to form much thicker composite units. Sand beds have scoured basal contacts, often marked by a thin layer of intraformational mud clasts (matrix supported). Beds are internally massive and lack sedimentary structures. There is evidence of bioturbation.

Lithofacies L7: Thin bedded, massive very fine sandstones and coarse siltstones – These are light gray to light brown colored, very fine grained, moderately well sorted to sorted very fine sandstones and coarse grained siltstones. Individual sandstone beds are less than 1.5 ft thick. Beds are composites consisting of basal intervals of massive sandstones, which may grade vertically into parallel laminated or cross-laminated sandstones. The tops of some beds display dish structures or evidence of fluid escape. Individual beds have scoured bases often marked by

thin layers of intraformational mud-clast conglomerate (matrix supported). Composite beds are often difficult to identify due to relatively uniform grain size.

Lithofacies L8: Thin bedded, graded, cross-laminated very fine sandstones and siltstones – This lithofacies consists of thin bedded (<1 foot) very fine grained, light gray to brown colored, moderately well to well sorted very fine sandstones interbedded with dark gray shales. Individual sand beds have sharp, erosive bases and are normally graded. A thin layer of shale rip-up clasts often overlies basal surfaces. Normally graded sandstone beds are characterized by vertical sequences of sedimentary structures indicative of deposition from waning flow (i.e. so-called Bouma sequence). Such sequences consist of a basal section of parallel laminated sandstones. Sand beds grade vertically into overlying beds of dark gray shale or lenticular laminated silty shale.

1.2.1.3 Lithofacies Interpretation

Sandstone beds display abundant evidence of deposition from waning traction currents including:

- 1) Erosional, scoured bases (often sole marked, with rip-up clasts) and gradational bed tops, which denote tractional currents with a subsequent decrease in the energy of the environment.
- 2) Normal graded bedding (individual beds fine upwards),
- 3) Common cross bedding or current lamination indicative of transport by high energy traction currents,
- 4) General lack of bioturbation,
- 5) Some fluid escape, load, or flame structures indicative of rapid deposition and subsequent dewatering and,
- 6) Vertical sequence of sedimentary structures recording gradation from high to low flow regime conditions (“Bouma” sequences).

The total sedimentary package described above is interpreted as basinal deposits, based on:

- 1) Preservation of delicate, very fine scale, parallel lamination within non-burrowed sections, which is suggestive of anoxic conditions in very calm waters.
- 2) Local presence of abundant preserved organics, probably marine kerogens (suggestive of very slow rates of deposition in poorly oxygenated or deoxygenated bottom waters)
- 3) Preservation of very fine scale finely laminated graded bedding within individual siltstone laminae, very fine to fine grain size and abundant argillaceous sediments, probably due to distal location during deposition.

1.2.1.3.1 Depositional Setting for Low Energy Environment

The finely parallel laminated siltstones (L1) were formed by suspension settling of silt and very fine sized particles from submarine density currents. However, for the most part, they lack evidence of deposition from tractional currents. Handford (1981) proposed that such deposits result from density stratification of the water column when shelf derived density currents periodically move out over the basin as an interflow suspended above the basin floor.

Suspension settling of thin layers of silt and very fine-grained sand resulted from eventual mixing of waters near the terminus of such flows. Normal hemipelagic sedimentation of shale and organics occurred between such flows.

Burrowed siltstone (L2) alternates with the parallel finely laminated siltstone (L1) and with thin shale beds. The transition from laminated to burrowed intervals or, less frequently into shales, is interpreted as recording periodic changes in bottom water chemistry, primarily in bottom water oxygen content. Such changes may have occurred in response to fluctuations in eustatic sea level through time.

1.2.1.3.2 Depositional Setting for High Energy Environment

Based on the association of traction current structures with the finer grained rocks, and evidence presented above for basal deposits, the sandstones represent deposition in submarine channels and fans. The Spraberry sandstones analyzed in this study are interpreted as deposits of deep-water origin, specifically deposits of waning traction currents that were responsible for the filling of erosional channel cuts on the higher energy, inner/middle portions of submarine fans.

Lithofacies L6 and L7 were formed from the channelized portions of the inner fan to non-channelized middle submarine fan. They are associated with thinly bedded sandstone/shale sequences (with lenticular/wavy and convoluted bedding) of lithofacies L3, interpreted as basinal, fine-grained tail of interflows.

Sandstones of lithofacies L8 are classical turbidite deposits. These deposits occur within the upper portions of channel fills and within non-channelized portions of the middle fan. Thinly interbedded sandstones and mudstones of lithofacies L8 are traditional distal turbidites: deposits of low density turbulent flows on the outer portion of the fan.

1.2.1.4 References

1. Basan, P. B. et al., 1978, Trace Fossils Concepts, SEPM short course No.5. P. 142-143.
2. Handford, C. R., 1981, Deep-water facies of the Spraberry Formation (Permian), Reagan County, Texas; a core workshop (No. 2); Siemers, Tillman, and Williamson.

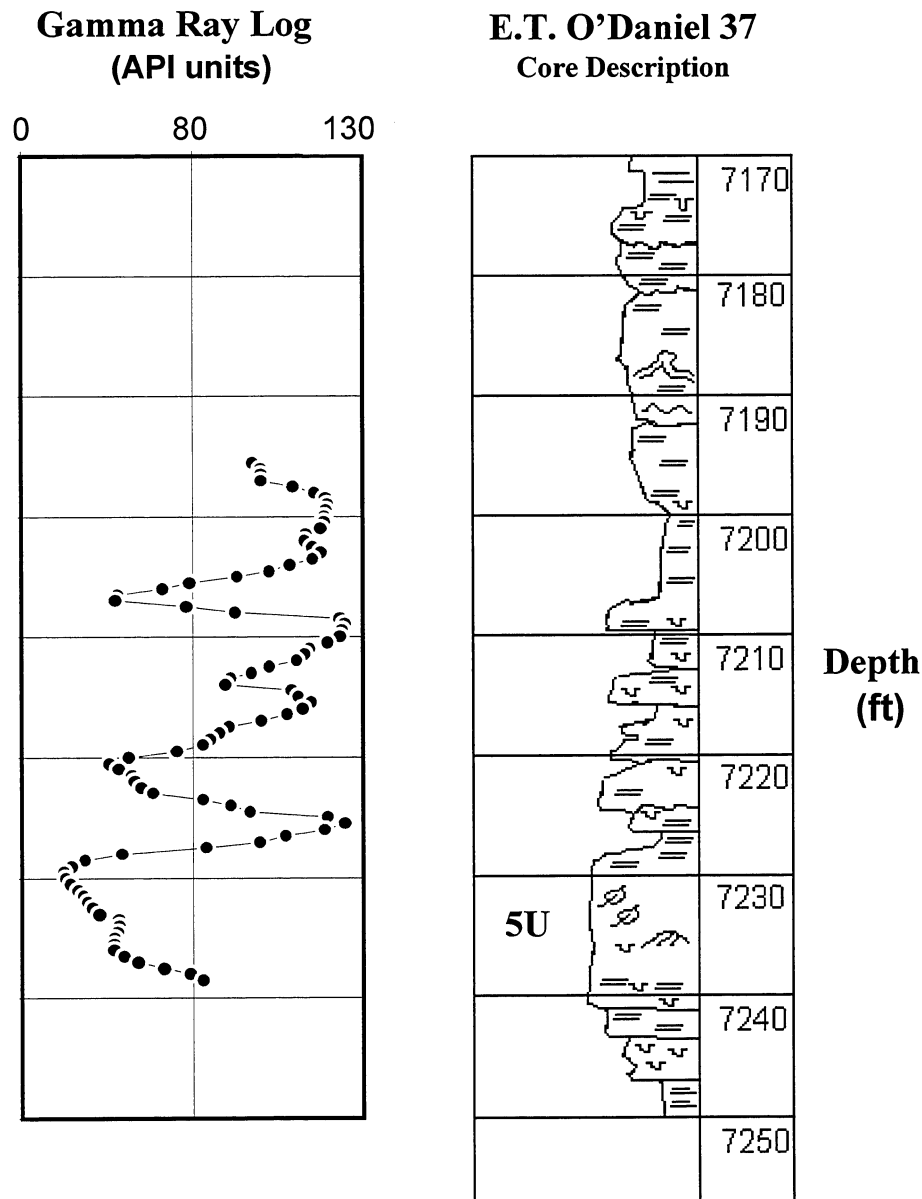


Fig. 1.2-1 Depth profiles showing the correlation of gamma ray log with core description for the E. T. O'Daniel 37 well.

1.3 PETROGRAPHY AND DIAGENESIS

1.3.1 Petrography

Thin section petrography, x-ray diffraction for clay mineralogy and fracture cements, and scanning electron photomicrographs were used to define mineralogy, rock fabric, texture, pore morphology and distribution, and diagenetic features and history for samples from three cores from the Spraberry Formation.

The three cores analyzed are from the upper Spraberry Formation. Only the two most important productive zones, units 1U and 5U, were studied. Two of the three cores contain both zones, while the Shackelford 138-A core contains only the 1U unit. A list of the different techniques applied to each well per unit and depth of coring is shown in Table 1.1-1.

Out of approximately 100 thin sections analyzed, 80 were point counted (see Table 1.3-1). Detailed point count analysis was conducted (300 points counted per thin-section) to determine the percentage amounts of detrital and authigenic minerals making the rock fabric, the amount and type of pore filling constituents, and the percentage of visible pore space. Based on this type of analysis, six small-scale lithofacies, referred to in this writing as rock types, have been described.

1.3.1.1 General Textures and Mineralogy

Spraberry reservoir rocks are typically low porosity, coarse siltstones to very fine sandstones that are intercalated with shaly non-reservoir rocks. Samples examined for this study cover a range of rock types from very fine and clay rich massive shales, through coarse laminated siltstones, to the very fine grained sandstones within the operational units 1U and 5U of the upper Spraberry Formation. Most of the carbonate muds and shales are matrix supported, while sandstones and siltstones display grain supported fabric.

Spraberry reservoirs have grain size ranging from 45 to 66 μm with an average of 60- μm (Rock Type "A") (see Table 1.3-1). Grain sorting varies from moderately well sorted clayey coarse siltstones to very well sorted clean sandstones. Grain shape ranges from subrounded to angular.

The rock fabric displays two main forms: massive and laminated. Mottled sedimentary fabric is not rare and it is associated with burrowing and/or dewatering action. Water escape pillars are commonly found within the Spraberry stratigraphic sequence. Burrowing produces patches of coarser grain size that look cleaner and sandier than surrounding shaly sediments. Other structures noted are cross stratification, which is fairly common in the very fine sandstones, and soft-sediment deformation.

Monocrystalline quartz is the dominant type of detrital grain. Other abundant detrital grains are plagioclase, K-feldspar and muscovite mica. Rock fragments, heavy minerals, and carbonate fragments are present in minor amounts. Detrital clay matrix (laminar clays + dispersed clays + organics) averages 22.4% in argillaceous laminated siltstones (Rock Type “F”) and 40.6% in shales (Rock Type “E”) (see Table 1.3-1). Typically clays, organic debris, carbonate mud, and considerable amounts of mica flakes and pyrite form a fine laminae. Massive very fine sandstones and siltstones (Rock Type “A”) contain only minor amounts of clay matrix.

Authigenic minerals observed in variable amounts depending on the petrographic category include quartz, dolomite and ferroan dolomite, calcite and pyrite. Barite is also abundant as fracture-filling cement. Amounts of primary and secondary porosity also show variable values for the different mineralogical facies (see Table 1.3-1).

In this study, XRD diffractograms were recorded for samples along 60 ft of core (Shackelford 138A) in order to define clay mineralogy within the various lithologies. Table 1.3-2 shows the results of XRD analysis of clay samples ($<2\mu\text{m}$, grain size) from the Shackelford 138A. Relative amounts of different clays were calculated in a semiquantitative manner using a series of formulas developed by G. Austin (personal communication). Illite occurs as the dominant clay mineral followed by chlorite, kaolinite and traces of mix-layer illite/smectite.

Illite clays are optically identified using SEM photomicrographs (Fig. 1.3-1). X-ray diffractograms show the different characters of clay peaks that can be observed between clean very fine sandstone at a depth of 7087 ft, and an argillaceous sample at 7104 ft depth (Fig. 1.3-2). The difference of peak intensity between these two lithologies is probably due to the fact that much of the clay in sample 7087 is diagenetic, while sample 7104 has dominantly detrital types of clays. The diffractogram for Shackelford 138A (7104 ft) presents sharper and longer peaks suggesting more abundance or probably better crystallinity of clay minerals than the sample at 7087 ft. (I) illite, (K) kaolinite and (CL) chlorite.

1.3.1.2 Porosity

Two major pore types and five subcategories were identified based on pore size, pore shape, and general pore morphology. Primary pores include intergranular macropores, intergranular mesopores, and micropores. Secondary pores are generally oversized (up to $50\mu\text{m}$) and are a product of dissolution of precursor grains and cements. All pore types determined and discussed here are summarized in Table 1.3-3.

1.3.1.3 Small Scale Lithofacies – Rock Types

Six rock types were identified based on microscopically observable features. Characteristics used to define each group include porosity, amounts of clays and organics, amounts of carbonate mud and cements, textural features such as relative abundance of laminae or massive fabric, burrows, grain sorting and grain size.

1.3.1.3.1 Rock Type “A”

Moderately good porosity, very fine sandstones and coarse siltstones, reservoir rocks - Very fine sandstones and siltstones are distinguished as the best quality reservoirs within the upper Spraberry Formation. Of arkosic to subarkosic composition, these light colored, massive to poorly laminated sediments represent the highest porosity rocks among all six petrographic categories. Rock Type “A” sandstones contain most of the different types of pores noted in Spraberry rocks; however, there are significant amounts of secondary pores (Pore Type 5) and primary pore types 1 and 2 (see Table 1.3-3 for definition of pore types).

1.3.1.3.2 Rock Type “B”

Slightly shaly laminated and/or patchy siltstones and very fine sandstones; low quality reservoir rocks - Not as much dissolution porosity is observed within these rocks as within Rock Type “A” rocks. Quartz and feldspar grains are again the main mineral species (arkosic composition). Relatively higher amounts of clay, organic matter, carbonate matrix and cements, and relatively lower porosity characterize this facies. Rock Type “B” exhibits considerably more lamination and burrowing than Rock Type “A.” These silica-cemented, slightly laminated and patchy very fine sandstones are considered low quality reservoir rocks of secondary importance.

1.3.1.3.3 Rock Type “C”

Silty Dolomite mudstones “Dolostone” - From the observation of core macro-samples these sedimentary rocks are described as dark gray very fine grained dolomites; possibly mudstones in “*Lithofacies 5.*” Thickness varies from a few centimeters to several tenths of centimeters. They are commonly massive but can show some laminae formed of a mixture of carbonate mud, clays, and organics. Thin section specimens show that a silty micritic dolomite is the major component of this facies. These rocks present a general lack of porosity and form non-reservoir rocks with good seal characteristics.

1.3.1.3.4 Rock Type “D”

Very “patchy” dolomitic siltstone - These samples, like Rock Types “A” and “B,” are arkosic to subarkosic in composition. The major detrital grains are quartz, followed by feldspars and minor rock fragments. Dolomite and calcite are pervasive cements forming patches scattered throughout the rock. Porosity amounts are moderate to low. A higher percentage of dolomite cement distinguishes Type “D” siltstones from the similar, but less dolomitic, Type “B” rocks. Rock Type “D,” calcareous “patchy” siltstones are marginal reservoirs.

1.3.1.3.5 Rock Type “E”

Shales and Silty Shales - Shales and silty shales, together with the silty dolomite mudstones (Rock Type “D”) show the lowest amount of pore space among the six categories described, while clay matrix is abundant. Color varies from gray to black. Non-reservoir rocks, these were probably hydrocarbon host rocks from deposition until migration of oil to high porosity units, and presently they form excellent seal rocks.

1.3.1.3.6 Rock Type “F”

Argillaceous Highly Laminated Siltstones - Argillaceous highly laminated siltstones form a category that can grade from relatively clean laminated siltstones to very low reservoir quality laminated shaly siltstones. Depending on the relative amounts of clays, organics, pyrite and other argillaceous materials, sediments will present thinner or thicker laminae between silts and shales. This is the most common lithology occurring throughout the upper Spraberry Formation in the three cores examined. Laminated shaly siltstones are darker in color, and differ from the cleaner siltstones (Rock Type “B”) in having significantly higher amounts of argillaceous matter. Laminated shaly siltstones tend to be matrix supported.

1.3.2 Diagenesis

Very fine sandstones and coarse siltstones of the upper Spraberry have been subjected to highly variable degrees of post-depositional alteration (diagenesis). Diagenesis has resulted in an overall reduction of original porosity and permeability. Variations in the extent of compaction, cementation and dissolution have overprinted the original rock fabric, and asserted certain control to spatial variations in reservoir quality within the upper Spraberry Formation.

1.3.2.1 Quartz and Feldspar Overgrowth, Authigenic Feldspar, and Pressure Solution

Quartz overgrowths: Quartz overgrowths are noted as euhedral grain boundaries or by the presence of vacuoles or dust rims that separate grain from cement. Quartz cement is most abundant in Rock Type “A” and “B.” In general, median values of quartz overgrowth percentages (from point count) vary from one category to another (see Table 1.3-1). The lower values of quartz cement found in Rock Type “B” suggests that the presence of larger amounts of clays and carbonate cements probably have somewhat inhibited growth of quartz cements.

Authigenic feldspar: Authigenic feldspar is a minor cementing agent occurring in quantities of 1% or less. Alteration and dissolution of weaker feldspar mineralogy is found repeatedly in the Spraberry Formation.

Pressure solution: Overpressuring during compaction in conjunction with several other factors can cause pressure solution. The effect of compaction is clearly observed within the matrix-free sandy petrographic categories and lithofacies. Flat and concave-convex grain suturing contacts are common in these lithofacies, denoting the pressure solution effect between quartz grains. It is possible that some of the silica in quartz overgrowths was derived from pressure solution processes.

1.3.2.1.1 Authigenic Clays

The Spraberry Formation contains abundant clay, although it is not an easy task to differentiate between depositional and authigenic clay. Detrital clays in the sand rich facies caused very low initial porosity and permeability, which were only decreased by compaction. Rock Type “E” and “F” presents a thick mixture of clays, organics, carbonate muds, and common associated pyrite

precipitates and mica sheets that appear very well compacted. It seems that Rock Type “A” and “B” have gained from having more pore space available so hairy illite flakes have developed. Both forms of clay described above are presently diagenetic forms, either through recrystallization of large clumps of compacted clays or neoformation of fibrous flakes.

1.3.2.1.2 Pyrite

Authigenic pyrite occurs in small quantities in all lithologies and is especially abundant in shales and shaly samples. Nodules of pyrite, 1 to 0.5cm, flattened due to burial during compaction are visible in hand specimens. Framboidal pyrite is also noted in association with organic-rich facies.

1.3.2.1.3 Carbonate

Authigenic carbonates are the most abundant cementing agents in the Spraberry Formation. Utilization of proper staining, along with observation in scanning electron microscopy, helped identify dolomite cementation and replacement of microorganisms and detrital grains. The authigenic character of the dolomite is quite clear when observed as large patches of poikilotopic cement and replacement of detrital grains.

1.3.2.1.4 Pore Space

Pore types have been identified on the basis of size, shape, origin and distribution using qualitative thin section and SEM photomicrographs of rock samples (see Table 1.3-3). These analytical procedures reveal that the pore systems of these rocks consist of varying proportions of five (5) pore types.

Type 5 pores, secondary dissolution pores, are moderately abundant in some parts of the upper Spraberry Formation. The most common recognizable secondary porosity feature is the partial or total dissolution of feldspar grains. Remnants of partially dissolved grains within a pore space with typical grain shape are often found in thin sections from the very fine clean sandstones and siltstones (Rock Type “A”). Relict features of cleavage with the typical extinction patterns of plagioclase (probable Ca rich) are also commonly found. Dissolution is also observed in unstable carbonate grains and cements.

One type of secondary pore is an oversized pore formed by dissolution of framework grains, patches of matrix, or cements. This type of pore has a greater diameter than the average detrital grain size. Moldic pores are also seen in thin sections from the Spraberry Formation, and are recognized by geometrical shapes of the precursor grains. Another very common secondary pore is the intra-constituent pore, which occurs mainly within framework grains, but also in cement and matrix. Secondary intergranular pores are very difficult to differentiate from primary intergranular pores due to their similar habit.

1.3.3 Paragenesis

Upper Spraberry sandstones have been subjected to several stages of diagenesis. Diagenesis has resulted in both the occlusion and, rarely, the enhancement of porosity and permeability. The

relative timing of various diagenetic events may be deciphered by examination of the spatial relationship of cements in thin section or with the scanning electron microscope. The following diagenetic sequence has been determined for upper Spraberry sandstones examined in this study:

1. Deposition of sediments with initial primary intergranular porosity. Some interstitial space within more poorly sorted and lower energy deposits filled by detrital clay matrix.
2. Basinal sediments that were deposited in anoxic bottom waters conditions experienced varying degrees of pyrite precipitation due to the production of H_2S by sulfate reducing bacteria at the sediment-seawater interface prior to burial.
3. Shallow burial. Minor adjustments in grain packing in response to burial loading. Some rocks, particularly clean sandstones of submarine channel origin, were subject to an early stage of silica overgrowth cementation. While volumetrically insignificant in controlling reservoir quality variations, these overgrowths aided in arresting compactional effects and preservation of porosity and permeability.
4. Precipitation of calcite cement (a near surface event-precipitation from connate waters in equilibrium with seawater).
5. Precipitation of chlorite, illite and smectite.
6. Dolomite cement precipitation.
7. Late stage precipitation of silica overgrowth (individual euhedral crystals rather than more extensive and massive overgrowths). Minor development of K-feldspar overgrowths on framework feldspar grains.
8. Late stage precipitation of fibrous illite clay growths on pore walls and within pore throats. Illite clay cement, while volumetrically insignificant, bridges pore throat openings dramatically reducing formation permeability.
9. Fracture formation after enough unconfinement effect is produced.
10. Fracture mineralization, mainly calcite and barite.

1.3.3.1 Porosity, Dissolution and Reservoir Quality Preservation

Various diagenetic processes have enhanced or damaged the initial pore structure of Spraberry rocks. The interaction of compaction effects, cementation, dissolution and fabric rigidity within the original rock texture has resulted in highly variable pore structures in Upper Spraberry rocks. A number of factors affect the formation, preservation, and damage of pore space:

1. Original rock texture: this controls grain size and sorting. Very fine grained, poorly sorted sandstones of submarine channel abandonment, distal turbidite, and basinal origin have smaller pore and pore throat sizes than coarser grained and better-sorted sandstones of submarine channel origin. Pore size distribution is more heterogeneous within the low energy, basinal siltstones and sandstones: a function of lamination and bioturbation.
2. Compaction: this controls grain packing and the degree of deformation of ductile grains. Compaction has resulted in a reduction of the original size of pore bodies and pore throats, and therefore has contributed to a general reduction in porosity and permeability during burial. Compaction must have affected in a greater manner the more ductile composition of the various clay rich lithofacies and petrographic categories (L1, L2, L3 and L4 section 1.2; and RT "E" and RT "F" section 1.3-Petrography).

3. Cementation: this also results in reduced pore and pore throat size and increased pore system tortuosity (in the case of sandstones with microquartz, carbonate and clay cements). Precipitation of authigenic clay can produce a dramatic increase in pore surface area, and in partitioning of intergranular pore space near pore walls into micropores (pores < 5 μm in diameter). Additionally, the bridging effect of pore throats by fibrous illite has an effect far in excess of the small volume of clay present, dramatically reducing formation permeability.
4. Dissolution: Dissolution of chemically unstable grains produces secondary porosity within very fine-grained sandstones and siltstones, usually improving permeability (Lithofacies L6, L7, L8 section 1.2; RT "A" section 1.3-Petrography).
5. Fabric rigidity: Despite being subject to burial loading, some of the Spraberry lithofacies and petrography categories examined in this study (Lithofacies L6, L7, L8 section 1.2; RT "A" and RT "B" section 1.3-petrography) have retained significant amounts of original intergranular porosity, resisting grain slippage and packing adjustments. Petrographic analysis suggests that this is the result of non-ductile fabric composition and early silica cementation, which arrested grain slippage by increasing the mechanical strength (rigidity) of the rocks.

An important event that perhaps followed the dissolution in the Spraberry Formation is the preservation of porosity due to significant increases in geopressures. High overburden effects are suggested by the pressure solution characteristics such as long and sutured grain boundaries found within the very fine sandy units of Spraberry Formation. The formation of regional vertical fracture systems, which are very important for fluid conductivity in the reservoirs, are also related in part to the occurrence of overpressure events within the reservoir sands (Lorenz, et al., 1991). Some characteristics of the Spraberry Formation are common to overpressured formations. Highly compressible shales, rich in organic fluids, are overwhelmingly more abundant in the Spraberry Formation than the rigid, fine, clean, and porous sandstones. In these clay-rich systems high amounts of fluids are gradually injected into the more porous sandstone and siltstones from the shales by compaction dewatering. After the lithification occurred, shaly rocks and carbonates that presently show a total lack of permeability formed a very good seal preventing escape of fluids from the enclosed sandy units. Very high pore pressure must have been preceded by periods of high lithostatic compression that promoted dissolution of silica at grain contacts. With the final buildup of overpressuring and due to reduction in effective stresses, both fracture formation and preservation of matrix porosity occurred.

The influence of secondary porosity in reservoir quality is important, but that much porosity is simply redistributed rather than newly produced (Bloch, S., 1994). Material dissolved in one place may be redeposited only a short distance away. Pore space formed by the dissolution of framework grains in the Spraberry Formation can increase the total amount of porosity but it is understood that an equally considerable improvement of permeability rarely occurs. Dissolution of very small grain and intra-granular material may produce pores that are too small or isolated to increase effective porosity. Pore space formed by dissolution of pore filling cements is often more important in substantially improving porosity and permeability. Physically and chemically relatively stable arkosic and subarkosic compositions such as the Spraberry reservoirs are the type of lithology that can preserve high amounts of dissolution porosity.

1.3.3.2 Hydrocarbon Emplacement

An interesting relationship exists between the progressive increase in crystallinity (lattice order) and the amount of illite with the simultaneous thermal maturation of hydrocarbon in potential source rocks. Catagenesis, the action of generating oil at a given temperature range during burial, seems to occur parallel to the abrupt transformation of illite/smectite sequences into the ordered R=1 polytype (Jadgozinski, H., 1949).

The relation between maturation of oil and alteration of clays is still not well understood. Temperature wise there is a range that goes from approximately 100°C (abrupt change to the ordered rectorite type of I/S; R=1) to 175°C where a higher stage of ordering of I/S is produced (R≥3) (Eslinger, et al., 1988). The “oil window,” or temperature range where hydrocarbon maturation occurs (65° to 175°) roughly coincides with the rectorite range of illitization shown above. The temperature of oil maturation is above the random I/S (R=0), yet just below the range temperature for a very ordered “Kalkberg” (I/S, R≥3), and closely coincides with the rectorite (I/S, R=1) range of temperatures. Spraberry rocks coincide with the typical assemblage of clays for ordered polytypes; however, possible paleo-temperatures found by others (60°-77°C; Houde, 1979 and Dutton, 1980) may only reach the initial part of the oil maturation stage. These temperatures are not enough to account for the lack of expandable smectite layers noted in the Spraberry, unless the time and kinetics with rocks of Permian time have worked in favor of the illitization processes. Another possibility is that a relatively low amount of smectite was present in the initial composition of the sediments. The latter is not very probable due to the high amount of smectitic clays that is usually present in this type of sediments.

1.3.3.3 Fracture Model

In this section we explain a diagenetic model for the fracturing of the Spraberry Formation. Macro-observations of core samples, microscopic analysis of thin sections, and information extracted from XRD and SEM analysis of clays have helped construct a history of burial, compaction, lithostatic pressure buildup for vertical, and horizontal stresses, pore pressure increase, reduction of unconfinement and fracturing.

The gradual increase in burial depth produced an increase of compaction, pressure, and temperature. The clay-rich nature of the Spraberry, interbedded with only a minor amount of fine sands and siltstones, provides a typical environment for production of significant overpressuring. Clay sediments mixed with organic matter are characterized by having the highest initial porosity and contain large amounts of fluid. Burial compaction and diagenesis of this material usually results in almost total destruction of porosity within the clayey sediments accompanied by a tremendous loss of fluids. At the same time that the principal vertical stresses are being increased, the pore pressure mainly within the sandy part of the formation is increased due to the migration of huge amount of fluids into the sands. Pressure solution features, typical of overpressured sands, have been found during petrographic analysis. These conditions probably caused the necessary reduction of principal effective stresses to a level at which enough unconfinement (Lorenz et. al. 1991) effect is created to cause fracturing. Then mineralization of

fractures occurred. Fracture cements analyzed by XRD, thin section observations, and SEM analysis have shown the presence of calcite, barite, and also quartz.

Pressure solution of grain boundaries and quartz overgrowth are abundant in the majority of the thin-section examined. Matrix free sandy siltstones and very fine sandstones show the effect of compaction. Grains show both flat and concave-convex contacts.

The following is a brief account of the result encountered on examination of horizontal cores retrieved from the upper Spraberry Formation. Horizontal cores from upper Spraberry 1U and 5U units provided invaluable evidence on fracture orientation, spacing, aperture, and mineralization. However many questions still remain to be answered concerning the origins of the various fracture sets, the relationship of the fracture network to rock matrix, and its effect to rock production. At least three sets of fractures are found within the upper and middle Spraberry cores. These sets have distinct orientations, spacing, mineralization, distribution with respect to lithology, and surface characteristics (Lorenz, 1997).

1.3.3.3.1 1U Fractures:

Fractures found in the 1U zone of the upper Spraberry have a NE strike, and tend to be partly mineralized with barite, quartz, and dolomite. Fractures with NE orientation have a maximum of seven ft and an average of about 3.2 ft. In the megascopic view, this set of fractures has fairly smooth and planar surfaces that show no evidence of movement or shear. Microscopic examination of 1U fracture surfaces shows that barite occurs in large crystals (1mm or more) with very smooth tabular faces. Barite crystals can partly to completely cover the surfaces of 1U fractures and appears to occlude porosity and may be responsible for reducing the crossflow of fluids and gas between rock matrix and fracture porosity. Quartz and dolomite occur in varying abundance as authigenic minerals on 1U fracture surfaces; however, their size and morphology do not seem to have the same deleterious effect on porosity. Indeed, although quartz crystals seem insignificant in terms of abundance and size, they provide numerous asperities that may prevent these fractures from closing even at reservoir pressure conditions. The presence of abundant euhedrally-terminated quartz demonstrates that fractures were open during certain periods of diagenesis.

1.3.3.3.2 5U Fractures:

The 5U zone of the upper Spraberry contains fractures with NNE and ENE orientations. These are two separate sets of fractures. The NNE set of fractures has stepped fracture surfaces indicating a shear origin, and minor amounts of fracture mineralization. These fractures have a fairly narrow spacing, with an average of about 1.6 ft and a maximum of about 5 ft. The ENE fracture set has smooth planar surfaces of tension origin with some calcite mineralization present. Spacing between fractures in this set is quite different than seen in the other two sets. The spacing is about 3.79 ft, but the maximum spacing is over 14 ft and the most common spacing is less than 2 ft. Like 1U fractures, these have a smooth planar appearance with no indication of shear, but there appears to be no surface mineralization under visual examination. Closer examination of 5U fractures shows that surface mineralization is present on these fractures, but not in the abundance of 1U fractures. Quartz and dolomite are both fairly common,

but barite is rare. Calcite cement was not seen in 1U fractures, however it has been observed in several 5U fractures of N70E orientation.

1.3.3.3.3 Other Fracture Sets:

Natural fractures in black shales overlying both the 1U and the 5U have an ENE orientation similar to unmineralized fractures in the 5U. No fractures were encountered in similar shales underlying reservoir zones. A set of hairline fractures, most completely healed with calcite cement, was also found in some Middle Spraberry cores.

The unique nature of each of these fracture sets implies that fracturing probably occurred as separate events and indicates that the Spraberry Formation has undergone a more complex stress history than might be construed from its fairly flat-lying nature.

1.3.3.3.4 Fracturing Paragenetic Sequences:

The N42E fracture set probably occurred first, as there is no barite mineralization within the few N80E fractures that were noted. Following fracturing, minor dolomite quartz precipitation occurred. Based on preliminary scanning cathodoluminescence studies (CL), it is believed that these cements were being precipitated both within the rock matrix and the fractures themselves contemporaneously. The barite was formed at a later time, deduced from the fact that there is little or no barite within the rock matrix.

Paragenesis of 5U fractures is more complicated, as there are two sets of fractures. The N70E fracture set is believed to have formed first since there are a couple of examples of these fractures causing termination of N32E fractures. As in the 1U, diagenesis of matrix and fracture probably occurred near the same time. Later movement of fluids through the fractures caused at least local precipitation of calcite within fractures and nearby rock matrix. The N32E fracture set formed subsequent to this first fracture event, and there is minor precipitation of quartz and dolomite within these fractures. Barite precipitation probably occurred following the first fracture event, but there is not enough evidence to determine its relation to the second fracture event. The fact that barite is not abundant in any 5U fractures and was only noted in samples containing N70E fractures suggests that the precipitation of Barite occurred between the two fracture events.

The earliest stages of diagenesis and dolomitization were followed by a period of fracturing, possibly the N70E fracture set in the 5U. The stresses or events that caused this fracture set may have been stronger deeper within the Spraberry. This is suggested by the presence of calcite-filled fractures within the middle Spraberry and the 5U, but not within the 1U. Precipitation of calcite cement within the N70E fractures followed. The next event was probably fracturing within the 1U that caused the N42E fractures. At least three phases of carbonate are present in some 1U samples, with dolomite being the first-formed phase followed by ankerite, then a ferroan dolomite. Ferroan dolomite is the most common phase seen within the 1U fractures. Non-luminescent quartz cement is seen both within fractures and rock matrix, suggesting that fracturing and precipitation of quartz and ferroan dolomite were occurring at the same time. Precipitation of barite within 1U fractures and possibly within the 5U followed. A third fracture

event then affected the 5U and formed the N32E. This was the only event that involved any obvious signs of incipient shear stress. The other fractures are solely tension-type fractures. Precipitation of quartz and dolomite within this fracture set then followed.

1.3.4 Discussion:

1.3.4.1 Relationship Between Depositional Features, Textures, Mineralogy, Provenance, Pore-Filling Constituents, Pore Space and Reservoir Quality

The very fine grain size shown by the Spraberry sandstones reflects their distal depositional position within the Permian basin. The angularity of about half of the detrital grains and the presence of numerous strain shadows is described by Warn and Sidwell (1953) as a physical wear that can only occur due to impact during long reworking and transportation by water. Suspension settling, saline density currents, and turbidites are the main mechanisms of sediment transport (Handford, 1981; N.Tyler and Gholston, 1988; Guevara, 1988). Very fine sandstones and siltstones commonly form the coarser bottom part of fining upward sequences having sharp erosional contacts with underlying shales and muddy burrowed tops.

Diagenetic processes have obviously overprinted original depositional characteristics. However, mineralogical composition due to provenance and depositional factors probably exerts the most important control on reservoir quality. For example, the dominantly arkosic composition of the Spraberry sandstones and siltstones helped maintain some reservoir quality because the rigid and low ductile character of the framework grains made these rocks more resistant to compression forces. Also, quartz rich rocks are more stable and resistant to chemical alteration. On the other hand, cleaner sandstones and siltstones tend to be more affected by precipitation of quartz and other types of cement into open pore spaces. Pressure solution is also more prevalent. To some extent, the presence of argillaceous materials may prevent nucleation of quartz or carbonate cements on grain surfaces. Spraberry reservoir rocks represent a balance between the mechanisms of pore space preservation and destruction.

In the Spraberry sands there are minor amounts of interstitial clay, silt, and organics that Warn and Sidwell (1953) tried to explain by considering deposition in mildly turbid waters, which do not allow for complete and final size sorting. Another possibility for the hydrodynamically unlikely occurrence of fine clay mixed with coarser silts and sands is the infiltration of detrital clays in sandstones (Walker et al. 1978). Thus, original low porosity after deposition with a moderately sorted grain fabric was further reduced by authigenic cements and compaction. Bloch and McGowen (1994) stated that “porosity is essentially independent of grain size but it is strongly controlled by sorting and decreases progressively from very well-sorted to poorly sorted sand.”

Another indirect depositional control on quality is the very fine grain size of these sands and silts, which probably causes marginal permeability in Spraberry reservoirs (Bloch and McGowen, 1994). Reducing the size of grains produces a proportionally equal decrease in pore size. Total porosity for a given volume of rock does not depend on grain size. However,

reservoir quality will rely less on total amount of porosity than it does on the pore size of the individual pores. Considerable reduction of grain size does cause a direct decrease in *pore throat aperture* and in the size of individual pores. A decrease in the pore throat aperture causes higher capillary pressures that further damage the conductivity of fluids throughout the reservoir. Bloch and McGowen (M. Wilson, 1994) have stated that at the reservoir scale, grain size is the primary control of permeability. A decrease in grain size from proximal to more distal facies is generally accompanied by decreasing permeability.

Visual differences between the organic-rich clays of the shaly facies (Rock Type “E” and “F”) and the much less abundant clays in the clean facies (Rock Type “A” and “B”) are quite obvious too. Shaly facies present deposited laminae with a matrix mixture of clays, organics, carbonate muds, and common associated pyrite precipitates and mica flakes that are parallel or sub-parallel to the bedding. The more porous rock types “A” and “B” show well defined fibrous illite, which differs from the poorly developed and compacted clays of Rock Type “E” and “F.”

The amount of expandable clays was small and was restricted to minor quantities of interbedded smectite with illite. The possibility that the expansion effect and high cation exchange capacity of smectites damaged porosity or permeability is relatively low. Small amounts of expandable clays suggest that the bad effect on any type of electric log or porosity logs, from bound water in interlayer between successive lattices of smectite is very low. However, structural water contained in illite and chlorite should still affect the response of electric logs. The main effect of the clays present in the Spraberry rocks is in the damage of reservoir pore space and fluid conductivity, by forming pore lining, pore coating, and pore filling.

Mineralogy, the presence of matrix-supported or grain-supported fabric, grain size, sedimentary structures, and ultimately, reservoir quality, vary with lithofacies type. This is, in turn, a product of deposition and diagenetic changes. The main controls over reservoir quality are clay matrix content, carbonate content, presence of quartz overgrowths, and pressure solution of grains by compaction.

Very fine sandstones and siltstones (Rock Type “A”) were observed to be very clean and present the highest level of porosity among the distinct lithofacies groups. However, the detrimental effect of silica cement was found to be most notable with these clean sandstones as well as in thinner intervals with lower reservoir quality (Rock Type “B”). Patchy dolomitic siltstones (Rock Type “D”) that have relatively high amounts of carbonate cements form a second category of possible reservoir rock. Substantial dissolution has taken place in some of these rocks, thus, they are considered moderately good quality reservoir rocks. Shales and shaly laminated siltstones (Rock Types “E” and “F”) are the dominant lithofacies present in most of the cores examined. These are seen as rocks of low to very poor reservoir quality as are Rock Type “C” micritic dolomitic mudstones.

1.3.4.2 References

1. Bloch, S., 1994, Secondary porosity in sandstones: Significance, origin, relationship to subaerial unconformities, and effect on pre-drill reservoir quality prediction. From Wilson M.

- D., Reservoir quality assessment and prediction in clastic rocks, 1994, SEPM short course 30, p. 137-162.
2. Bloch, S., and McGowen, J. H., 1994, Influence of depositional environment on reservoir quality prediction. From Wilson M. D., Reservoir quality assessment and prediction in clastic rocks, 1994, SEPM short course 30, p. 41-57.
 3. Dutton, S. P., 1980, Petroleum source rock potential and thermal maturity, Palo Duro basin, Texas: Texas Univ. Bur. Econ. Geology Geol. Circ. 80-10, 48 p.
 4. Eslinger, E., and Pevear, D., 1988, Clay Minerals for petroleum geologists and engineers: SEPM short course notes No. 22., SEPM, Tulsa OK.
 5. Guevara, E. H., 1988, Geological characterization of Permian submarine fan reservoirs of the Driver Waterflood Unit, Spraberry Trend, Midland Basin, Texas; BEG, UT Austin; Report of Investigation No. 172.
 6. Handford, C. R., 1981, Deep-water facies of the Spraberry Formation (Permian), Reagan County, Texas; a core workshop (No. 2); Siemers, Tillman, and Williamson.
 7. Houde, R. F., 1979, Sedimentology, diagenesis, and source bed geochemistry of the Spraberry sandstone, subsurface Midland basin, West Texas, Unpub. MS thesis, UT Dallas.
 8. Jadgozinski, H., 1949, Eindimensionale Felordnung in Kristallen und ihr Einfluss auf die Rontgeninterferenzen. I. Berechnung des Fehlordnungsgrades aus der Rontgenintensitaten: Acta Crystallogr. 2, 201-207.
 9. Lorenz, J. C., Teufel, L. W., and Warpinski, N. R., 1991, Regional fractures 1: A mechanism for the formation of regional fractures at depth in flat-lying reservoirs. AAPG Bull., V. 75, no. 11, p. 1714-1737.
 10. Lorenz, J. C., 1997, "Horizontal Core Fracture Description," paper presented at the Spraberry Symposium, Parker & Parsley Development Company and U.S. Department of Energy, Midland, TX (Jan. 1997)
 11. Lorenz, J. C., 1997, Non-Congruent Natural Fracture Sets in Adjacent Beds at Depth: Data From Horizontal Cores from the Spraberry Formation, Midland Basin, TX, presented at: AAPG Hedberg Research Conference, Reservoir Scale Deformation – Characterization and Prediction, June 22-28, 1997, Bryce, Utah.
 12. Tyler, N. and Gholston, J. C., 1988, Heterogeneous deep-sea fan reservoirs, Shackelford and Preston waterflood units, Spraberry Trend, West Texas; BEG, UT at Austin, Report of Investigation No. 171.
 13. Walker, T. R., 1978, Deep-water sandstone facies and ancient submarine fans: Models for exploration of stratigraphic traps: AAPG Bull., v. 62, pp. 932-966.
 14. Warn, F. G. and Sidwell, R., 1953, Petrology of the Spraberry Sands of West Texas: Jour. Sed. Petrology, v. 23, pp. 67-74.

Table 1.3-1 Mineralogical averages for point counts of thin sections for six categories of small-scale lithofacies. Summary of data from three cores from three different wells.

PETROGRAPHIC POINT COUNT SUMMARY BY ROCK TYPE																													
	TEXTURE		GRAIN COMPOSITION										MATRIX					CEMENT COMPOSITION					POROSITY						
	ROCK TYPE	GRAIN SIZE (mm)	MONOCRYSTALLINE QTZ.	POLYCRYSTALLINE QTZ.	SUMA QRTZ	CHERT	MUSCOVITE	K-FELDSPAR	PLAGIOCLASE	IRF	MRF	SRF	CARBONATE FRAGMENTS (CALCITE)	ACCESSORY MINERALS	LAMINAR	DISPERSED	ORGANICS	DEPOSITIONAL CARBONATE (DOLOMITE)	SUMA MATRIX	UNDIFFERENTIATED CLAY	QUARTZ OVERGROWTHS	CALCITE	DOLOMITE	PYRITE	PRIMARY	SECONDARY	MICRO	TOTAL POROSITY	
	MAXIMUM	66.0	44.7	6.0	47.0	1.7	2.7	16.7	14.7	2.0	4.0	2.7		3.0	4.3	4.3	2.3	7.7	12.3	8.3	7.0	0.3	7.3	2.0	13.3	7.7	1.3	18.7	
	MINIMUM	45.0	36.0	1.0	39.0	0.3	0.3	6.3	3.7	0.7			0.3					0.7	1.7	1.0	3.3	0.3	2.7	0.7	7.3	2.7		10.3	
	AVERAGE	60.0	40.2	2.7	42.8	1.0	1.4	11.8	6.8	1.2	0.5	0.2		1.6	1.5	1.2	1.6	3.7	6.6	3.6	5.2	0.3	4.9	1.1	9.8	4.4	0.2	14.3	
	MAXIMUM	66.0	47.0	5.7	52.0	1.3	4.7	17.3	11.7	1.7	1.7	2.7	1.0	4.3	13.0	3.0	5.3	7.7	25.0	12.7	7.0			8.7	4.0	8.7	4.7	1.7	13.0
	MINIMUM	40.0	29.0	0.7	30.0	0.7	0.3	6.3	3.3	0.7	0.7	0.3	0.7	1.0	0.7	1.3	0.7	1.3	5.0	0.7	2.7			1.0	0.7	0.3	1.0	0.7	1.0
	AVERAGE	57.3	40.2	2.5	42.5	1.0	1.9	11.5	6.3	1.0	1.1	1.3	0.8	2.1	5.2	1.7	2.5	4.0	11.6	5.1	4.5			4.4	2.0	4.9	2.9	1.1	7.5
	MAXIMUM	60.0	23.7		23.7	0.3	2.0	5.7	2.7	0.7	0.7	7.7			2.7	2.7	8.7	38.3	41.0	4.3			3.3	31.3	3.7				
	MINIMUM	50.0	19.7		19.7	0.3	0.3	3.3	1.0	0.3	0.3	3.7			1.3	2.7	0.3	25.0	33.0	4.3			1.7	21.3	0.7				
	AVERAGE	54.8	22.3		22.3	0.3	1.2	4.1	1.8	0.5	0.5	5.7			2.0	2.7	4.2	30.7	36.1	4.3			2.5	26.4	2.1				
	MAXIMUM	60.0	39.3	4.7	42.0		2.3	8.0	3.7	0.3	0.7	0.3	2.0		4.3	2.3	2.7	25.7	35.0	3.0	4.7	3.0	18.3	3.0	4.3	4.0		7.3	
	MINIMUM	56.0	27.3	1.0	27.3		1.0	5.0	2.0	0.3	0.3	0.7			1.7	1.3	1.3	9.3	14.0	1.0	2.3	1.7	13.7	3.0	2.0	1.3		3.3	
	AVERAGE	58.3	34.9	2.3	36.8		1.8	6.3	3.1	0.3	0.4	0.3	1.1		2.3	1.6	1.9	17.6	22.2	2.4	3.7	2.5	16.1	3.0	3.1	2.5		5.6	
	MAXIMUM	62.0	44.3	3.3	44.3	0.3	7.7	9.3	5.3	0.7	1.0	0.3	2.3	3.7	44.0	3.3	9.7	4.7	56.7	20.7	1.3	2.3	2.0	6.7			1.0	1.0	
	MINIMUM	25.0	21.0	3.3	21.0	0.3	1.0	1.3	0.7	0.3	0.3	2.0	0.3		25.0	0.7	4.3	1.3	34.0	4.3	1.3	2.3	0.7	0.3			0.3	0.3	
	AVERAGE	39.2	29.0	3.3	29.3	0.3	5.5	4.9	2.9	0.5	0.7	0.3	2.2	1.7	30.7	2.1	7.1	2.2	41.1	13.3	1.3	2.3	1.3	3.0			0.7	0.7	
	MAXIMUM	58.0	42.7	4.0	46.7		5.3	16.3	11.7	0.7	1.7	0.7	0.7	2.0	19.3	8.0	5.3	8.7	33.3	14.0	4.7	1.0	4.3	5.0	4.7	2.3	0.7	7.0	
	MINIMUM	40.0	34.0	1.0	35.0		1.3	7.3	1.3	0.3	0.3	0.7	0.7	0.7	3.3	1.0	0.7	2.0	7.3	1.0	2.0	1.0	1.7	2.3	1.0	0.7	1.0		
	AVERAGE	52.6	38.8	2.0	40.0		3.0	11.7	5.6	0.5	0.7	0.7	1.1		13.4	4.2	3.0	3.4	22.8	6.1	3.0	1.0	3.1	3.5	2.4	1.2	0.7	2.9	

Table 1.3-2 X-ray diffraction data for clay mineralogy covering all lithologic types in the Spraberry Formation.

CLAY COMPOSITION from XRD ANALYSIS (parts in 10)				
Sample Depth (ft)	Illite	Chlorite	Kaolinite	I/S
7069	4	4	1	1
7076	10	--	--	--
7081	6	2	1	1
7082	6	2	1	1
7083	5	3	2	1
7085	7	2	1	--
7087	4	4	1	1
7290	6	3	1	--
7092	6	3	1	--

Table 1.3-3 A summary of the pore types encountered in SEM samples from the Spraberry Formation.

SUMARY OF PORE TYPES			
PORE TYPE	PORE MORPHOLOGY	PORE SIZE	PORE CONECTIVITY
PT1	Primary intergranular macropores with irregular shapes.	Relatively Large 30-40 μm	Relatively well interconnected, pore throats radius of 0.75-2 μm
PT2	Primary intergranular macropores with irregular shapes	15-30 μm	Moderately interconnected, pore throats radius of 0.4-1.0 μm
PT3	Primary intergranular mesopores generally Polyhedral pore shapes	5-15 μm	Poorly interconnected through pore throats <0.5 μm
PT4	Micropores. Pores are developed within clay cement rims on framework sand grains, between fibrous illite growths (often bridging pore throat), within partially dissolved grains, and within shale	Much less than 5 μm	No connectivity
PT5	Secondary dissolution pores crated by selective leaching of chemically unstable framework sand grains or cements. Usually polygonal in shape.	Oversized up to 40 μm	Very good connectivity

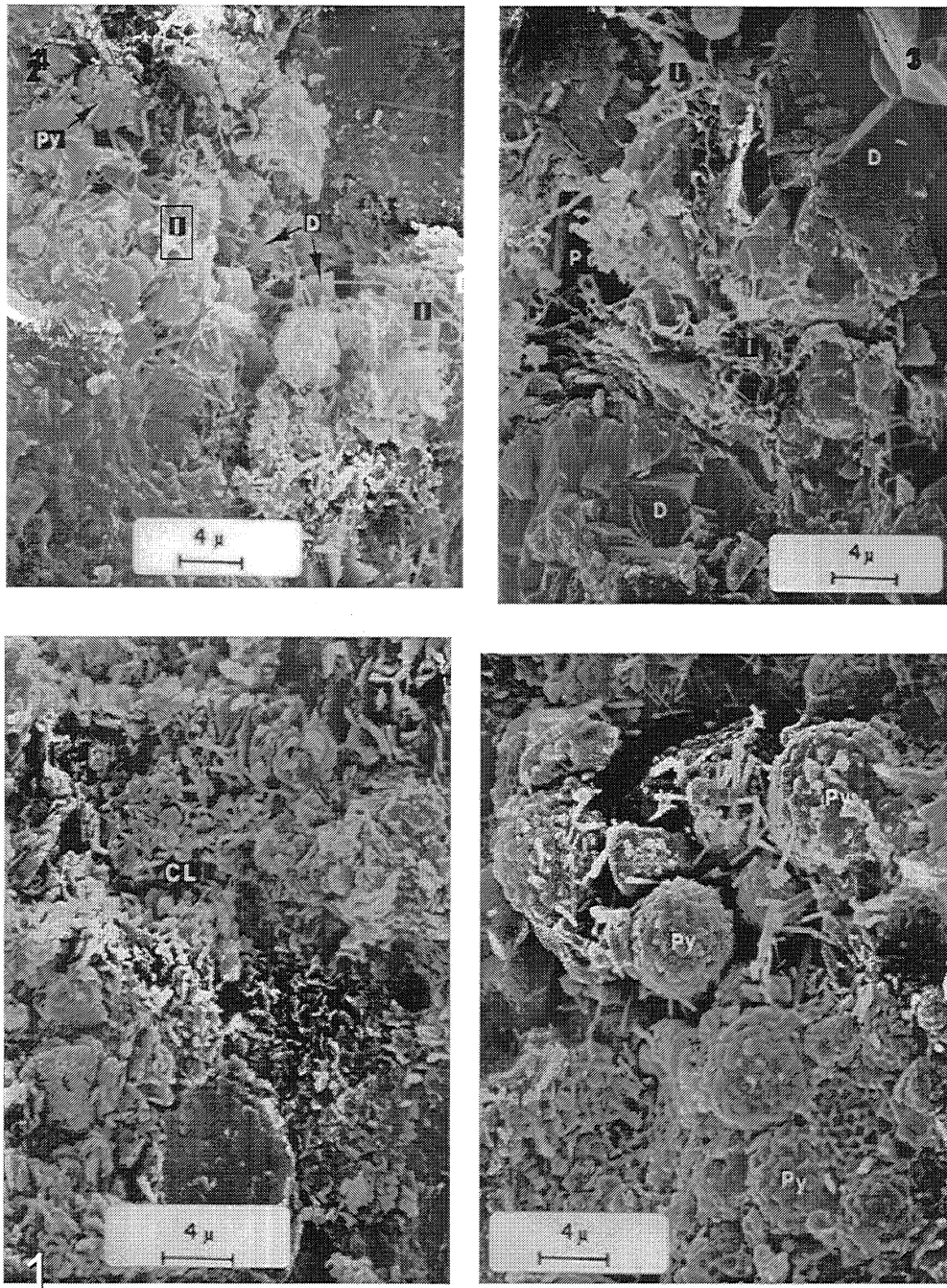
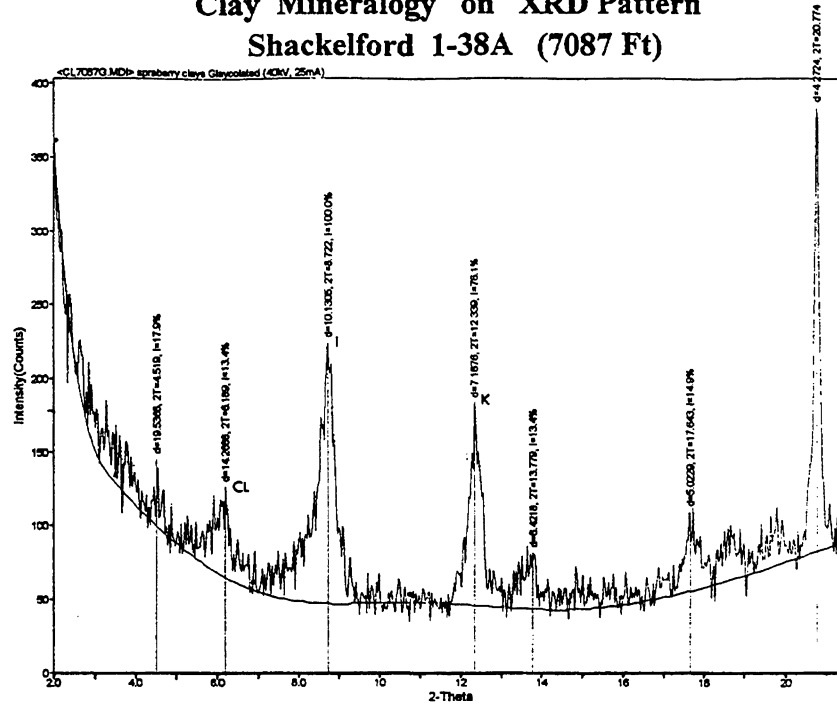


Fig. 1.3-1 SEM photomicrographs showing different types of illite clay accumulation, dolomite cement, and pyrite occurrence in the Spraberry Formations

Clay Mineralogy on XRD Pattern Shackelford 1-38A (7087 Ft)



Clay Mineralogy on XRD Pattern Shackelford 1-38A (7104 Ft)

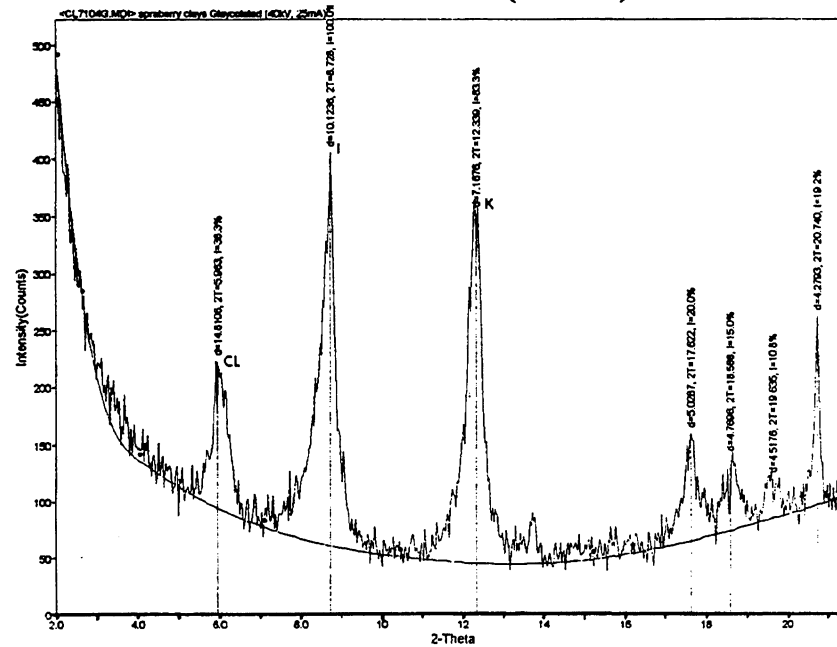


Fig. 1.3-2 Two X-ray diffractograms showing clay mineralogical composition.

1.4 PETROPHYSICS: Combined Rock and Fluid Character

Integration of geological and petrophysical data allows development of a rock-fluid model for upper Spraberry rocks. This study identifies the different rock types that comprise the subject reservoirs, marginal reservoirs and non-reservoir rocks. A rock type is defined as an interval of rock with unique pore geometry, determined mineralogical composition and is related to certain specific fluid flow characteristics.

The rock-fluid model relates fluid flow characteristics to rock types defined in the previous section (1.3: Petrography and Diagenesis). Analytical techniques used to develop this model include porosity-permeability analysis of core plug samples, air minipermeameter measurements on core slabs, thin section analysis, scanning electron microscope analysis of the pore structures, air-mercury capillary pressure, pore body and pore throat size distributions and GR log of each well. Integration of results from these various analytical techniques reveals that the six (6) small-scale lithofacies described using thin-section analysis are consistent with the petrophysical model shown in this section.

1.4.1 Gamma Ray Log Resolution

A method of distinguishing between shales, clay rich siltstones and very fine sandstones units uses gamma-ray logs (Fig.1.2-1) and is widely implemented in the field practice. This method has shown to provide good differentiation between lithological characteristics in many investigations (Guevara, 1988; Tyler and Gholston, 1988). Data from different analytical techniques combined with the gamma-ray log response for the E.T. O'Daniel 37 core are shown in Fig. 1.4-1. The gamma-ray deflection curves show good correlation with core descriptions. Thicknesses for sandy beds are fairly well predicted by the deflection to the left, however peak heights do not define facies quality very accurately. The latter is due to the limited sensitivity of the gamma ray tool to differentiate mineralogical sources other than clay amount in the matrix.

1.4.2 Determination of Petrophysical Properties

Three different methodologies were used to analyze petrophysical properties: (1) A computer-controlled scanning air-minipermeameter (CCSAM), (2) imbibition experiments with air, oil and synthetic brine, and (3) petrophysical properties with injection of nitrogen, helium and mercury.

1.4.2.1 Computer-Controlled Scanning Air-Minipermeameter (CCSAM)

Although the air permeability curves show good relationship with gamma-ray curves and core descriptions, the vertical air permeability variation is much more complex in character (Fig. 1.4-1). A number of factors affect the formation heterogeneity: clay and organic rich laminae, burrowing, cementation, pore morphology, pore distribution, pore throat aperture, level of interconnection of pores and rock wettability.

1.4.2.2 Methodology for Obtaining Petrophysical Properties

1.4.2.2.1 Permeability determination with Nitrogen Flow Through Rock Type:

Core plug samples of 1 in. and 1.5-in. diameters were used to measure petrophysical properties of the different lithofacies for two cores from the Upper Spraberry Formation. Parameters measured include porosity (ϕ), permeability (k), and grain density (Reservoirs Inc., 1996). A core holder with a specific confining pressure is used. Formulas for the calculation of permeability, porosity and water saturation are given below. The permeability resulted from injection of nitrogen gas into the samples at a constant pressure until a constant flow rate of gas through the sample is attained (steady-state conditions). Permeability (k) is a function of flow rate (q), viscosity of the fluid (μ), length of the core plug (L), transversal area of core plug (A), and drop in flow pressure (ΔP):

$$k_b = \frac{q\mu L}{A\Delta P} \dots\dots\dots(1)$$

1.4.2.2.2 Helium Porosity Determination

Boyle's law was used to calculate the porosity for each core plug sample:

$$P_1 \times V_1 = P_2 \times V_2 \dots\dots\dots(2)$$

Helium was used as the gas phase. Two chambers of known volumes were connected, one containing helium at a given pressure (P_1) and another (matrix cup) with a core plug. The helium is expanded into the matrix cup and an equilibrium pressure (P_2) is recorded. The initial volume (V_1) of the sole helium chamber is known, thus the volume of the new system helium chamber and matrix cup (V_2) is determined using the Boyle's Law. By subtracting V_1 from V_2 the total pore volume (PV_t) for the given core plug is obtained. The porosity (ϕ) is simply the fraction between the total pore volume (PV_t) and the core plug bulk volume (V_b) determined from mercury immersion (*Archimedes principle*) and corroborated by measuring the core plug dimensions.

$$\phi = \frac{PV_t}{V_b} \dots\dots\dots(3)$$

Grain density (GD) for each core plug is a function of the grain volume and weight of the clean and dry core material. Grain volume (GV) is the result of subtracting the total pore volume (PV_t) from the bulk volume (V_b) for each plug sample:

$$GV = V_b - V_t \dots\dots\dots(4)$$

GD is then the amount of weight of grain or core material (W_{dry}) per volume of grain (GV) in the given sample:

$$GD = \frac{W_{dry}}{GV} \dots\dots\dots (5)$$

These sets of data are analyzed using cross-plots correlating pairs of data to define relationships and quality controls. For instance it is observed in Fig. 1.4-2 that porosity and permeability increase or decrease more or less simultaneously below a depth of 7195 ft, while the relationship of ϕ and K above this depth is more complex. Implications regarding variability and lithological controls on rock-fluid behavior will be further discussed in the following sections.

1.4.2.2.3 Mercury Injection Techniques: Capillary Pressure, Pore Distribution, Pore Throat and Connectivity

Mercury injection (Reservoirs Inc., 1996) into core plugs is used to determine capillary pressures, pore throat sizes, connectivity, relative quality of different rocks and Leverett's "J" function. This procedure utilizes a vacuumed injection chamber to hold a core plug. A specific distance between the injection of mercury and the core plug was allowed to avoid undesirable pressure changes. Mercury starts invading the core pore system specific applied pressure or threshold pressure. This specific threshold pressure remains constant until mercury intrusion ceases. At this point the pressure and the amount of mercury injected is recorded. The pressure is then increased incrementally and the same procedure is repeated. In this case the range of pressures selected was 0-2000 psia and 0-60,000 psia for high-pressure measurements. The test results were used to calculate pore throat radii and Leverett's "J" function.

1.4.2.3 Rock Types and Rock-Fluid Properties

The Rock Types previously described (see section 1.3) were defined based on their petrophysical properties. For each of these we found a rock-fluid model with unique pore geometry, a determined mineralogical composition and certain specific fluid flow characteristics. Each of these six rock-fluid models is directly related to their analogous previously described petrographic categories.

1.4.2.3.1 Discussion of Petrophysical Properties

Accurate representation of rock-fluid properties is necessary when obtaining petrophysical data. Laboratory techniques that implement injection of nitrogen, helium and mercury into core plug samples are very accurate in obtaining reservoir properties. This section presents permeability and porosity data from nitrogen and helium injection respectively (Reservoir Inc., 1996). Helium is capable of filling up all connected space inside a rock sample thus giving accurate porosity values. Mercury, a non-compressible fluid, is a non-wetting fluid that does not react with the rock and also possesses the ability to completely occupy pore space. Thus, measurements using mercury injection are very accurate in determining pore throat values.

The goal of this work was to define reservoir rock character and to distinguish it from all other types of rocks encountered within the Spraberry strata sequence. The different data sets were analyzed to determine correlations between porosity and permeability behavior and lithologic

controls on reservoir quality. Capillary pressure analysis is presented to define pore throat systems for each rock type.

1.4.2.3.2 Permeability, Porosity and Water Saturation Relationships:

Core plug samples selected for detailed analysis in this study have a wide dynamic range of porosity (0.4 to 13.7%) and permeabilities (0.01 to 1.97 md). The dispersion of porosity–permeability data is such that permeabilities range over an order of magnitude for any given value of porosity (Fig. 1.4-3 and 1.4-4). This dispersion of porosity–permeability data reflects changes in the volumetric distribution of pore types within the reservoir.

The first striking point that can be drawn from the depth profile of porosity and permeability (Fig. 1.4-2) for E.T. O’Daniel is the difference in correlation match approximately below and above the depth of 7175 ft. Above this depth there is a poor match between porosity and permeability due to great variation in lithology. A number of heterogeneities at various scales tend to deteriorate fluid conductivity. These include dispersed and laminated clay matrix, abundant organic matter, bioturbation, soft sediment deformation within shaly laminae, and silica cement within sandy laminae. In this way pore interconnection is considerably reduced for many samples while its total porosity remains relatively high. However, the sandy areas that comprise the reservoir interval 5U unit (below 7175 ft) exhibit a better correlation between porosity and permeability. Better fluid conductivity is related to bigger pore spaces and pore throat radius present in Rock Types “A” and “B” within this area.

A set of six cross plots are presented in Figs. 1.4-3 and 1.4-4 relating porosity and permeability data (Reservoir Inc. 1996) to observable lithofacies (see section 1.2) as defined from core plug samples of Shackelford 138-A (Fig. 1.4-3) and E.T. O’Daniel 37 (Fig. 1.4-4). Strong evidence is presented for depositional controls on porosity and permeability. For instance, Lithofacies 6 (massive sandstone and siltstone), a product of high-energy deposition, shows the best reservoir properties in the porosity-permeability cross plot. Massive dolostone (Lithofacies 1) and shale (Lithofacies 2), from low energy environments, show very low reservoir quality. However the clusters of points for each lithofacies type are not totally distinct from each other. The overlapping of depositional lithofacies in these graphs is probably caused by a number of factors including diagenesis, similarity in pore-structure produced by different depositional environments and the somewhat subjective nature of specifying lithofacies based on hand specimens.

Presented in Fig. 1.4-5 and 1.4-6 are contiguous intervals of fluorescing pay zone and non-pay shaly zones with permeability, porosity and water saturation relationships that suggest strong mineralogical control. Areas of non-fluorescence ordinarily contain higher amounts of clays although they may appear quite similar to fluorescent rocks when viewed in normal light. Although some porous areas exist, non-fluorescent intervals exhibit much less permeability than fluorescent zones. The low permeability in these relatively porous intervals is probably related to higher amounts of clay minerals that affect pore throat connectivity. Relatively similar sandy units do not show obvious evidence of major heterogeneity in core samples. Petrophysical properties measured in the lab show important variations between fluorescing pay zones and

non-pay zones richer in clay content, as in the core analysis of the Shackelford 1-38A (see Fig 1.4-5).

Data from the, Shackelford 138A and E.T. O'Daniel 37 cores shown in Fig. 1.4-7 correlate porosity with S_w measurements. The linear relation with a negative slope clearly indicates the trend of decreasing water saturation with porosity increase. The variation of both variables along the depth profile is presented in Fig 1.4-1. This depth profile shows a strong increase of water saturation within the non-pay, low porous muddy zone. This depth profile of S_w and porosity further indicates that lithological control is strongly related to fluid-rock behavior.

Previous reports have analyzed wettability data from Spraberry core plug samples using brine and oil injection and spontaneous imbibition of brine. From these measurements, initial water saturation, core permeability, and core wettability have been determined. These are very important factors because of their effect on final oil recovery.

When some mineral facie are water-wet, it means that they posses a hydrophilic character; thus water will preferentially be attached to the surface of this mineral. If it were the case of a hydrophobic mineral facie, this would probably be preferentially and electrochemically related to the oil phase.

Pore walls in the Spraberry sands are formed by a variety of different minerals including quartz, different types of feldspar, micas, accessory minerals, carbonate cements, clays, organic matter, pyrite and other less abundant minerals. These different mineralogical species present distinct wetting behaviors at the microscopic level. The clay rich zones tend to be water-wet in the Spraberry formation, which contrast with the mixed oil-water-wettability behavior of clean siltstones and sandstones. Due to this characteristic, the argillaceous and less porous rocks within the studied intervals exhibit much higher water saturation than the cleaner siltstones and sandstones.

Due to variations in composition from one core plug to another, the behavior of the capillary pressure- S_w curve presents considerable differences (Fig. 1.4-9). The Amott wettability index to water (I_w) was determined to be between 0.22 and 0.35. As a result of this mineralogical heterogeneous character, the Spraberry reservoirs are considered weakly or moderately water-wet.

The microscopic displacement efficiency during spontaneous water imbibition varies from 10% to 15% depending upon core permeability. In turn permeability depends on rock properties such as pore throat size, pore size distribution, pore connectivity, tortuosity, and rock-fluid properties such as capillary pressure and wettability.

Spraberry sandstones have been found to imbibe oil spontaneously without requiring any pressure input, due to the partially oil wet character of the rocks. This behavior does not favor oil recovery by conventional water flood techniques. At a certain point, water injection would not be able to move any more of the oil that is trapped in hydrophobic intergranular pore cavities.

1.4.2.3.3 Grain Density and Porosity Relationships:

Presented in Fig.1.4-8 are additional analyses of lithological controls on reservoir quality. Grain density is strongly related to lithological character. There is a hyperbolic relation with a positive slope for porosity and grain density data from the core. A cluster of points in the top left corner can be discriminated as carbonate muddy rocks with their typical high grain density, very low porosity and petrographic characteristics. Table 1.4-1 summarizes the general trends found in the petrophysical data for three major subdivisions of rock types: 1) Clean sandy rocks, 2) Shaly and silty non-fluorescent rocks, and 3) Dolostones.

Notice that these three subdivisions represent the major trends that occur in the Spraberry Formation (i.e. Rock Types “A,” “B,” “C,” “E,” and “F”). Patchy dolomitic siltstone “Rock Type D” falls between “B” and “F” (see Fig.1.4-8). This category shows slightly higher grain density range and lower porosity than “B” due to the higher amounts of dolomite cement present.

1.4.2.3.4 Capillary Pressure and Pore Throat Relationships:

Mercury injection data from core plug samples from the Shackelford 138A and E.T. O’Daniel 37 is presented in this section. A set of cross plots that correlate porosity, permeability and pore throat data is shown in Fig. 1.4-10. The results show consistency between rock-fluid parameters and those obtained in the petrographic study. Summarized in Table 1.4-2 are the results (average values) for each rock type from helium, nitrogen and mercury injection.

The analysis of petrophysical data emphasizes the heterogeneous nature of the Midland basin deposits. From this data, one can see distinct differences among Rock Types occurring in the upper Spraberry Formation. As expected from thin section analysis, Rock Types “A” and “B” present the best potential reservoir rocks. These consist of very fine sandstones and siltstones with variable pore structures. Rock Types “C,” “D” and “F” required higher pressures to pass fluid through tight pore systems with very small pores and pore throat radii. No measurements of Rock Type “E” (shale) samples were made due to its obvious poor reservoir quality. Rock Types “C,” “D,” “E” and “F” are considered to be marginal reservoirs to poor or non-reservoir rocks. They are dolostones and patchy dolomitic siltstones, and shales and shaly siltstones with variable organic content. The following detailed enumeration of results for each Rock Type includes description of the different petrographical and petrophysical parameters affecting their pore system.

1.4.2.4 Description of Rock Types

Rock Type A – The average values of porosity and permeability are 11.07% and 0.445 md respectively. This rock type is dominated by intergranular macropores of Pore Type 1 (30-40µm), Pore Type 2 (15-30µm) and secondary dissolution Pore Type 5 (50µm). Intergranular macropores (PT1) are relatively large and are well interconnected through large pore throats of relatively uniform size. The rock is very fine to fine grained, well-sorted sandstone to coarse siltstone, with massive sedimentary fabric. Thin section analysis reveals that the hydrocarbon-

bearing samples classified as Rock Type “A” have relatively well preserved intergranular pore systems. Quartz overgrowths, patchy dolomite cement, and dispersed pore-filling clays produce some reduction of total pore volume. Illite, chlorite and smectite have also reduced pore volume. These minerals have formed pore linings and caused pore throat bridging, which in turn has resulted in the partitioning of pore space near pore walls into micropores (Pore Type 4 <5 µm in diameter). Type 2 pores are much less abundant than Type 1 pores. Type 3 pores are not significant components of the pore system. Capillary pressure data shows a relatively high average value of 156.7 psia necessary to intrude the larger system of pore throat radii (0.53 µm) reflecting moderate obstruction of the intergranular pore system. Relatively high displacement pressures for sandstones with moderate porosity are the product of small pore throats and significant amount of pore lining and pore bridging illite clay and carbonate cements.

Rock Type B – These are lesser quality reservoir rocks with average values of 9.49% for porosity and 0.041md for permeability. They are very fine to fine grained, moderately to well sorted siltstones dominated by Type 2 pores (intergranular macropores 15-30 µm diameter). Type 3 (intergranular mesopores 5-15 µm diameter) are less abundant, but common within these rocks. Silica cement is present filling pore spaces. Carbonate and clay cementation has partitioned pore space near pore walls into micropores (Type 4 pores). Pore Types 1 and 5 are not significantly developed. The larger pore throat radii averages 0.15 µm and has displacement pressure of 629.9 psia.

Rock Type C – These are carbonate muds (dolostones) equivalent to the carbonate debris flow deposits of Lithofacies 1. These carbonates have very low porosity (0.70% avg.) and permeability (0.013 md avg.) and are not reservoir rocks. For this reason the pore structures of these rocks have not been studied in any detail (two samples studied). Very small pore throat apertures of 0.0035 µm need extremely high displacement pressures (10,464 psia) to intrude them. These are essentially moderate quality seal rocks rather than potential reservoirs.

Rock Type D – Porosity for these patchy dolomitic siltstones is 4.70% and very low permeability averages 0.01 md (one sample). Rocks of Type “D” are moderately well to well sorted siltstones and sandstones dominated by Type 3 pores (intergranular mesopores 15 µm diameter). They display poorly preserved pore systems and have massive, laminated, or disturbed sedimentary fabrics. Type 2 pores (intergranular macropores 15-30 µm diameter) are less abundant. Microporosity (Type 4 pores) is developed within clay cement rims on grains. The microporous clays tend to severely obstruct intergranular pores. Type 1 macropores scarcely occur within these rocks. Type 5 (dissolution) pores are also very rare. Pore throat radii (0.045 µm) are considerably obstructed; thus, moderately high displacement pressure (1,196 psia) is required to intrude them.

Rock Type E – Porosity found for these samples averages 3.14%, while average permeability is 0.025md. These are very tight rocks with very high amounts of clay, organic matter, and carbonate mud mixed within an argillaceous matrix. Type 5 rocks are shales characterized by micropores (Pore Type 4) and very small modal pore throat radii. Data from capillary pressure mercury injection was not recorded for these samples due to their extremely low reservoir quality. These rocks commonly form permeability seals, not reservoir rocks.

Rock Type F – Average porosity and permeability for five samples are 6.36% and 0.022 md respectively. Rock Type “F” are moderately to poorly sorted clay rich siltstones. Samples display massive, laminated, or disturbed sedimentary fabrics, and are characterized by the virtual absence of visible porosity. Intergranular pore space is severely occluded by abundant detrital clays or dolomite cement. Estimated microporosity is high for clay-rich samples, but low for the dolomite-cemented samples. Main pore types present are mesopores of 5 to 15 μm . Though porosities and permeabilities are slightly higher than Rock Type D (patchy dolomitic siltstones), the average value for modal pore throat radii is considerably smaller (0.039 μm). Displacement pressure necessary to intrude the larger set of pore throats in Rock Type “F” is 2,637.8 psia, more than double that used in Rock Type “D.”

1.4.3 Summary

Rock Types “A” and “B” are potential reservoir rocks. These are distinguished from one another by different pore structures. Rock Type “A” has the best reservoir quality and is characterized by the largest intergranular and dissolution macropores and largest interconnecting pore throats. Rock Types “B,” “D,” and “F” are characterized by progressively poorer reservoir quality, the result of reduced pore and pore throat sizes. Rock Types “C” and “E” are carbonate muds and shales that completely lack reservoir properties and form moderate quality seal rocks.

The occurrence of the largest pores and pore throats in Rock Type “A” is a function of several factors including:

1. Rock Type “A” is the coarsest grained sandstones and siltstones.
2. Rock Type “A” very fine sandstones and siltstones are better sorted than other Spraberry rocks and contain smaller amounts of depositional micritic mud, carbonate cements, clay matrix, clay cements, and organics.
3. Rock Type “A” very fine sandstones and siltstones are characterized by relatively open grain packing (compactional effects are not pronounced).

The reservoir quality of Rock Type “A” and “B” is strongly tied to mineralogical and textural properties such as grain size, grain sorting, clay type and content, and carbonate cement. These are parameters that strongly control pore and pore throat size, permeability, capillary pressure, and wettability. Individual pores and pore throats in Spraberry sandstones are of relatively small sizes and this, in turn, is related to the very fine sand and siltstone grain size of these rocks (J. Neasham, 1977).

Rock Type “B” has a more complex pore structure than Rock Type “A.” This complexity is a function of finer grain size, increased occurrence of depositional shale laminae (as well as some organics), carbonate and silica cements, and increased effects of compaction. Owing to the presence of shale laminations in some samples, substantially reduced vertical permeability is noted when compared with Rock Type “A.” These factors contribute to produce small pore size (these rocks are generally characterized by pores of less than 30 μm diameter) and pore throat size as well as a large standard deviation of pore and pore throat sizes. While varying little in total porosity from Rock Type “A” sandstones, reduced permeability in Rock Type “B”

sandstones is a function of this smaller pore and pore throat size and slightly higher amounts of clays and carbonates.

Rock Type “D” and “F” siltstones present varying degrees of heterogeneities, as a result binary, skewed, and uniform pore size distributions are all noted. Lithologies are a mixture of: 1) Micropore-dominated, shale/organic layers (distorted in the case of bioturbated rocks) and; 2) Primary intergranular pore-dominated sand layers with dolomite patches, and dispersed clays. The pore systems of Rock Type “D” differ from good reservoir rocks “A” and “B,” in that most of the porosity in these rocks is poorly interconnected and consists of intergranular mesopores (generally 5-15 μm diameter).

Rock Types “C” and “E” are essentially nonporous and impermeable seal rocks. High pressure mercury injection capillary pressure data indicate that displacement pressures are very high, ranging from 1000 to 15,000 psia. These tightly cemented samples have very small modal pore throat radii, ranging from 0.004 to 0.05 microns.

1.4.4 References

1. Guevara, E. H., 1988, Geological characterization of Permian submarine fan reservoirs of the Driver waterflood Unit, Spraberry Trend, Midland Basin, Texas; BEG, UT Austin; Report of Investigation No. 172.
2. Neasham, John W., The morphology of dispersed clay in sandstones reservoirs and its effect on sandstones shaliness, pore space and fluid flow properties, Society of Petroleum Engineers, paper SPE 6858, Annual Technical Conference and Exhibition held in Denver, CO, October 9-12, 1977. Shell Development Company.
3. Reservoirs Inc., 1996, Internal report: Core analysis, Parker & Parsley Development, L. P. Midland County, Texas.
4. Tyler, N. and Gholston, J. C., 1988, Heterogeneous deep-sea fan reservoirs, Shackelford and Preston waterflood units, Spraberry Trend, West Texas; BEG, UT at Austin, Report of Investigation No. 171.

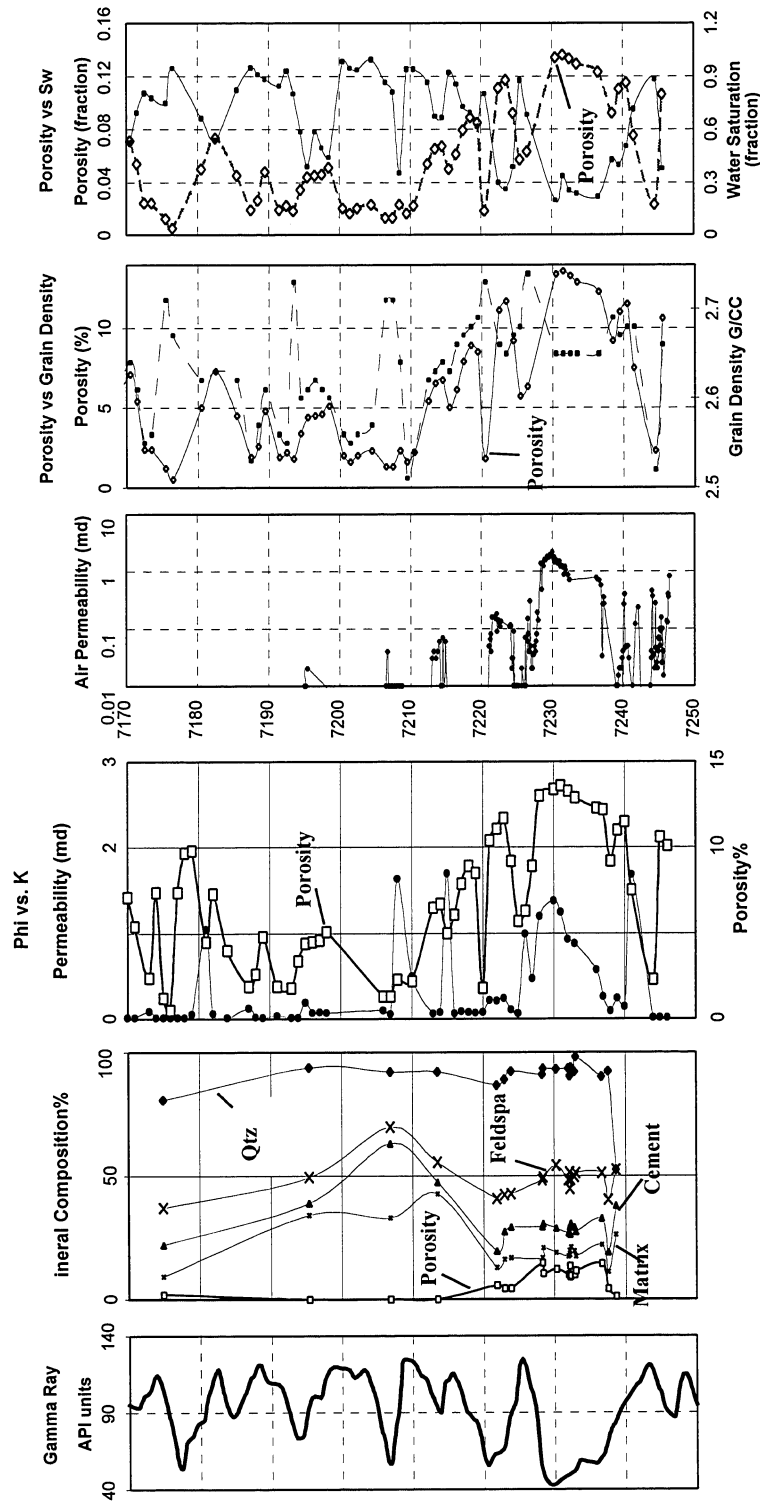
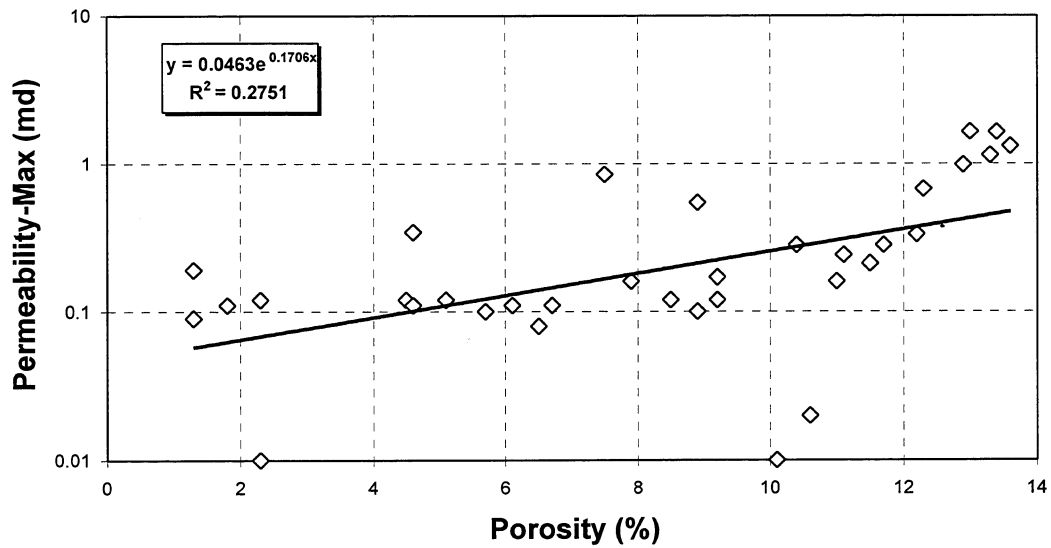


Fig. 1.4-1 Core E.T O'Daniel 37 - Integration of Petrographic and Petrophysics Data

Porosity vs. Permeability
E.T. O'Daniel 37 Core
(only samples from depths range 7195-7245 ft)



Porosity vs. Permeability
E.T. O'Daniel 37 Core
(only samples from depths range 7080-7195 ft)

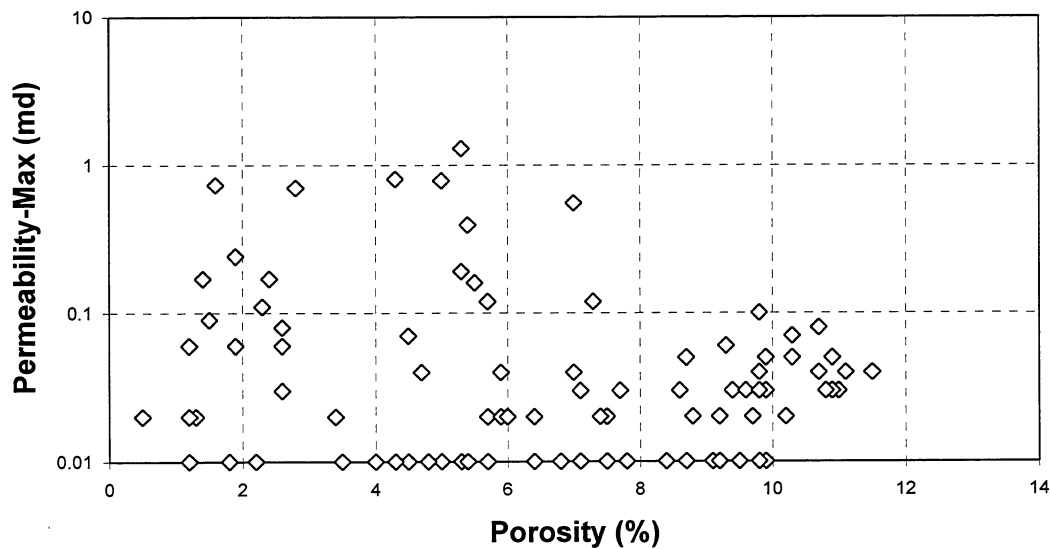


Fig. 1.4-2 Cross plots illustrate the differences in porosity-permeability correlation for samples above and below 7195 ft depth for E.T. O'Daniel 37 core

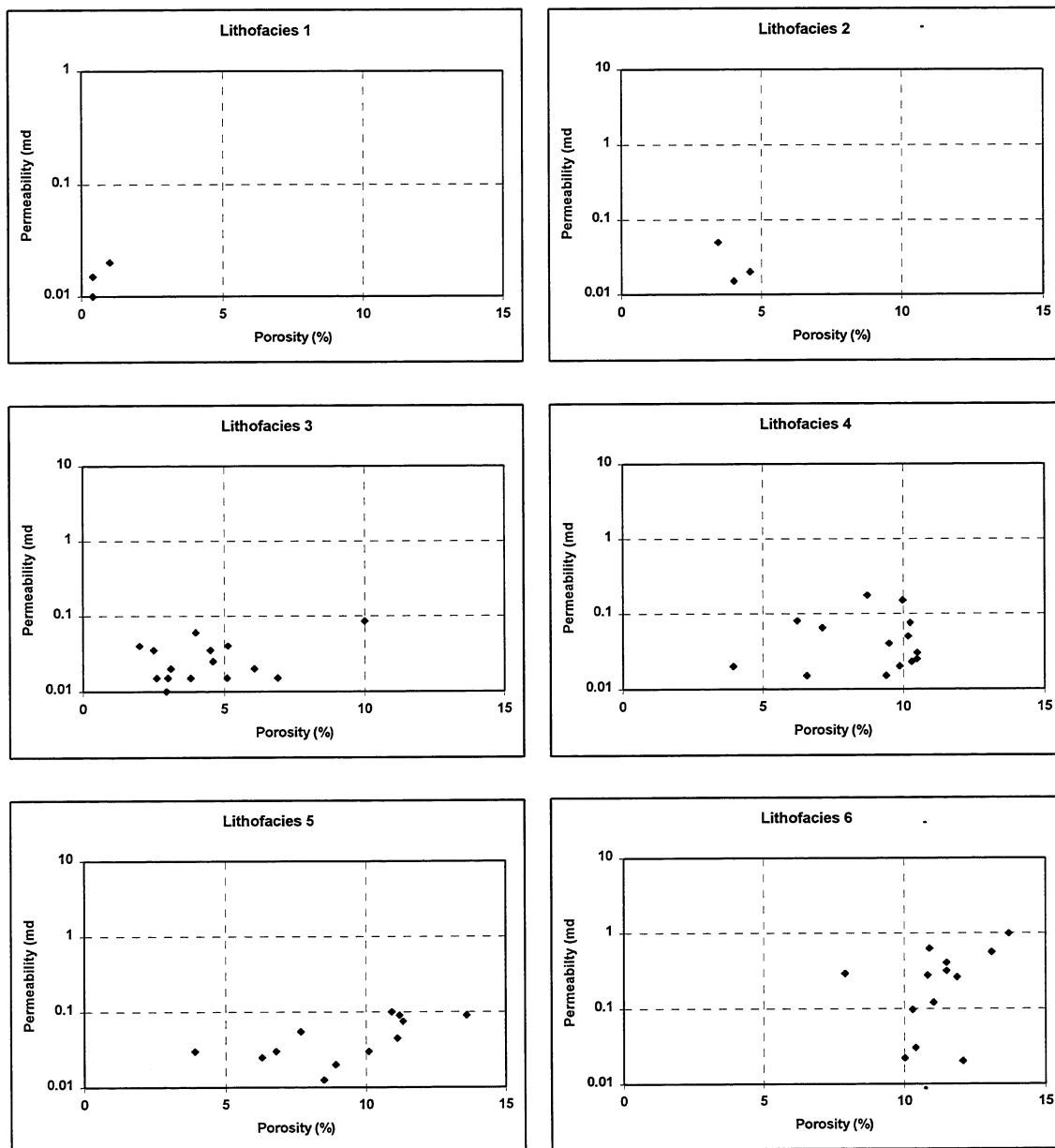


Fig. 1.4-3 Set of porosity-permeability cross plots shows the lithological control upon ϕ and k. Shackelford 138-A core.

(Data compiled from Reservoirs Inc. internal report)

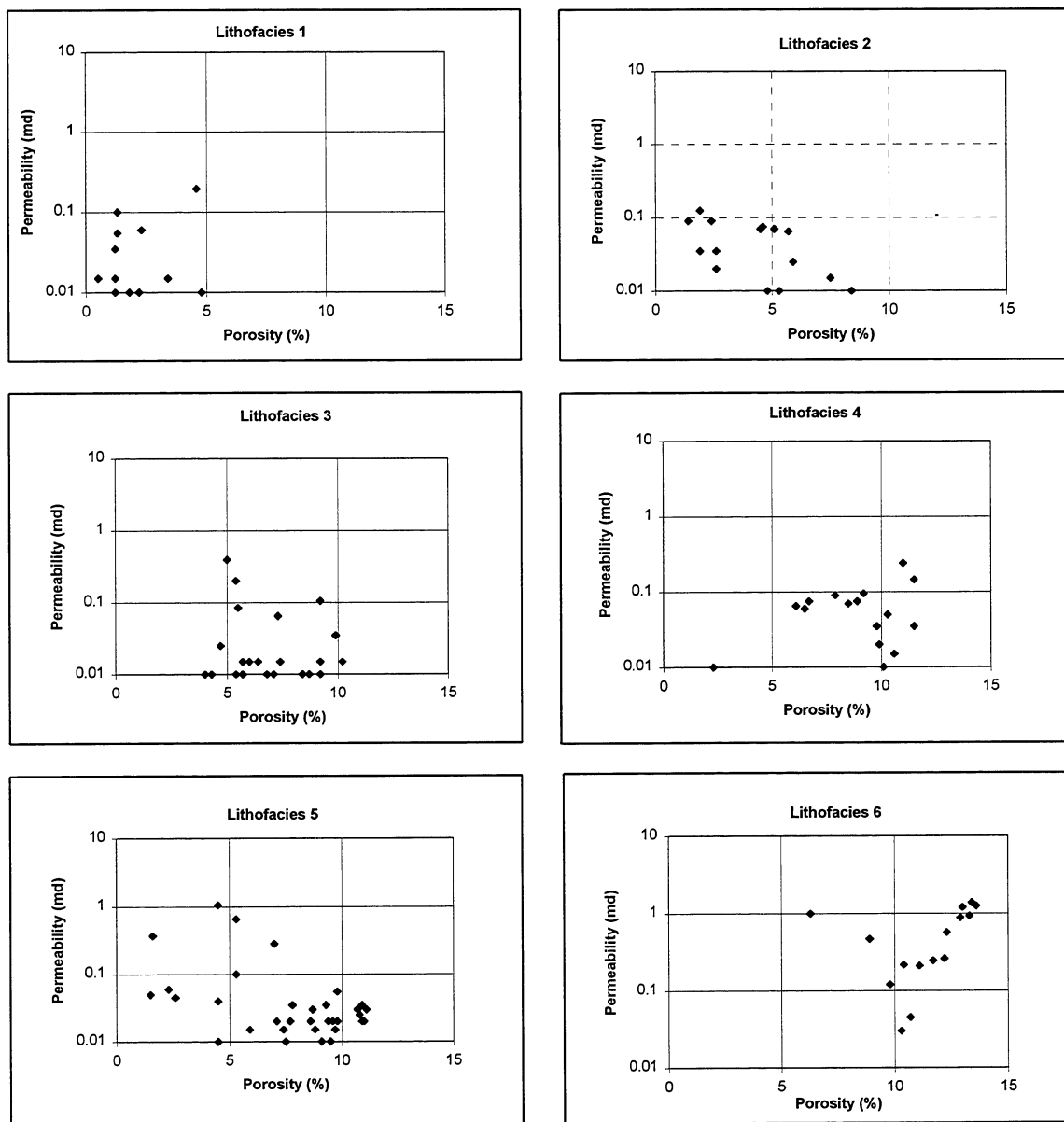


Fig. 1.4-4 Set of cross-plots showing the lithological control upon porosity and permeability for six large-scale lithofacies. Core E.T. O'Daniel 37.

(Data compiled from Reservoirs Inc. internal report)

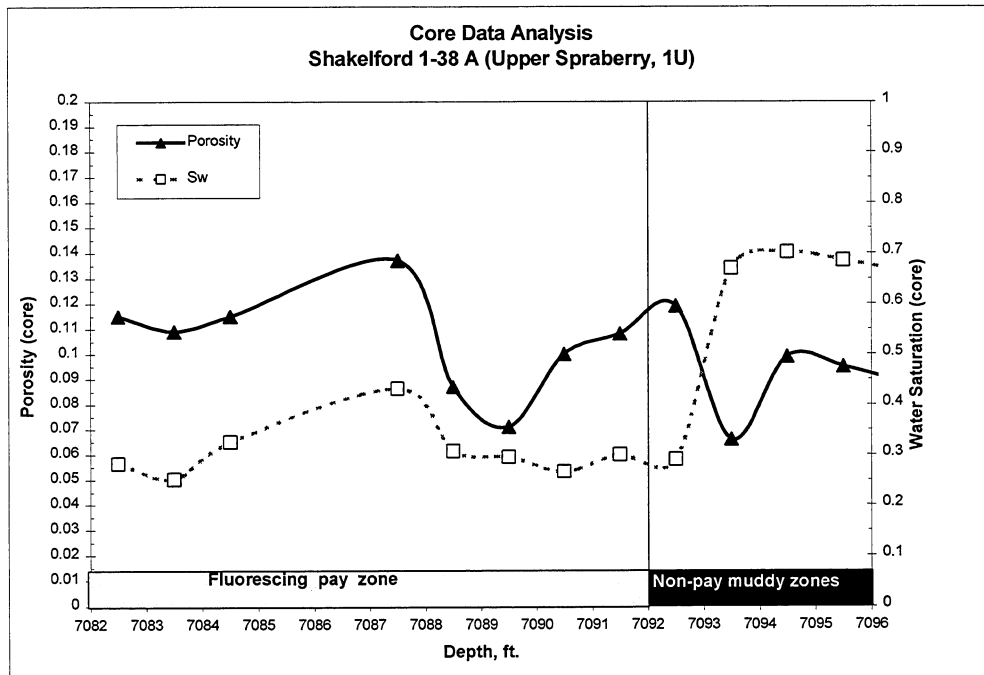


Fig. 1.4-5 Comparison of fluorescing pay zone and non-pay zones richer in clay content. For Shackelford 1-38A

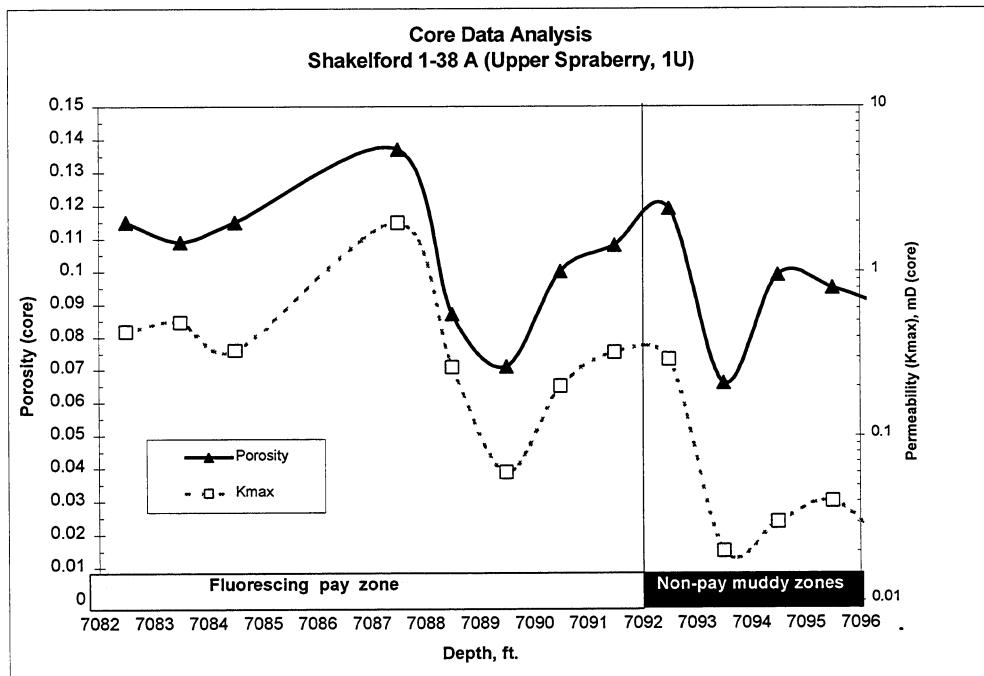


Fig. 1.4-6 Non-fluorescent zones are commonly lower quality reservoirs and non-reservoir rocks strongly affected by pore lining and pore bridging clays.

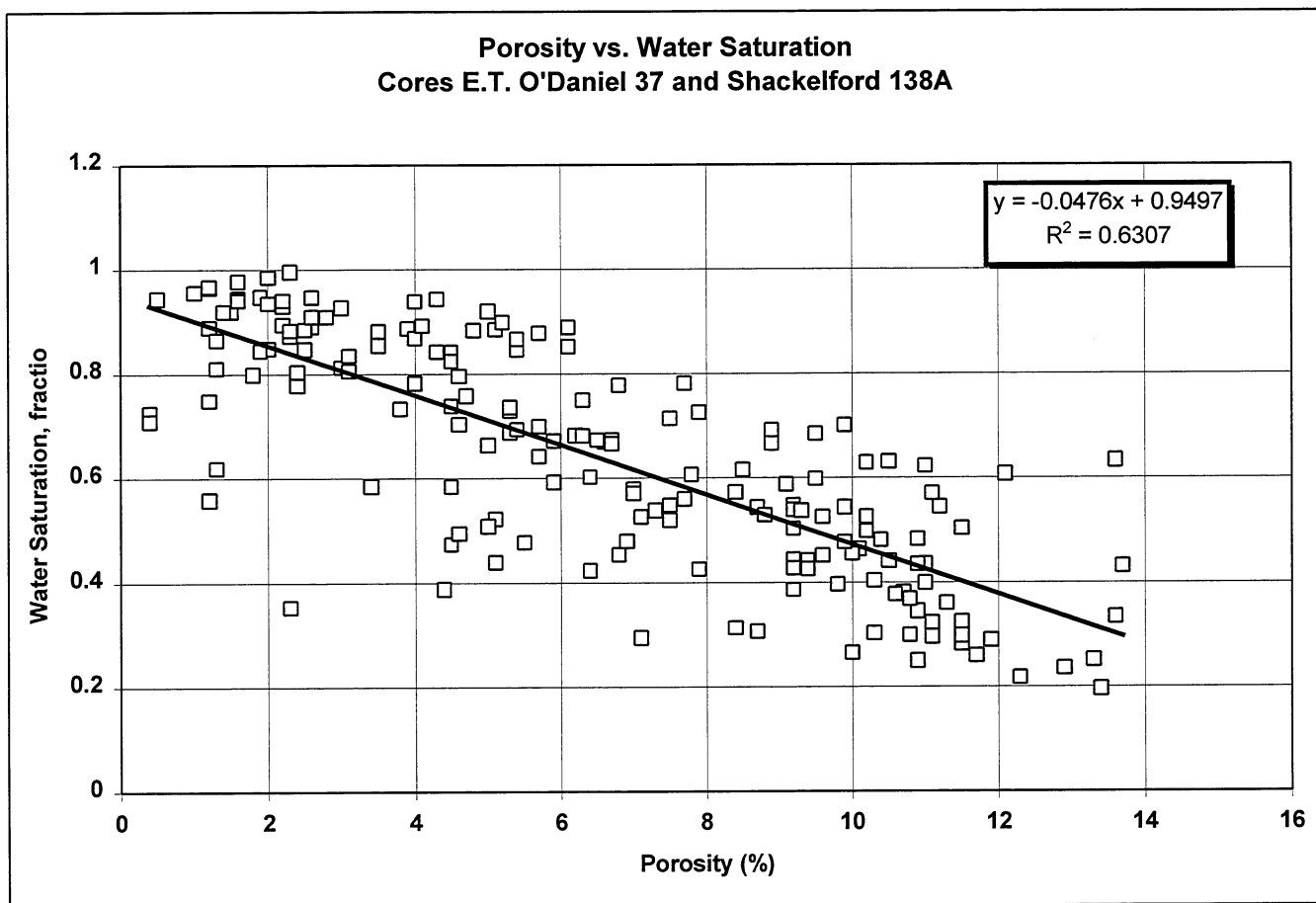


Fig. 1.4-7 Porosity vs. water saturation form the E.T. O'Daniel 37 and Shackelford 1-38A.

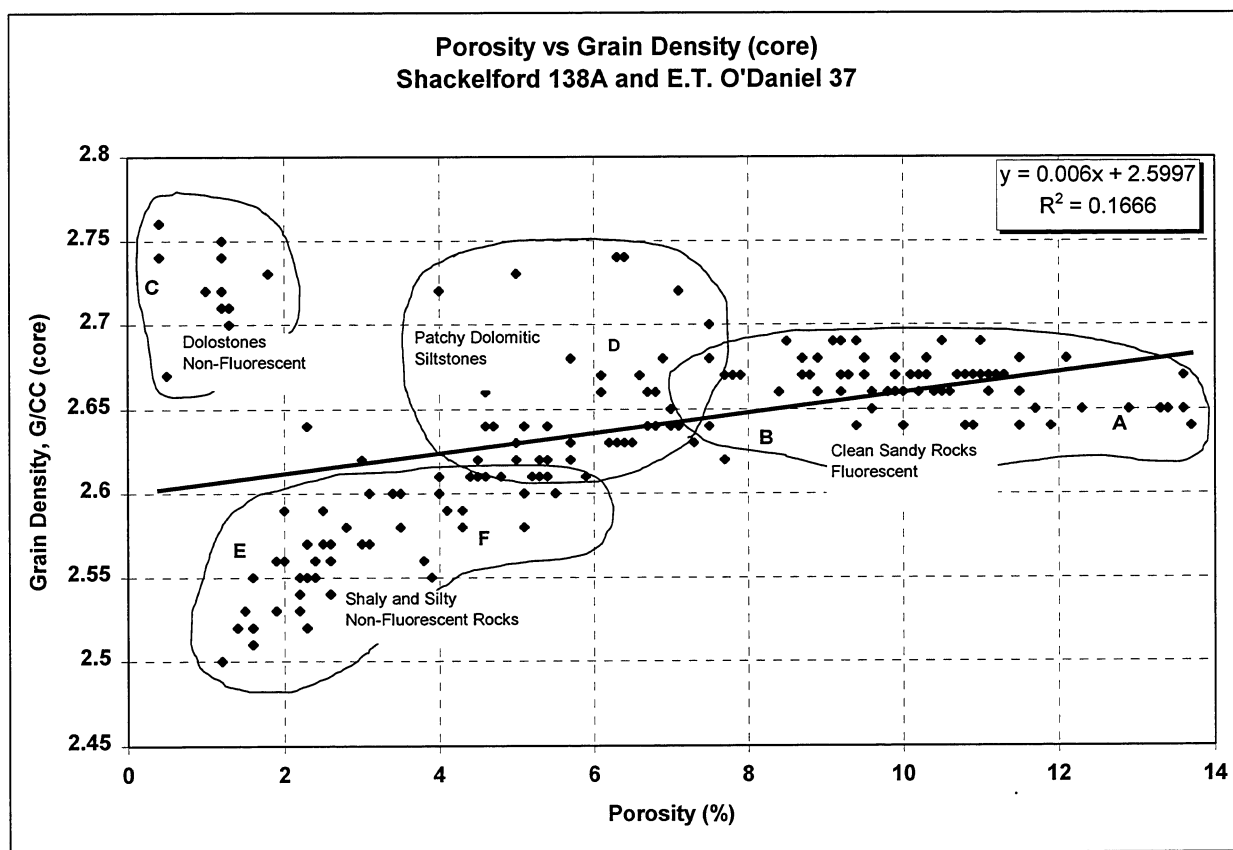


Fig. 1.4-8 Grain density vs. porosity cross-plot suggests strong lithological controls on reservoir quality.

Table 1.4-1 Summary of grain density data correlated with the major Rock Types.

Major lithologic types - small scale categories - upper Spraberry formation			
Main Group	Clean Sandy Rocks	Shaly and Silty Non-Fluorescent Rocks	Dolostones
Description	Mostly massive structure, low clay amounts, good porosity and pore throat radius, main mineral component is quartz. Include Rock Types "A" and "B"	Laminated, bioturbated, or convoluted, very low porosity, main mineral component are clays and quartz. Include Rock Types "E" and "F"	Mostly massive carbonate rich mudstones, poor porosity to total absence of pore space, main mineral components are dolomite mud, and quartz. Include Rock Type "C"
Fluorescent Capacity	Fluorescent	Non-Fluorescent	Non-Fluorescent
Grain Density	2.70 to 2.64 g/cc	2.60 to 2.51 g/cc	2.75 to 2.73 g/cc
Porosity (helium)	12% ("A") 9.95% ("B")	3.8% ("E") 7.3% ("F")	1.0%
Permeability (nitrogen, avg.)	0.64 md ("A") 0.12 md ("B")	0.056 md ("E") 0.034 md ("F")	0.048 md ("C")
Sw (from J-function)	35% ("A") 44% ("B")	75% ("E") 61% ("F")	79%

Table 1.4-2 Summary of helium, nitrogen and mercury injection data for plugs of different Rock Types that form the Spraberry Formation.

ROCK TYPE	POROSITY (%)	PERMEABILITY (md)	MODAL PORE THROAT RADIUS (μm)	DISPLACEMENT PRESSURE RANGE (psia)	AMOUNT OF SAMPLES
A	12	0.64	0.53	74.8-161	7
B	9.95	0.12	0.15	300-602	7
C	1.0	0.05	0.0035	11,943-4,980	2
D	8.0	0.18	0.045	987	1
E	3.8	0.06	0.0075	3,491	2
F	7.2	0.03	0.06	1,434	3

Water-Oil Capillary Pressure in Spraberry Sands

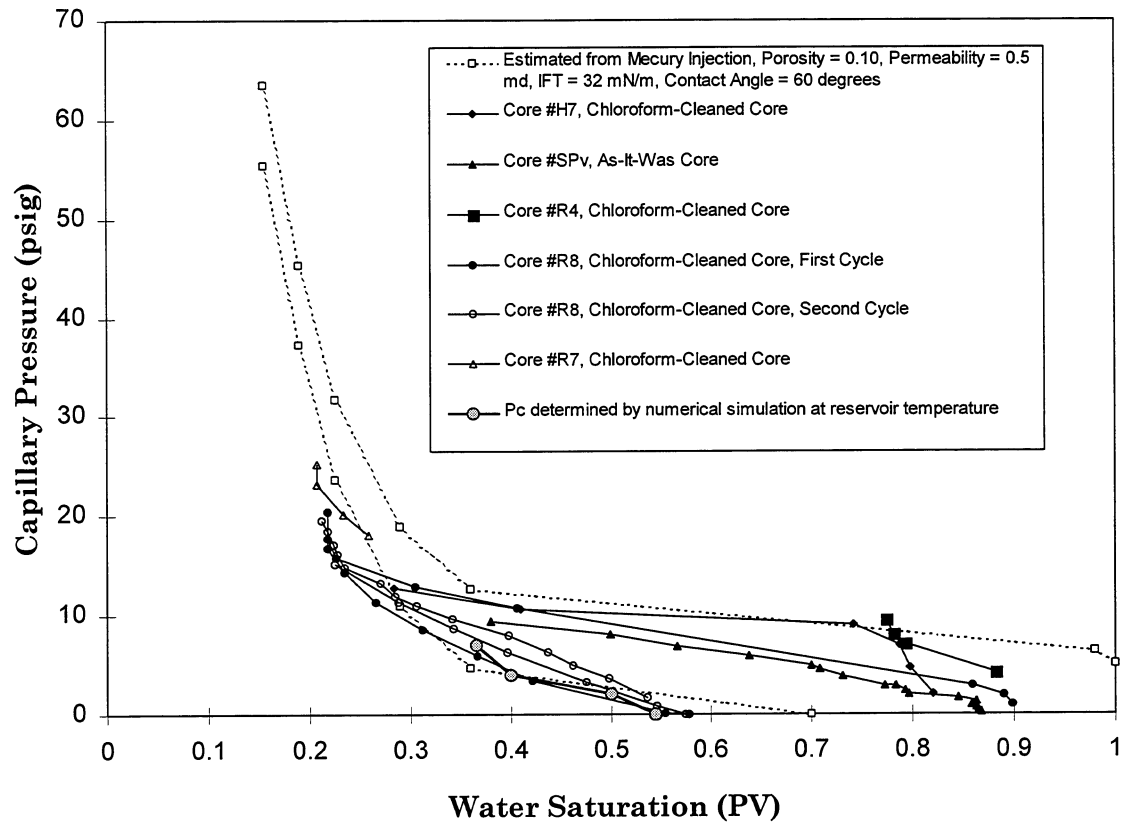


Fig. 1.4-9 Graph showing several curves for S_w and capillary pressure from imbibition experiments done with core plugs from various depths.

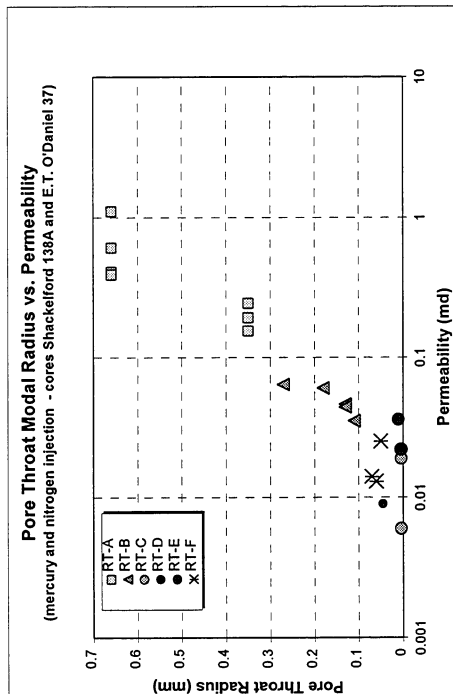
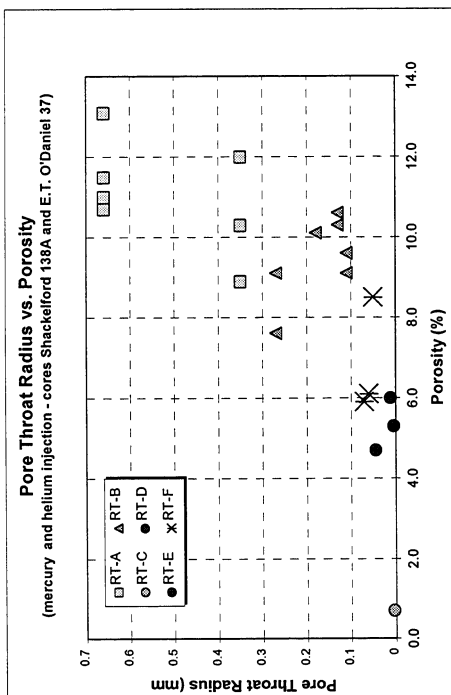
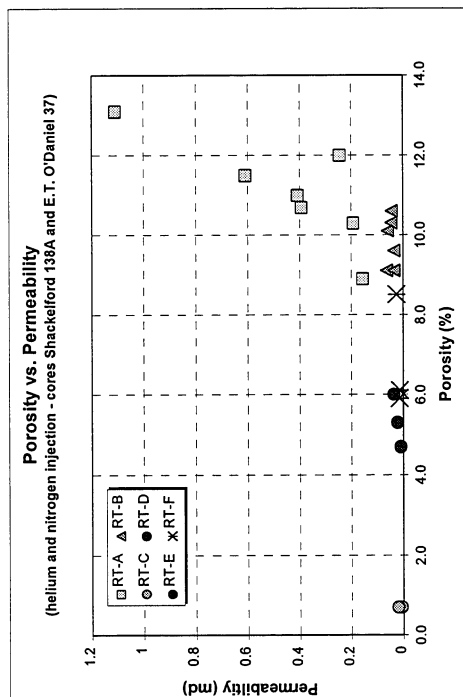


Fig. 1.4-10 Three cross-plots presenting mercury injection data correlated with porosity-permeability and pore throat radius. Cross-plots suggest that rock-fluid behavior is linked to lithological variability for the six Rock Types under study.

2 INVESTIGATION OF CRUDE OIL/BRINE/ROCK INTERACTION

2.1 EXPERIMENTAL STUDY OF CRUDE/BRINE/ROCK INTERACTION AT RESERVOIR CONDITIONS

2.1.1 Introduction

In the previous section, the fluid/rock interactions were described from a geological/petrophysical perspective. We further define this interaction in this section and expand the understanding of the interactions of the Spraberry reservoir rock, oil and brine. Spraberry rock-wetting behavior was determined by performing water imbibition experiments. The experiments used Spraberry oil, synthetic reservoir brine and Spraberry core at reservoir temperature (138°F). This section presents the experimental results on the effect of temperature and aging on brine imbibition, brine displacement and rock wettability using low permeability Spraberry cores.

A schematic of the experimental program is presented in Fig. 2.1-1. Briefly, the water imbibition rate was found to increase with temperature and the ultimate recovery was also affected by the temperature condition, becoming higher as the temperature increased.

The aging of low permeability cores saturated with oil had little effect in the rate of imbibition or oil production rate, particularly after seven days or more aging time with oil. However, the ultimate oil recovery after 21 days of imbibition decreased with the increase in aging time. Increasing the temperature during the brine displacement process appears to increase the displacement recovery.

The experimental data under reservoir conditions also confirm that the Spraberry reservoir rock are weakly water-wet with an Amott wettability index to water of 0.24 to 0.35, depending on the temperature of the brine during displacement. Heterogeneity in rock properties, such as initial water saturation and permeability of the cores used in the experiment, causes less influence than the aging time on the recovery mechanism.

2.1.2 Experimental Material

Core samples. The reservoir cores used in this study were core plugs prepared from 4-in. diameter cores taken from the Spraberry Shackelford Unit 1-38. The cores were cut to 3.80 cm in diameter and about 5.10 cm in length. The air permeabilities of the Spraberry cores were measured, varying from 0.1 to 1.5 md and the porosity ranged from 9.5 to 12%. The absolute permeabilities to brine ranged from 0.10 to 0.51 md.

A traditional toluene Dean-Stark extraction method was used to clean the very tight core samples from the Spraberry formation. The method removes water and light components by raising the temperature of the core and boiling off the light end components. To ensure the core sample is sufficiently clean, injecting chloroform into the core sample under a pressure of 200 psi until the output of the chloroform was clear followed this step. The Spraberry cores were heated in an oven at 100°C for at least two days to dry completely. After cleaning the

core porosities were determined to be about 10%, and the absolute permeabilities to brine ranged from 0.10 to 0.33 md. The physical properties of the reservoir core samples after cleaning are presented in Table 2.1-1.

Brine composition. Synthetic Spraberry brine was used in the experiments and was prepared by dissolving NaCl and $\text{CaCl}_2 \cdot 2\text{H}_2\text{O}$ in distilled water. The brine composition is shown in Table 2.1-2. The viscosity and density of the synthetic brine at elevated temperature are presented in Fig.2.1-2 and Fig.2.1-3, respectively.

Oil samples. Spraberry dead oil is used in the investigation. Table 2.1-3 (as given by Chang and Buckley (1997)) summarizes the physical and chemical properties of the oil samples. The composition of the sample, determined by gas chromatography analysis, is listed in Table 2.1-4 (Siagin, 1997). The viscosity of Spraberry oil was determined using a Cannon-Fenske routine viscometer and the density was determined using a digital density meter. The plots of oil viscosity and density at elevated temperature are shown in Fig. 2.1-4 and Fig. 2.1-5, respectively. The interfacial tensions (IFT) of the oil/brine system was also measured using a pendant drop instrument and de Nouy Ring (see Fig. 2.1-6). The plot of IFT at different elevated temperature is presented in Fig. 2.1-7. Both methods show agreement in the measured IFT at room and reservoir temperature. However, pressure is shown to influence the IFT little if any at all. In addition, the volumetric expansion with temperature increase was also measured and is shown in Fig. 2.1-8.

2.1.3 Experimental Procedures

Saturating Spraberry Core with Brine. The dry core sample was weighed on a balance after measuring its air permeability. The core sample was then saturated with deaerated brine, using a vacuum pump, for 24 hours. Porosity and pore volume (PV) were determined from the dry and saturated weights of core samples, from bulk volume, and from brine density. After saturating the core samples with brine, a period of about three days was allowed for the brine to achieve ionic equilibrium with the rock. The core sample was then inserted into a Hassler core holder. A confining pressure of 500 psig was used to measure the core's absolute permeability to brine.

Saturating the Core with Oil. The core sample was saturated with oil by flowing oil through the core confined in a Hassler core holder with a confining pressure of 500 psig. The oil was injected into a brine-saturated core to establish initial water saturation. Injection was stopped after 2 to 5 PV oil effluent from the core. The lowest initial saturation achieved was 32%.

Aging Procedure. In an oil reservoir, the adsorption equilibrium between the rock surface and the oil is established over geologic time of the rock-oil system. In an effort to restore the adsorption equilibrium, the Spraberry core samples were aged prior to each of the imbibition tests by saturating and immersing the core samples in an oil bath at the reservoir temperature (138°F) for a certain period of time. To investigate the effect of adsorption equilibrium level on the imbibition process, the aging period was varied from zero to thirty days.

Spontaneous Imbibition Test. The spontaneous imbibition experiments were performed using the imbibition apparatus schematically shown in Fig. 2.1-9. As can be seen from this figure,

the apparatus basically is a simple glass container equipped with a graduated glass cap. To perform an imbibition test, a core sample was immersed in the glass container filled with preheated brine solution. The container was then covered with the graduated cap. After fully filling the cap with brine solution, the container was then stored in an air bath that had been set at a constant temperature of 138°F. Due to capillary imbibition action, oil was displaced from the core sample by the imbibing brine. The displaced oil accumulated in the graduated cap by gravity segregation. During the experiment, the volume of produced oil was recorded against time. Before taking the oil volume reading, the glass container was gently shaken to expel oil drops adhering to the core surface and the lower part of the cap so that all of the produced oil accumulated in the graduated portion of the glass cap. At an early stage of the test the oil volume was recorded every half-hour while toward the end of the test the oil volume reading was made every 24 hours. Excluding the core preparation, one series of tests was usually completed within 21 days.

Brine displacement. After the spontaneous imbibition in brine was completed, the core sample was subjected to forced displacement by water using a pressure ranging from 120 to 200 psi depending on the wetting condition. The injections were performed under room and reservoir conditions. At the conclusion of the imbibition test under reservoir temperature, the core and apparatus was cooled several hours to achieve an equilibrium temperature before brine displacement under room temperature performed. Brine displacement was performed under reservoir condition. Once the imbibition test was stopped, the core was flushed by preheated brine right away. The amount of oil produced was used to determine the wettability index for water (I_w).

2.1.4 Results and Discussion

In considering the spontaneous imbibition experiments performed under reservoir conditions, a series of imbibition experiments were performed at reservoir temperature (138°F) and elevated pressure (13.5 psi and 1000 psi). Berea sandstone cores were used in this experiment to verify the effect of pressure on the imbibition process. During spontaneous imbibition more oil is recovered using a homogeneous and high permeability porous medium, as would be expected. The results as presented in Fig 2.1-10 shows that changes in pressure give small effects on imbibition rate and recovery. An additional imbibition reference recovery curve for very strongly water-wet conditions is also plotted in Fig. 2.1-10. Performing a spontaneous imbibition experiment under reservoir temperature using refined oil (Soltrol-130) generated the reference curve. This behavior has also been confirmed by previous studies (Mugan, 1972; Hjelmeland, 1986, Anderson, 1986; Cuiec, 1995). The temperature effects shown in Fig 2.1-11 are considered more critical to imbibition than the pressure effects.

2.1.4.1 Effect of Temperature on Spontaneous Imbibition

A series of experiments were run to investigate the effect of temperature on spontaneous imbibition using a volumetric method. Four Spraberry cores were used to investigate the effect of temperature during imbibition tests. Two of these cores were prepared for spontaneous imbibition under reservoir temperature (138°F). The other two cores were prepared for spontaneous imbibition under ambient conditions (70°F). All cores were established at almost the same initial water saturation of about 34%. The preparations to establish initial water

saturation were made at room temperature condition and the cores were not aged in oil for this test.

During the test sequences, the distinction between the aging temperature (T_a), the imbibition temperature (T_{imb}), and the displacement temperature (T_d) is necessary. The aging temperature is the temperature condition applied when the core is aged in oil. The imbibition temperature is the temperature condition when spontaneous imbibition is performed. Finally, the displacement temperature is applied during brine displacement after the imbibition test is conducted.

The effect of temperature on the rate of brine imbibition in low permeability Spraberry cores is presented in Fig. 2.1-12. Two measurements were carried out for each temperature condition and good reproducibility is indicated in Fig. 2.1-12. The results demonstrate that during the process of brine imbibition into low permeability core the water is imbibed by the rock quicker at reservoir (elevated) temperature than at room temperature. The ultimate recovery is also affected by temperature. Higher ultimate recovery can be expected if the temperature is increased with all other parameters remaining constant.

These results agree with previous studies (Handy, 1960; Anderson (1986); Reis (1990); Babadagli, 1995; Tang, G.Q., et al., 1996). Handy stated that the rate of imbibition increased with an increase in temperature due to oil/water interfacial tension, oil viscosity and water viscosity. This is true if the contact angle is not affected by changes of temperature. In addition, based on the surface physical chemistry (Anderson, 1986), an increase in temperature tends to increase the solubility of wettability-altering compounds and desorb from the surface. A decrease in the viscosity ratio of oil and water due to increasing temperature result in oil being displaced more easily and the ultimate recovery being improved.

A sensitivity test of the imbibition mechanism to temperature was performed. After oil recovery ceased at the end of the imbibition test performed under ambient temperature, the experiment temperature was changed to reservoir temperature (see Fig. 2.1-13). As indicated in Fig. 2.1-13, changing the temperature from ambient to reservoir results in a dramatic increase in the rate of spontaneous imbibition, just as was shown in the Berea core in Fig. 2.1-11. The increase in imbibition rate results in an improvement in recovery. The result approaches the ultimate recovery for imbibition under reservoir temperature since the beginning of the test.

According to Tang (1996), in contrast to the large change in imbibition recovery for crude oil, increasing the temperature during the course of imbibition had essentially no effect on refined oil. Therefore, the crude oil/brine/rock interactions are responsible for the dramatic increase in oil recovery with temperature increase rather than changes related to the rock properties alone. Dangerfield, et al, (1985) performed a similar study using chalk core samples and the results were comparable. Changes in temperature using refined oil was not verified in this study

2.1.4.2 Effect of Aging Time

The effect of aging commencement of the imbibition process was investigated using 11 cores aged in oil at 138°F. The aging time varied from 0 to 30 days. For comparison two cores were

not aged in oil. Oil recovery from spontaneous imbibition tests plotted against time in hours shows that the rate of imbibition for cores without aging is faster than that for the aged cores (see Fig. 2.1-14). Slightly different imbibition rates at the beginning of the imbibition test are observed for Spraberry cores aged from seven to 30 days. However, oil recovery after 21 days of imbibition decreases substantially from 15% to 10% IOIP with increase in aging time for no aging to 30 days of aging (Fig. 2.1-15). A more representative reservoir condition is obtained when the Spraberry core is aged before the imbibition test under reservoir temperature.

The effects of aging become less important to the recovery mechanism if forced imbibition or brine displacement takes place after spontaneous imbibition. Figure 2.1-16 shows a plot of total recovery (i.e., recovery after imbibition plus recovery after brine displacement) versus aging time. The total oil recoveries appear to remain constant for core aged more than seven days. For the Spraberry, a reasonable time to start the brine imbibition and displacement test is after the core has aged in oil at reservoir conditions for at least seven days.

2.1.4.3 Effect of Temperature on Brine Displacement

After imbibition tests, all core plugs were displaced by brine. As shown in the experimental program presented in Fig. 2.1-1, brine displacements were performed under two different temperatures (i.e. room and reservoir temperature). Total recovery (recovery after imbibition plus recovery after brine displacement) versus aging time at elevated temperatures during the displacement process is shown in Fig. 2.1-17. The total recoveries for Spraberry cores aged more than seven days and flooded by brine at room temperature after imbibition at reservoir temperature remained constant at an average of about 35% IOIP. When brine displacement was performed at reservoir temperature, the total oil recoveries improve to 65% IOIP for Spraberry cores with and without aging in oil. Increases in temperature during the brine displacement process appear to increase the displacement recovery, thus significantly increasing total recovery. Also evident is that total recovery of 44% after brine imbibition and displacement occurred at room temperature, with no aging effect from Spraberry cores tested under this condition.

2.1.4.4 Wettability Index

The wettability index is determined on the basis of oil recovery by imbibition and from brine displacement. The relationship is expressed as :

$$I_w = \frac{R_{imb}}{R_{imb} + R_{bf}} \quad (1)$$

where R_{imb} is oil recovery by imbibition and R_{bf} is oil recovery by brine displacement flooding. A high index indicates a more water-wet system, a lower index indicates a less water-wet rock.

A plot of wettability index to brine versus aging time for brine displacement at different temperatures is shown in Fig. 2.1-18. This figure shows that the wettability index is about 0.35 for brine imbibition at reservoir temperatures with brine displacement at room temperature. The wettability index is 0.24 for brine imbibition and displacement both at reservoir temperature. This result can be explained as the effect of the low viscosity ratio between oil and brine at high temperatures. As the temperature rises, the viscosity ratio of oil to brine decreases. The decrease in viscosity at higher temperatures is much greater for oil than that for

brine. Thus, an increase in temperature can result in a substantial decrease in viscosity ratio of oil to brine.

When brine is injected to displace oil at high temperature, a decrease in the viscosity ratio of oil and water due to increasing temperatures results in oil being recovered more easily from the core and produces an improvement in the ultimate recovery, due to the higher temperature brine displacement.

As observed previously, the oil recoveries after brine imbibition decreased corresponding to longer aging time. If the oil recovery resulting from brine displacement experiments performed at reservoir temperatures is higher than the recovery with brine at room temperatures, then the wettability index will be lower.

As a comparison, Fig. 2.1-18 also shows the plot of the wettability index versus aging time for both brine imbibition and displacement at room temperature. Without aging the cores in oil, the wettability index is about 0.22. This low value is due to low oil recovery obtained with brine imbibition. This result is close to the wettability index for brine imbibition and displacement both at reservoir temperatures.

2.1.4.5 Heterogeneity in Rock Properties

The initial water saturation and permeability of different low permeability Spraberry cores were not the same. The effects of initial water saturation and core permeability on the recovery mechanisms are also needed. Initial water saturations were found to vary over a range of 32% to 43%, due to the difficulty of establishing constant values for initial water saturation in a low permeability matrix. The initial water saturations of these cores do not provide a great enough variance to conclusively state the initial water saturation does not have an effect on the recovery. However, the initial water saturation data in this experiment does indicate for the range under discussion that both imbibition and total recovery are affected only slightly if at all by the initial water saturations in these cores (see Fig. 2.1-19 and 2.1-20). If the initial water saturations have a great enough variance or range then an increase in initial water saturation will decrease capillary pressure, which results in a decreases of the ultimate oil recovery.

Cores used in this study have variable permeabilities, which ranged from 0.1 to 0.5 md. To investigate the effect of core permeability on the recovery mechanism, oil recoveries from imbibition were plotted against permeability as shown in Fig. 2.1-21. The results show that the imbibition recoveries were slightly affected by core heterogeneity. Total recovery values indicate no effect by heterogeneity (Fig. 2.1-22). In summary, the results show that aging time has a large influence on imbibition recovery with permeability affecting the imbibition recovery slightly.

2.1.5 Conclusions

1. This study using Spraberry oil, brine and Berea sandstone shows that the effect of pressure is much less important than the effect of temperature.
2. Low permeability Spraberry core imbibes water more readily at higher temperature (i.e. reservoir temperatures).

3. Ultimate recovery is higher at greater temperatures (i.e. reservoir temperature).
4. Spontaneous imbibition rate is increased at higher temperature resulting in higher ultimate recovery.
5. This study using Spraberry crude oil shows temperature to have substantial effect on recovery mechanism.
6. The oil/brine/rock interactions are responsible for dramatic increase in oil recovery with temperature rather than changes to rock properties alone.
7. A more representative reservoir condition is obtained when the core is aged at reservoir conditions before the imbibition test is performed.
8. Oil recovery by imbibition decreased from 15% of IOIP at no aging to 10% of IOIP after 30 days of aging.
9. Aging become less important to recovery if forced imbibition or displacement is to be used.
10. The wettability index at reservoir temperature is 0.24 indicating the Spraberry to be a very weakly water-wet rock.
11. Wettability index does not appear to be affected by aging time at reservoir temperature.
12. Higher permeability increases the imbibition recovery slightly. The permeability range used in these experiments does not affect total recovery.

2.1.6 References

1. Anderson, G. W., "Wettability Literature Survey- Part 1 : Rock/Oil/Brine Interaction and the Effects of Core Handling on Wettability," *JPT*, (Oct. 1986).
2. Babadagli, T., "Temperature Effect on Heavy-oil Recovery by Imbibition in Fractured Reservoirs," *Journal of Petroleum Science and Engineering* 14 (1996), 197-208.
3. Chang, V., and Buckley, J.S., "COBR Interaction of Some Medium Gravity Crude Oils," PRRC internal report, PRRC 98-4 (1997).
4. Cuiec, L., "Wettability Laboratory valuation Under Reservoir Conditions: A New Apparatus," paper 9529 presented at the 1995 SCA, Calgary.
5. Dangerfield, J.A., and Brown, D.A., "The Ekofisk Field," North Sea Oil and Gas Reservoirs, J. Klepe et al (eds.), Graham and Trotman, London (1985).
6. Handy, L.L., 1960, "Determination of Effective Capillary Pressure For Porous Media from Imbibition Data," *Petroleum Transaction of AIME*, 219, p. 75.
7. Hjelmeland, O.S. and Larrondo, L.E., "Experimental Investigation of the Effects of Temperature, pressure and Crude Oil Composition on Interfacial Properties," *SPE* (July 1986), 321.
8. Mugan, N., "Relative Permeability Measurements Using Reservoir Fluids," *SPEJ*, (Oct. 1972), 398-402.
9. Reis, J.C., "Oil Recovery Mechanisms in Fractured Reservoirs during Steam Injection," SPE 20204 presented at the SPE/DOE Seventh Symposium on Enhanced Oil Recovery, Tulsa, April 22-25, 1990.
10. Siagian, W.U., "A Laboratory Study of the Extraction of Hydrocarbons from Crude Oil by High Pressure Carbon Dioxide," MS thesis, New Mexico Institute of Mining and Technology, Socorro, NM (1997).

11. Tang, G.Q., and Morrow, N.R., "Effect of Temperature, Salinity and Oil Composition on Wetting Behavior and Oil," paper SPE 36680 presented at the SPE Annual Technical Conference and Exhibition, Denver, Oct. 6-9, 1996.

Table 2.1-1 The Physical Properties of the Reservoir Core Samples

Core No.	Diameter, (cm)	Length, (cm)	k _{brine} , (md)	PoreVolume, (cc)	Porosity, (%)	S _{wi} (%)
SPR-1HR	3.608	6.579	0.22	6.55	9.74	34.36
SPR-2HR	3.607	6.579	0.34	7.11	10.58	43.72
SPR-3HR	3.607	5.842	0.51	7.08	11.86	40.66
SPR-4HR	3.607	5.669	0.30	6.93	11.97	33.62
SPR-5HR	3.607	5.702	0.24	6.94	11.92	36.59
SPR-6HR	3.607	5.563	0.21	5.65	9.94	38.03
SPR-7HR	3.607	5.433	0.14	5.61	10.11	32.22
SPR-8H	3.608	6.487	0.17	7.28	10.98	34.04
SPR-9H	3.607	6.502	0.33	6.81	10.26	41.29
SPR-10H	3.607	5.804	0.12	6.66	11.24	39.96
SPR-11H	3.607	5.842	0.10	6.39	10.71	40.55
SPR-12H	3.607	5.685	0.38	6.42	11.05	34.54
SPR-13R	3.594	5.829	0.10	6.16	10.42	35.03
SPR-14R	3.594	5.723	0.13	6.03	10.38	33.62
SPR-15R	3.594	6.111	0.22	5.13	8.28	41.53

Table 2.1-2 Composition of Synthetic Spraberry Reservoir Brine

Salts Content	Concentrations (mg/L)
NaCl	122,699
CaCl ₂ •2H ₂ O	7,497
Total Dissolved Solids	130,196

Table 2.1-3 Properties of Spraberry Crude Oil*

API Gravity @ 60°F	31.1
Acid Number (mg KOH/g oil)	0.085 ± 0.022
Base Number (mg KOH/g oil)	2.65 ± 0.040
Density @ 25°C (g/ml)	0.8635
Refractive index @ 20°C	1.47824 ± 0.00007
PRI with n-C7	n/a
Asphaltene ppt with n-C ₅ (wt%)	0.39
Asphaltene ppt with n-C ₇ (wt%)	0.16
Molecular Weight	180

* Chang, V., and Buckley, J.S., (1997)

Table 2.1-4 Spraberry Crude Oil Composition**

Components	Mole fractions
C ₁	0.0211
C ₂	0.0172
C ₃	0.0351
C ₄	0.0212
C ₅ - C ₁₀	0.5137
C ₁₁ - C ₂₀	0.2151
C ₂₁ - C ₃₀	0.0710
C ₃₀ - C ₃₆	0.0302
C ₃₇ ⁺	0.0740
Total	1.0000

** Siagian, W.R., (1997)

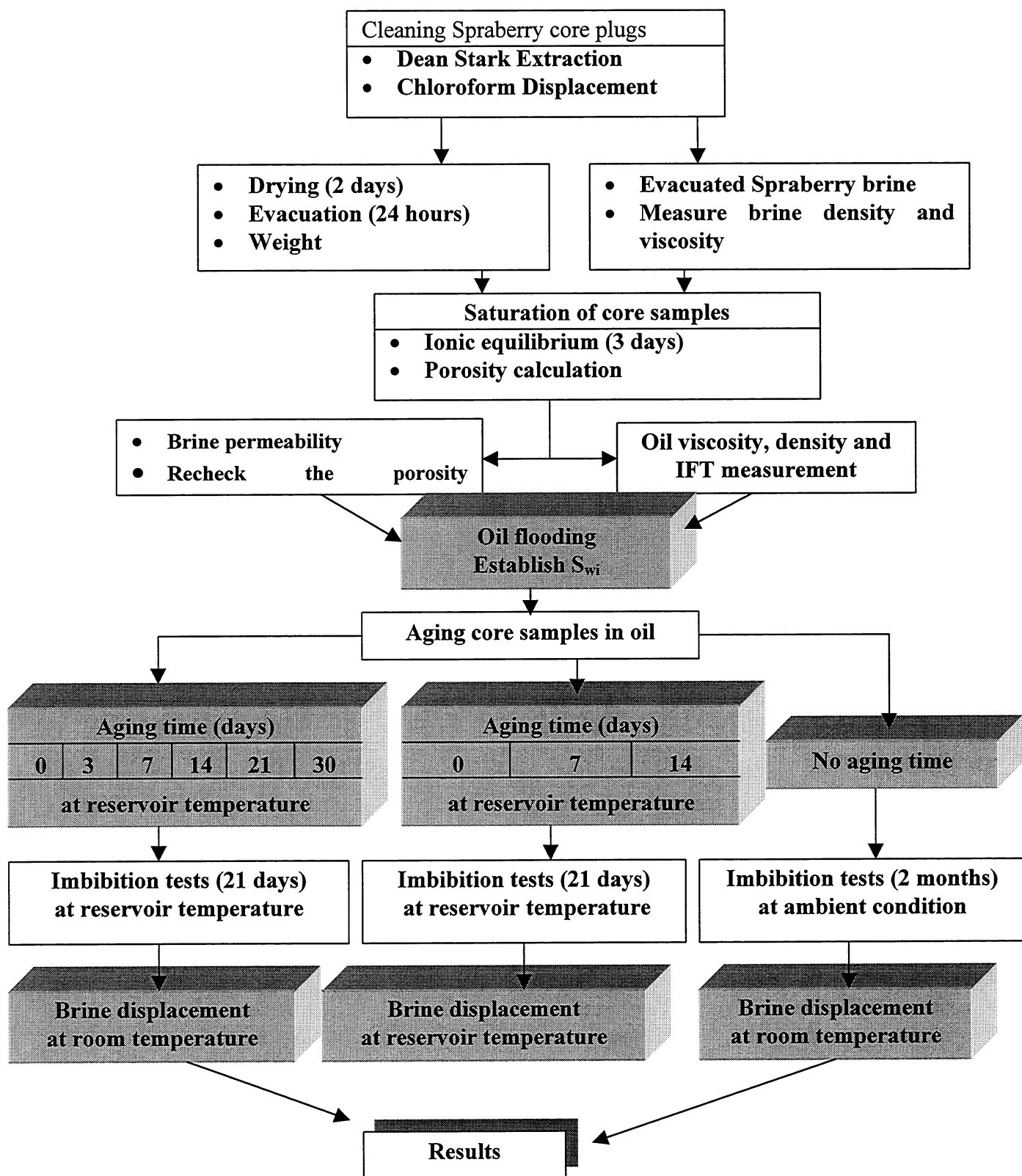


Fig. 2.1-1 Schematic experimental program.

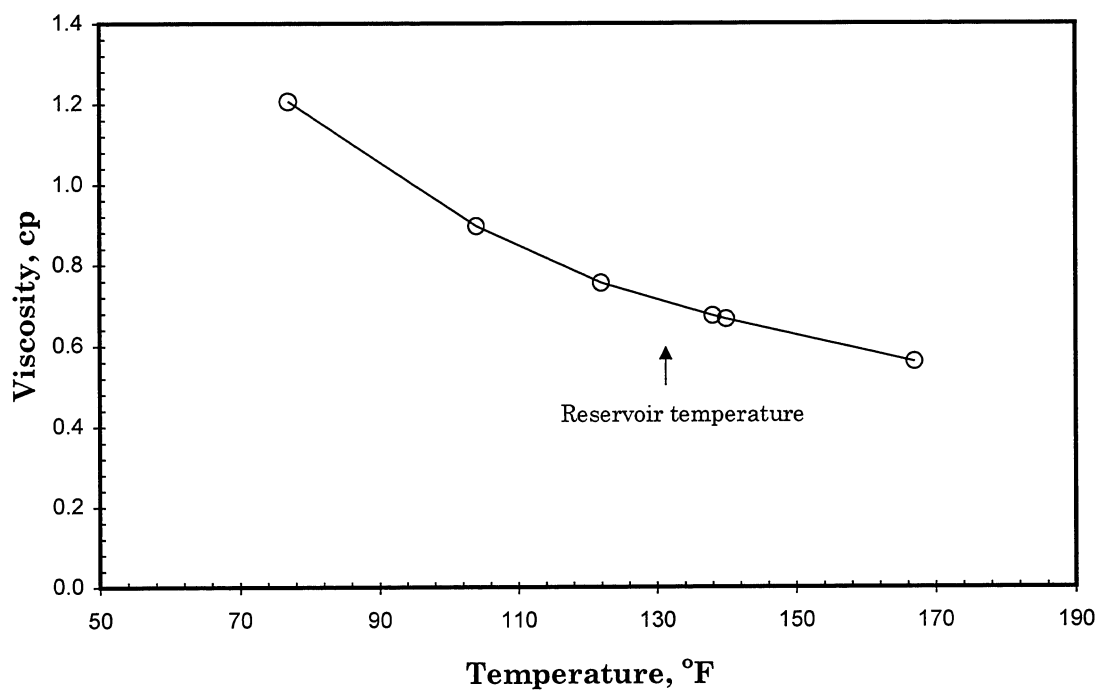


Fig. 2.1-2 Variation in viscosity of synthetic Spraberry brine with temperature increase.

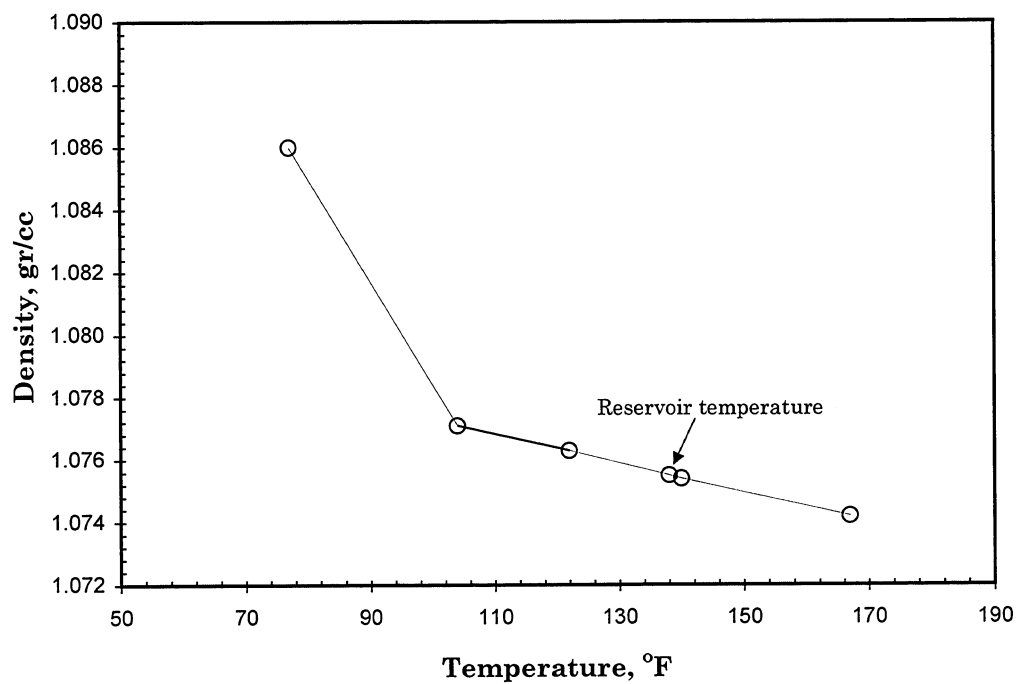


Fig. 2.1-3 Variation in density of synthetic Spraberry brine with temperature increase.

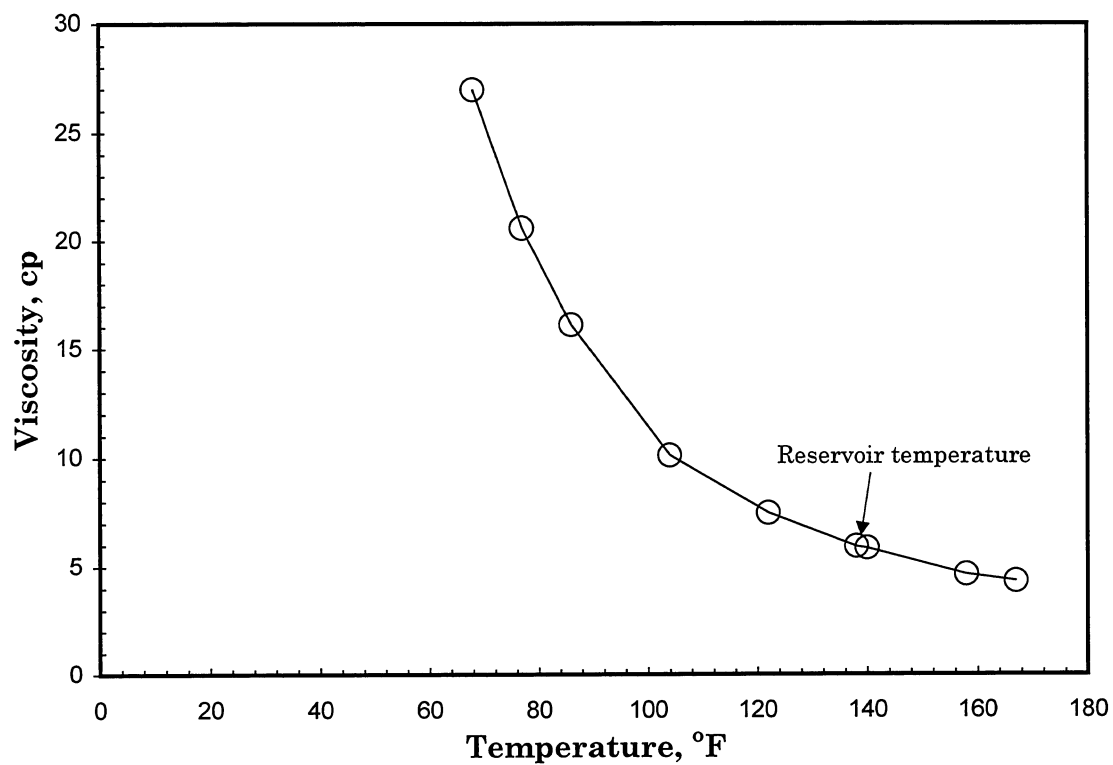


Fig. 2.1-4 Variation in viscosity of Spraberry oil with temperature increase.

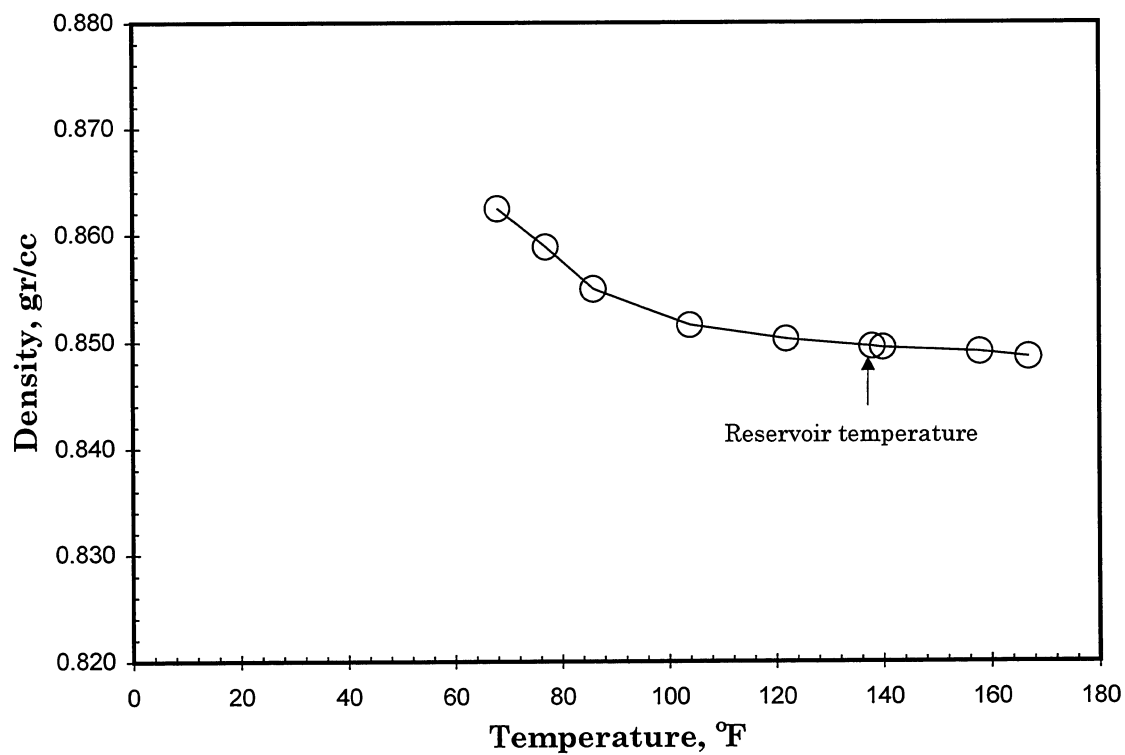


Fig. 2.1-5 Variation in density of Spraberry oil with temperature increase.

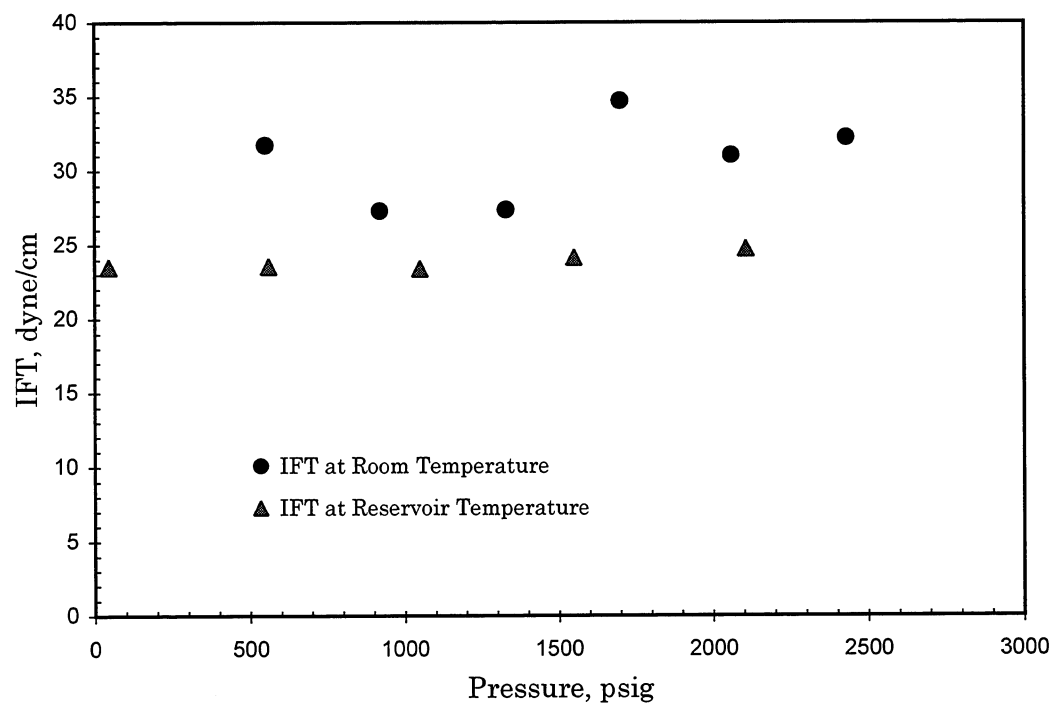


Fig. 2.1-6 Interfacial tension of Spraberry oil – brine at elevated pressure.

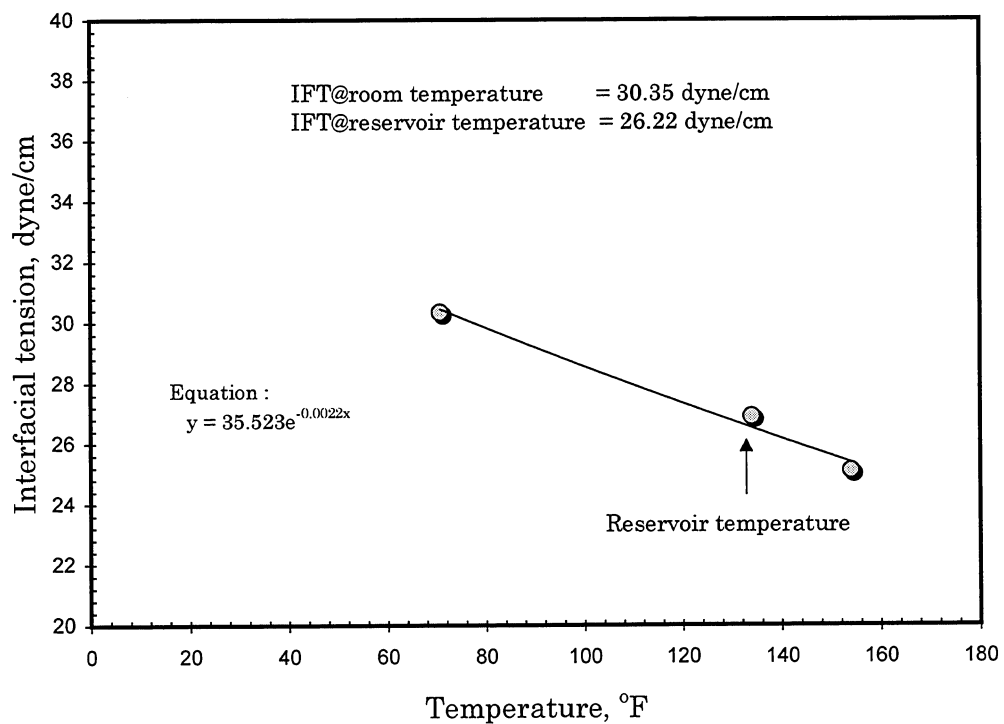


Fig. 2.1-7 Interfacial tension of Spraberry oil – brine at elevated temperature.

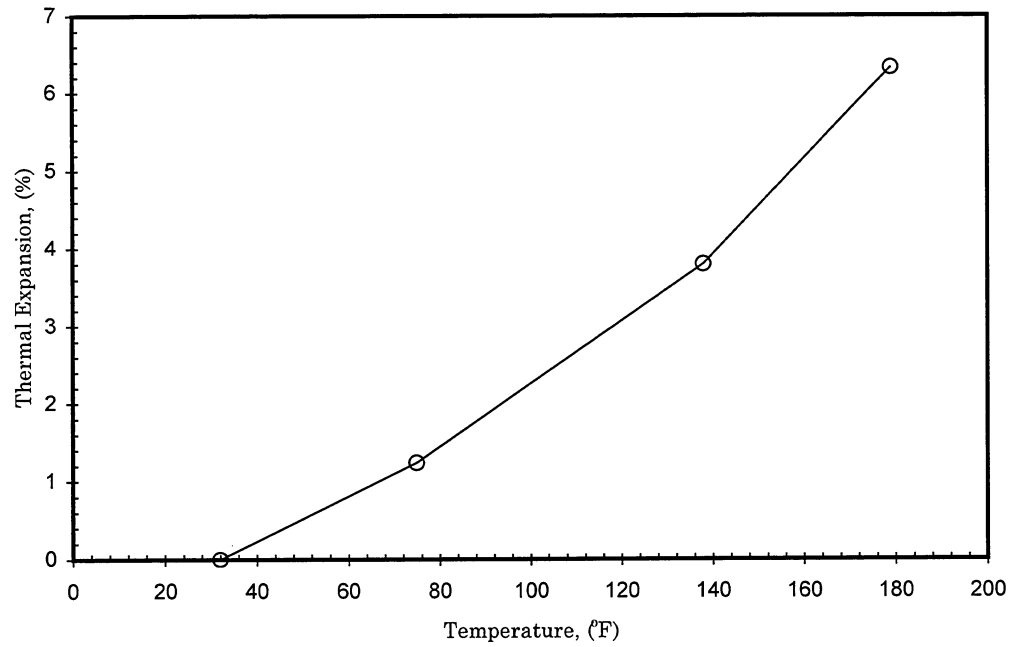


Fig. 2.1-8 Thermal expansion of Spraberry oil.

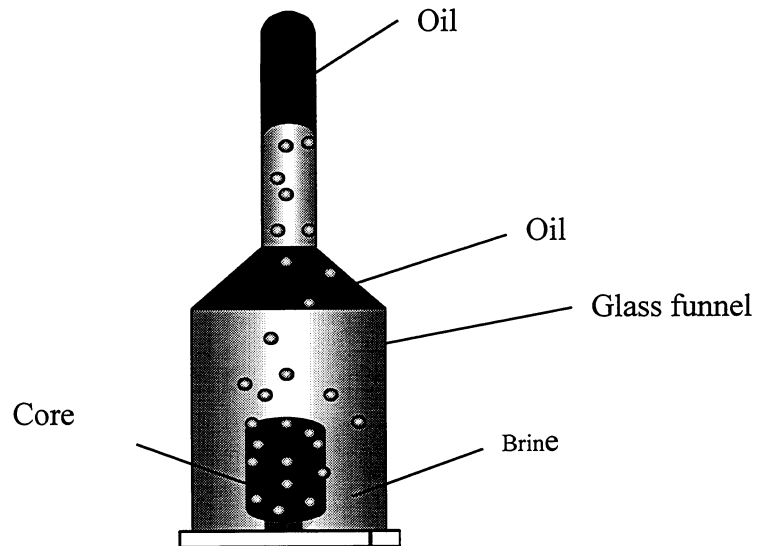


Fig. 2.1-9 Spontaneous imbibition apparatus.

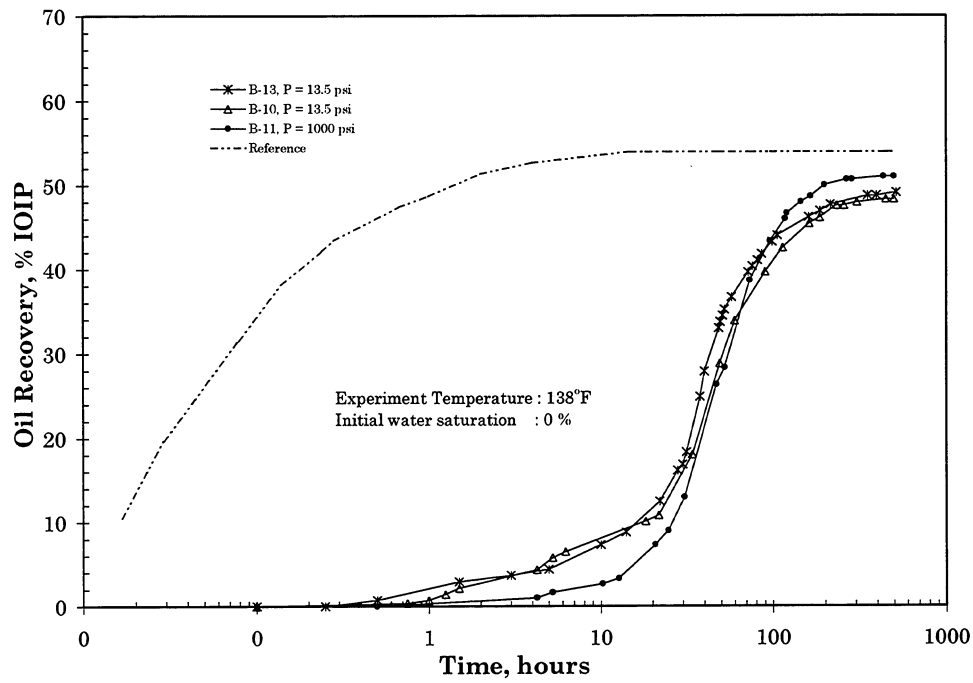


Fig. 2.1-10 Effect of elevated pressure on rate of imbibition and recovery using Berea sandstone

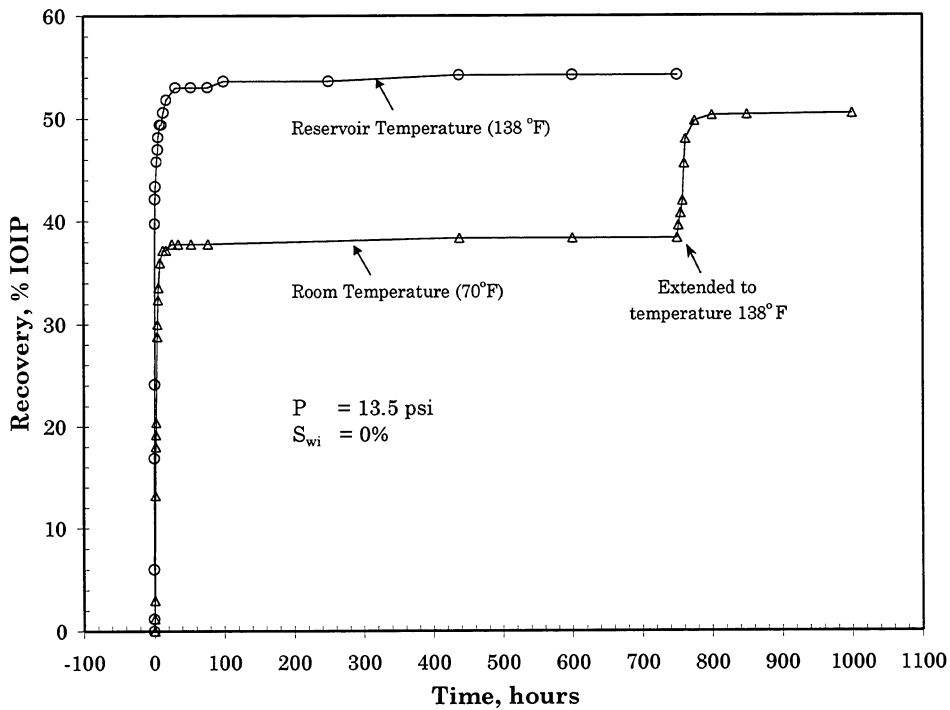


Fig. 2.1-11 Effect of changing temperature on rate of imbibition and recovery using Berea sandstone.

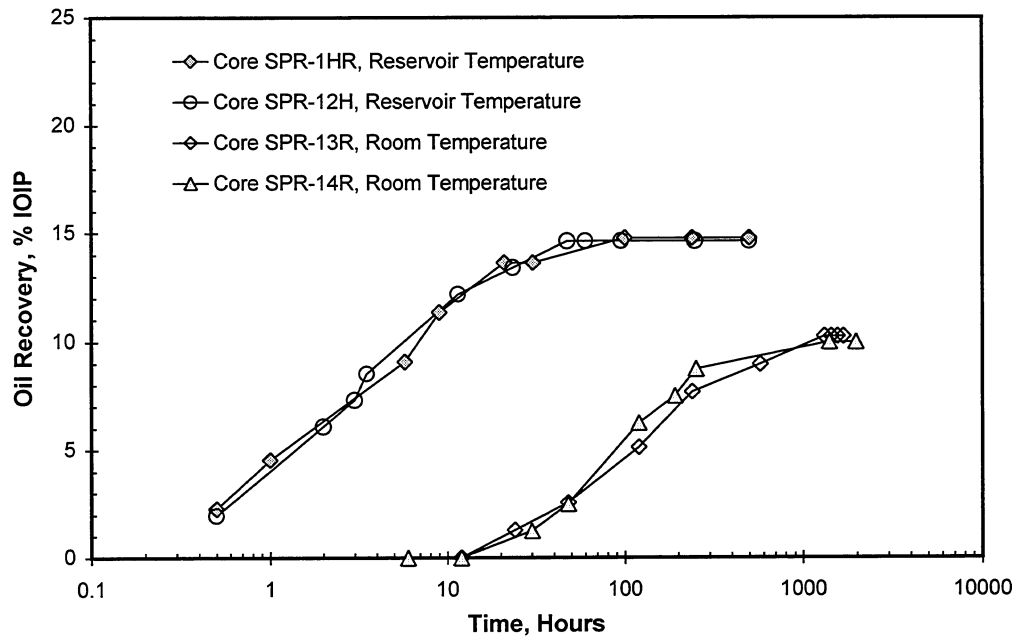


Fig. 2.1-12 Effect of temperature in imbibition tests.

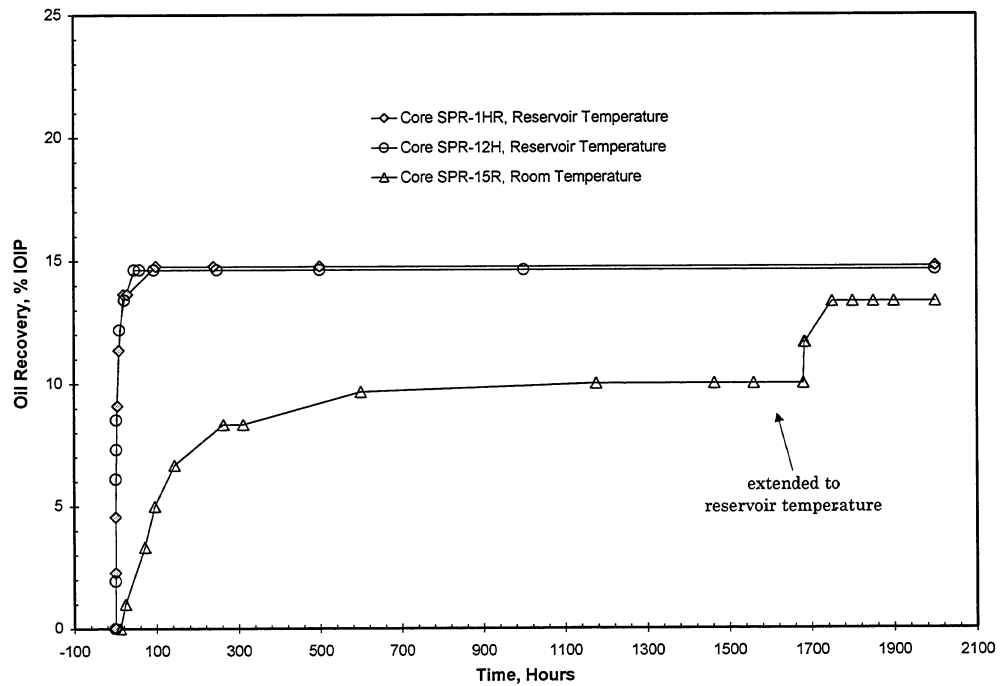


Fig. 2.1-13 Effect of temperature changes on oil recovery by imbibition.

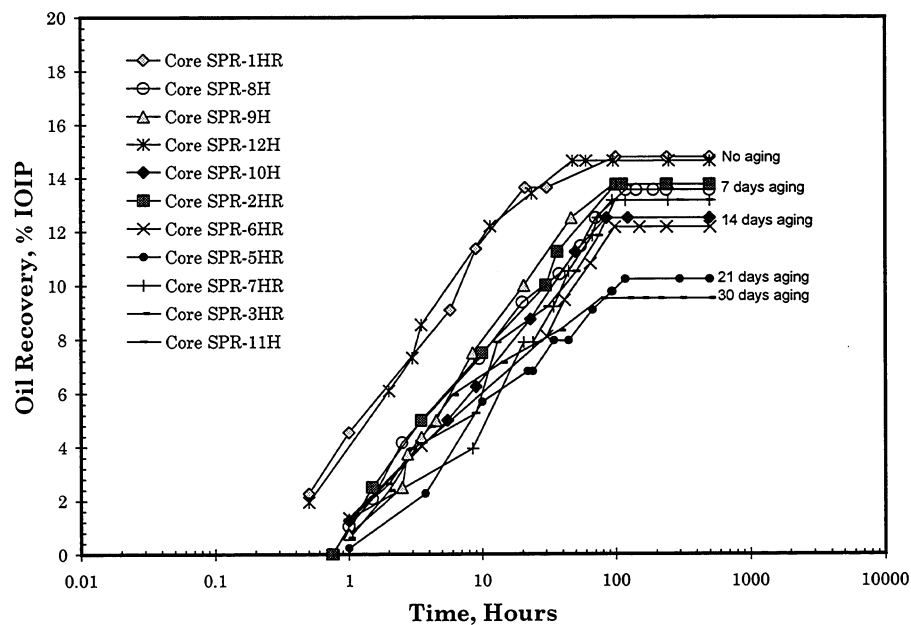


Fig. 2.1-14 Oil recovery curve obtained from imbibition experiment performed at reservoir temperature.

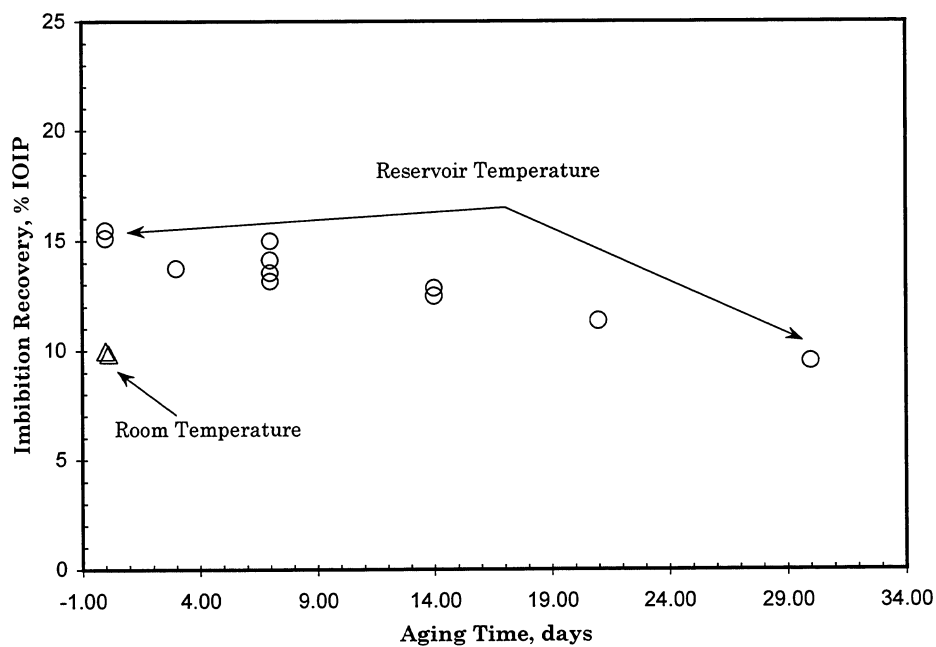


Fig. 2.1-15 Effect of aging time on the recovery of oil by imbibition.

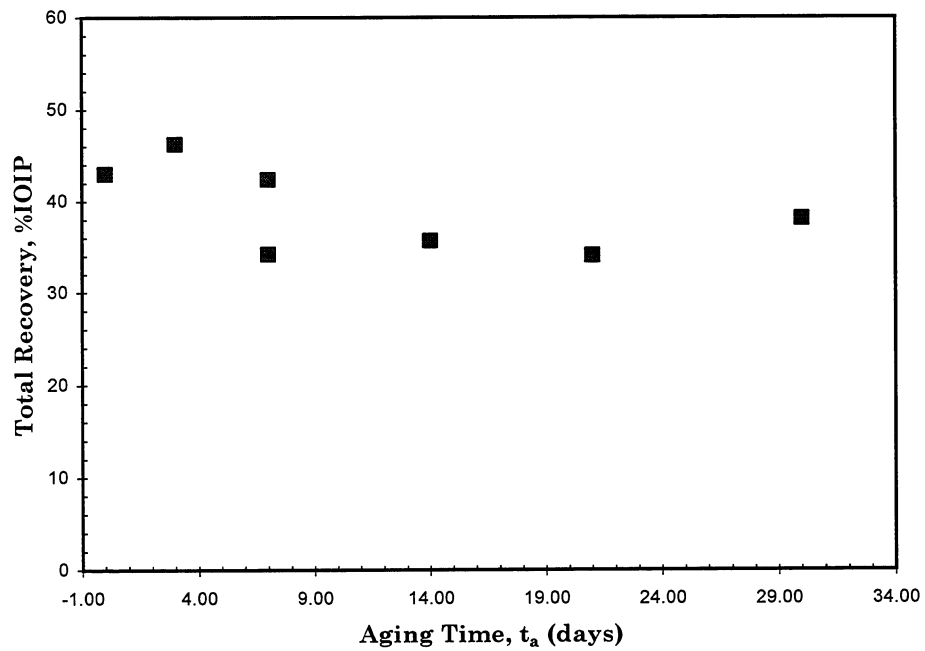


Fig. 2.1-16 Total recovery (imbibition plus displacement) versus aging time to exclude the effects of aging time on the recovery mechanism.

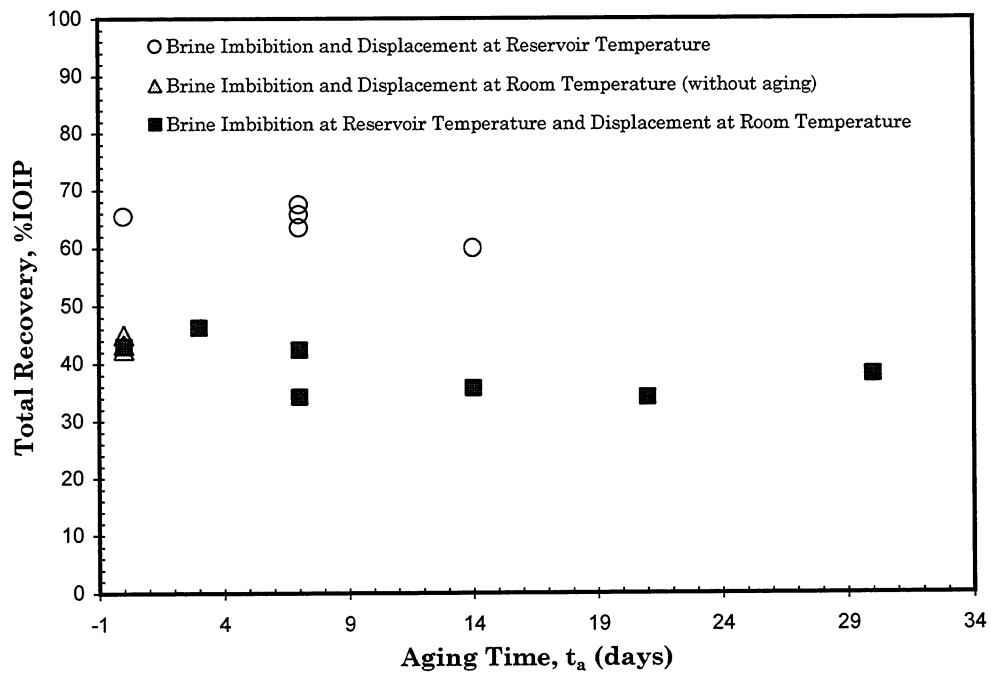


Fig. 2.1-17 Effect of aging time on total recovery at elevated temperatures.

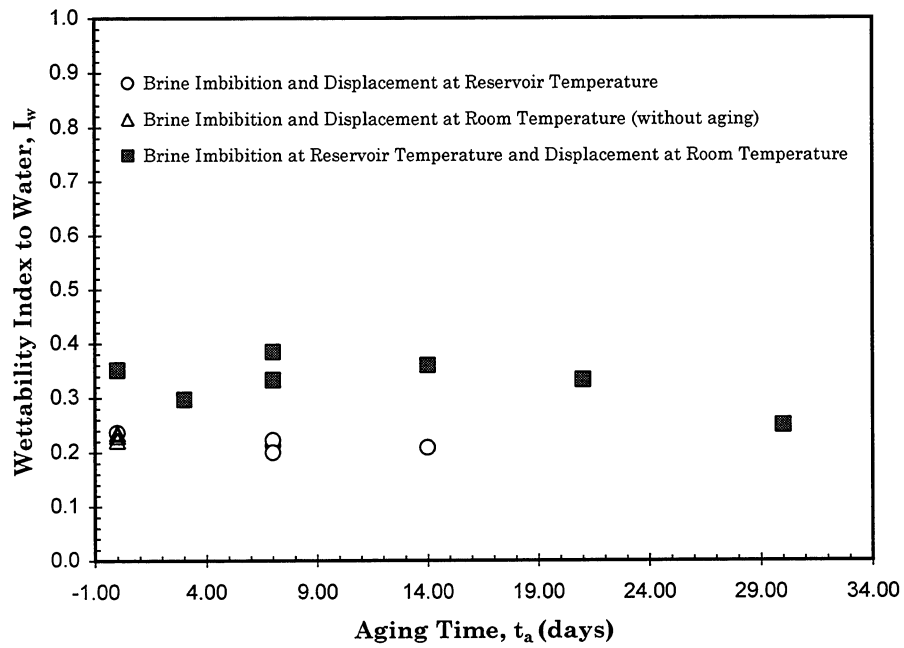


Fig. 2.1-18 Wettability index to water versus aging time for the different experiment temperatures.

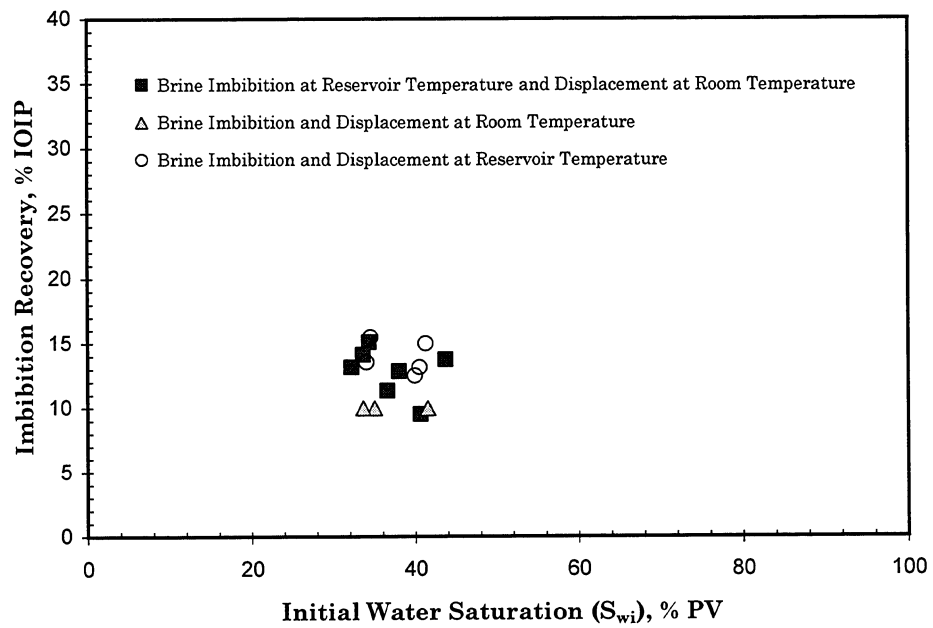


Fig. 2.1-19 Effect of initial water saturation on oil recovery by imbibition.

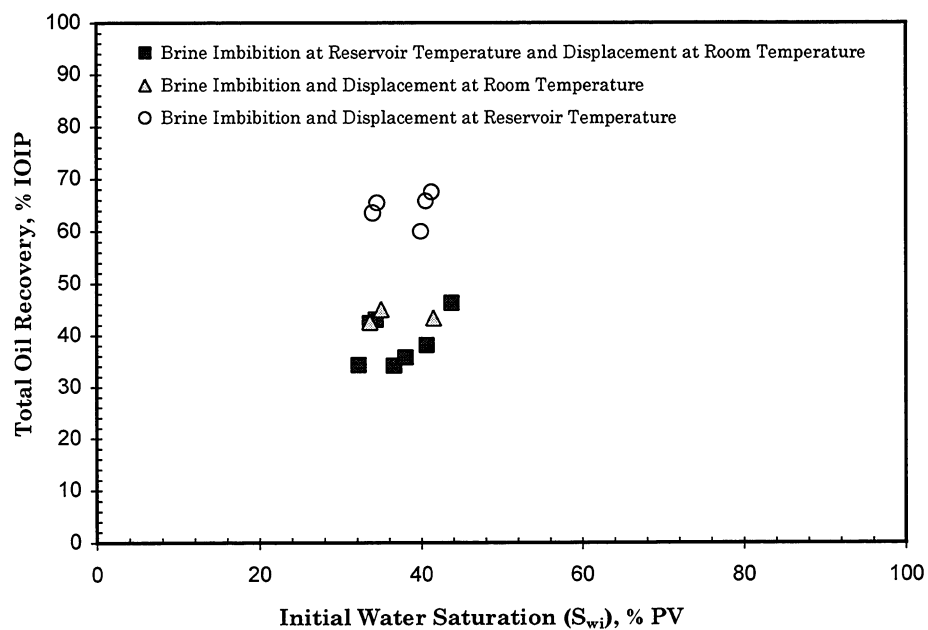


Fig. 2.1-20 Effect of initial water saturation on total recovery.

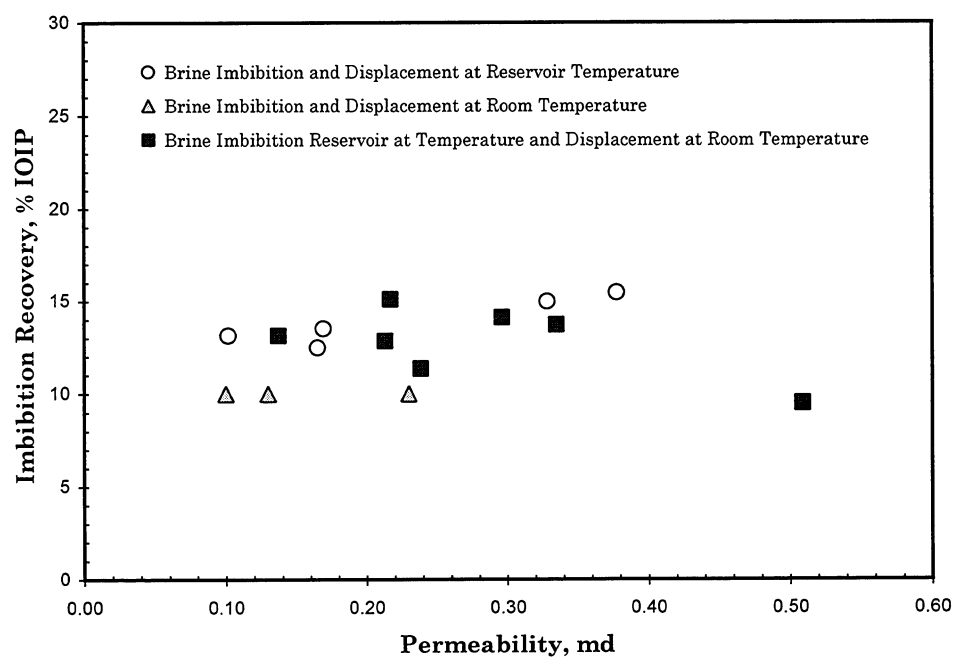


Fig. 2.1-21 Effect of permeability on recovery by imbibition.

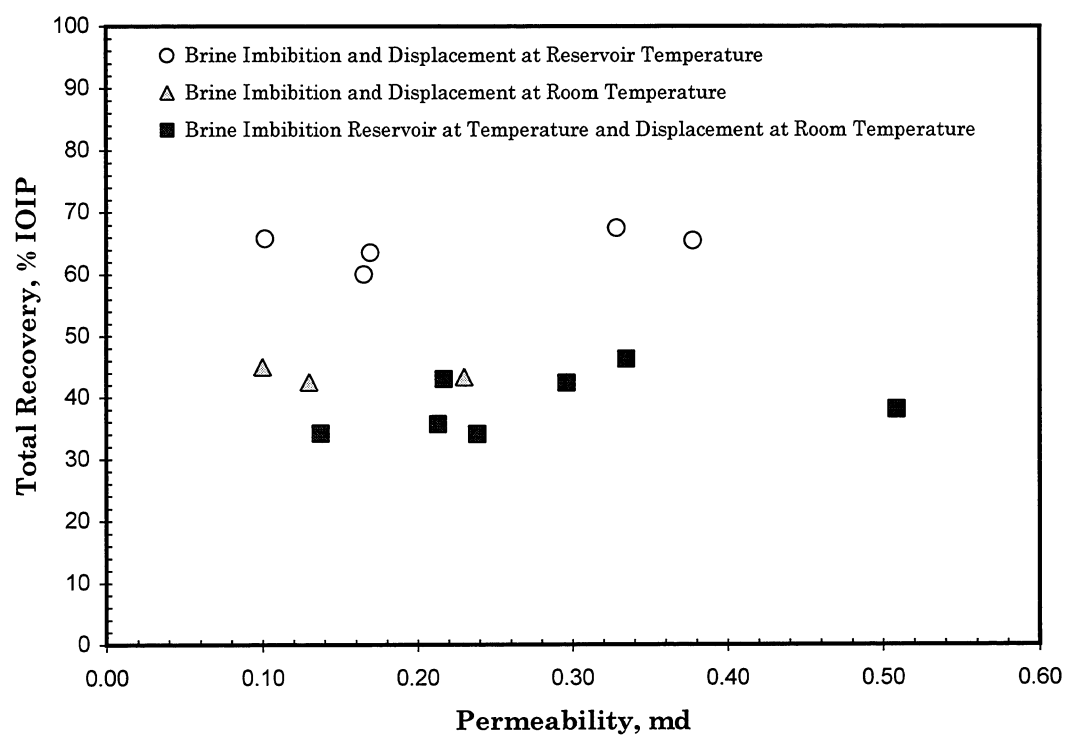


Fig. 2.1-22 Effect of permeability on total oil recovery.

2.2 SPONTANEOUS IMBIBITION MODELING OF SPRABERRY CORES USING A FINITE DIFFERENCE SCHEME

2.2.1 Introduction

This section presents the numerical modeling of the spontaneous imbibition experiment presented in the previous section. A fully finite-difference implicit scheme was developed to solve non-linear diffusion of the spontaneous imbibition equation. The objectives of this study were to simulate and to understand the imbibition process in low permeability Spraberry core. The numerical results satisfactorily matched the laboratory spontaneous-imbibition experiment data. By matching the experimental data with the simulation output, the matrix capillary pressure was determined. Once the important capillary pressure parameter is determined, then key variables of relative permeability, oil and water viscosities and initial water saturations, on the imbibition rate can be evaluated. Also, the sensitivity of the capillary pressure on imbibition in the Spraberry rock could be evaluated.

2.2.2 Background

Imbibition plays a very important role in the recovery of oil from the naturally fractured Spraberry area. An understanding of the imbibition process and the key parameters that control the imbibition process are crucial. To understand the physical process of imbibition, the spontaneous imbibition experiment was conducted using core, oil and synthetic brine. When oil saturated core contacts with brine, the imbibition process starts immediately. The amount of oil produced is recorded against time. Spontaneous imbibition experiments usually take a long time. Sensitivity studies to investigate the effect of some parameters on imbibition rate can become very lengthy.

Two parameters present a problem. The capillary pressure is difficult to determine and the water saturation profiles at different times and locations can be difficult and time consuming to determine. To quantify the effects of these two parameters on the imbibition process in a reasonable and effective length of time, numerical modeling or simulation is used.

Several studies have been conducted to simulate the spontaneous imbibition process in a core plug. These studies were concerned primarily with the capillary pressure as the only driving force in the spontaneous imbibition process. Blair (1964) presented 1D-numerical solutions describing the imbibition of water and the countercurrent flow of oil in porous rocks. Blair concluded that the rate of imbibition varies with capillary pressure, relative permeability curves, oil viscosity, and initial water saturation.

Beckner *et al* (1987) proposed modeling imbibition as a diffusion process with a nonlinear diffusion coefficient. They assumed that the oil phase gradient ahead and behind the front is negligible. In other words, no countercurrent oil flow exists. Knowing this weakness, they used equations for imbibition with countercurrent flow described by Blair (1964). They set total velocity equal to zero in the fractional flow equation and ignored gravity and source terms. Bech *et al* (1989) and Dutra *et al* (1991) have used this diffusion equation.

Chen *et al* (1995) used the diffusion equation to conduct numerical experiments of countercurrent imbibition in a single matrix block to identify flow characteristic. They used the nonlinear diffusion equation describing countercurrent flow derived by Blair (1964). They solved that equation numerically by using a semi-implicit method.

Baker and Wilson (1997) used a “black oil” DRS Ver. 3.5 simulator to study numerical simulation of a laboratory scale imbibition experiment. They used a radial coordinate and modeled the matrix and fracture systems explicitly. The fracture system simulated the shock front that provided the driving mechanism for the initiation of the imbibition process, while the matrix system represented the core plug. They studied the variation of relative permeability and matrix capillary pressure on the behavior of the recovery curve by matching the laboratory imbibition data. They concluded that imbibition recovery was sensitive to relative permeability and capillary pressure.

In this study, the spontaneous imbibition tests were conducted under reservoir conditions using core plugs taken from low permeability Spraberry formation (see Section 2.1). Spraberry oil and synthetic Spraberry brine were used as wetting and non-wetting fluids. The work described in this section was performed to develop the mathematical model for matching the laboratory imbibition data. The matching data can be used to study the spontaneous imbibition process in detail and to investigate the effect of key variables on the imbibition rate.

2.2.3 Experimental Data

Based on results of previous imbibition experiments as presented in Section 2.1, four representative core samples were used as a comparison of the simulation data. The physical properties of the reservoir core samples and fluids are presented in Table 2.2-1. The experimental procedure is described in Section 2.1.3.

2.2.4 Mathematical Formulation

A mathematical formulation of the spontaneous imbibition process is described here. In deriving the governing equations, some assumptions are used:

- gravity terms are negligible,
- capillary pressure is the only driving force where total velocity is zero, and
- fluid and rock are incompressible.

The simultaneous flow of two-phases in a porous media is described in four basic flow equations (Eqs. 1 to 4) as described below:

$$\nabla \cdot \vec{u}_w + \phi \frac{\partial S_w}{\partial t} = 0 \dots\dots\dots(1)$$

$$\nabla \cdot \vec{u}_o + \phi \frac{\partial S_o}{\partial t} = 0 \dots\dots\dots(2)$$

$$p_o - p_w = p_c(S_w) \dots\dots\dots(3)$$

$$S_o + S_w = 1 \dots\dots\dots(4)$$

By using Darcy's law, the water and oil velocities can be written as

$$\bar{u}_w = -\frac{k}{\mu_w} k_{rw} \nabla p_w \dots\dots\dots(5)$$

$$\bar{u}_o = -\frac{k}{\mu_o} k_{ro} \nabla p_o \dots\dots\dots(6)$$

The total flow for countercurrent imbibition is defined as

$$\bar{u}_T = \bar{u}_o + \bar{u}_w \dots\dots\dots(7)$$

Combining Eqs. 3, 5,6 and 7 gives

$$\bar{u}_w \left(1 + \frac{k_{ro}}{\mu_o} \frac{\mu_w}{k_{rw}}\right) = \bar{u}_T + \frac{k}{\mu_o} k_{ro} \nabla p_c \dots\dots\dots(8)$$

Implementing the assumption that the capillary pressure is the only driving force, then the total velocity can be set to be zero and Eq. 8 becomes

$$\bar{u}_w = \frac{k}{\mu_o} k_{ro} f_w \nabla p_c \dots\dots\dots(9)$$

Where water fractional flow is defined as

$$f_w = \left(1 + \frac{k_{ro}}{\mu_o} \frac{\mu_w}{k_{rw}}\right)^{-1} \dots\dots\dots(10)$$

Substituting Eq. 9 into Eq. 1, a governing equation for describing the spontaneous imbibition process is obtained as follows:

$$\nabla \cdot D(S_w) \frac{\partial S_w}{\partial x} = -\phi \frac{\partial S_w}{\partial t} \dots\dots\dots(11)$$

Where the non-linear capillary diffusion coefficient is defined as

$$D(S_w) = \frac{k}{\mu_o} k_{ro} f_w \frac{\partial p_c}{\partial S_w} \dots\dots\dots(12)$$

Because of the non-linear capillary diffusion coefficient, Eq. 11 must be solved by numerical methods.

2.2.5 Finite-Difference Scheme

In order to solve Eq. 11 numerically, discretization in 2D finite-difference form was implemented. The left-hand side was discretized by applying Taylor series using central difference and the right-hand side using backward difference. The superscript indicates the

time level. n is the old time level for which we have a complete solution and all variables and properties. $n+1$ is the new time level for which the solution is unknown. With this notation, our finite-difference approximations to the 2D spontaneous imbibition equation is

$$\begin{bmatrix} & & D_{i,j+1/2} & & \\ D_{i-1/2,j} & -D_{i-1/2,j} & -D_{i+1/2,j} & -D_{i,j-1/2} & -D_{i,j+1/2} & D_{i+1/2,j} \\ & & D_{i,j-1/2} & & \end{bmatrix} \begin{bmatrix} S_{wi} \end{bmatrix}^{n+1} = -\frac{\phi h_x h_y}{\Delta t} [S_{wi}^{n+1} - S_{wi}^n] \dots\dots\dots (13)$$

$D_{i-1/2,j}$ and $D_{i+1/2,j}$ are evaluated using arithmetic averaging as below

$$D_{i-1/2,j} = \frac{D_{i,j} + D_{i-1,j}}{2} \dots\dots\dots (14)$$

$$D_{i+1/2,j} = \frac{D_{i,j} + D_{i+1,j}}{2} \dots\dots\dots (15)$$

Note that the relative permeabilities and capillary pressure are functions of water saturation; thus, Eq. 13 must be solved iteratively. Once the new saturations are solved using the initial guess, these new water saturations are compared with the old water saturations until acceptance convergence has been reached.

The core plug is totally immersed in the water and therefore, boundary conditions are set to be $1-S_{or}$. This implies that instantaneous imbibition occurs at the matrix-fracture interface. Initial conditions are required to begin the time step sequence. In this study, initial conditions are specified equal to initial water saturation.

2.2.6 Results and Discussions

In order to match the recovery from the imbibition experiments, only capillary pressure was altered and other parameters were kept constant. The following relative permeability correlations from Honarpour *et al* (1986) as inputs:

$$k_{ro} = k_{ro}^o (1 - S_w^*)^3 \dots\dots\dots (16)$$

$$k_{rw} = k_{rw}^o (S_w^*)^3 \dots\dots\dots (17)$$

For the base case, the maximum oil relative permeability (k_{ro}^o) was set to 1.0 and the maximum water relative permeability (k_{rw}^o) was set to 0.3. In these relationships, the S_w^* is expressed as $S_w^* = \frac{(S_w - S_{wi})}{(1 - S_{or} - S_{wi})}$. The residual oil saturation (S_{or}) was set to 0.5437 and irreducible water saturation (S_{wi}) was set to 0.37. Those average values of S_{or} and S_{wi} values are obtained from Table 2.2-1.

The average of residual oil saturations after spontaneous imbibition experiments was still very high. Therefore, the water saturation changes during the simulation are very small, which causes the numerical solution to become unstable and the result cannot be obtained. In order to approach this problem, three higher residual oil saturations of 0.2, 0.3 and 0.4 were used. Once the numerical solution matched with the experimental data, the matrix capillary pressures from different residual oil saturations were obtained. Then, the matrix capillary pressure for 0.54 residual oil saturation was estimated as shown in Fig. 2.2-1. The low-capillary pressure curve obtained indicates that the Spraberry matrix is weakly water-wet. The weakly water-wet indication is also found by the measurement of wettability index (average Amott index is 0.3, see section 2.1). Figure 2.2-2 shows four experimental data and numerical solution matches for recovery against time using residual oil saturation of 0.2.

The diffusion coefficient as shown in Fig. 2.2-3 is strongly non-linear due to varying capillary pressure and relative permeability curves as functions of water saturation. Therefore, using constant capillary pressure and relative permeability curves to solve the spontaneous imbibition equation, which is always solved by an analytical solution, may fail to predict oil recovery by spontaneous imbibition.

2.2.6.1 The Effect of Capillary Pressure.

In order to investigate the sensitivity of imbibition capillary pressure on the imbibition rate, three different capillary pressures were used with multiplication in order of 0.1, 1 and 10 to the matching result of capillary pressure. Capillary pressure is assumed to be the only driving force in the spontaneous imbibition process. Thus, increasing the capillary pressure will increase the imbibition rate as shown in Fig. 2.2-4.

2.2.6.2 The Effect of Oil and Water Relative Permeabilities.

In order to investigate the sensitivity of relative permeability curves on the imbibition rate, three cases of oil relative permeability and water relative permeability curves were used. The results in Figs. 2.2-5 and 2.2-6 show that oil recovery by imbibition is sensitive to the oil relative permeability curves while no significant effect was observed in changing the water relative permeability curves. The imbibition rate was sensitive to the oil relative permeability. The capillary diffusion coefficient as given by Eq. 12 is a function of the square of the oil relative permeability and thus affects the imbibition process much more strongly.

2.2.6.3 The Effect of Oil and Water Viscosity.

To examine the effect of oil viscosity on the imbibition rate, simulation runs were made for three different oil viscosities, 0.59, 5.9 and 59 cp and three different water viscosities of 0.068, 0.68 and 6.8. In each case the fluid and rock properties were the same as those described in Table 2.2-1. The effect of different oil viscosities on the imbibition rate is shown in Fig. 2.2-7, where the oil volumes recovered as a function of time for three oil viscosities are plotted. The lower the oil viscosity, the easier for counter-current flow of oil and water in the porous matrix as water imbibes into the core plug. Increasing or decreasing water viscosity has no effect on the imbibition rate as shown in Fig. 2.2-8. The viscosities for water are exaggerated, but were made to delineate effects of this parameter. Again, like the oil relative permeability, the oil

viscosity is squared in the capillary diffusion term of Eq. 12, causing any changes to magnify by that power.

2.2.6.4 The Effect of Initial Water Saturation.

The effect of initial water saturation on the imbibition rate is studied using four initial water saturation of 0, 0.2, 0.34, and 0.4. The results indicated that the imbibition rate is sensitive to the changes of initial water saturations. As initial water saturation decreases, the capillary pressure is greater, resulting in higher imbibition rate and in turn, higher oil volume recovered as shown in Fig. 2.2-9.

2.2.7 Conclusions

1. A 2D fully implicit numerical model has been developed to simulate the laboratory static spontaneous imbibition experiment.
2. The spontaneous imbibition equation might only be solved by the numerical method due to strong non-linear capillary diffusion.
3. The imbibition model developed here predicts a low imbibition capillary pressure for the Spraberry core. The capillary pressure was obtained by matching experimental oil recovery data. Results indicate that the wettability of the Spraberry core plug was weakly water-wet.
4. The rate of imbibition was sensitive to capillary pressure, oil relative permeability, oil viscosity and initial water saturation.
5. The rate of imbibition was not sensitive to water relative permeability and water viscosity.

2.2.8 Nomenclature

D = diffusion coefficients, ML^3T^{-2}
 f = fractional flow, dimensionless
 h = distance, L
 k = permeability, L^2
 k_r = relative permeability, dimensionless
 p = pressure, MLT^{-2}
 P_c = capillary pressure, MLT^{-2}
 S = saturation, fraction
 t = time, T
 u = velocity, LT^{-1}
 ϕ = porosity, fraction

Subscripts

i = initial condition
 i,j = integer denoting cell location in the x- and y- directions.
 o = oil
 w = water
 x,y = x-,y- direction, respectively

Superscripts

n = integer indicating time level

2.2.9 References

1. Baker, R and Wilson, G.: " Numerical Simulation of Laboratory Scale Imbibition Experiment," Internal Report, Epic Consultant Services Ltd., (April 1997).
2. Bech, N., Jensen, O.K., and Nielsen, B.: "Modeling of Gravity-Imbibition and Gravity-Drainage Processes," *SPE*. (Feb. 1991) 129-136.
3. Beckner, B. L., Ishimoto, K., Yamaguchi, S., A. Firoozabadi and Aziz, K.: "Imbibition-Dominated Matrix-Fracture Fluid Transfer in Dual Porosity Simulators," paper SPE 16981 presented at the 1987 SPE Annual Technical Conference and Exhibition, Dallas, TX., Sept. 27-30.
4. Blair, P.M.: "Calculation of Oil Displacement by Countercurrent Water Imbibition," SPEJ Sept. 1964, 195-202; *Trans.*, AIME, **231**.
5. Chen, J., Miller, M.A. and Sepehrnoori, K.: "Theoretical Investigation of Countercurrent Imbibition in Fractured Reservoir Matrix Blocks," paper SPE 29141 presented at the 1995 Symposium on Reservoir Simulation, San Antonio, TX., Feb. 12-15.
6. Honarpour, M., Koederitz, L. and Harvey, A. H.: Relative Permeability of Petroleum Reservoirs, CRC Press, Inc., Boca Raton, FL, (1986).
7. Dutra, T. V. and Aziz, K.: "A New Double-Porosity Reservoir Model for Oil/Water Flow Problems," paper SPE 21248 presented at the 1991 SPE Symposium on Reservoir Simulation, Ca., Feb 17-20.

Table 2.2-1 Core and Fluid Properties

Core Properties						Fluid properties at 138°F	
Cores #	Length, (cm)	Diameter, (cm)	Permeability to brine, (md)	Porosity, (%)	S_{wi} , (%)	μ_o , (cp)	5.92
SPR-8H	6.487	3.608	0.17	10.98	34.05	μ_w , (cp)	0.68
SPR-9H	6.502	3.607	0.33	10.26	41.29	ρ_o , (gr/cc)	0.850
SPR-10HR	5.433	3.607	0.14	10.11	39.96	ρ_w , (gr/cc)	1.076
SPR-11H	5.842	3.607	0.10	10.71	40.55	IFT, (dyne/cm)	26.22

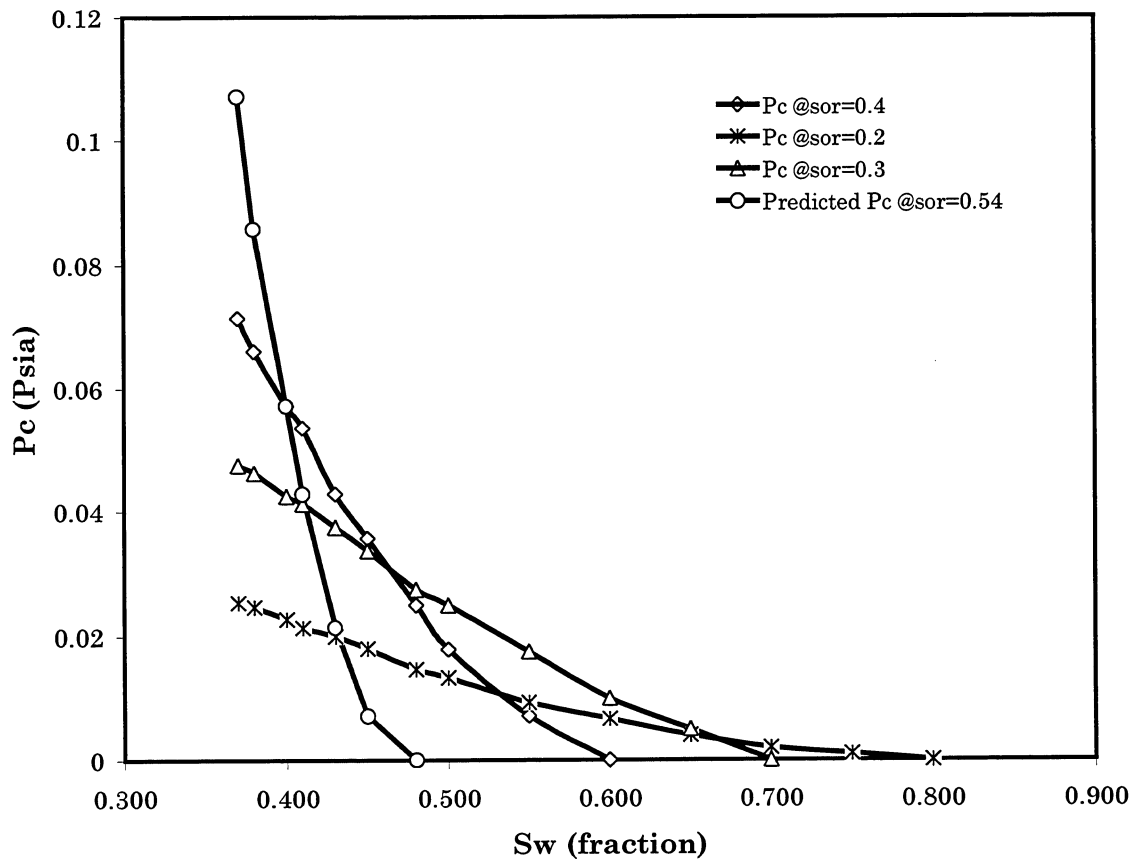


Fig. 2.2-1 Imbibition capillary pressure obtained from matching spontaneous imbibition data.

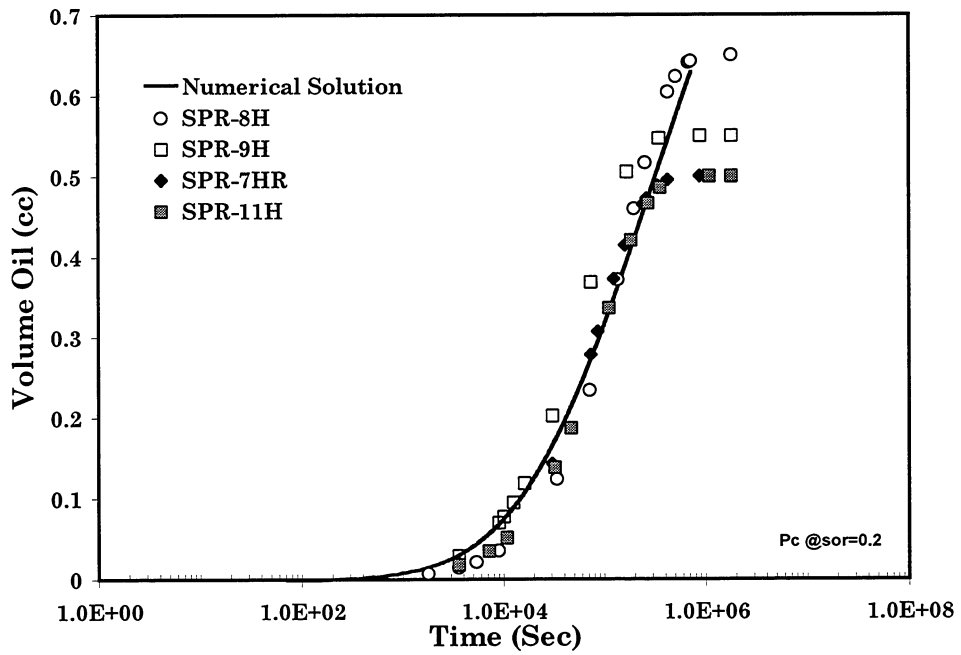


Fig. 2.2-2 Matching between spontaneous-imbibition experiments with numerical solution.

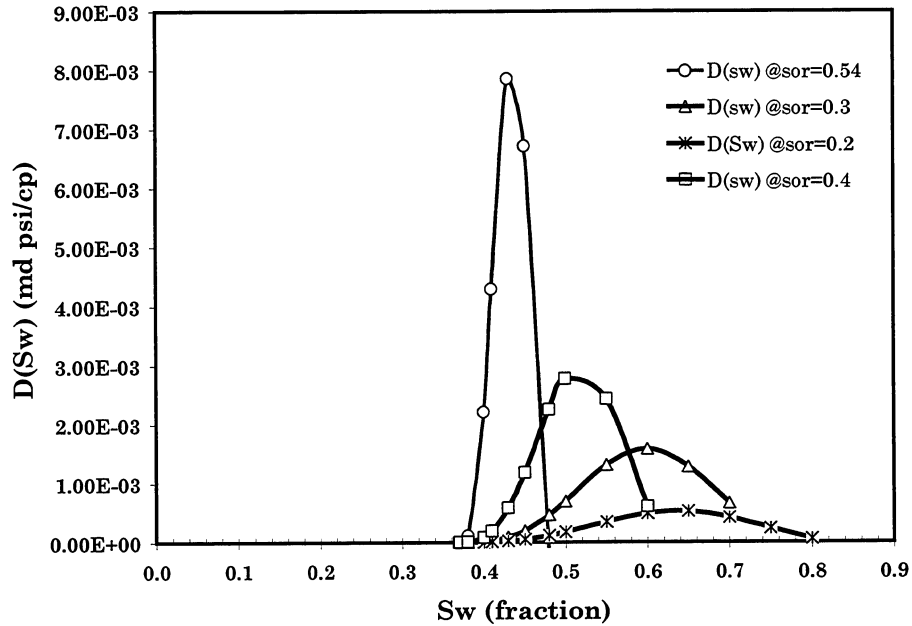


Fig. 2.2-3 Non-linear diffusion coefficient.

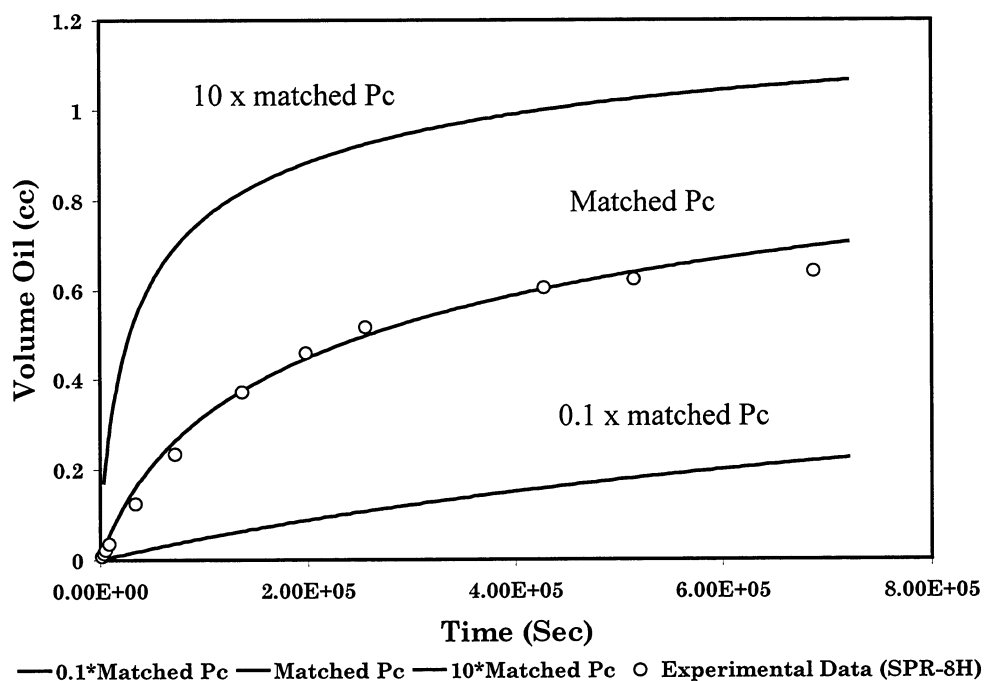


Fig. 2.2-4 Effect of different capillary pressures on oil volume recovered.

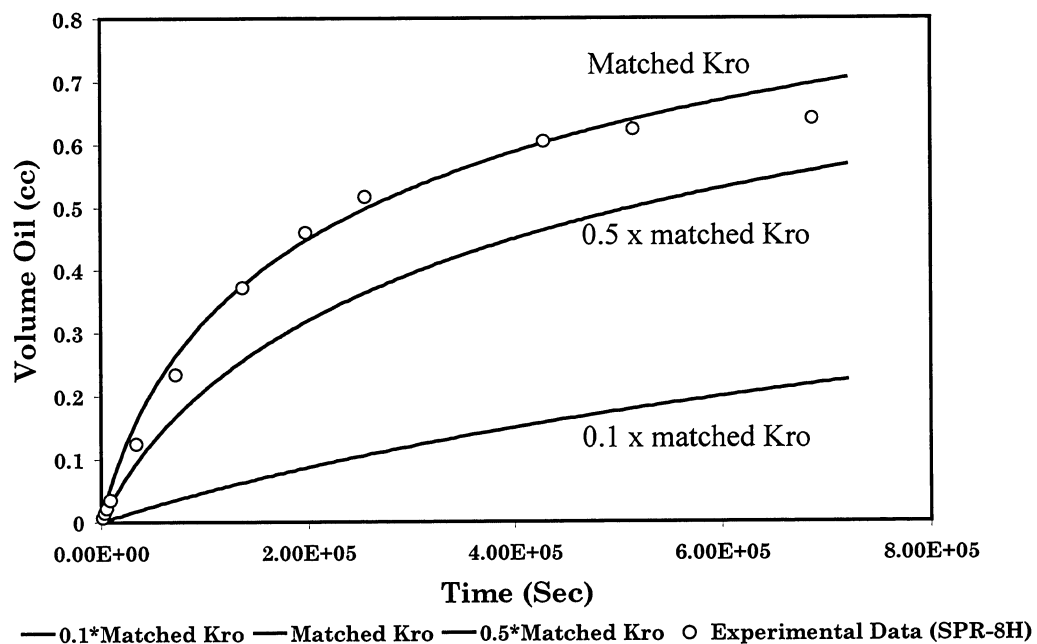


Fig. 2.2-5 Effect of different oil relative permeabilities on oil volume recovered.

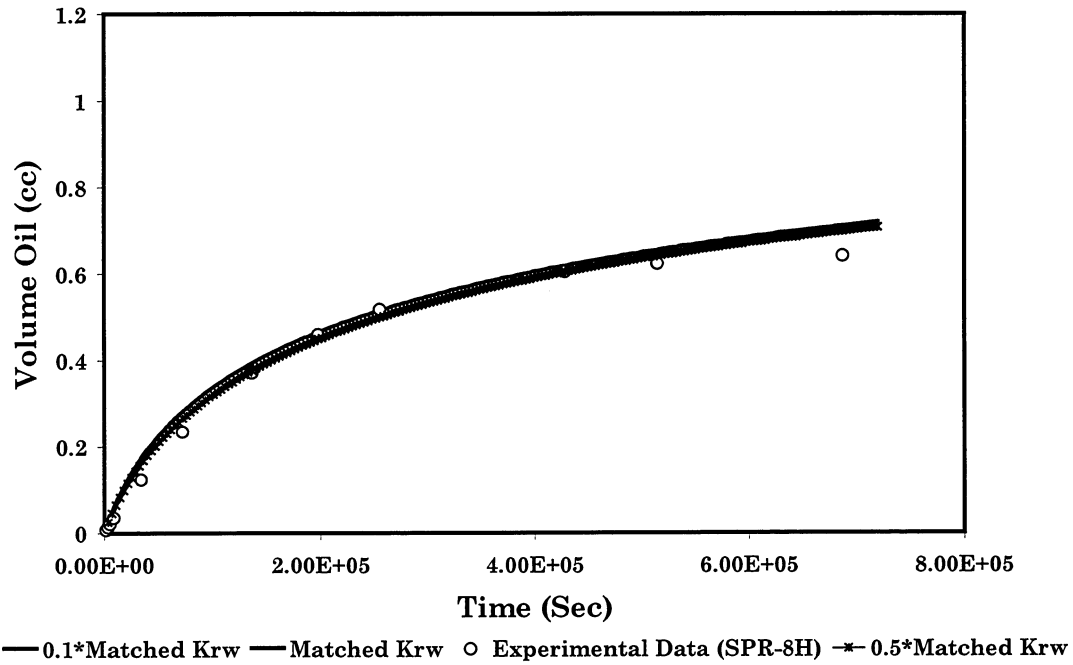


Fig. 2.2-6 Effect of different water relative permeabilities on oil volume recovered.

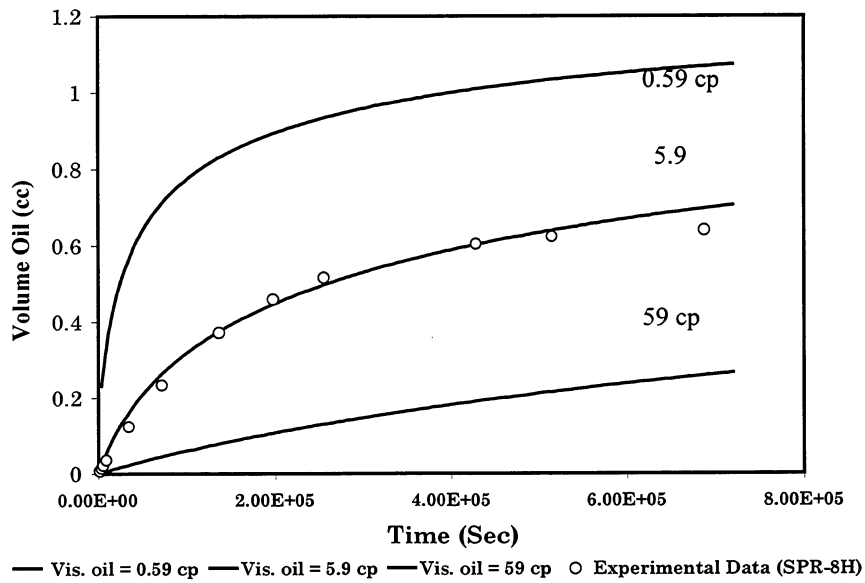


Fig. 2.2-7 Effect of different oil viscosities on oil volume recovered.

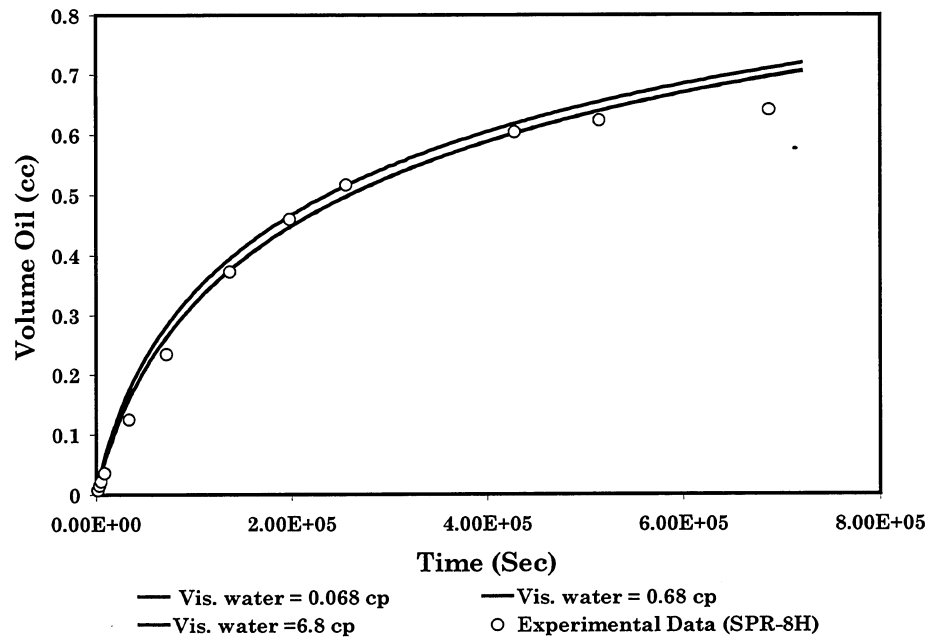


Fig. 2.2-8 Effect of different water viscosities on oil volume recovered.

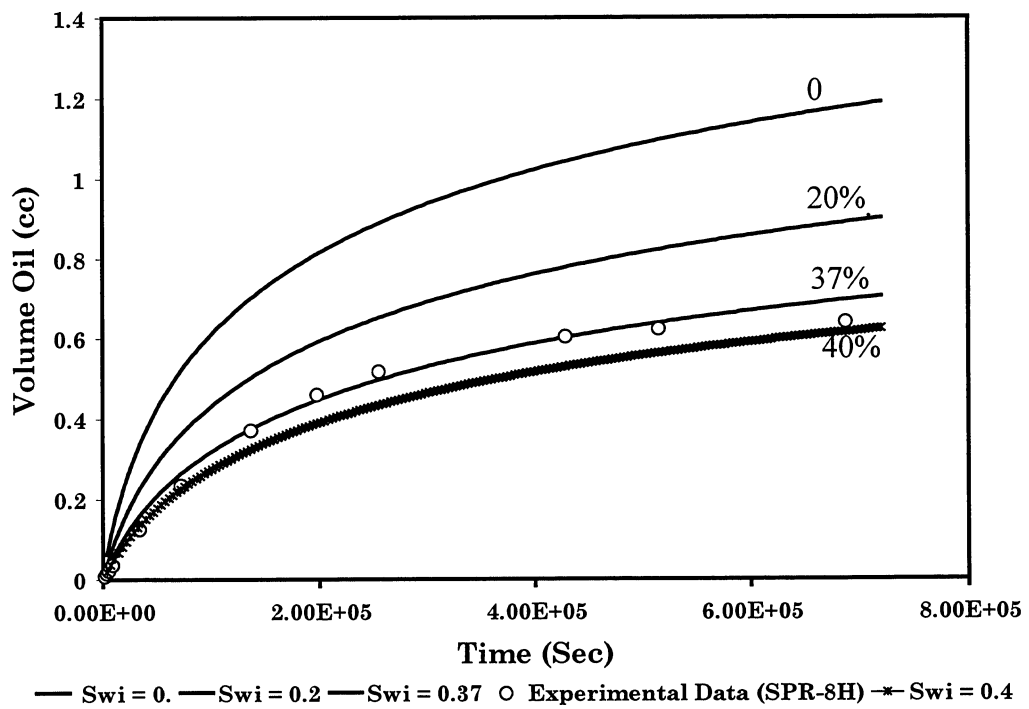


Fig. 2.2-9 Effect of different initial water saturations on oil volume recovered.

2.3 IMBIBITION-FLOODING MODELING OF ARTIFICIALLY FRACTURED CORE

2.3.1 Background

In naturally fractured reservoirs, an exchange of fluids occurs between the matrix and the fracture system. Fluid displacement in the fracture network occurs due to its higher conductivity compared to the matrix. Viscous forces and capillary phenomena control the fluid transfer process.

In 1952, Brownscombe and Dyes introduced the concept of a process for imbibition flooding. The process was visualized in term of a single fracture into which water is injected at one end, production occurring at the other end. As the injected water flows toward the producing end, it is imbibed into the matrix and oil flows out into the fracture flow stream. If the rate of natural imbibition into the matrix is greater than the injection rate, all of the water will imbibe into the matrix and only oil will reach the producing end of the fractures. Any water injected above the rate of natural imbibition will increase the water-oil ratio. The water-oil ratio is a function both of the injection rate and the imbibition rate. Several laboratory and numerical studies have been conducted regarding this subject.

Kleppe and Morse (1974) investigated imbibition from a single matrix block surrounded by fractures. They studied the effects of the injection rate on the recovery performances using Berea core and numerically verified the results. They found that matrix oil recovery by imbibition of water from the fracture system was sensitive to oil production. In addition, they measured relative permeability and capillary pressure of the core.

Kazemi and Merrill (1977) used a two-dimensional, two-phase, semi-implicit, numerical simulator to simulate water imbibition and oil recovery in artificially fractured and unfractured cores. Straight-line permeabilities and a low capillary pressure were used for the fracture. The main matching parameter was the matrix capillary pressure. The final matrix capillary pressure after history matching was very close to that measured in the same matrix using a centrifuge. Babadagli (1994) performed laboratory experiments to examine the influences of the injection rate on the capillary imbibition behavior and saturation distribution in the matrix. The system was fully saturated by the oil phase, and the water phase was injected through the fracture, displacing the oil in the fracture by viscous forces and oil in the matrix by capillary imbibition. The experimental model was then matched by a numerical model and used to qualitatively evaluate the configuration effect on capillary imbibition transfer. They observed that the limiting value of the injection rate (critical rate) was defined as a function of maximum matrix capillary pressure and matrix permeability.

Experimental work using Berea, Spraberry oil and synthetic Spraberry brine was carried out, proceeded by numerical modeling using the ECLIPSETM simulator to match the experimental data.

2.3.2 Experimental Study

A core flood experiment at a low rate of injection into the fracture of a synthetically fractured Berea core was performed under reservoir temperature. A low permeability Berea core sample was cut in cylindrical shape, 3 in. long and 1.5 in. in diameter. The fracture pattern on the core sample was generated along the long axis using a hydraulic cutter as shown in Fig. 2.3-1. The cut sections were put back together without polishing the cut surfaces and without spacers. Synthetic Spraberry brine and Spraberry crude oil were used as wetting and non-wetting phases. The properties of rock and fluids used in this experiment are shown on Table-2.3-1.

The experimental procedure is described in detail as follows:

- The dimensions and weight of the core sample were measured.
- The core sample was inserted into a Hassler-type core holder using a confining pressure of 500 psi to saturate the core with oil. About 2-5 pore volumes (PV) of Spraberry crude oil passed through the core sample using the constant pressure of 30 psi supplied by a nitrogen tank.
- The volume of oil effluent was measured to determine the oil rate. By using Darcy's law, the absolute matrix permeability to oil was calculated.
- After permeability measurements, the oil-saturated core was taken from the core holder and covered with aluminum foil to prevent air penetration into the core sample.
- The core was cut in half using a hydraulic cutter to generate a fracture horizontally along the axis of the core.
- The oil-saturated, artificially fractured core was then weighed to determine core pore volume and porosity.
- The core was inserted back into the Hassler-type core holder.
- The effective permeability of the fractured core then was determined by injecting oil into the fractured core in the core holder. The fracture permeability (Guo and Svec, 1998) was calculated using the following equation and assuming the fracture porosity of 1%:

$$k_e = k_m + \phi_f k_f \dots\dots\dots(1)$$

where k_e (md), k_m (md) k_f (md) and ϕ_f (fraction) are the effective reservoir permeability, matrix permeability, fracture permeability and fracture porosity, respectively.

The fracture width, w_f (cm), is determined by the correlation developed by Seright *et al* (1996):

$$w_f = 0.000131 \sqrt{k_f} \dots\dots\dots(2)$$

- The oil-saturated, artificially fractured core was again taken from the core holder to clean the spill oil from the core surface.
- The core was inserted back into the core holder to start the experiment.
- Wrapping plastic and aluminum foil around the injection end, to allow the injected brine to flow only through the fracture, sealed off the face of the matrix.
- The entire system was place in an insulated box with constant surrounding air temperature of 138°F, as shown in Fig. 2.3-2.

- Synthetic Spraberry brine was injected into the fracture with constant brine rate of 4.0 cc/hour.
- The oil and brine produced were collected at the other end of the fractured core section for about 48 hours until oil production ceased. The volumes of fluids were measured and referenced with time of production. The results are presented in Table 2.3-2.

2.3.3 Numerical Model

Figure 2.3-1 shows the modeling of the grid block to represent the shape of the Berea core. The size of the fracture is enlarged. The rectangular grid block was used to overcome the difficulty of modeling the cylindrical core shape. The pore volume of the rectangular shape was set to be the same as the cylindrical core pore volume. The dimensions of both shapes are shown in Fig. 2.3-1.

The single porosity simulation model is more representative in modeling single fractures as created in artificially fractured core, a is dual porosity model usually used in modeling fractured reservoirs. However, the single porosity simulation model has to be able to duplicate the behavior of dual porosity simulation, which has different properties for matrix and fracture media.

The properties of the fracture are added in the single porosity simulator, such as porosity, permeability, relative permeability and capillary pressure. Three layers were used in the model, with the fracture layer between the matrix layers. In addition 10 x 10 grid blocks were used in the x and y direction. The fracture layer was injected at one end with constant water rate of 4.0 cc/hour. Oil and water were produced at the opposite end of the fracture layer. Relative permeability for the matrix layer was calculated from the following relationships (Kazemi and Merrill, 1979).

$$k_{rw} = S_w^3 \dots\dots\dots(3)$$

$$k_{ro} = (S_o - S_{or})^3 \dots\dots\dots(4)$$

Relative permeability for the fracture layer was assumed to be a straight line for both k_{rw} and k_{ro} .

The initial condition from the simulator is obtained from the hydrostatic equilibrium calculation. For instance, initial water saturation is determined by capillary pressure, which is based on the difference between oil pressure and water pressure. Thus, it is difficult to use the equilibrium option to represent initial conditions for the laboratory experiment. Instead of using the equilibrium option, initial water saturation and pressure were used since those were known initially from laboratory experiments.

2.3.4 Results and Discussions

In the experimental process, all the oil was stored only in the matrix. The fracture was assumed not to store any oil initially. Once brine injection was started with a constant rate of 4.0 cc/hr, oil was produced simultaneously. However, at the beginning of injection, water was not produced for a period of time. This indicated that water was imbibing into the rock and oil was expelled from the matrix to the fracture. Also inferred was that the injection rate in the Berea porous medium was lower than the spontaneous imbibition rate. After two hours of brine injection, the spontaneous imbibition rate declined as the matrix capillary pressure was reached. Consequently, water started to be produced before being completely imbibed. Water was produced until 100% water-cut was achieved.

There are two mechanisms involved during the waterflood production of oil: (1) spontaneous imbibition and (2) displacement. During spontaneous imbibition oil is expelled from the matrix to the fracture by counter-current imbibition and is then displaced by the brine along the fracture to the production point. This displacement process in the fracture is a function of brine injection rate while the rate of oil production is dependent on the imbibition rate.

In numerical modeling of the imbibition flooding process, the matrix capillary pressure controlling the imbibition mechanism was the primary parameter adjusted to match the experimental data. Meanwhile, the fracture capillary pressure was set to zero. The water production rate, cumulative water production, oil production rate, cumulative oil production, oil recovery and the water cut were parameters used to match between observed experimental data and the numerical model. The final matches can be seen in Figs. 2.3-3 to 2.3-8. The matrix capillary pressure for matching the experimental study is shown in Fig. 2.3-9. This matrix capillary pressure indicates that the wettability of the matrix is strongly water-wet. From the spontaneous imbibition test the Amott wettability number was calculated to be 0.88. This value for the Amott wettability number also confirms the wettability of this Berea core to be water-wet.

2.3.5 Conclusions

1. Experimental imbibition flooding was performed on artificially fractured Berea core using Spraberry crude oil and synthetic Spraberry brine under reservoir temperature of 138°F and confining pressure of 500 psia.
2. Laboratory results indicate that the imbibition water into the core matrix occurred during the injection of brine into a fracture at a constant rate of 4.0 cc/hour.
3. The numerical simulation results matched the experimental data.
4. Matrix capillary pressure was obtained from the numerical simulation after final matches were achieved.
5. The matrix capillary pressure indicates that the wettability of Berea core used in this study is strongly water-wet.

2.3.6 References

1. Babadagli, T.: "Injection Rate Controlled Capillary Imbibition Transfer in Fractured Systems," paper SPE 28640 presented at the 1994 Annual Technical Conference and Exhibition New Orleans, Sep. 25-28.
2. Brownscombe, E.R. and Dyes, A.B.: "Water-imbibition Displacement-A Possibility for the Spraberry," *Drilling and Production Practice of API* (1952), 383-390.
3. Guo, B. and Svec, R.: "A Preliminary Analysis of Permeabilities in the Teague-Blinabry Reservoir based on Step-Rate Test on Well Lamunyon Federal #62 and Whole Cores from Well Lamunyon Federal #50," PRRC 98-12 (1998).
4. Kazemi, H. and Merrill, L.S.: "Numerical Simulation of Water Imbibition in Fractured Cores," paper SPE 6895 presented at the 1977 Annual Fall Technical Conference and Exhibition, Denver, Oct. 9-12.
5. Kleppe, J. and Morse, R.A.: "Oil Production from Fractured Reservoirs by Water Displacement," paper SPE 5084 presented at the 1974 SPE Annual Meeting, Houston, Oct. 6-9.
6. Seright, S.R.: "Improved Methods for Water Shutoff," Annual Report to DOE under Contract No. DE-AC22-94PC91008, November, 1997.

Table 2.3-1 Core and fluid properties

Core Properties		Fluid Properties	
D (cm)	3.786	Oil	Spraberry oil
L (cm)	6.8936	Water	Spraberry brine
k_m (md)	28.09	μ_o (cp)	3.52
ϕ_m (%)	17.16	μ_w (cp)	0.68
k_f (md)	3429	S_{wi} (%)	0
ϕ_f (%)	1.0	S_{or} (%)	40
w_f (cm)	0.0076	V_o (cc)	13.317

Table 2.3-2 Imbibition data from laboratory experiment

Time (hr)	Water Rate (cc/hr)	Water (cc)	Oil Rate (cc/hr)	Oil (cc)	Oil Rec. (fraction)	Water Cut (fraction)
0.00	0.00	0.00	0.00	0.00	0.00	0.00
0.20	0.00	0.00	5.00	1.00	0.08	0.00
0.45	0.00	0.00	4.00	2.00	0.15	0.00
0.63	0.00	0.00	7.64	3.40	0.26	0.00
0.85	0.00	0.00	4.15	4.30	0.32	0.00
1.17	0.00	0.00	3.79	5.50	0.41	0.00
1.67	0.00	0.00	1.20	6.10	0.46	0.00
1.97	1.67	0.50	3.00	7.00	0.53	0.36
2.28	4.54	1.90	1.62	7.50	0.56	0.74
3.32	3.82	5.90	0.05	7.55	0.57	0.99
5.60	3.95	14.90	0.02	7.60	0.57	0.99
7.17	4.21	21.50	0.03	7.65	0.57	0.99
11.17	3.75	36.50	0.01	7.70	0.58	1.00
15.67	4.00	54.50	0.02	7.80	0.59	0.99
21.72	4.00	78.70	0.01	7.85	0.59	1.00
23.00	4.44	84.40	0.04	7.90	0.59	0.99
28.13	3.90	104.40	0.01	7.95	0.60	1.00
38.68	4.00	146.60	0.00	8.00	0.60	1.00
46.15	4.00	176.50	0.00	8.00	0.60	1.00
48.05	3.74	183.60	0.00	8.00	0.60	1.00

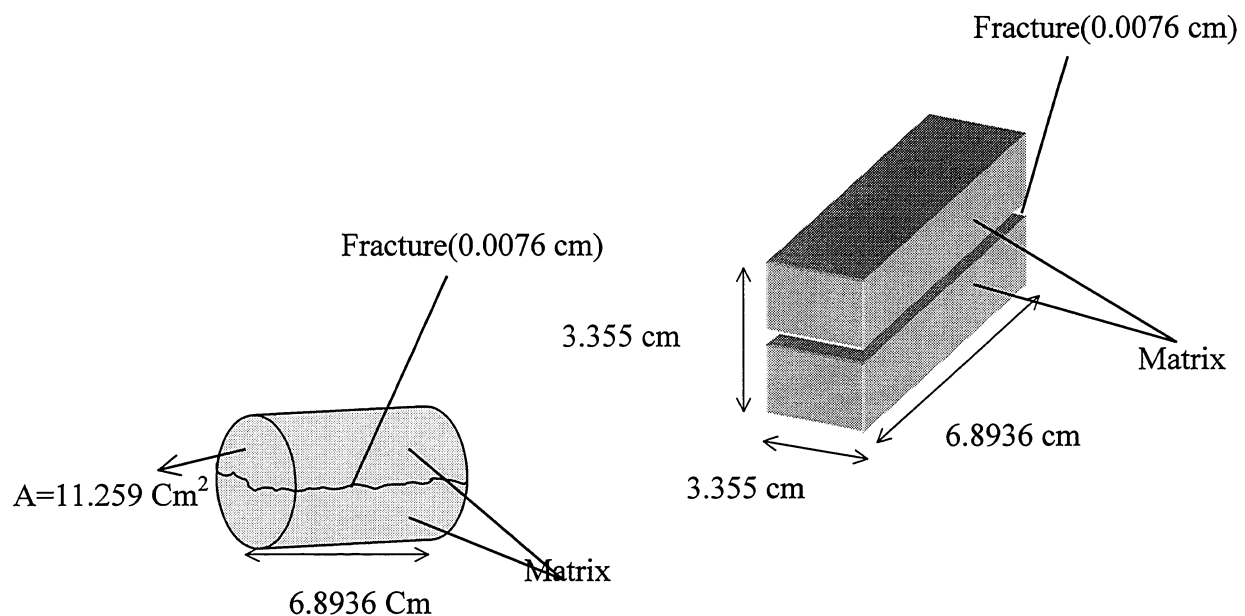


Fig. 2.3-1 - Grid block modeling to represent the core

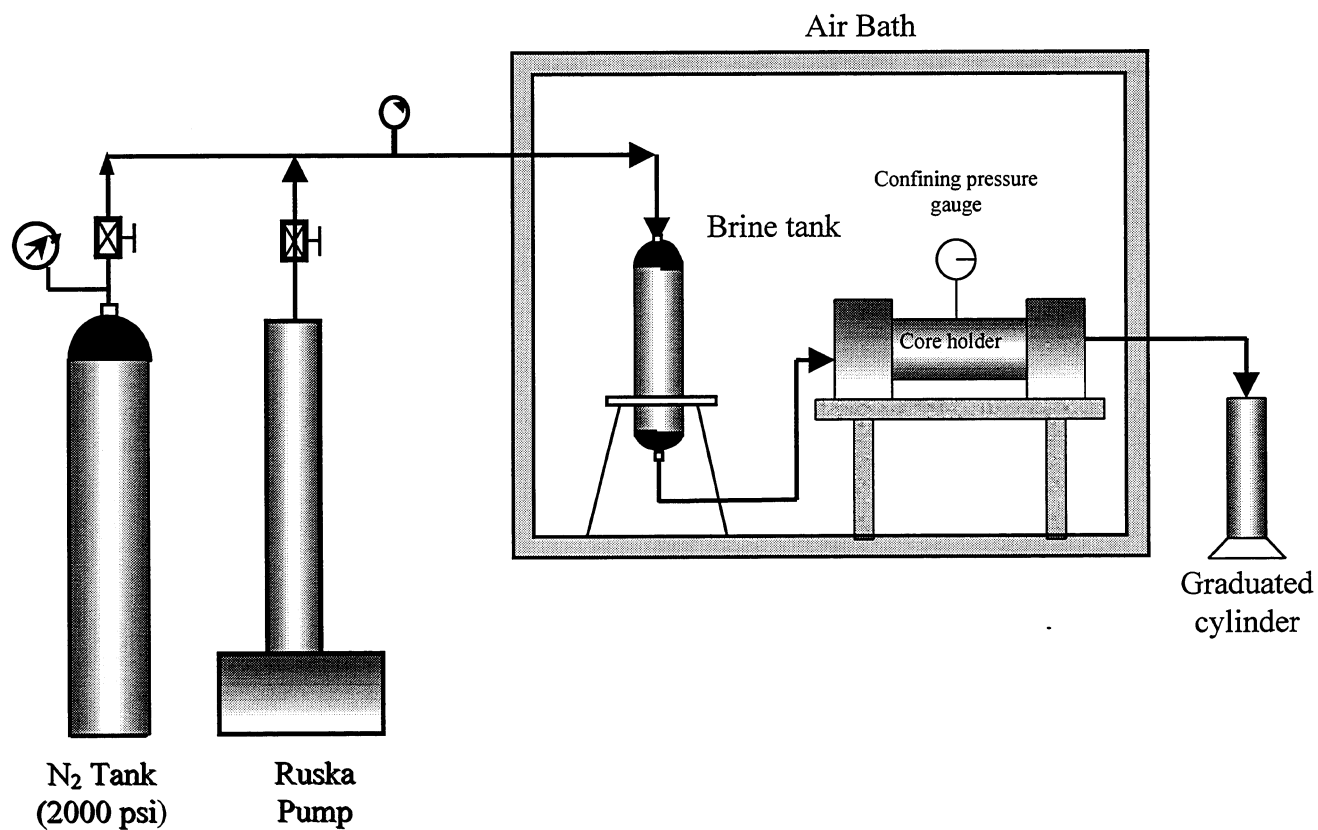


Fig. 2.3-2 - Experimental setup of imbibition-flooding.

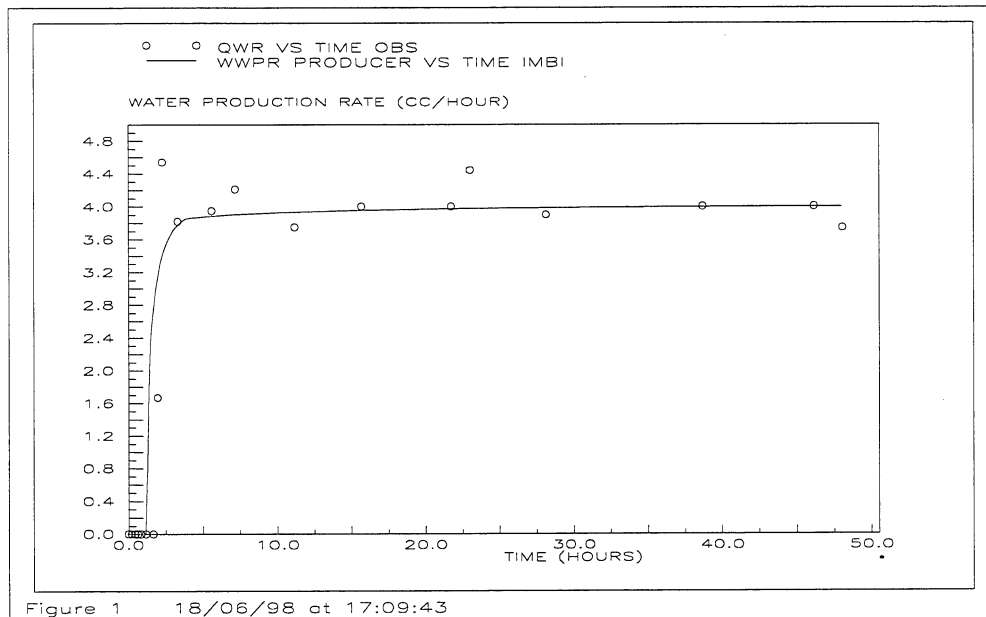
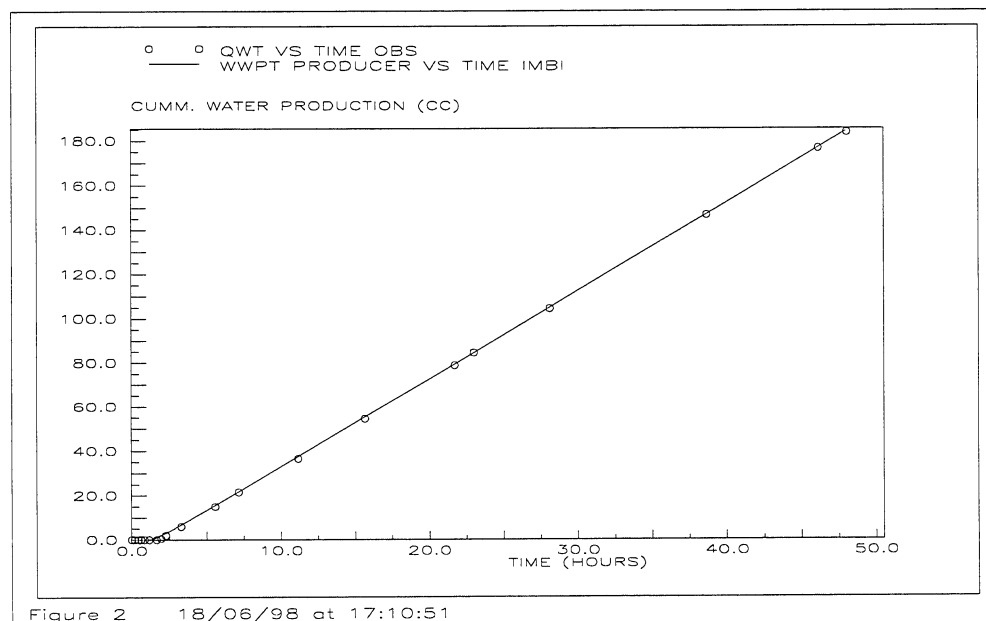


Fig. 2.3-3 Matching between observed experimental data and numerical model for water



production rate.

Fig. 2.3-4 Matching between observed experimental data and numerical model for water production.

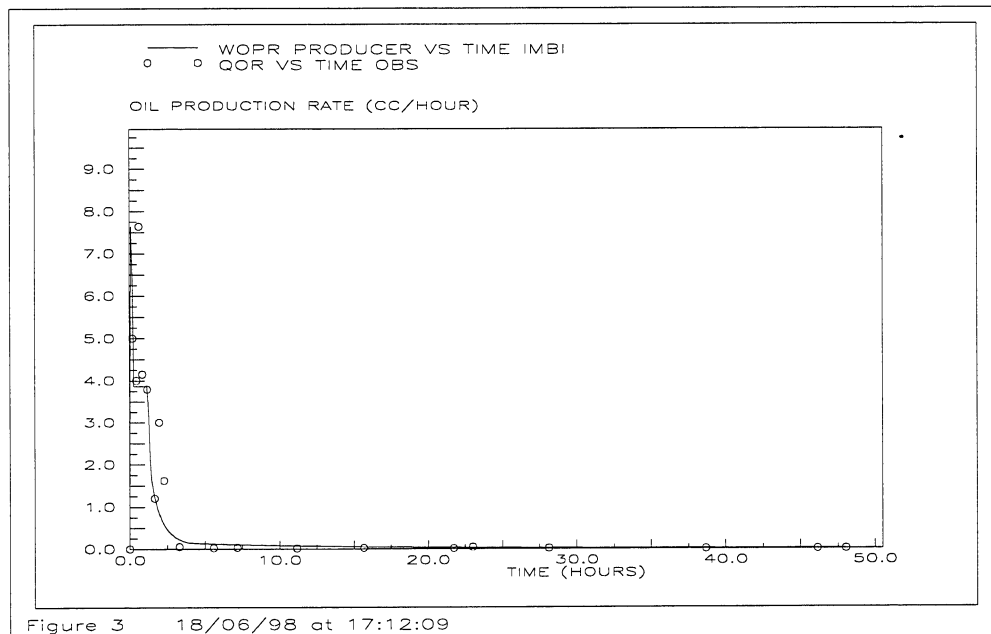


Fig. 2.3-5 Matching between observed experimental data and numerical model for oil production rate.

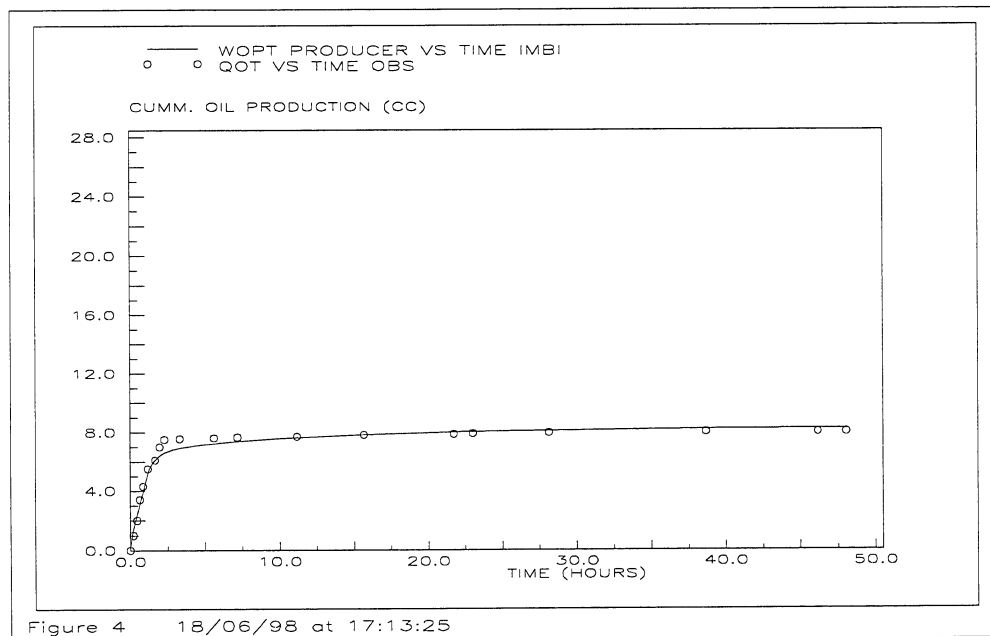


Fig. 2.3-6 Matching between observed experimental data and numerical model for oil production.

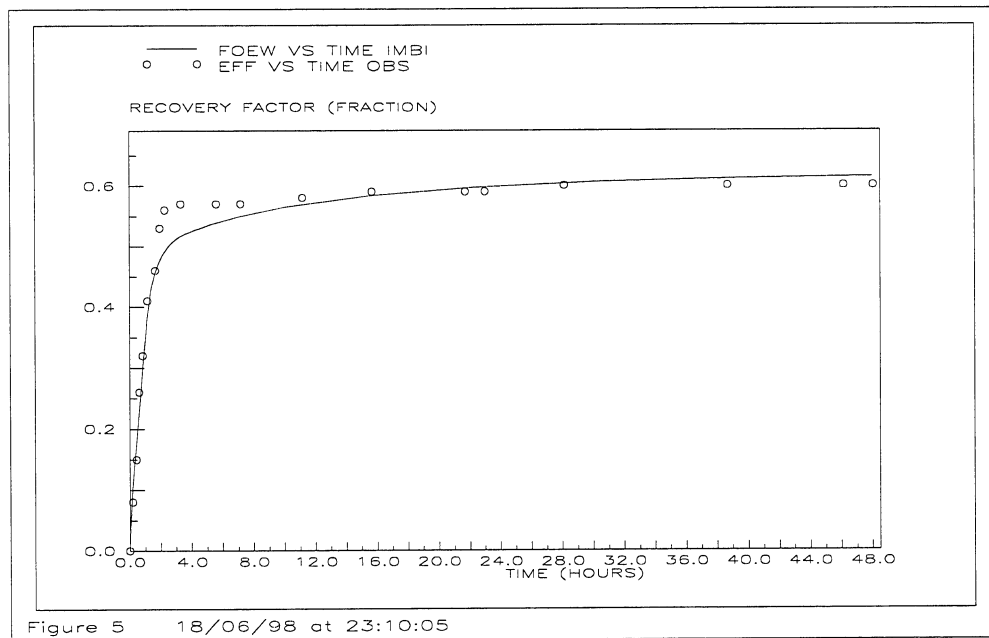


Fig. 2.3-7 Matching between observed experimental data and numerical model for oil recovery.

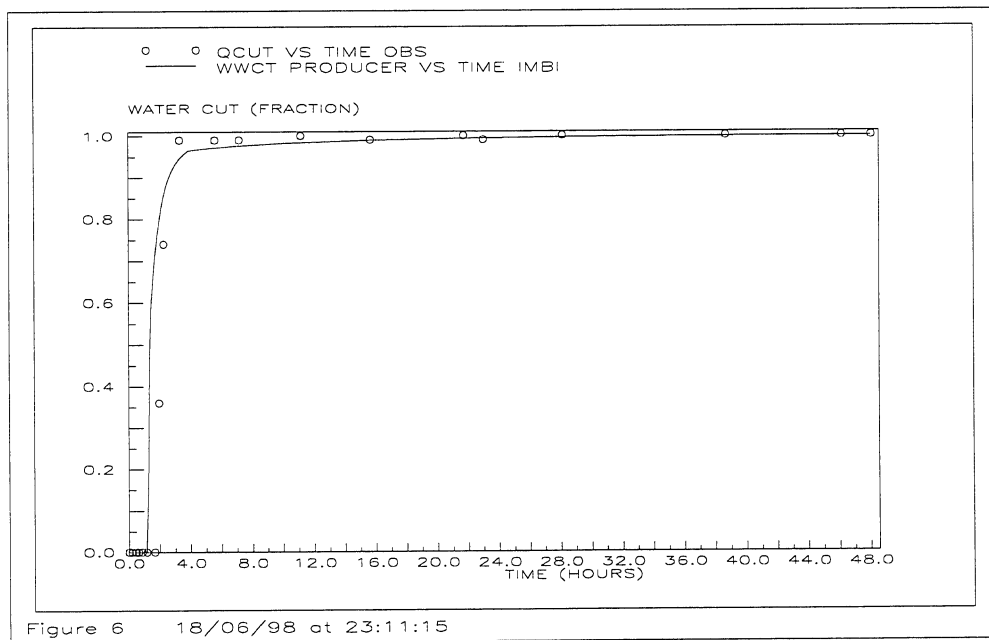


Fig. 2.3-8 Matching between observed experimental data and numerical model for water cut.

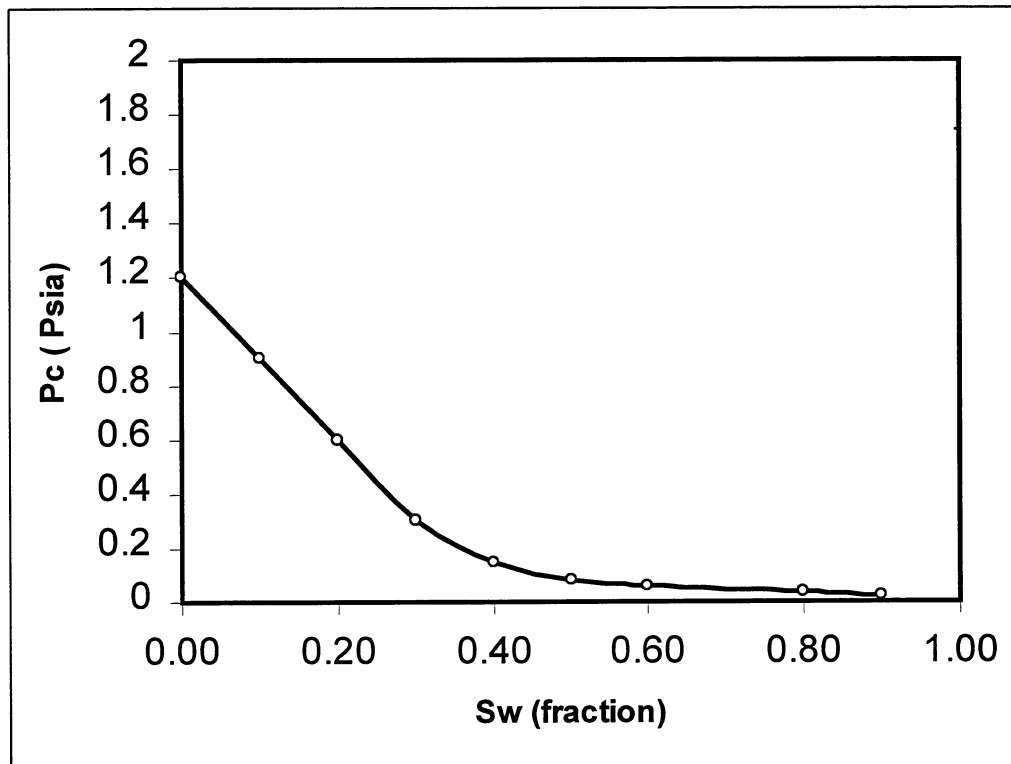


Fig. 2.3-9 Capillary Pressure Curve

3 RESERVOIR PERFORMANCE ANALYSIS

3.1 ANALYSIS OF IMBIBITION MECHANISM IN THE NATURALLY FRACTURED SPRABERRY RESERVOIR

3.1.1 Introduction

There are several mechanisms that can contribute to oil recovery in naturally fractured reservoirs. Spontaneous imbibition is particularly important in the recovery of oil by water injection from fractured reservoirs with low matrix permeability. A rock's ability to imbibe water spontaneously is dependent on its water-wetness quality. This imbibition property is a dominant factor in the rate of oil recovery. The rate of spontaneous imbibition in a porous medium is basically determined by the net effect of the capillary pressure driving force and the opposing viscous resistance to flow. Understanding imbibition and capillary phenomena is critical to develop the interactions and efforts between these parameters and other key parameters in the oil recovery mechanism (i.e., matrix permeability, fracture spacing and rate of imbibition).

In this section, the contribution of spontaneous imbibition to the oil recovery mechanism in the West Texas Spraberry reservoir is evaluated. Waterflood recovery in the Spraberry reservoir is dominated by counter-current imbibition of water. The imbibition experiments conducted under reservoir conditions suggest that the oil recovery by water imbibition is only 13% of the original oil in place. The scale-up of imbibition experimental results to field scale imbibition flooding uses several assumptions of the rate law that governs mass transfer (Guo, et al., 1998). The developed scaling equation is then applied to evaluate scaling up from core geometry to matrix block geometry in the 1U and 5U Units of the Upper Spraberry zone. The results are in agreement with the observed 8 to 15% IOIP for 40 years of waterflooding in the Upper Spraberry sand.

Fluid saturation, waterflooding efficiency, and recovery are also reviewed in this section. Based on analysis of fluid saturation of the field, the volumetric sweep efficiency in the Spraberry reservoir is much higher than the displacement efficiency. This characteristic suggests that the waterflood failed primarily because of very poor imbibition displacement efficiency. A sensitivity study of the imbibition model after 40 years of waterflooding in the Spraberry Trend with oil recovery of only 13% IOIP shows that the imbibition mechanism has not been affected. The degrees of heterogeneity in the matrix and the fracture system control recovery during waterflooding in the Spraberry.

3.1.2 Concept of Process

In the Spraberry reservoir, oil is stored in a very tight matrix, with virtually all permeability concentrated in a large number of natural fractures. Due to these fractures, oil cannot be displaced from the matrix by means of conventional waterflooding. Channeling and bypassing through the fractures would result in extremely poor recovery. Based on Brownscombe and Dyes's (1952) study, waterflood performance in the Spraberry reservoir is believed to be dominated by counter-current imbibition of water. The counter-current imbibition occurs when a liquid-filled, porous rock is contacted by another fluid that preferentially wets the rock (wetting fluid). The capillary pressure gradient mechanism causes the wetting fluid to invade

the rock pore, with less-wetting phases being displaced at the same time in the opposite direction. In the Spraberry, the wetting phase is water and the less-wetting phase is oil. When waterflooding is performed in this type of reservoir, the intent is to fill the fractures with water to initiate spontaneous counter-current imbibition, displacing the oil from the matrix block into the surrounding fractures.

As mentioned previously, the rate of imbibition is governed primarily by capillary pressure (i.e., corresponding to the wettability of the matrix rock), matrix permeability and fracture spacing (i.e., the amount of surface area exposed to imbibition). The rate of imbibition and the rate of water injection then govern the producing water-oil ratio. The oil production process during the mature stage of a waterflood in a naturally fractured reservoir may be considered analogous to a bucket of fluid with a small hole in the bottom dripping liquid onto a conveyor belt (Guo. et al., 1998). Liquid leaking from the bucket is analogous to oil produced from the matrix by the imbibition process, and the conveyor belt is analogous to water flow in the fracture that brings the produced oil to the production well. Above a certain threshold, if one increases the speed of the conveyor belt, the rate of the oil produced from the matrix does not increase. In naturally fractured reservoirs, high injection rates result in a greater amount of water production, but the imbibition process remains the rate-limiting step. In this case, understanding the imbibition mechanism provides a tool to narrow the range of key parameters, i.e., matrix permeability, fracture spacing, fracture orientation, ultimate recovery, and the rate of imbibition. Some of these parameters will be utilized for scaling of imbibition data.

3.1.3 Scaling of Imbibition Data

The analytical model for describing oil recovery by water imbibition was developed by Aronofsky et al (1958). This recovery model can be applied using small reservoir core samples to scale the laboratory imbibition data to field dimensions. All laboratory parameters are converted into dimensionless forms (Mattax and Kyte, 1962). The following conditions must be met for scaling imbibition:

1. The gravity effects are negligible.
2. The shape and the rock type used in the laboratory must be identical to that of the matrix block of the reservoir.
3. The wettability and relative permeability represents the matrix block.
4. The capillary pressure functions for the matrix block and the laboratory model must be related by direct proportionality through Leverett's dimensionless J-function.
5. The viscosity ratio of oil to water must be duplicated.
6. The equations used in this study refer to the above assumptions.

3.1.4 Imbibition Recovery Model

In order to apply the experimental imbibition data to field scale imbibition waterflooding, the dimensionless time (t_D) initially proposed by Mattax and Kyte (1962) and then modified by Ma et al. (1995) is used:

$$t_D = Ct \sqrt{\frac{k_m}{\phi}} \frac{\sigma}{\mu_g} \frac{\cos(\theta)}{L_c^2} \dots\dots\dots(1)$$

where t is imbibition time, C is a constant, k_m is permeability, ϕ is porosity, σ is interfacial tension, μ_g is the geometric mean, and θ is the contact angle. The characteristic length, L_c , of the matrix block is given in another relation defined by Ma et al (1995) :

$$L_c = \sqrt{\frac{V}{\sum_{i=1}^n \frac{A_i}{x_{Ai}}}} \dots\dots\dots(2)$$

In the above equation V is the volume of a matrix block where there are n fracture faces exposed to imbibition, A_i is the surface area of face i and x_{Ai} is the distance from the fracture face to the center of the matrix block.

Aronofsky (1958) showed that for a reservoir experiencing recovery due to imbibition, the recovery versus time curve could be approximated by the following equation:

$$R_{imb} = R_{\infty} (1 - e^{-\lambda t}) \dots\dots\dots(3)$$

Then, the recovery equation is normalized as:

$$R_n = \frac{R_{imb}}{R_{\infty}} = 1 - e^{-\lambda t} \dots\dots\dots(4)$$

where R_{∞} is the ultimate recovery and λ is a curve fitting parameter, which can take any real numerical.

Based on laboratory imbibition experiments conducted under reservoir temperature using Spraberry cores and oil, recoverable oil by water imbibition can be up to 13% of IOIP. In analysis of the imbibition data from Spraberry cores, all of the imbibition experimental data presented in Section 2.1 (Fig. 2.1-13) are plotted in Fig. 3.1-1 using the dimensionless time variable, defined by Eq. (1). As a comparison, the experimental data from imbibition tests under ambient conditions are also plotted in Fig. 3.1-1. In these experiments, the rate of imbibition at reservoir temperature is greater than the rate of imbibition at ambient condition.

A composite imbibition curve is shown in Fig. 3.1-2. A curve-fitting imbibition data obtained for a very strongly water-wet Berea sandstone with zero initial water saturation is also shown for reference. Ma and Morrow (1997) derived a correlation for this curve as :

$$R = R_{\infty} \left(1 - \frac{1}{(1 + 0.04 t_D)^{1.5}} \right) \dots\dots\dots(5)$$

where R_{∞} is the ultimate recovery by spontaneous imbibition data and t_D is dimensionless time. The composite imbibition curves obtained from Berea sandstone were then used to compare the imbibition curves obtained from Spraberry rock as shown in Fig. 3.1-2. To achieve the best match of the experimental data from Spraberry cores, an average recovery curve was established using Eq.(4) by adjusting the value of λ . A curve fit of Eq.(4) for the

experimental data as shown in Fig. 3.1-2 is obtained when the following relation is used for Spraberry cores as:

$$\lambda t = 0.0053 t_D \dots\dots\dots (6)$$

Substituting Eq. (6) into Eq. (4) and the recovery curve fit presented in **Fig. 3.1-2** can be expressed as:

$$R_n = \frac{R}{R_\infty} = 1 - e^{-0.0053 t_D} \dots\dots\dots (7)$$

Using the dimensionless time t_D defined by Eq. (1), the decline rate or the rate coefficient, which has unit 1/days, can be expressed as:

$$\lambda = 0.0053 C \sqrt{\frac{k_m}{\phi}} \frac{\sigma \cos(\theta)}{\mu_g L_c^2} \dots\dots\dots (8)$$

The experimental data was then normalized and fit to an empirical model using Eq. (1) and substituting into Eq. (7). Then, the recovery can be expressed as:

$$R_n = \frac{R}{R_\infty} = 1 - e^{-0.0053 C t \sqrt{\frac{k_m}{\phi}} \frac{\sigma \cos(\theta)}{\mu_g L_c^2}} \dots\dots\dots (9)$$

The characteristic length (L_c) for a matrix block in the reservoir is assumed to be half of the fracture spacing (L_s). Equation (9) can be used for analysis of the recovery mechanism in a naturally fractured reservoir during waterflooding.

3.1.5 Production Decline Model

Guo. et al., (1998) modified an analytical model for decline curve analysis based on imbibition theory and the rate law that governs mass transfer as developed by Gupta and Civan (1996). Decline of oil production rate is expressed as:

$$q_o = 0.0053 C V_o \sqrt{\frac{k_m}{\phi}} \frac{\sigma \cos(\theta)}{\mu_g L_c^2} e^{-0.0053 C t \sqrt{\frac{k_m}{\phi}} \frac{\sigma \cos(\theta)}{\mu_g L_c^2}} \dots\dots\dots (10)$$

where V_o is the original oil in place recoverable by imbibition. The above equations are valid when consistent units are used. The derivation of Eq. (10) is presented elsewhere (see Schechter, 1997).

3.1.6 Analysis of Recovery Mechanism

3.1.6.1 Recovery Based on Laboratory Scaling of Imbibition Data

The oil recovery in the 1U Unit (data from Well Shackleford 138) and 5U Unit (data from Well E.T. O'Daniel 37) of the Spraberry reservoir were calculated using log-derived porosity and permeability (Banik and Schechter, 1996) as shown in Fig.3.1-3 and 3.1-4. In Figs. 3.1-5 and 3.1-6 show the plot of oil recovery together with pore size of rocks versus well depth. The pore size is the square root of ratio of permeability and porosity $\frac{k}{\phi}$, which is proportional to a

macroscopic radius in porous medium. The characteristic length (L_c) for a matrix block in the reservoir core, which is half of the maximum fracture spacing of 3.79 ft as determined from fractured core analysis (Lorenz, 1996), was used in the scaling equation (Eq. (1)). The calculations of imbibition recovery were performed using Eq. (9) on the basis of 13% ultimate oil recovery from imbibition data. In the analysis of five years' waterflooding performance, pore size of 1U and 5U Units is plotted versus well depth as presented in Fig. 3.1-5 and 3.1-6, respectively. The oil recoveries are then plotted in the same figures, respectively. As shown in these figures, the integration of recovery profiles along the depth of the pay zone resulted in an estimation of average oil recovery of about 9% IOIP for 1U sand and 11% IOIP for 5U sand.

The effect of time on recovery profiles was investigated. Several scenarios were performed at 1, 5, 10, 20 and 40 years waterflood. The recovery calculations based on the imbibition model are plotted against well depth for Upper Spraberry 1U and 5U sands as presented in **Fig. 3.1-7** and **3.1-8**, respectively. Within 10 years of waterflood initiation, the average recovery is 11% and 13% for oil recovered from 1-U Sand and 5U sand, respectively. When the waterflooding is extended up to 20 years, the recovery improves to 12.5% for the 1-U sand. At 20 years there is no more oil recovered from 5U sand indicating that the waterflooding performance in the 5U sand has reached ultimate recovery. After 40 years of waterflooding, there is no increase in oil recovery from both 1U and 5U sands. Thus, the scaling from coreflood geometry to reservoir matrix block geometry in the 1U and 5U Units of the Upper Spraberry zones resulted in oil recovery of only 13% IOIP for 40 years waterflooding.

On further analysis, the calculated recovery of 1U and 5U sands were plotted versus time. The average permeability and porosity for both sand units (1U and 5U) as input data in the calculation is tabulated in Table 3.1-1. Waterflooding in this field has been practiced for 40 years, the recovery analysis is performed on the basis of this time period. Equation (9) was then utilized to analyze 40 years of waterflood performance in the Spraberry Trend Area reservoir. The result is plotted in Fig. 3.1-9. This figure indicates that the time required to recover oil on the basis of the contribution of imbibition mechanism from 5U Unit sand is almost double that of the permeability of the 1U Unit sands. Based on Table 3.1-1, the average porosity for both sand units are almost the same. However, the average permeability in 5U Unit is higher than that in 1U Unit. Figure 3.1-9 shows that the matrix permeability is one of the key factors affecting this oil recovery mechanism.

As expected the higher permeability results in faster recovery of oil, until an ultimate recovery of about 13% IOIP is reached. For the Spraberry, this was achieved within 11 years' waterflooding. This suggests that the imbibition process cannot induce the production of oil after 11 years of waterflooding in the Spraberry. This also confirms that the calculated

imbibition oil recoveries are in agreement with the observed 8 to 15% IOIP after 40 years of waterflooding in the Upper Spraberry sand. The ultimate recovery for each zone is indicated to be the same for each zone in Fig. 3.1-9.

3.1.6.2 Recovery Field Performance

Evaluation of the fluid saturation of the Spraberry field is an important parameter to be determined. The initial water saturation (S_{wi}) and current oil saturation (S_{or}) are crucial data for estimating waterflood performances, i.e., displacement efficiency and volumetric sweep efficiency. These data can be used to explain the low recovery in Spraberry Trend Area reservoir.

3.1.6.2.1 Fluid Saturation.

Water saturations have been evaluated on the basis of permeability cutoff criteria to determine the oil saturation of the Spraberry field. In 1953, Elkin used a cutoff of $S_{wi} = 60\%$, which roughly corresponds to a permeability of 0.1 md. Baker (1996a) determined the average water saturation of cores taken from four wells in the Spraberry field. He used an absolute permeability cutoff value of 0.3 and 0.8 md for these cores. The average water saturation was determined to be 49.3% and 52.6% for cutoff of 0.3 md and 0.8 md, respectively. These values corresponded to 50.7% and 47.4% oil saturation (assuming no gas saturation to be present).

By reviewing all methods of analysis to estimate initial water saturation, Baker concluded that the initial water saturation in the Spraberry rock is about 30% to 40%. The water saturation data and reservoir oil recovery by waterflood were then used to determine the displacement efficiency and volumetric sweep efficiency. Initial water saturation was established based on cores taken from 46 wells drilled prior to waterflooding were evaluated before 1954 Schechter (1996b). Core data taken from wells before waterflooding was initiated. In this study, the initial water saturations based on data from Guo (1995) were re-plotted against the absolute permeability of cores, as presented in Fig. 3.1-10. The correlation of the average initial water saturation was then determined to be:

$$S_{wi} = 0.20 + 0.13e^{-0.6(k-0.1)} \dots\dots\dots(11)$$

Where S_{wi} is the initial water saturation and k is absolute permeability of the core in millidarcies. From the plot, the high water saturations in the higher permeability rock are probably associated with a microporosity system in which both the oil and the water are immobile (Baker, 1996a).

Current water saturations (S_w) were obtained by analyzing cores taken from wells that were waterflooded (data from Guo, 1995). By assuming there is no gas saturation, the current oil saturation can be determined. The results of this analysis are presented in Table 3.1-2. These data will be used later to determine the displacement efficiency and volumetric sweep efficiency.

3.1.6.2.2 Displacement Efficiency ($E_{displ.}$).

The displacement efficiency is the ratio between the amount of oil displaced and amounts of oil contacted by displacing fluid (Lake, 1989). Initial water saturation and current water

saturation of the rock can determine the displacement efficiency. Assuming that the oil and gas are produced during waterflooding (no gas saturation in the rock after waterflooding), the displacement efficiency can then be determined using the following equation:

$$E_{displ.} = \frac{1 - S_{wi} - S_{or}}{1 - S_{wi}} = \frac{\bar{S}_w - S_{wi}}{1 - S_{wi}} \dots\dots\dots(12)$$

where S_{wi} is initial water saturation, S_{or} is residual oil saturation, and \bar{S}_w is current water saturation.

3.1.6.2.2.1 Volumetric Sweep Efficiency (E_{vol}).

The volumetric sweep efficiency is defined as the ratio between the volume of oil contacted by the displacing fluid and the volume of oil originally in place (Lake, 1989). It can be calculated using the correlation between oil recovery (E_R) and displacement efficiency. The equation can be defined as :

$$E_R = E_{displ.} \times E_{vertical} \times E_{areal} \dots\dots\dots(13)$$

if

$$E_{vol} = E_{vertical} \times E_{areal}$$

therefore,

$$E_{vol} = \frac{E_R}{E_{displ.}} \dots\dots\dots(14)$$

Oil recovery in the Spraberry field after more than 40 years of waterflooding is estimated in the range of 8 to 15% IOIP. Thus, the displacement and volumetric sweep efficiency in the Spraberry can be determined using the water saturation data presented in Table 3.1-2 and the estimated oil recovery from waterflooding. The results are presented in Table 3.1-3.

The results show that the volumetric sweep efficiency in the Spraberry reservoir ranges from 47 to 83%, which is much higher than the displacement efficiency (15 to 26%). The high volumetric sweep efficiencies are also supported by infill drilling and pressure interference testing data. The infill drilling programs in Spraberry tend to produce wells with high water cuts indicating that water has contacted a large portion of the reservoir fracture system (Baker, 1996a), and pressure interference test during waterflooding showed conclusively that pressure communication was very good (Elkin, 1960). Low displacement efficiency is indicated by the low recovery from imbibition experiments. The results show that the waterflood was less successful than typical waterfloods primarily because of low imbibition displacement efficiency, not because of poor volumetric sweep efficiency. However, the maximum recovery by imbibition, as indicated previously, is about 13%.

3.1.7 Sensitivity Study of Imbibition Model

Previously, several key parameters involved in the analysis of the oil recovery mechanism based on the imbibition model have been described. Understanding the individual parameters of the recovery mechanism helps define the effects, interaction, and range of these key parameters. Matrix permeability and fracture spacing are used in this study to define and limit

the uncertainty of the reservoir model. The imbibition process has a dominant effect on oil production. The imbibition process is analyzed here by performing sensitivity studies in the Humble Pilot Waterflood.

A pilot waterflood program was inaugurated on Humble's L.H. Shackelford B lease in the west central portion of the Spraberry Trend Area in March 1955. The pilot consisted of four injection wells with a center producer, creating a confined 80-acre, five spot pattern. Oil production from the center well increased within six months initiating of water injection. The water injection was then stopped and the center well still produced oil at a higher rate than prior to injection.

The reservoir performance in this pilot study demonstrated non-conventional waterflood characteristics according to observed Spraberry area response. Injected water appeared to displace oil from the fractures and simultaneously imbibed into the matrix. When injection was stopped, the water continued to imbibe into the matrix rock and displace oil from the matrix, which resulted in improvement of oil production. The imbibition mechanism is believed to strongly affect the waterflood recovery mechanism in the Spraberry trend.

The Humble pilot was considered a successful Spraberry waterflood. Subsequently, full-scale waterflood was initiated. However, the performance did not emulate the results of the Humble pilot. Understanding the difference between this pilot and field-wide waterflooding is vitally important for improving waterflood performance in the Spraberry Trend Area.

3.1.7.1 Reservoir Parameters.

The initial oil in place (IOIP) in the Humble pilot area was estimated to be about 724,181 reservoir barrels. The mechanism of primary oil production in the Spraberry Trend Area is believed to be dominated by solution gas drive (Elkin, 1953). The gas saturation after reservoir repressurization by waterflooding was assumed to be zero because gas dissolved into the fluid during production. The reservoir parameters used in the calculation of oil recovery based on the experimental data and the imbibition model as presented in Section 3.1.4, are summarized in Table 3.1-4.

A recent horizontal core study by Lorenz (1996) showed three distinct fracture sets. The fracture sets present in cores from the 1U and 5U reservoir trend NNE, NE and ENE. Table 3.1-5 presents the spacing of these sets. As shown in Table 3.1-5, the arithmetic average of the fractures spacing is 2.86 ft. All data were then used as the input for performing the sensitivity analysis of oil recovery for 15 years of waterflooding experience.

3.1.7.1.1 Matrix Permeability.

Matrix permeability is an important parameter in modeling imbibition data. The higher the permeability the less time required for the water to imbibe into the matrix block and displace oil.

In this study, to investigate the effect of matrix permeability on field recovery mechanisms, four values of permeability (i.e., 0.01, 0.03, 0.10 and 0.30 md) are used. Based on the experimental imbibition results from core plugs, the imbibition efficiency is 13% and the constant rate of imbibition (λ) is 0.0053. Using initial water saturation as a function of

absolute permeability (Eq. 11), an average fracture spacing of 2.86 ft, and an average porosity from logs of 10.02%, the oil recovery using the imbibition model for 15 years of waterflooding is simulated and the result is presented in Fig. 3.1-11. From figure 3.1-11, the recovery rates of this pilot field, as expected, are dependent on the matrix permeability. An increase in the matrix permeability results in an increase in the rate of recovery. It takes approximately six years for the reservoir with the highest matrix permeability to reach the ultimate recovery of 13%. The production rate drops from 185 Bpd to below 10 Bpd within six years of production (see Fig. 3.1-12). Reservoirs that have low matrix permeability, even after 15 years of waterflooding recoveries still have not reached ultimate recovery of 13%.

3.1.7.1.2 Fracture Spacing.

Effective permeability is a function of fracture spacing. A decrease in fracture spacing results in an increase in fracture density and therefore an increase in the fracture permeability.

To investigate the effect of fracture spacing on the recovery of 15 years of waterflooding, the four sets of fracture spacing shown in Table 3.1-5 was used in a sensitivity study. The calculated matrix permeability was 0.1 md while the other parameters were held constant as in the previous calculation in the sensitivity of matrix permeability. The model assumes that all fractures are evenly spaced, perpendicular and extend the full length of the zone.

The results presented in Fig. 3.1-13 shows that recovery is sensitive to fracture spacing. Increasing the fracture spacing yields improvement in recovery. For example, ultimate recovery is achieved within five years for the shortest fracture spacing, while ultimate recovery is not yet reached for the longest spacing after 15 years of waterflooding. When the average fracture spacing is 2.86 ft, ultimate recovery will be reached after 15 years of waterflooding.

3.1.7.1.3 Production Decline.

The sensitivity analysis for the production decline parameters is presented in Fig. 3.1-14. Figure 3.1-14 shows that the decline rate constant increases with matrix permeability and also increases with decreasing fracture spacing. This figure shows that for the lowest fracture spacing (1.62 ft), the decline rate constant increases rapidly with small increases in permeability. The matrix permeability and the fracture spacing apparently affect the decline rate constant.

3.1.8 Conclusion

The imbibition experiments conducted under reservoir conditions suggest the following conclusions;

1. Spraberry oil recoverable by water imbibition could be up to 13% of original oil in place.
2. Imbibition data from laboratory core experiments can be scaled to reservoir dimension.
3. The results of the scaling from core geometry to matrix block geometry in the 1U and 5U Units of the Upper Spraberry zone is in agreement with the observed 8 to 15% IOIP for 40 years of waterflooding in the Upper Spraberry sand.
4. The oil recovery mechanism during imbibition waterflooding in naturally fractured reservoir has been analyzed using the mass transfer rate law (Guo, et al., 1998).
5. Analysis of field fluid saturation indicates that the volumetric sweep efficiency in the Spraberry reservoir is much higher than the displacement efficiency. This indicates that the

waterflood in Spraberry trend was less successful than typical waterfloods, primarily because of very poor imbibition displacement efficiency.

6. A sensitivity study of the imbibition model presents a convincing argument that the effect of the imbibition mechanism on oil recovery resulted in only 13% IOIP after 40 years of waterflooding.
7. The degree of heterogeneity in the matrix and natural fractures controls the Spraberry waterflooding recovery process.

3.1.9 Nomenclature

A_i	= Area of imbibition, L^2
C	= Constant = 0.018849
K_m	= Matrix permeability, L^2
L_c	= Characteristic length, L
L_s	= Effective fracture spacing, L
N	= Number of fracture surfaces exposed to imbibition
R_{imb}	= Imbibition recovery at time t (%IOIP)
R_∞	= Ultimate recovery at economic limit (%IOIP)
t	= time, T
t_D	= Dimensionless time
V	= Volume of oil in place recoverable by imbibition, L^3
V_o	= Volume of original oil in place recoverable by imbibition, L^3
X_{Ai}	= Distance from fracture face to no-flow boundary, L
ϕ	= Porosity
λ	= Empirical constant from Aronofsky's model, T^{-1}
μ	= Viscosity,
σ	= Interfacial tension
θ	= Contact angle

3.1.10 Reference

1. Aronofsky, J.S., Masse, L., and Natanson, S.G., "A Model for the Mechanism of Oil Recovery from the Porous Matrix due to Water Invasion in Fractured Reservoirs," paper T.P. 4703 in Petroleum Technology, *AIME*, vol. 213, 1958.
2. Baker, R., memo from Epic Consulting Service Limited, March 6, 1996a.
3. Baker, R., "Reasons for the Relatively Low Recovery of the Spraberry Waterfloods," memo from Epic Consulting Service Limited, June, 1996b.
4. Elkin, L.F., "Reservoir Performance and Well Spacing, Spraberry Trend Area Field of West Texas," *Trans. AIME*, Volume 198, 1953.
5. Elkin, L.F. and Skov, A.M., "Determination of Fracture Orientation from Pressure Interference," *Trans. AIME*, Volume 219, 1960.
6. Guo, B., "Imbibition and Drainage Studies in Spraberry Reservoir Rock," in Proceedings of Characterization and fluid Flow, Naturally Fractured Reservoir Forum, Petroleum Recovery Research Center New Mexico Tech, Socorro, NM, April 19, 1995.

7. Guo, B., and Schechter, D.S., and Baker, R.O., "An Integrated Study of Imbibition Waterflooding in the Naturally Fractured Spraberry Trend Area Reservoirs," SPE Permian Basin Oil and Gas Recovery Conference, Midland, 25-27 March 1998.
8. Gupta, A. and Civans, F., "An Improved Model for Laboratory Measurement of Matrix to Fracture Transfer Function Parameters in Immiscible Displacement," paper SPE 28929 presented at the 69th Annual Technical Conference and Exhibition, New Orleans, Sept. 25-28, 1994.
9. Lake, L.W., "Enhanced Oil Recovery," Prentice-Hall, Inc., New Jersey, 1989.
10. Lorenz, J., "Summary of Observations and Interim Interpretations: Fractures in Horizontal Spraberry Cores, E.T. O'Daniel Well #28," Dec. 12, 1996.
11. Ma, S., and Morrow, N.R., "Mathematical Modeling of Spontaneous Imbibition Data for Strongly Water-Wet Systems," unpublished manuscript, (1997).
12. Schechter, D.S., McDonald, P., Sheffield, T., and Baker, R., "Reservoir Characterization and CO₂ Pilot Design in the Naturally Fractured Spraberry Trend Area," paper SPE 35469 presented at the SPE Permian Basin Oil & Gas Recovery Conference Midland, 27-29, March 1996, (a).
13. Schechter, D.S., "Advanced Reservoir Characterization and Evaluation of CO₂ Gravity Drainage in the Naturally Fractured Spraberry Trend Area," First Annual Technical Progress Report to DOE under Contract No. DE-FC22-95BC14942, Dec. 17, 1996, (b).
14. Schechter, D.S., "Advanced Reservoir Characterization and Evaluation of CO₂ Gravity Drainage in the Naturally Fractured Spraberry Trend Area," Second Annual Technical Progress Report to DOE under Contract No. DE-FC22-95BC14942, October, 1997.

Table 3.1-1 The Average Absolute Permeability and Porosity For Both Sand Units (1u And 5u) in Spraberry Trend Area Reservoir.

Sand Units	Absolute Permeability (md)	Porosity (%)
1U Sand	0.34	10.10
5U Sand	0.70	9.93

Table 3.1-2 Evaluation of Water Saturation and Current Oil Saturation ^(a)

Source of Data	Year	$k_{air}(md)$	$S_{wi}^{(b)}(\%)$	$S_w(\%)$	$S_{or}(\%)$
Tippett 5	1963	0.76 – 1.31	26 – 29	37 – 40	63 – 60
Nannie Parish 7	1974	0.13 – 0.40	31 – 33	43 – 50	50 – 57
Judkin A5	1987	0.15 – 0.70	29 – 33	40 – 50	50 – 60
Pembroke 9407	1990	0.06 – 0.80	29 – 33	42 – 50	50 – 58
Shackleford-138	1993	0.01 – 0.15	33 – 34	45 – 50	50 – 55

Notes : (a) from Guo (1995) (b) using Eq. (11)

Table 3.1-3 Evaluation of Displacement Efficiency (E_d) and Volumetric

Source of Data	Year	$S_{wi}(\%)$	$S_w(\%)$	$E_{displ}^{(c)}(\%)$	$E_{vol}^{(d)}(\%)$
Tippett 5	1963	26 – 29	37 – 40	15 – 16	76 – 83
Nannie Parish 7	1974	31 – 33	43 – 50	18 – 26	47 – 68
Judkin A5	1987	29 – 33	40 – 50	15 – 26	47 – 78
Pembroke 9407	1990	29 – 33	42 – 50	19 – 25	48 – 64
Shackleford-138	1993	33 – 34	45 – 50	18 – 25	49 – 65

Note : - (c) using Eq. (12) - (d) using Eq. (14)

- Average of reservoir oil recovery is 12% IOIP

Table 3.1-4 Reservoir parameters as input data

Area	80 acre
Net Pay	20 ft
Bulk Volume	69,696,000 ft ³
Porosity	10.02%
Pore Volume	6,983,539.20 ft ³
Water saturation	31.53 – 33.72%
Gas Saturation (assumed after waterflood initiated)	9.0 – 9.3%
Oil Saturation	57.3 – 59.2%
Initial Oil In Place	712,404 – 735,957 rb
Imbibition Efficiency	13%
Recoverable Oil	92,613 – 95,674 rb
Oil Formation Volume Factor	1.294 rb/STB
Interfacial Tension	26.22 dyne/cm
Viscosity	2.01 cp

Table 3.1-5 Fracture Spacing

Fracture Set	Spacing Range (ft)	Average Spacing (ft)
NNE	0.05 - 4.50	1.62
NE	0.73 - 5.75	3.17
ENE	0.04 – 13.00	3.79
Average		2.86

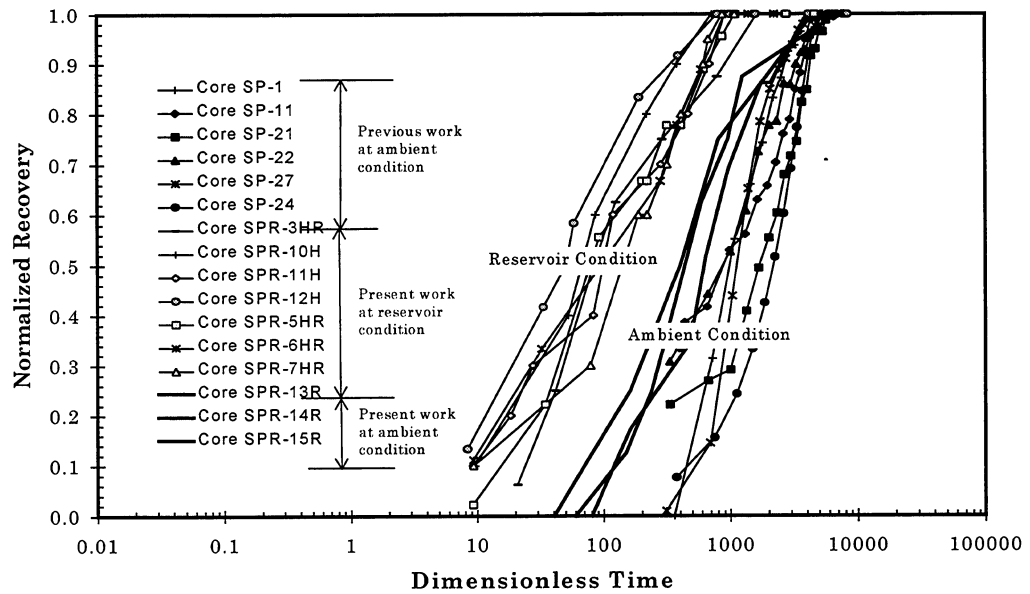


Fig. 3.1-1 Oil recovery curves obtained under reservoir condition plotted using dimensionless variables and compared with oil recovery curves obtained under ambient condition.

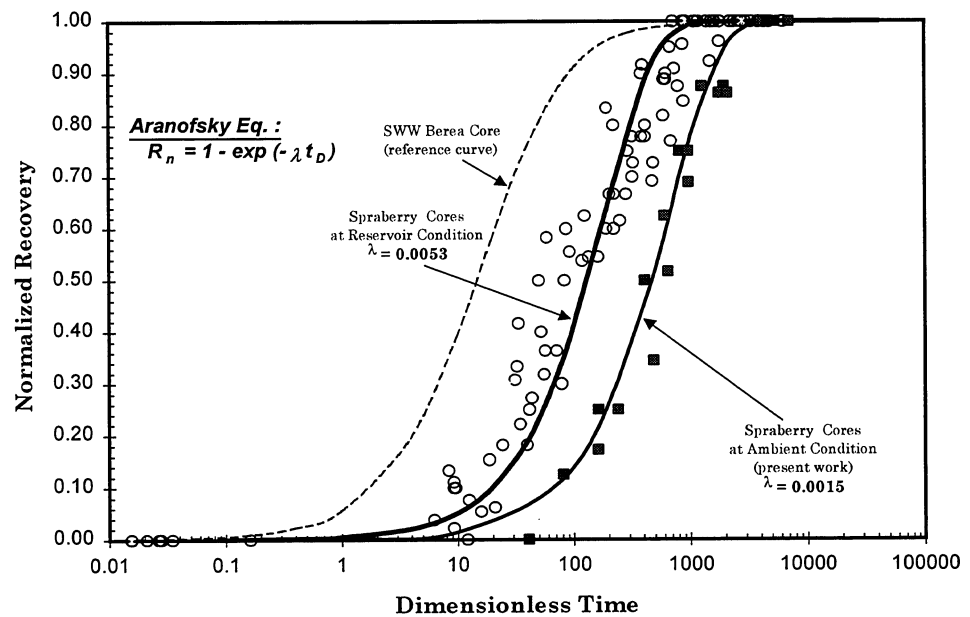


Fig. 3.1-2 Averaging of imbibition curves using the Aranofsky equation to fit the imbibition experimental data by adjusting empirical constant λ .

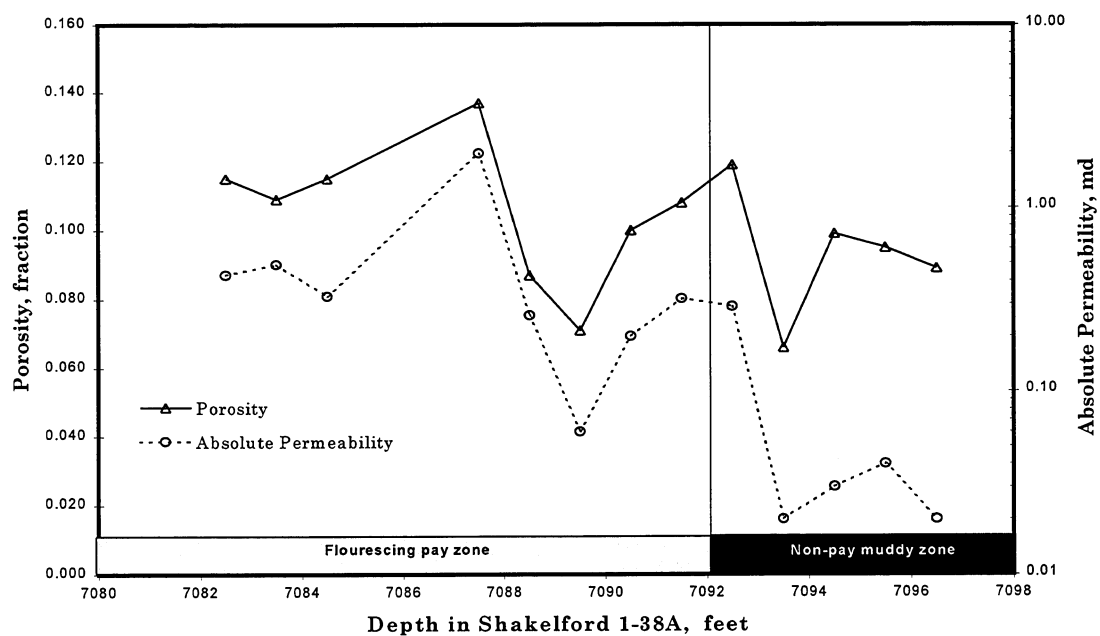


Fig. 3.1-3 Porosity and absolute permeability of Upper Spraberry 1U Unit versus depth (data taken from Well Shackleford 1-38A).

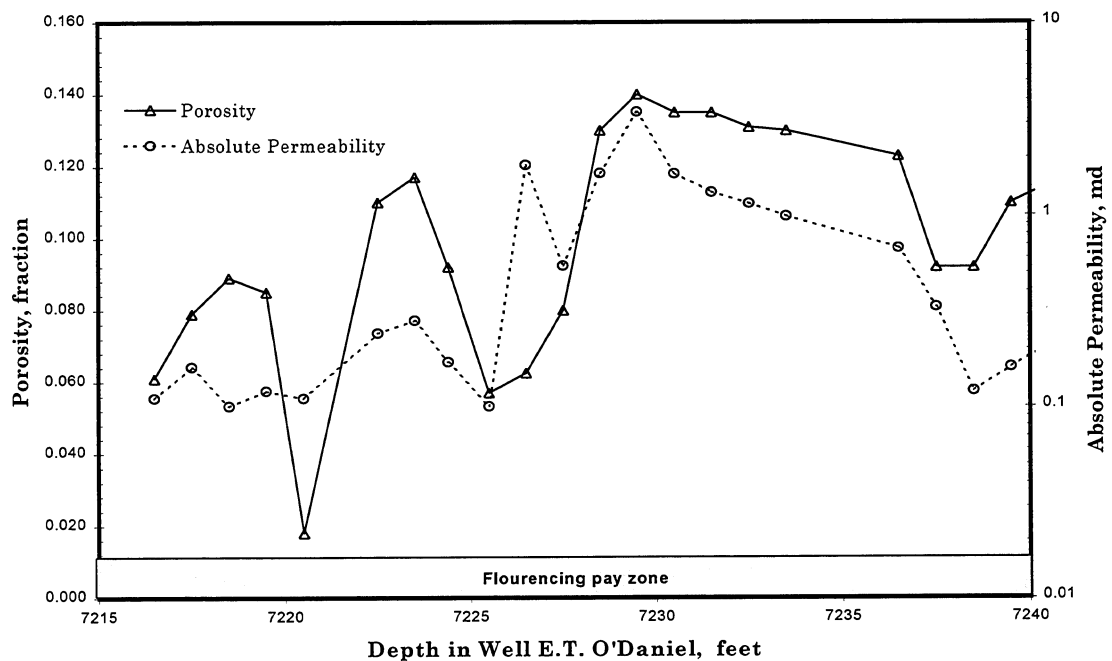


Fig. 3.1-4 Porosity and absolute permeability of Upper Spraberry 5U Unit versus depth (data taken from Well E.T. O'Daniel 37).

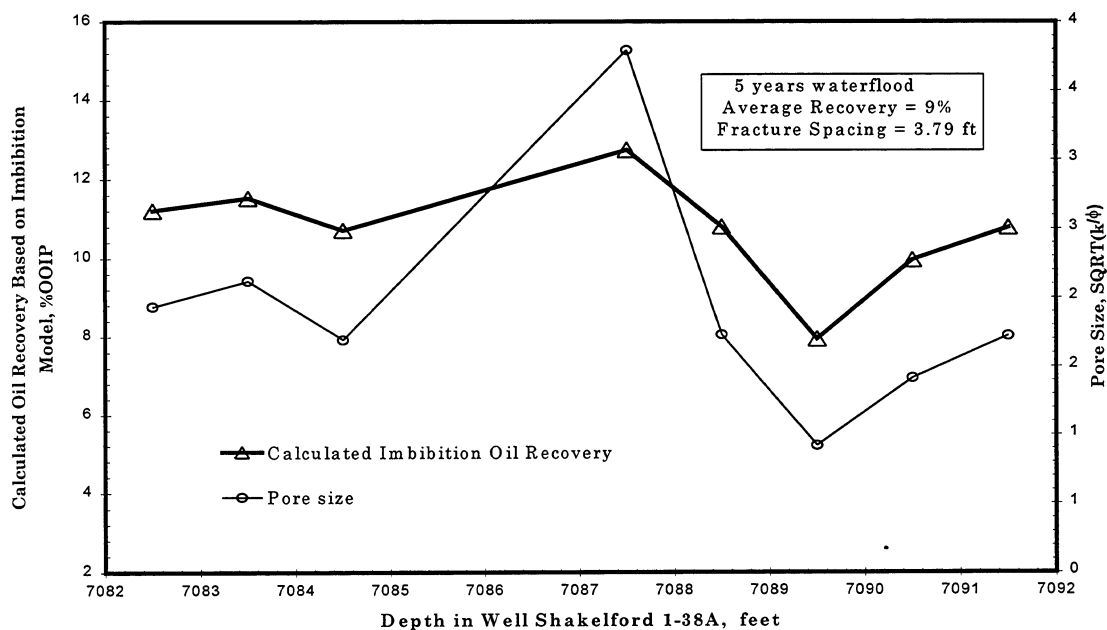


Fig. 3.1-5 Calculated imbibition oil recovery for five years of waterflooding from Upper Spraberry 1U formation, based on scaling of experimental data and fracture spacing of 3.79 ft.:

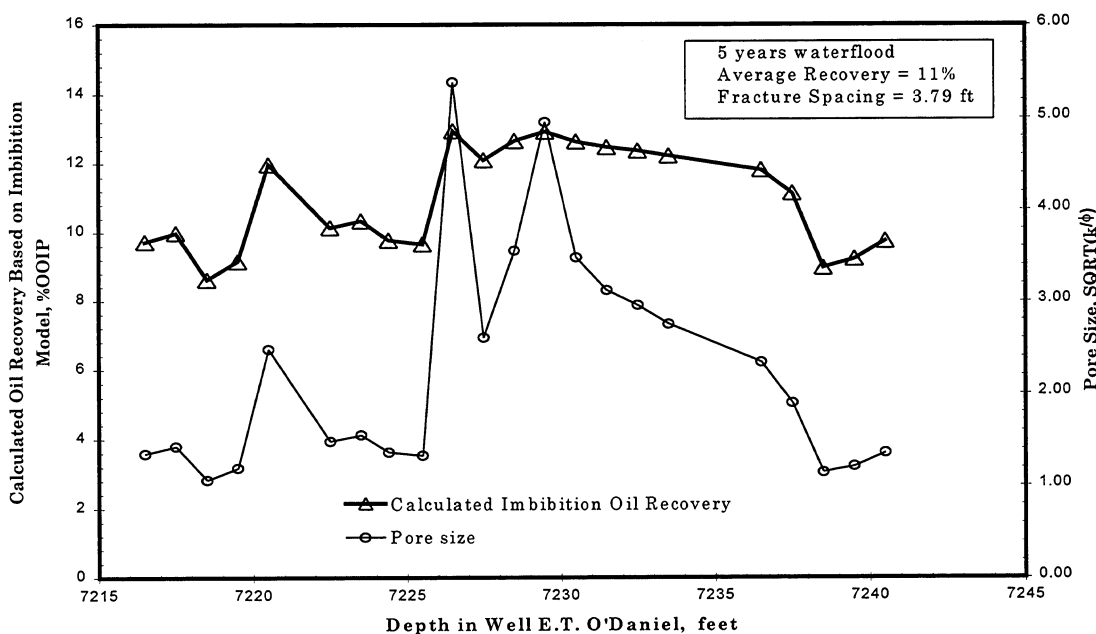


Fig. 3.1-6 Calculated imbibition oil recovery for five years of waterflooding from Upper Spraberry 5U formation, based on scaling of experimental data and fracture spacing of 3.79 ft

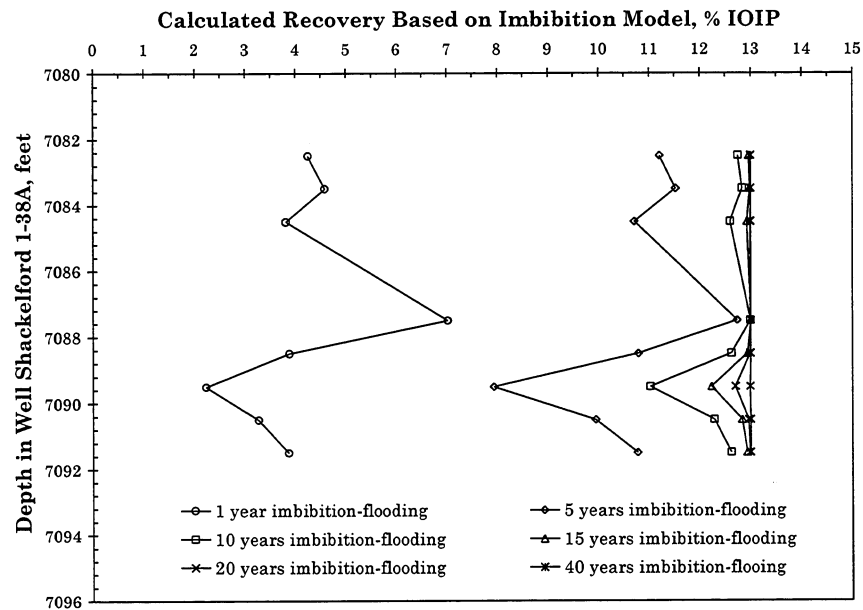


Fig. 3.1-7 History of waterflood recovery profiles from Upper Spraberry 1U formation, based on scaling of experimental data and fracture spacing of 3.79 ft

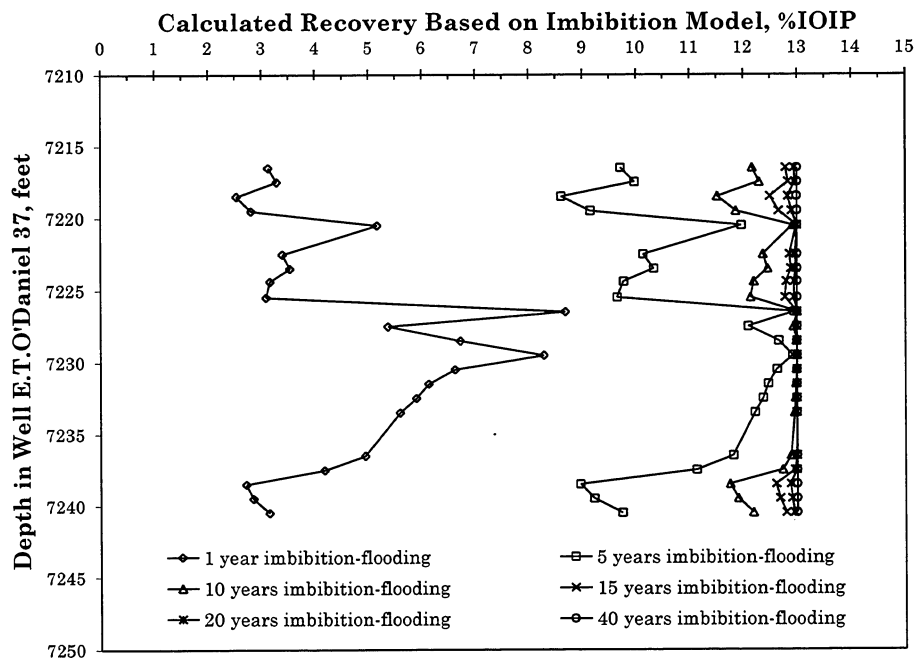


Fig. 3.1-8 History of waterflood recovery profiles from Upper Spraberry 5U formation, based on scaling of experimental data and fracture spacing of 3.79 ft

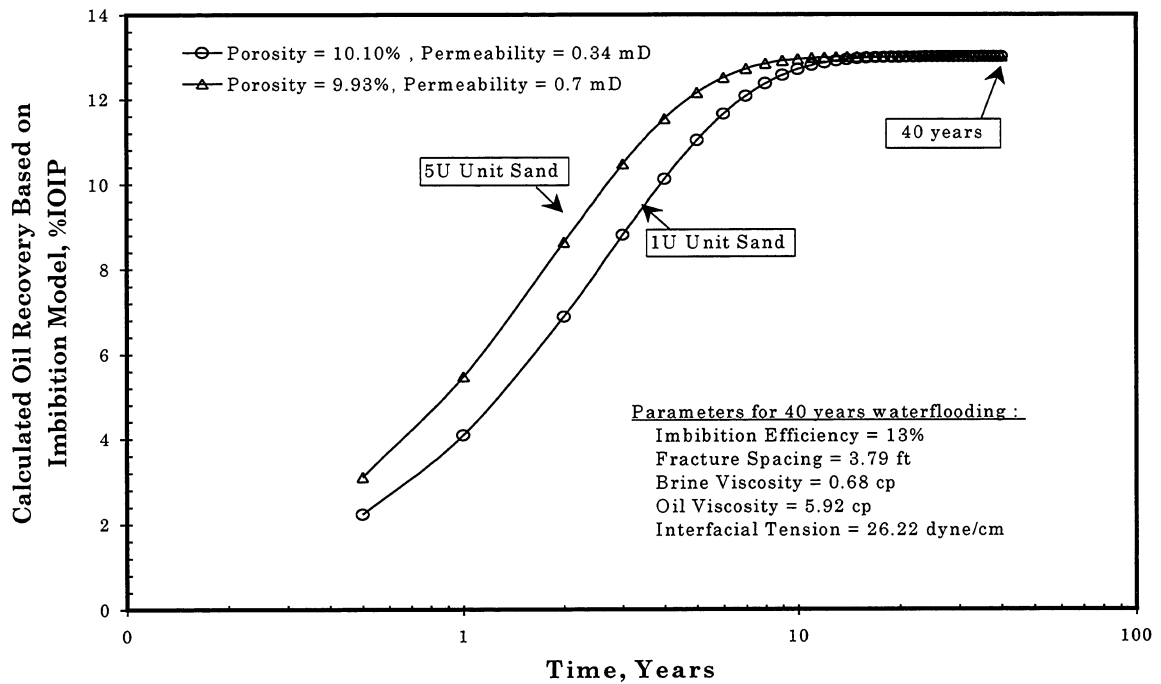


Fig. 3.1-9 Calculated imbibition oil recovery for 40 years of waterflooding from Spraberry 1U and 5U formation, based on scaling of experimental data and fracture spacing of 3.79 ft.

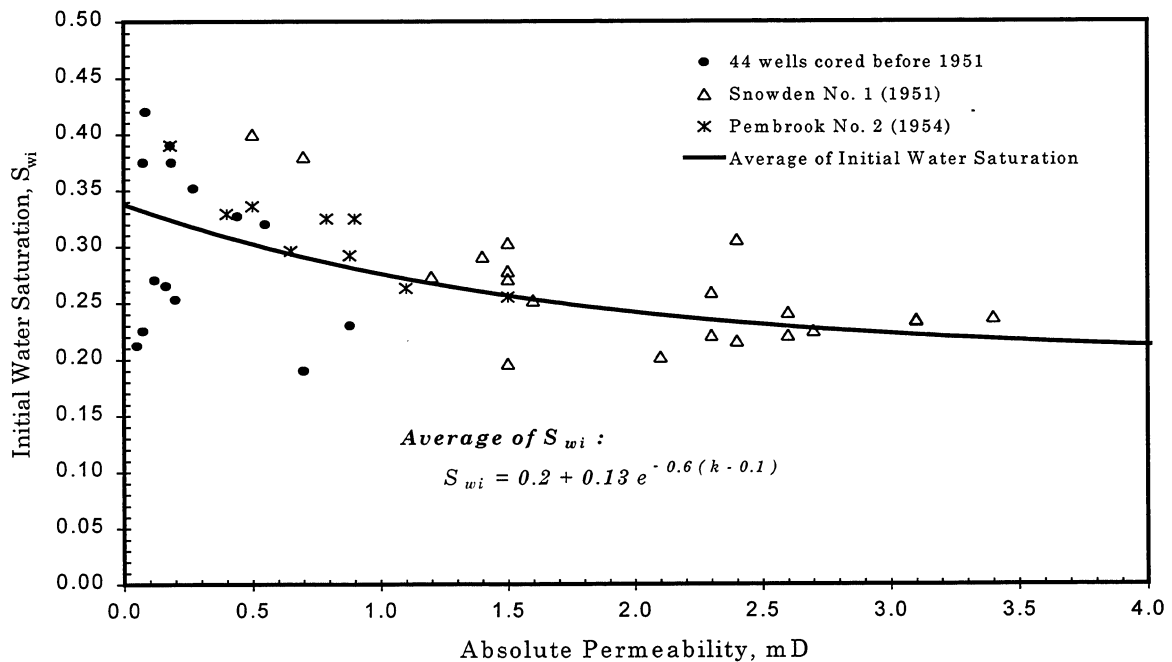


Fig. 3.1-10 Initial water saturation in the Spraberry reservoir

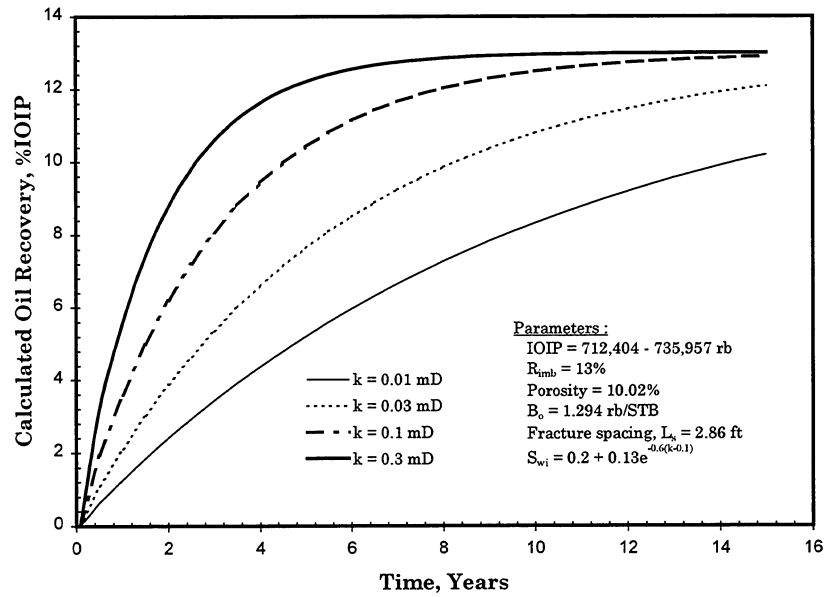


Fig. 3.1-11 Effect of matrix permeability on oil recovery mechanism.

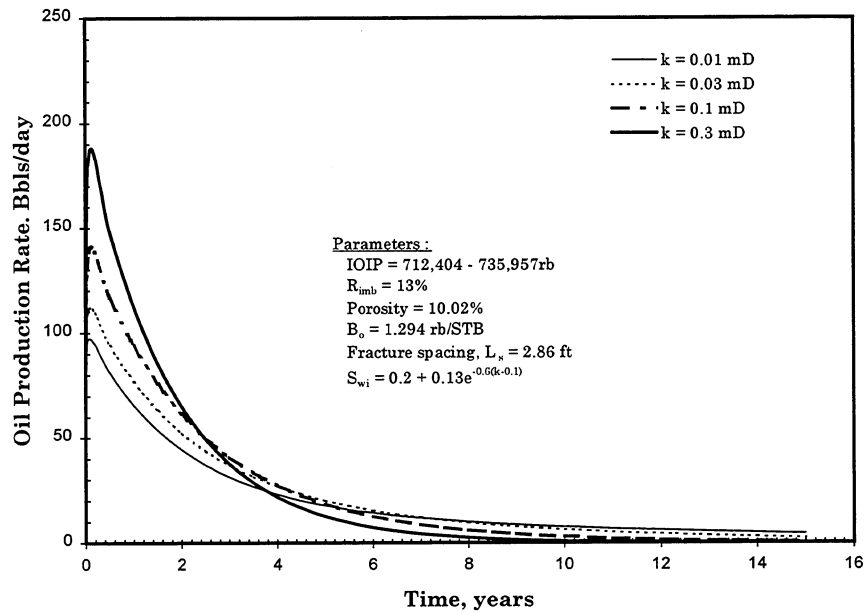


Fig. 3.1-12 Effect of matrix permeability on calculation of production rates

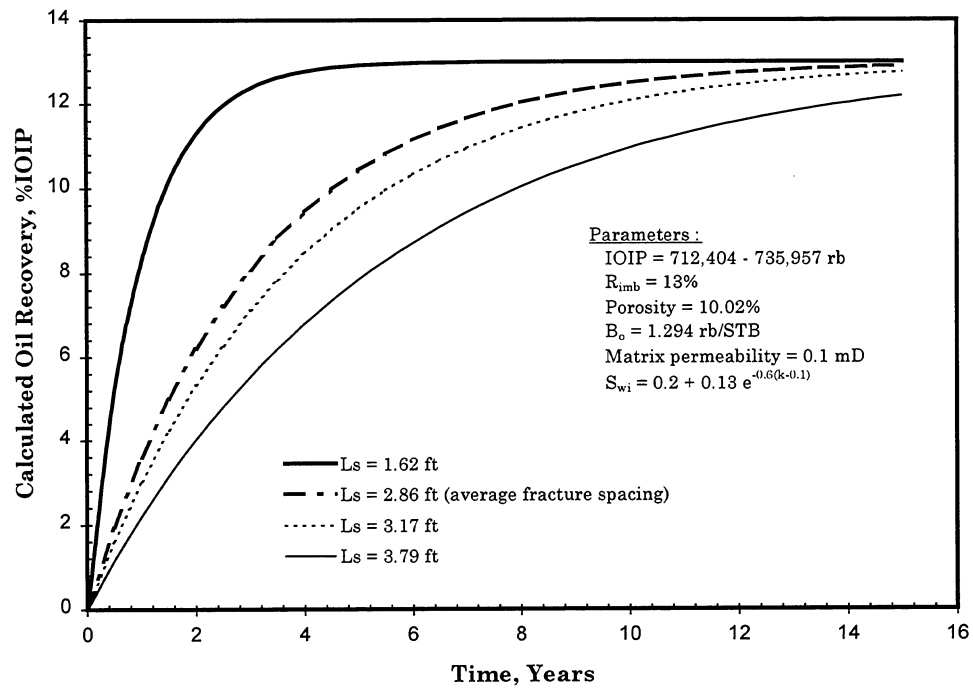


Fig. 3.1-13 Effect of fracture spacing on recovery mechanism

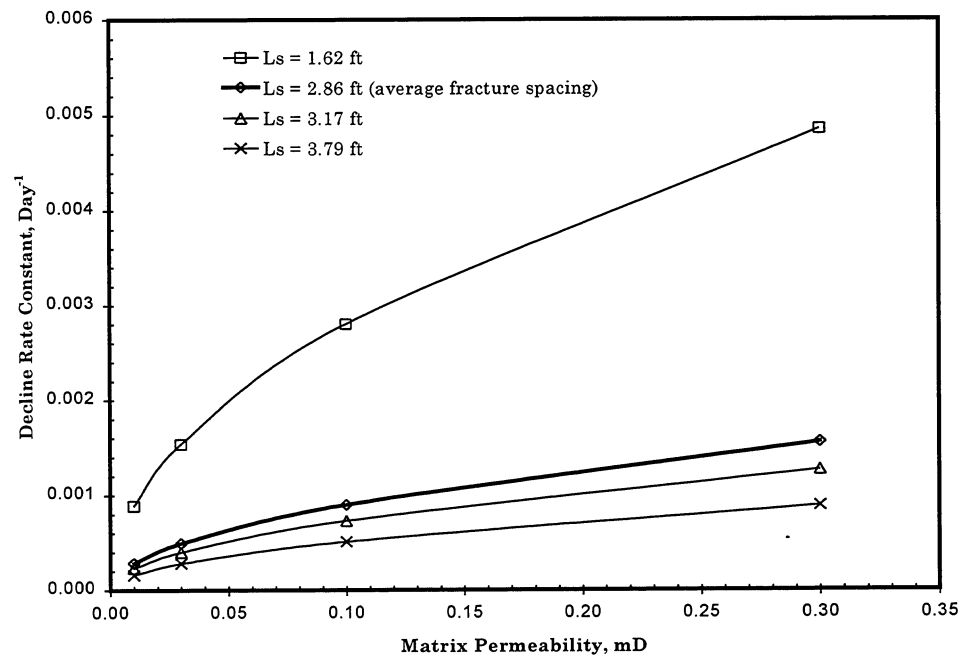


Fig. 3.1-14 Effect of matrix permeability and fracture spacing on decline rate constant

3.2 DETERMINATION OF INPUT PARAMETERS FOR SIMULATION OF CO₂ FLOODING

3.2.1 Introduction

The three-phase, three-dimensional, dual-porosity reservoir simulator is a useful tool for analyzing performance of fractured oil reservoirs. However, history matching of dual porosity reservoirs is more difficult because the simulator requires more input parameters that are usually not easy to determine. Among many of the parameters are primary permeability, secondary porosity and permeability, and permeability anisotropy. Rough data input into the simulator results in high uncertainties in reservoir performance predictions, which is the traditional GIGO (garbage-in garbage-out) problem. This section describes a new approach to determine some of the input parameters for simulation of CO₂ flooding the naturally fractured Spraberry Trend Area reservoir in West Texas.

The results of this investigation demonstrate that the primary permeability, or the absolute matrix permeability, to be used in the simulator should be determined from the oil/water drainage capillary pressure curve. Although core flood data provide good estimates of matrix porosity, permeability derived from the core floods depend strongly upon the fluid type and wetting behavior of the rock in low permeability regions. The matrix permeability that is estimated from water-oil capillary pressure is more realistic for reservoir simulation. Water-oil capillary pressure should be from direct measurements or scaled from mercury injection results if interfacial tension and contact angle data are available.

The secondary porosity due to natural fractures has been estimated based on the average fracture intensity and aperture. Fracture intensity and aperture were determined from horizontal coring. The secondary permeability due to natural fracture has been estimated based on a parallel flow mathematical model. The results are consistent with values derived from well test analyses and are being verified by scale-up of core flood data obtained using naturally fractured cores. The scaling model is presented in this section.

3.2.2 Absolute Matrix Permeability

The absolute matrix permeability of a porous medium is a term familiar to all reservoir engineers. However, the appropriate application of the parameter in multiphase flow analysis is not so obvious. The absolute matrix permeability is theoretically a property of the porous medium itself, and is generally not affected by the fluids in the pores. This means that the same absolute permeability should be measured for a given porous medium regardless of fluid type used in the measurement. This is essentially true for high permeability media. However, the absolute permeability has been found to depend strongly on the fluid properties in low permeability media.

Table 3.2-1 shows air, water, and oil permeabilities of eight core samples taken from the Spraberry Trend Area reservoir. The dependence of the absolute permeability on fluid properties is interpreted to be due to wettability of the porous material to different fluids. The effect of the wetting behavior on fluid transport is less significant in large pores where the majority of the fluid volume flows far from the pore wall where wetting effects dominate resistance to flow. Fluid flow is affected more significantly in small pores where fluid flows near the pore wall and wetting capillary effects dominate resistance to flow.

By definition, if any individual phase occupies 100% of the pore space, then the permeability of this phase is the absolute permeability. Thus the air permeability, water permeability, and oil permeability are all true absolute permeabilities for the flow of the three individual phases. A question then arises: Which absolute permeability should one use in the reservoir simulation? To answer this question, the simulator simulates the examination of the flow process. In miscible CO₂ flooding, multiphase flow is known to exist and water is a draining phase. Since CO₂ is miscible with oil in the reservoir, water-oil drainage capillary pressure should dominate the pressure-flow rate relation during the displacement process. Thus, the absolute matrix permeability should be estimated from the water/oil drainage capillary pressure curve.

3.2.3 Relationship between Capillary Pressure and Rock Permeability

Capillary pressure curves have long been used in the petroleum industry for analyzing behavior of oil reservoirs (Leverett, 1941; Leverett, Lewis and, True, 1942). A great amount of information about porous materials, such as pore size distribution, can be obtained based on capillary pressure curves (Ritter and Drake, (1945). Purcell (1949) essentially bases the currently used methods for determination of rock permeabilities from capillary pressure curves on the work. By combining Poiseuille's equation and Darcy's Law for a hypothetical porous medium composed of a large number of parallel, cylindrical capillary tubes of equal length, Purcell proposed the following equation:

$$k = 2F\phi\sigma^2 \cos^2 \theta \int_0^1 P_c^{-2} dS_b \dots\dots\dots(1)$$

where k is permeability, F is the lithology factor accounting for differences between the flow in the hypothetical porous medium and that in naturally occurring rocks, σ is interfacial tension, θ is the contact angle, ϕ is porosity, P_c is capillary pressure, and S_b is non-wetting phase saturation as a fraction of bulk volume.

Thomeer (1960) found that when the capillary pressure and saturation data are plotted on a log-log paper, a smooth curve best fitting the points approximates a hyperbola, which is mathematically expressed as follows:

$$\log(P_c / P_d) - \log(S_b / S_{b\infty}) = -C^2 \dots\dots\dots(2)$$

where P_d is the displacement pressure (threshold), $S_{b\infty}$ is the non-wetting phase saturation at infinite capillary pressure, C^2 is a pore geometrical factor. Thomeer also plotted air permeability against $S_{b\infty}/P_d$ on log-log paper for constant C values. Linear relationship was observed from the plots. No explanation was given in Thomeer's paper about why such a linear relationship exists.

Swanson (1981) presented a simple correlation between permeabilities and mercury capillary pressures based on the shape of the initial-residual curve. The curve bent at initial saturations greater than about 0.42. The point at which the curve bent was considered to be an indication of a transition from broadening spatial distribution and trapping to fine structure trapping and intrusion of the non-wetting phase into corners of pores. With no knowledge of where the bending point corresponds on general capillary pressure curves, Swanson chose a point "A" through which a 45-degree tangent line can be drawn as an approximation. Because the ratio of non-wetting phase saturation to the capillary pressure at point A, $(S_b/P_c)_A$ is maximal and easy to graph, Swanson chose the ratio as a parameter for relating the capillary pressure curve to permeability. Values of the parameter $(S_b/P_c)_A$ were determined on 319 sandstone and carbonate samples representing 74 formations using the tangent approach. A linear relation between $(S_b/P_c)_A$ and air/brine permeability was observed. Based on the linear relation, Swanson presented a homograph for estimating brine permeabilities from capillary pressure curves.

Walls and Amaefule (1985) applied Swanson's parameter $(S_b/P_c)_A$ for tight gas sands. They developed a linear correlation between $(S_b/P_c)_A$ and permeability similar to, but better than, Swanson's correlation in the low permeability (<0.1 md) region. Because Swanson's procedure requires the construction of 45° lines tangential to the capillary pressure curves in order to define $(S_b/P_c)_A$, Walls and Amaefule found it difficult to generate $(S_b/P_c)_A$ automatically using a computer routine. They therefore developed a new procedure for ease of computer generation of the parameter $(S_b/P_c)_A$. The new procedure involves tabulating, or plotting, $(P_c / S_b)^{1/2}$ versus S_b data. A minimum value, $(P_c / S_b)_{\min}^{1/2}$, can be found from the plot for each sample. The Swanson parameter, $(S_b/P_c)_A$, can then be determined with the following equation.

$$(S_b / P_c)_A^{-1/2} = (P_c / S_b)_{\min}^{1/2} \dots\dots\dots(3)$$

However, Walls and Amaefule (1985) did not provide any proof of Eq. (3). Equation (3) is believed to have been established based on the fact that S_b / P_c takes its maximal at point A, as stated by Swanson. This equation will be proved in the next section.

3.2.4 Analytical Determination of Swanson Parameter $(S_b / P_c)_A$

Swanson's parameter $(S_b/P_c)_A$ is very useful in estimating rock permeability from capillary pressure data. However, as shown by Walls and Amaefule (1985), the graphic

procedure presented by Swanson for determination of the parameter is time consuming. Walls and Amaefule's tabulating/graphic procedure is also not convenient to use in computerized analysis. It is highly desirable to develop a simple equation for calculation of the parameter. Derivation of such an equation can be done if capillary pressure data can be fitted to Eq. (2). In fact, the equation of the 45° line passing through the origin of the hyperbola represented by Eq. (2) can be expressed as follows in the log-log P_c - S_b scale:

$$\log(P_c / P_d) = -\log(S_b / S_{b\sim}) \dots\dots\dots(4)$$

where the negative sign comes from the slope of the line. Combination of Eqs. (2) and (4) gives the solution of coordinates of the intersection between the capillary pressure curve and the 45 degree line (point "A" in Swanson's paper) as follows:

$$S_{bA} = 10^C S_{b\sim} \dots\dots\dots(5)$$

and

$$P_{cA} = 10^{-C} P_d \dots\dots\dots(6)$$

Dividing Eq. (5) by Eq. (6) yields a simple expression for Swanson's parameter:

$$(S_b / P_c)_A = 10^{2C} (S_{b\sim} / P_d) \dots\dots\dots(7)$$

Eq. (7) can also be derived by observing that S_b/P_c is maximal (P_c/S_b is minimal) at point A as shown below.

Eq. (2) gives:

$$P_c = P_d 10^{-C^{2/\log(S_b/S_{b\sim})}} \dots\dots\dots(8)$$

Dividing Eq. (8) by S_b yields:

$$P_c / S_b = 10^{-C^{2/\log(S_b/S_{b\sim})}} P_d / S_b \dots\dots\dots(9)$$

Let $f(S_b) = P_c/S_b$. and taking the derivative then

$$\frac{\partial f}{\partial S_b} = 10^{-C^{2/\log(S_b/S_{b\sim})}} P_d / S_b^2 \left\{ \frac{C^2}{[\log(S_b / S_{b\sim})]^2} - 1 \right\} \dots\dots\dots(10)$$

Since $f(S_b)$ is minimal at point A, application of $\frac{\partial f}{\partial S_b} = 0$ to Eq. (10) and solving for S_b

give:

$$S_{bA} = 10^C S_{b\sim} \dots\dots\dots(11)$$

and

$$P_{cA} = 10^{-C} P_d \dots\dots\dots(12)$$

Dividing Eq. (11) by Eq. (12) yields a simple expression for Swanson's parameter:

$$(S_b / P_c)_A = 10^{2C} (S_{b\sim} / P_d) \dots\dots\dots(13)$$

which is identical to Eq. (7). This also proves that Walls and Amaefule's tabulating/graphic method for determining the Swanson parameter is valid.

3.2.4.1 Advantages of Using Eq. (13)

The first advantage of using Eq. (13) to determine Swanson's parameter is simplicity. Compared to Swanson's graphic procedure and Walls' tabulating/graphic procedure,

Eq. (13) is much easier to use in computerized calculations. The second advantage of using Eq. (13) is the accuracy of the result compared to Swanson's graphic procedure and Walls and Amaefule's tabulating/graphic procedure where significant error can result from reading coordinates of the point A from a log-log plot. For example, the capillary pressure data presented in Fig.1b in Swanson's paper, the Swanson parameter is determined to be 0.48 based on Swanson's graphic procedure, while Eq. (13) gives a value of 0.47. For the capillary pressure data shown in Fig. 4 in Swanson's paper (Fig. 1 in Walls and Amaefule's paper), the Swanson parameter is determined to be 0.61 based on Swanson's graphic procedure, while Eq. (13) gives a lower value of 0.44.

3.2.4.2 Application of Eq. (13) to the Spraberry Sand

The parameters for equations (13) can be determined by curve matching between the oil-water drainage capillary pressure for a Spraberry core. This match is shown in Fig. 3.2-1 and gives the following parameters for the Spraberry sand:

$$C = 0.24 \quad S_b = 0.098 \quad P_d = 7 \text{ psig.}$$

The Swanson's parameter can then be determined based on Eq. (13):

$$(S_b / P_c)_A = 0.042$$

Swanson (1981) proposed the following correlation for the determination of water permeability:

$$k_w = 431 \left(\frac{S_b}{P_c} \right)_A^{2.109} \dots\dots\dots(14)$$

Substituting $(S_b / P_c)_A = 0.042$ into Eq. (14) results in $k_w = 0.538$ md, which should be used as the absolute matrix permeability in the simulation of the water flooded Spraberry Trend Area reservoir.

3.2.5 Secondary Porosity

The secondary porosity, ϕ_f , due to natural fractures may be estimated based on the average fracture aperture and fracture spacing using a simple relation:

$$\phi_f = \frac{w}{S_f} \dots\dots\dots(15)$$

where w and S_f are fracture aperture and spacing respectively. As discussed in our Second Annual Report (Schechter,1997) the average fracture aperture in the Spraberry Trend Area may be taken as 0.0025 in.. Based on recent fracture characterization (Schechter,1997), three distinct fracture sets, trending NNE, NE, and ENE, are present in cores from the 1U and 5U units in the Upper Spraberry zone. The average fracture spacing of the three fracture sets are 1.62, 3.17, and 3.79 ft, respectively. Since the three sets of natural fractures co-exist in the reservoir pay zones, the distance between natural fractures in all sets must be lower than 1.62 ft. In fact the distances between most of the NNE fractures are less than 1 ft. If we assume that the average distance between the inter-set natural fractures is 0.5 ft (or 6 in.), substituting $w = 0.0025$ in. and $S_f = 6$ in. into Eq. (15) yields $\phi_f = 0.0004$. Well testing (Baker, 1994a; Baker, 1994b) has not clearly

demonstrated dual porosity pressure transient behavior in the Spraberry Trend. This indicates that fracture volume is less than 1/1000 of the matrix volume (Van Golf, 1982), which is consistent with the low value of ϕ_f estimated here.

3.2.6 Secondary Permeability

The secondary permeability due to natural fractures is also called fracture permeability in well test models and dual-porosity simulators. However, it is different from the fracture permeability that is frequently used in hydraulic stimulation analysis where the hydraulically induced, proppant-filled fracture is treated as a porous medium that has an intrinsic permeability. The fracture permeability for a hydraulically induced fracture is a property of the fracture itself, while the secondary permeability due to natural fractures is a defined parameter for the fracture network and its magnitude depends on both fracture conductivity and fracture intensity. In the following analyses, these two permeabilities are distinguished using terms *secondary permeability* k_s and *intrinsic fracture permeability* k_f . These two parameters differ by a factor that equals the secondary porosity as shown in this section.

The secondary permeability is the highest in the fracture on-trend direction and the lowest in the fracture off-trend direction. The permeability anisotropy may be estimated based on well testing data as shown in Second Annual Report of this project (Schechter, 1997). Here we present two approaches for estimating the on-trend secondary permeability. This first one is called parallel flow model, and the second one is referred to as the scaling model.

3.2.6.1 Parallel Flow Model

Assuming parallel flow in the fracture and matrix, a simple interrelationship between the effective on-trend reservoir permeability, matrix permeability, and intrinsic fracture permeability has been derived (see Appendix A for details):

$$k_e = (1 - \phi_f)k_m + \phi_f k_f \dots\dots\dots(16)$$

where k_e , k_m , and k_f are the on-trend effective reservoir permeability, matrix permeability, and intrinsic fracture permeability, respectively. The second term in the right-hand-side of Eq. (16) is the secondary permeability k_s in the on-trend direction:

$$k_s = \phi_f k_f \dots\dots\dots(17)$$

We can estimate the intrinsic fracture permeability in the on-trend direction using the following expression (Schechter, 1997).

$$k_f = \frac{\phi_f^3 w^2}{12} \dots\dots\dots(18)$$

where ϕ_f is the fracture porosity accounting for volume of minerals, crushed rock, and proppant introduced during hydraulic fracturing operations.

Mineralized fractures were found in the 1U unit of the Upper Spraberry with an average percentage of mineral-filling in the fractures of about 75%. Hairline fractures found in the 5U unit of the Upper Spraberry are not mineralized. If we assume the fracture porosity to be about 0.25, substituting $\phi_f = 0.25$ and $w = 0.0025$ in. into Eq. (18) results in $k_f = 78,125$ md. The secondary permeability in the on-trend direction can then be estimated using Eq. (17): $k_s = (0.0004) (78,125) = 31$ md. which is very close to the on-trend fracture permeability derived from well testing analyses (Schechter,1997).

3.2.6.2 Scaling Model

If the permeability of a core plug with representative natural fractures are measured, the secondary permeability can also be estimated using a scaling model presented here. The interrelationship between plug permeability k_p , intrinsic fracture permeability k_f , and fracture conductivity K_f is given by:

$$k_p \frac{\pi d^2}{4} = k_f h w = K_f h \quad \text{.....(19)}$$

where d and h are plug diameter and total fracture length measured in the cross sectional area of the plug, respectively. Solving the left part of Eq. (19) for k_f yields:

$$k_f = k_p \frac{\pi d^2}{4 h w} \quad \text{.....(20)}$$

Substituting Eqs. (15) and (20) into Eq. (17) gives

$$k_s = k_p \frac{\pi d^2}{4 h S_f} \quad \text{.....(21)}$$

If fracture conductivity, rather than plug permeability, is measured, the intrinsic fracture permeability can be determined by solving the right part of Eq. (19) for k_f :

$$k_f = \frac{K_f}{w} \quad \text{.....(22)}$$

Substituting Eqs. (15) and (22) into Eq. (17) gives

$$k_s = \frac{K_f}{S_f} \quad \text{.....(23)}$$

It is important to note that fracture aperture w , a parameter that is difficult to measure, does not appear in Eqs. (21) and (23), which makes the two equations easy to use. We are currently measuring the k_p using a Spraberry core plug with natural fractures to test the validity of Eq. (21).

3.2.7 Conclusions

The CO₂ flooding project is undergoing Phase II, i.e., Field Demonstration. Pilot scale reservoir simulation for the CO₂ flooding is necessary for both initial pilot design and design modification in the future. In order to perform a quality simulation study with a dual porosity reservoir simulator, it is vitally important to use reliable reservoir parameters as input data. In the first quarter of 1998, we conducted investigations on refinement of reservoir parameters to be used in the pilot scale simulation of CO₂ flooding. We concluded that the absolute permeability of the rock matrix to be input into the dual porosity simulator should be the permeability determined from drainage oil-water capillary pressure curve rather than air permeability, water permeability, or oil permeability. Its value is 0.538 md. We also concluded that the secondary porosity and the on-trend secondary permeability due to natural fractures can be estimated using a simple mathematical model based on fracture characterization data. Their values in the Spraberry Trend Area are estimated to be 0.0004 and 31 md respectively. These numbers

are consistent with that estimated from well test interpretation (Schechter, 1997) and are being verified using experimental data and a scaling model.

3.2.8 References

1. Baker, R.: "Pressure Test Analysis for Midkiff 25-08," (April 1994a)
2. Baker, R.: "Vertical Pulse Test Analysis of Shackelford 1-38A," (April 1994b)
3. Leverett, M.C.: "Capillary Behavior in Porous Solids," *Trans. AIME* (1941) **142**, 151.
4. Leverett, M.C., Lewis, W.B. and True, M.E.: "Dimensional Model Studies of Oil Field Behavior," *Trans. AIME* (1942) **146**, 175.
5. Purcell, W.R.: "Capillary Pressures --- Their Measurement Using Mercury and the Calculation of Permeability Therefrom," *Trans. AIME* (1949) **186**, 39.
6. Ritter, H.L. and Drake, L.C.: "Pore Size Distribution in Porous Materials," *Ind. and Eng. Chem.* (1945) **17**, 782.
7. Schechter, D.S.: "Advanced Reservoir Characterization and Evaluation of CO₂ Gravity Drainage in the Naturally Fractured Spraberry Trend Area," Second Annual Technical Progress Report, U.S. DOE Contract No. DE-FC22-95BC14942 (Dec 1997).
8. Swanson, B.F.: "A Simple Correlation Between Permeabilities and Mercury Capillary Pressures," *JPT*. (December 1981) 2498-2504.
9. Thomeer, J.H.M.: "Introduction of a Pore Geometrical Factor Defined by the Capillary Pressure Curve," *JPT*. (March 1960) 73-77.
10. Walls, J.D. and Amaefule, J.O.: "Capillary Pressure and Permeability Relationships in Tight Gas Sands," paper SPE 13879 presented at the SPE Low Permeability Reservoirs Symposium held in Denver, Colorado, May 19-22, 1985.
11. Van Golf-Racht, D.T.: *Fundamentals of Fractured Reservoir Engineering*, Elsevier Scientific Publishing Co., New York, 1982.

Appendix A - Interrelationship between Effective On-Trend Reservoir Permeability, Matrix Permeability and Intrinsic Fracture Permeability in Naturally Fracture Reservoirs

A simple relationship between effective on-trend reservoir permeability, matrix permeability and intrinsic fracture permeability in naturally fractured reservoirs can be analytically established based on an assumption of parallel flow in matrix and fracture.

Consider a fractured porous medium shown in Fig. 3.2-2. If the pressure drop across the length L is ΔP , according to Darcy's law, the total flow rate Q of a fluid with viscosity μ is expressed as

$$Q = \frac{k_e A \Delta p}{\mu L} \quad \dots\dots\dots (A.1)$$

where k_e and A are the effective permeability and total cross sectional area, respectively. If we use k_m and A_m to denote matrix permeability and matrix cross sectional area respectively, the flow rate through the matrix body Q_m is expressed as

$$Q_m = \frac{k_m A_m \Delta p}{\mu L} \quad \dots\dots\dots (A.2)$$

Similarly, if we denote intrinsic fracture permeability and fracture cross sectional area by k_f and A_f respectively, the flow rate through the fractures Q_f is expressed as

$$Q_f = \frac{k_f A_f \Delta p}{\mu L} \quad \dots\dots\dots (A.3)$$

Since

$$Q = Q_m + Q_f \quad \dots\dots\dots (A.4)$$

Substitutions of Eqs. (A.1), (A.2) and (A.3) into Eq. (A.4) yield

$$k_e = \frac{A_m}{A} k_m + \frac{A_f}{A} k_f \quad \dots\dots\dots (A.5)$$

Since

$$A = A_m + A_f \quad \dots\dots\dots (A.6)$$

and

$$\phi_f = \frac{A_f}{A} \quad \dots\dots\dots (A.7)$$

where ϕ_f is the secondary porosity due to fracture, Eq. (A.5) is rewritten as

$$k_e = (1 - \phi_f) k_m + \phi_f k_f \quad \dots\dots\dots (A.8)$$

Equation (A.8) represents a general relationship between the effective on-trend reservoir permeability, matrix permeability and intrinsic fracture permeability in naturally fractured reservoirs.

In most oil and gas reservoirs ϕ_f is much less than 1. Equation (A.8) thus degenerates to

$$k_e = k_m + \phi_f k_f \quad \dots\dots\dots (A.9)$$

This equation indicates that intrinsic fracture permeability linearly contributes to the effective on-trend reservoir permeability with a proportionality factor of ϕ_f , the secondary porosity due to the fractures.

The first term in Eq. (A.9) for matrix permeability is usually much smaller than the second term. The effective on-trend reservoir permeability is thus dominated by intrinsic fracture permeability:

$$k_e \approx \phi_f k_f. \dots\dots\dots (A.10)$$

The secondary porosity ϕ_f due to fracture can be shown to relate to the fracture width (aperture) w and fracture spacing S_f through the following equation:

$$\phi_f = \frac{w}{S_f}. \dots\dots\dots (A.11)$$

Therefore, if w and S_f are estimated from fracture characterization and k_f is measured on core plugs, the secondary porosity and the effective on-trend reservoir permeability k_e can be estimated from Eq. (A.10). This effective on-trend reservoir permeability may be compared with the on-trend effective permeability derived from well tests.

Table 3.2-1 Air, Water, and Oil Permeabilities of Spraberry Trend Area Reservoir Cores

Core Sample	Porosity%	Absolute Permeability (md)		
		Air	Water	Oil
SP-1	10.0	0.43	0.28	0.09
SP-2	10.1	0.45	0.22	0.1
SP-3	9.8	0.44	0.23	0.14
SP-4	10.0	0.46	0.14	0.06
SP-5	10.7	0.49	0.27	0.09
SP-6	9.85	0.43	0.22	
SP-7	10.4	0.34	0.2	0.08
SP-10	12.8	0.36	0.15	0.05

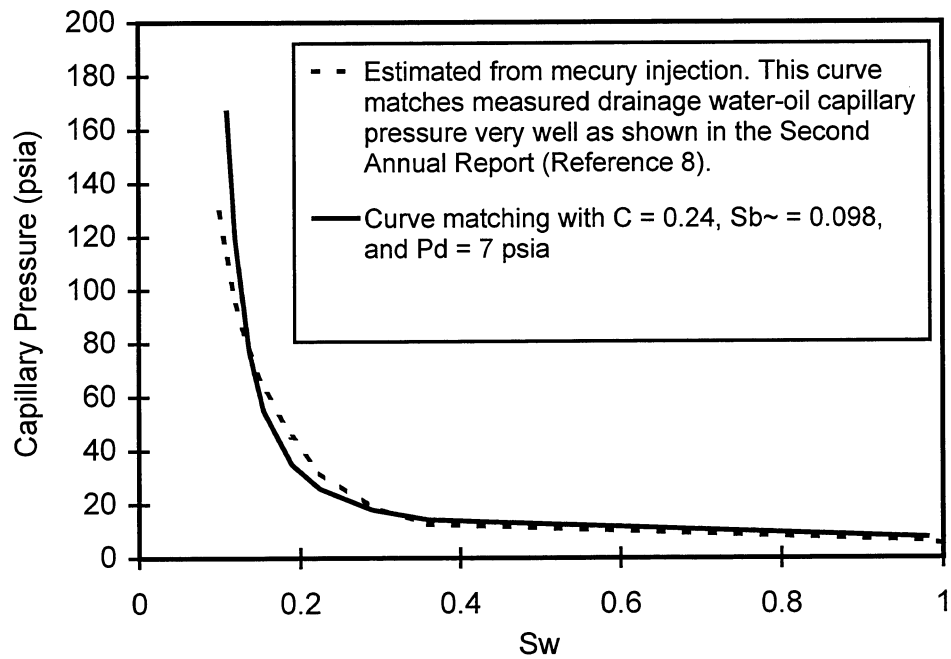


Fig. 3.2-1 Curve matching of oil-water drainage capillary pressure for a Spraberry core.

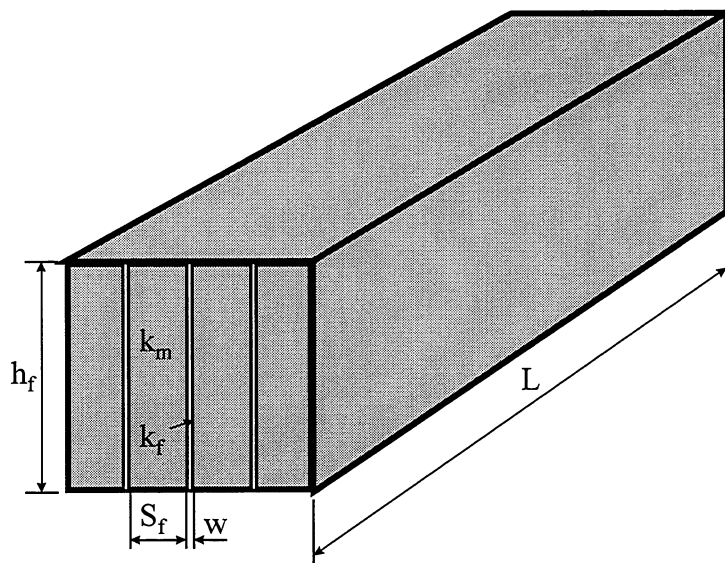


Fig. 3.2-2 A parallel-flow model for simulating fluid flow in naturally fractured reservoirs.

3.3 NUMERICAL MODELING OF SOLID DEFORMATION AND STRESS-DEPENDENT PERMEABILITY IN NATURALLY FRACTURED RESERVOIRS

During the first year of this project, we analyzed the productivity behavior of Spraberry wells using a newly developed mathematical model. In the second year of this project, we modified the mathematical model with consideration of mechanical skin due to fluid damage to the matrix permeability. In the third year of this project, the stress-sensitive permeability was studied in detail including the effect of deformation. A model coupling the solid deformation and the motion of fluid flow was developed using a fully implicit finite-difference scheme. A comparison between conventional dual-porosity and stress dual-porosity simulators has been made. The effect of stress-sensitive permeability to the well productivity was demonstrated.

3.3.1 Introduction

Fractures are the main fluid flow paths in naturally fractured reservoirs. Therefore, the productivity of naturally fractured reservoirs relies on the magnitude of fracture permeability. When the pore pressure depletes due to oil/gas production rates in highly stress-sensitive naturally fractured reservoirs, the confining stresses on the reservoir rock increase over the hydraulic pressure in the pores of the rock causing compaction of the rock. The interaction between fluid flow and rock volumetric deformation causes significant reduction in fracture permeability. This, in turn, may reduce the reservoir productivity.

In current conventional dual-porosity simulators the stress-sensitive reservoir is simulated by using pressure-sensitive permeability, where permeability is treated as a function of pore pressure and the effect of rock deformation due to changes of the stress-state is neglected. Hence, productivity predictions obtained using conventional dual-porosity simulators in reservoir with stress-sensitive characteristic may be misleading. A numerical modeling study of the stress dual-porosity simulator was undertaken to incorporate the effect of solid deformation in the naturally fractured reservoir.

Although naturally fractured reservoirs have been the subject of much research, not many studies cover the effect of solid deformation on the changes in fluid pressure. Uncertainties still exist in the governing equation describing this process as found in the cited references (Huyakorn and Pinder, 1983, Unger and Aifantis, 1990, Bai et al., 1993, Chen and Teufel, 1997). The governing equation used in this study is adopted from Chen and Teufel (1997), which is considered conceptually more consistent than other reviewed in the literature.

The main thrust of this study is to develop numerical simulation schemes to simulate naturally fractured reservoirs incorporating solid deformation and stress-sensitive permeability.

3.3.2 Technical Approach

In this section, governing equations for coupled fluid flow and poroelastic models in porous media are presented. The development of governing equations involves the mathematical representation of conceptual models, the process underlying the conceptual models and the assumption of governing equations.

3.3.2.1 Dual-Porosity/Dual-Permeability Fluid Flow Model

The concept of the dual-porosity system considered in this study is identical to the single-phase flow equations given by Barenblatt *et al* (1960). These equations were derived under the following assumptions: (1) Fluid flow is single-phase laminar (2) Fluid is

slightly compressible (3) Gravity effects are negligible and pressure gradients are small
(4) Transfer of fluid from matrix to fractures occurs under pseudo-steady state conditions.
The governing equations for the conventional dual-porosity model is presented below:

$$\nabla \cdot \left(\frac{k_1}{\mu} \nabla p_1 \right) = (c_1 + \phi_1 c_f) \frac{\partial p_1}{\partial t} - \Gamma \dots\dots\dots(1)$$

$$\nabla \cdot \left(\frac{k_2}{\mu} \nabla p_2 \right) = (c_2 + \phi_2 c_f) \frac{\partial p_2}{\partial t} - \Gamma \dots\dots\dots(2)$$

where c , ϕ , c_f and Γ are medium compressibility, porosity, fluid compressibility and interporosity flow, respectively. Subscripts 1 and 2 denote matrix and fracture, respectively.

The fluid flow governing equation for dual-porosity was modified to include the effect of solid displacement. Three basic principles constituting this model are mass conservation, Darcy's law and an equation of state.

Mass conservation:

$$\text{Fluid: } \nabla \cdot (\rho \phi_n v_n) + \frac{\partial(\phi_n \rho)}{\partial t} + (-1)^n \rho \Gamma = 0 \dots\dots\dots(3)$$

$$\text{Solid: } \nabla \cdot (\rho_s (1 - \phi_t) v_s) + \frac{\partial(1 - \phi_n \rho_s)}{\partial t} = 0 \dots\dots\dots(4)$$

$$\text{Darcy's law: } \phi_n (v_n - v_s) = - \frac{k_n}{\mu} \nabla p_n \dots\dots\dots(5)$$

Equation of state (isothermal fluid compressibility):

$$c_n = \frac{1}{\rho} \frac{\partial \rho}{\partial p_n} \dots\dots\dots(6)$$

The subscript $n = 1$ denotes the matrix block while $n=2$ for the fractures and s for solid phase. By combining those three principles, the governing equation for fluid flow and the effect of solid deformation on the change of fluid pressure can be written as:

For the matrix system:

$$\nabla \cdot \left(\frac{k_1}{\mu} \nabla p_1 \right) = b_{11} \frac{\partial p_1}{\partial t} + b_{12} \frac{\partial p_2}{\partial t} + b_{13} \frac{\partial(\nabla \cdot u)}{\partial t} - \Gamma \dots\dots\dots(7)$$

For the fracture system:

$$\nabla \cdot \left(\frac{k_2}{\mu} \nabla p_2 \right) = b_{21} \frac{\partial p_1}{\partial t} + b_{22} \frac{\partial p_2}{\partial t} + b_{23} \frac{\partial(\nabla \cdot u)}{\partial t} + \Gamma \dots\dots\dots(8)$$

where the coefficients are represented by:

$$\begin{aligned}
b_{11} &= \phi_I c_I + \phi_I c_{pI} (\beta_I - \alpha_I) & b_{12} &= \phi_I c_{pI} (\beta_2 - \alpha_2) \\
b_{13} &= \frac{\phi_I c_{pI}}{c_b} & b_{21} &= \phi_2 c_{p2} (\beta_I - \alpha_I) \\
b_{22} &= \phi_2 c_{p2} (\beta_2 - \alpha_2) & b_{23} &= \frac{\phi_2 c_{p2}}{c_b} \\
c_{pI} &= \frac{\alpha^* c_b^*}{\phi_I} & c_{p2} &= \frac{\phi_t}{\phi_2} (c_p - c_p^*) \\
c_p &= \frac{\alpha c_b}{\phi} & \alpha_I &= \frac{\alpha^* c_b^*}{c_b} \\
\alpha_2 &= \alpha - \frac{\alpha^* c_b^*}{c_b} & \alpha &= 1 - \frac{c_s}{c_b} \\
\beta &= 1 - \frac{c_s}{c_p} & \beta_I &= \frac{c_p^* \beta^*}{c_p} \\
\beta_2 &= \beta - \beta_I
\end{aligned}$$

In equations 1 through 6, ρ is the fluid density, ϕ_n is the effective porosity, ϕ_t is the total effective porosity, v_n is the fluid velocity vector, p_n is the fluid pressure, k_n is the permeability, μ is the viscosity, c_n is the fluid compressibility, t is time, b_{nm} is the porosity-compressibility coefficients, c_p is the pore compressibility, c_b is the bulk compressibility, c_s is the solid compressibility, β_n is the effective stress coefficient associated with the pore volumetric change, α is the effective stress coefficient associated with the bulk volumetric change, ∇ and $\nabla \cdot$ denote gradient and divergence, respectively. The interaction between the matrix and fracture systems is governed by interporosity flow between these media that occurs under pseudo-steady state conditions (Barenblatt *et al.*, 1960, Warren and Root, 1963):

$$\Gamma = \frac{\sigma}{\mu} k_I (P_I - P_2) \dots\dots\dots(9)$$

where Γ is the volumetric flow rate from the matrix to the fractures per unit of bulk volume. For dual-porosity/dual-permeability, both the fracture and matrix systems have the ability to transport fluid to the wellbore. Fluid may also be transferred from the matrix system to the fracture system. Therefore, the production or injection well must be added in equation 7 and 8. In the dual-porosity case, where the matrix permeability is small and only acts as a source term, the fluid flow is transferred only through the fractures to the wellbore. Therefore, the left-hand term of equation 7 is negligible compared to the right-hand term. Using this assumption, equation 7 reduces to

$$b_{11} \frac{\partial p_I}{\partial t} + b_{12} \frac{\partial p_2}{\partial t} + b_{13} \frac{\partial(\nabla \cdot u)}{\partial t} = \frac{\sigma}{\mu} k_I (P_I - P_2) \dots\dots\dots(10)$$

The above statement expresses that the matrix permeability is a function of both macroscopic and intrinsic properties. For example, when we refer to the dual-porosity case, setting macroscopic matrix permeability equal to zero, this formulation only implies that no fluid is produced at the wellbore via the matrix system. It does not imply that intrinsic matrix permeability in the interporosity flow is zero.

The parameter σ is a shape factor that reflects the geometry of the matrix block (Gilman and Kazemi, 1982). This parameter controls the flow between the fractures and matrix and is defined as

$$\sigma = 4\left(\frac{1}{L_x^2} + \frac{1}{L_y^2} + \frac{1}{L_z^2}\right) \dots\dots\dots(11)$$

where L_x , L_y , and L_z are the characteristic dimensions of the matrix blocks that correspond to fracture spacing in the x-, y- and z- direction respectively. This shape factor was derived from a finite-difference approximation of flow between fractures and matrix systems for a grid block shown in Fig. 3.3-1. Two-dimensional mass conservation is expressed as

$$\frac{\partial}{\partial x}\left(T_{i,j} \frac{\partial p}{\partial x}\right) + \frac{\partial}{\partial y}\left(T_{i,j} \frac{\partial p}{\partial y}\right) = \frac{\partial(\phi S)_{i,j}}{\partial t} \dots\dots\dots(12)$$

Assuming the length of the matrix block is much larger than the fracture width, $L_x \gg W_f$, thus the fracture width can be ignored. Then the discretization of finite difference equation of Fig. 3.3-1 would be

$$\begin{aligned} & \frac{1}{L_x} \left(T_{i+1/2,j} \frac{p_{f_{i+1,j}} - p_{ma_{i,j}}}{L_x/2} - T_{i-1/2,j} \frac{p_{ma_{i,j}} - p_{f_{i,j}}}{L_x/2} \right) + \\ & \frac{1}{L_y} \left(T_{i,j+1/2} \frac{p_{f_{i,j+1}} - p_{ma_{i,j}}}{L_y/2} - T_{i,j-1/2} \frac{p_{ma_{i,j}} - p_{f_{i,j}}}{L_y/2} \right) = \frac{(\phi S)_i^{n+1} - (\phi S)_i^n}{\Delta t} \dots\dots\dots(13) \end{aligned}$$

If fracture pressure and transmissibility changes between matrix block are negligible, then the mass conservation can be written as

$$4\left(\frac{1}{L_x^2} + \frac{1}{L_y^2}\right)(T)(p_{ma} - p_f) = \frac{(\phi S)_{i,j}^{n+1} - (\phi S)_{i,j}^n}{\Delta t} \dots\dots\dots(14)$$

Therefore, the left-hand side of equation 14 expresses the flow from matrix to fractures and the shape factor for one-dimensional flow is written as

$$\sigma = 4\left(\frac{1}{L_x^2} + \frac{1}{L_y^2}\right) \dots\dots\dots(15)$$

The other important parameter to emphasize is the representation of the production or injection well in a particular gridblock. The well is located in the center of the grid block and the grid block pressure, p_{ij} , is not the wellbore flowing pressure, p_{wf} . In addition, the grid block at the well location is not normally the well drainage-boundary pressure. Additional expressions are required to compute the p_{wf} and to calculate an equivalent radius from the block center. The wellbore flow rate can be represented in terms of pressure drop at the well as shown in equation 16 below:

$$q = J(p_{ij}^{n+1} - p_{wf}) \dots\dots\dots(16)$$

For pseudo-steady state flow into a wellbore, the productivity index (J) is defined by

$$J = \frac{7.08 \times 10^{-3} k_{eff} h}{\mu \ln\left(\frac{r_e}{r_w} - \frac{3}{4} + S\right)} \dots\dots\dots(17)$$

where k_{eff} is the effective permeability in md, h is the formation thickness, μ is the viscosity, r_e is the equivalent grid block radius, r_w is the wellbore radius, $-\pi/2$ is the value if J is based on grid block pressure and S is the skin factor.

For anisotropic permeabilities, effective permeability is defined as

$$k_{eff} = \sqrt{k_x \times k_y} \dots\dots\dots(18)$$

Assuming isotropic permeabilities, square grid blocks, single phase flow and a well at a center of interior block, Peaceman (1978) showed that the equivalent radius, r_e , is about

$$r_e = 0.2\Delta x \dots\dots\dots(19)$$

or, in the case of anisotropic permeabilities, the equivalent radius is defined as

$$r_e = \frac{0.28 \left(\sqrt{\frac{k_y}{k_x}} \Delta x^2 + \sqrt{\frac{k_x}{k_y}} \Delta y^2 \right)^{1/2}}{\left(\frac{k_y}{k_x} \right)^{1/4} + \left(\frac{k_x}{k_y} \right)^{1/4}} \dots\dots\dots(20)$$

Around the wellbore, two inner boundary conditions can be specified: constant wellbore flow rate and constant wellbore flowing pressure. When constant wellbore flow rate is specified, the wellbore flowing pressure is determined after the grid block pressure at the

well location is obtained. This grid block pressure is used to recalculate the p_{wf} from Eq. 13. When the wellbore flowing pressure other than rate is specified, the finite-difference equations must be modified. The rate is replaced by equation 13. This means that $J(p^{n+1})$ is added to the center coefficient while $J(p_{wf})$ is added to the right-hand side. After pressure changes converge from specified tolerance at each time step, Eq. 13 can be used to solve for the rate

3.3.2.2 Poroelastic Model

In the poroelastic model, the rock can be assumed to behave in a linear elastic fashion for the stress change and rock deformation induced within the reservoir. Furthermore, the rock mass is assumed to be isothermal and the governing equation comprises three parallel basic principles as in fluid flow modeling: stress equilibrium, strain-displacement and strain-stress pressure relations.

In the absence of body forces, the stress equilibrium equation is:

$$\sum_{j=1}^3 \frac{\partial \tau_{ij}}{\partial x_j} = 0 \quad \dots\dots\dots(21)$$

where τ_{ij} is the total stress on the medium, which can be expressed as

$$\tau_{ij} = \sigma_{ij} - (\alpha_1 p_1 + \alpha_2 p_2) \delta_{ij} \quad \dots\dots\dots(22)$$

where σ_{ij} is referred to as the effective stress acting on the solid skeleton, p is the fluid pressure, and α is the effective stress coefficient. The solution of the effective stress is in incremental form and after an elapsed time t can be expressed as

$$\sigma_{ij} = \sigma_{ij}^0 + \Delta \sigma_{ij} \quad \dots\dots\dots(23)$$

where σ_{ij}^0 is the initial effective stress and $\Delta \sigma_{ij}$ is the effective stress increment. Similar expressions apply for incremental forms of displacement, strain and pressure. The strain components are defined by the average displacement components as

$$\varepsilon_{ij} = \frac{1}{2} \left(\frac{\partial u_i}{\partial x_j} + \frac{\partial u_j}{\partial x_i} \right) \quad \dots\dots\dots(24)$$

where ε_{ij} is the strain of the solid skeleton. The increment of strain is assumed equal to the strain, since the initial strain can be negligible. The initial strain may be caused by such factors as temperature changes and shrinkage. u is defined as the incremental displacement vector. For isotropic porous material, the linear elastic of strain-stress-pressure equations takes the form

$$\sigma_{ij} = 2G\epsilon_{ij} + \frac{2G\nu}{1-2\nu}e\delta_{ij} - (\alpha_1 p_1 + \alpha_2 p_2)\delta_{ij} \dots\dots\dots(25)$$

where G is the shear modulus, ν is Poisson's ratio, e is volume strain of solid skeleton and δ_{ij} is Kronecker's delta ($\delta_{ij}=1$ for $i = j$, $\delta_{ij} = 0$ for $i \neq j$). The volume strain of solid skeleton, e , relates to the divergence of solid displacement as

$$e = \nabla \cdot u \dots\dots\dots(26)$$

Combining those three basic principles through equations 18, 21 and 22, the governing equation for solid displacement on the change of fluid pressure can be written as:

$$G\nabla^2 u_i + \frac{G}{1-2\nu} \frac{\partial(\nabla \cdot u)}{\partial x_i} = \alpha_1 \frac{\partial p_1}{\partial x_i} + \alpha_2 \frac{\partial p_2}{\partial x_i} \dots\dots\dots(27)$$

For the two dimensional case, equations 7, 8, and 27 are a set of a system of partial differential equations that lead to four equations in four unknowns, p_1, p_2, u_x , and u_y

So far, the governing equations used to describe fluid flow and poroelasticity in a fractured reservoir have been presented. Next, these equations are solved using the appropriate initial and boundary conditions.

3.3.2.3 Initial and Boundary Conditions

The initial conditions are implemented by assigning the value of both matrix and fracture pressures for the fluid flow model and stress or displacement for the poroelastic model to each grid block. At times greater than zero, boundary conditions for fluid flow and poroelastic models must be specified. There are two boundary conditions for the fluid flow model: inner and outer boundary conditions. The inner boundary is used to specify the boundary condition around the wellbore. The simulator allows for two conditions, either constant rate or constant bottomhole pressure. Outer boundary conditions reflect the far field boundary condition. Two outer boundary conditions are considered, Dirichlet-type and Neumann-type boundary conditions. The first boundary condition is applied for an infinite boundary condition or constant pore pressure at the boundary system. The second boundary condition is applied for a close outer boundary condition or zero flow-rate at the boundary system.

In addition, two outer boundary conditions also exist for the poroelastic model, Dirichlet-type and Neumann-type boundary conditions. The Dirichlet-type boundary condition refers to solid displacement at the boundary. Zero solid displacements are considered for non-deformable boundaries while the Neumann-type boundary refers to imposing normal stress at the boundary. A mixed boundary condition can be modeled in the

simulation in which the displacement components are prescribed over part of the boundary and the stress components over the rest of boundary.

3.3.3 Results and Discussions

Our purpose was twofold: (1) to develop a rigorous, robust dual porosity simulator incorporating effects of stress sensitivity in a fractured reservoir (2) to compare the simulator against commercial dual-porosity simulators.

In order to make a comparison between conventional dual-porosity and stress dual-porosity simulators, the correlation of permeability as the function of pore pressure was used. The correlation was obtained from the Humble waterflood simulation (Putra and Schechter, 1997) as seen in Fig. 3.3-2. Constant permeability-porosity and variable permeability-porosity were two cases used in both simulators. Constant permeability-porosity was used to verify the stress dual-porosity simulator while the variable permeability-porosity was used to verify the conventional dual-porosity simulator.

The discretization grid consisted of 25 blocks in the x-direction and 25 blocks in the y-direction with 100 ft length of each grid block. In order to simulate a closed system and non-deformable outer boundary conditions, the flow rate and the displacement were set equal to zero. The model parameters used here are presented in Table 1. The well was located in the middle of the model and produced with a constant flow rate of 100 bbl/d. The simulation was run using a time step of 10 days. Initial conditions are set to zero for both displacement and pore pressure.

The solid displacement distribution in the x-direction is shown in Fig. 3.3-3. The maximum displacement for the x-direction will be to the right-hand side and minimum displacement will be in the opposite direction. The direction of magnitude is different because the inner boundary condition for displacement is set to be zero.

Fracture pressure distribution at 10 days is shown in Fig. 3.3-4. Constant rate of 100 b/d was used as the inner boundary condition and the no-flow boundary condition is used for the outer boundary condition. At this time, pressure distribution in y-direction still acts as infinite acting reservoir, but pressure distribution in x-direction has reached boundary condition. This is because of different magnitude of permeability in x- and y-directions.

As mentioned earlier, once fluid production is initiated, pore-pressure starts to decrease causing deformation of the solid part, which, in turn, increases the effective stress as seen in Fig. 3.3-5. The maximum effective stress is observed to occur close to the wellbore and decreases as the distance from the wellbore increases. Thus, the maximum reduction of fracture permeability due to stress-sensitive permeability occurs near the wellbore and will disappear as distance from the wellbore increases as shown in Fig. 3.3-6 and 3.3-7. Once the pore pressure reaches the outer boundary system, the pore pressure at that boundary starts decreasing because zero flow-rate was set up in the boundary system.

Both simulators were used to predict the flow rate as a function of wellbore pressure with two cases; (1) constant permeability-porosity and (2) variable permeability-porosity. Several constant flow-rates from 300 bbl/d to 10 bbl/d were simulated at 10 days. The grid block pressure at the well location obtained at the various rates was used to back calculate the bottom hole pressure using Eq. (13). For the variable permeability-porosity case, a significant reduction in predicted flow rates is seen as wellbore pressure decreases in both simulators (Figs. 3.3-8 and 3.3-9). This is because in the stress and pressure-sensitive permeability, both simulators allow fracture permeability and porosity changes as pressure changes. Due to fracture permeability decreases, a high-pressure gradient has to be maintained at the well to sustain the same flow rate as the constant permeability case. This results in a lower bottomhole pressure.

An interesting result occurred when constant permeability-porosity was applied as shown in Fig. 3.3-10. Both simulators gave similar bottomhole pressures because stress transfer effect did not show any significant contributions. However, when variable permeability-porosity was used, bottomhole pressure from the conventional dual-porosity simulator deviated from the stress dual-porosity simulator after using a high constant flow-rate above 100 b/d. This deviation results from neglecting the stress transfer effect. If the stress transfer is neglected at high production rate, then the interpretation of stress sensitivity in natural fractured reservoirs can be erroneous.

3.3.4 Conclusions

Conclusions drawn based on the present study are summarized below:

1. A numerical model of solid deformation and stress-pressure dependent permeability in naturally fractured reservoirs has been developed.
2. The comparisons of constant and variable permeability-porosity performances between conventional and stress dual-porosity simulator were made.
3. The variable permeability-porosity shows a significant reduction in the production rate as compared to constant permeability-porosity.
4. Both conventional and stress dual-porosity simulators with constant permeability-porosity can be used to predict reservoir performance.
5. Conventional dual-porosity with variable permeability cannot be used for high production rates in naturally fractured reservoirs.
6. The stress transfer effect in naturally fractured reservoirs has been demonstrated to be important.

3.3.5 Nomenclature

b	=	porosity-compressibility coefficients, LT^2/M
c	=	compressibility, LT^2/M
e	=	volumetric strain, dimensionless
E	=	Young's modulus, M/LT^2

G	=	shear modulus, M/LT^2
h	=	formation thickness, L
J	=	productivity index, L^2T/M
k	=	permeability, L^2, md
L	=	characteristic dimension of matrix block, L
p	=	fluid pressure (positive for compression), M/LT^2
q	=	source/sink term, L^3/T
r	=	radius, L
S	=	skin factor, dimensionless
t	=	time, T
u	=	displacement, L
v	=	fluid velocity vector, L/T
V	=	volume, L^3
x,y,z	=	spatial coordinates, L
α	=	effective stress coefficient associated with the bulk volumetric change, dimensionless
β	=	effective stress coefficient associated with the pore volumetric change, dimensionless
δ_{ij}	=	Kronecker's delta ($\delta_{ij}=1$ for $i=j$, $\delta_{ij}=0$ for $i \neq j$)
ε	=	strain, dimensionless
ϕ	=	porosity, fraction
Γ	=	interporosity flow, $L^3/T/L^3$
μ	=	fluid viscosity, m/Lt
ν	=	Poisson's ratio, dimensionless
ρ	=	fluid density, M/L^3
σ	=	shape factor, L^{-2}
∇	=	gradient
$\nabla \cdot$	=	divergence

Subscripts

b	=	bulk
c	=	confining
eff	=	effective
f	=	fluid
ij	=	grid block location in i - and j -directions
n	=	index of primary and secondary pores
p	=	pore
s	=	solid
t	=	total
w	=	wellbore
1	=	primary pores
2	=	secondary pores

Superscripts

$*$	=	single porosity non-fractured system
0	=	initial condition

3.3.6 References

1. Bai, M., Elshworth, D., and Rogiers, J.C.: "Modeling of Naturally Fractured Reservoirs Using Deformation Dependent Flow Mechanism," *Int. J. Rock Mech. Min. Sci. & Geomech.* (1993), 1185-1191.
2. Barenblatt, G.I., Zehlto, Iu, P., and Kochina, I.N.: "Basic Concepts in Theory of Seepage of Homogeneous Liquids in Fissured Rocks (Strata)," *Priklad. Mat. Mekh.* (1960) 24 (5), 825-864.
3. Chen, H.-Y. and Teufel, L.W.: "Coupling Fluid Flow and Geomechanics in Dual-Porosity Modeling of Naturally Fractured Reservoirs," paper SPE 38884 presented at the 1997 SPE Annual Technical Conference and Exhibition, San Antonio, TX, Oct. 5-8.
4. Gilman, J.R. and Kazemi, H.: "Improvements in Simulation of Naturally Fractured Reservoirs," paper presented at the 6th 1982 SPE Symposium on Reservoir Simulation in New Orleans, LA, Jan. 31-Feb. 3.
5. Huyakorn, P.S. and Pinder, G.: *Computational Methods in Subsurface Flow*, Academic, San Diego, CA (1983) 229-288.
6. Kazemi, H. *et al.*: "Numerical Simulation of Water-Oil Flow in Naturally Fractured Reservoirs," *SPEJ*, December 1976, 317-26, *Trans., AIME*, 261.
7. Peaceman, D.W.: "Interpretation of Well-Block Pressures in Numerical Reservoir Simulation," *SPEJ*, June 1978, 183-94, *Trans., AIME*, 265.
8. Putra, E. and Schechter, D.S.: "Numerical Simulation of a Waterflood Pilot in the Naturally Fractured Spraberry Trend," Second Annual Technical Progress Report (DOE Contract No.: DE-FC22-95BC14942) (1997).
9. Unger, D.J. and Aifantis, E.C.: "Notes: Completeness of Solutions in Double Porosity Theory," *Acta Mechanica* 75, 269-274 (1988).
10. Warren, J.E. and Root, P.J.: "The Behavior of Naturally Fractured Reservoir," *SPEJ*. (Sept. 1963) 245-255; *Trans., AIME*, 228.

Table 3.3-1 Model Parameter Employed

Young's modulus, psi	10^6
Poisson ratio	0.2
Fluid viscosity, cp	10
Initial pore pressure, psi	0
Initial stress, psi	0
Thickness, ft	50
Flow rate, B/D	100
No. of grid block in x-direction, ft	25(100 ft each)
No. of grid block in y-direction, ft	25(100 ft each)
Matrix rock compressibility, psi^{-1}	10^{-8}
Matrix bulk compressibility, psi^{-1}	10^{-6}
Matrix fluid compressibility, psi^{-1}	10^{-5}
Fracture rock compressibility, psi^{-1}	10^{-8}
Fracture bulk compressibility, psi^{-1}	10^{-6}
Fracture fluid compressibility, psi^{-1}	10^{-5}
Matrix porosity, fraction	0.1 or $(0.1\exp(-0.0004*dp))$
Fracture porosity, fraction	0.01 or $(0.01\exp(-0.0004*dp))$
Matrix permeability, md	0.1 or $(0.1\exp(-0.0004*dp))$
Fracture Spacing, ft	5
Fracture permeability in x-dir, md	2.5 or $(2.5\exp(-0.0004*dp))$
Fracture permeability in y-dir, md	150 or $(150\exp(-0.0004*dp))$

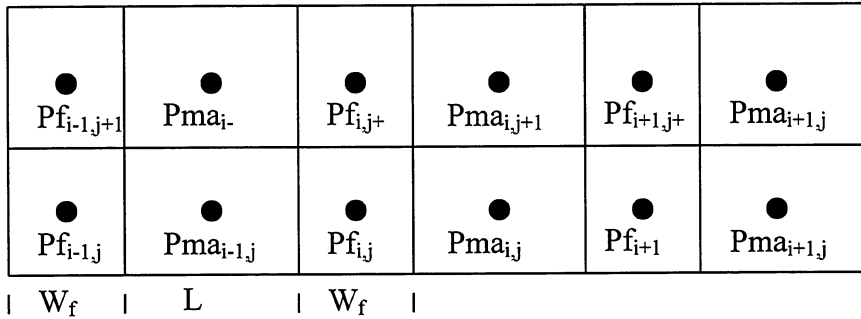


Fig. 3.3-1 Two-dimensional fracture-matrix idealization

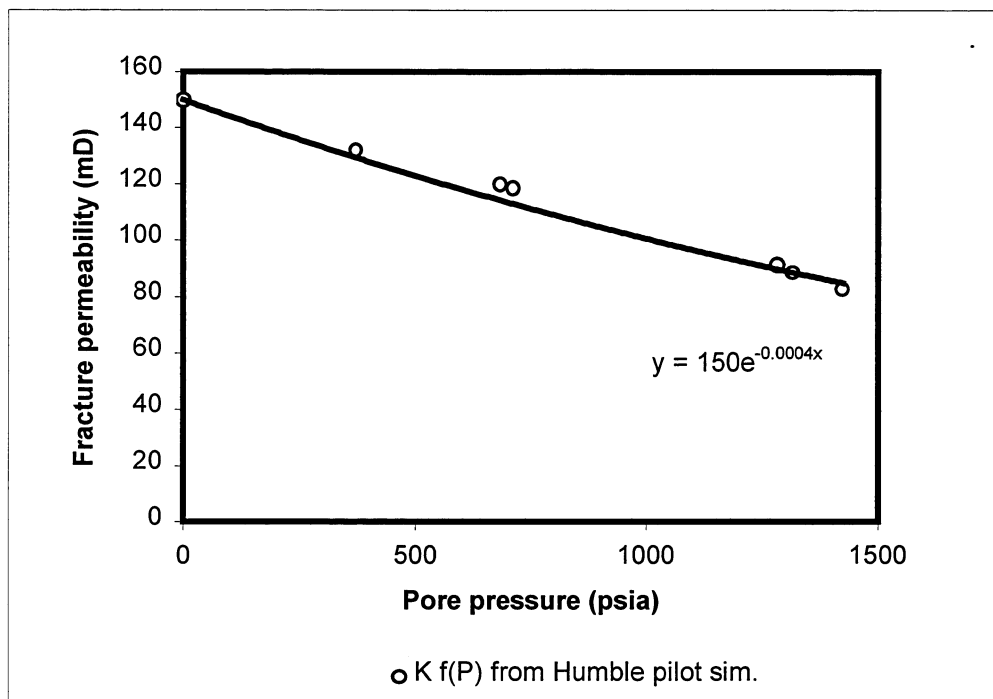


Fig. 3.3-2 Permeability reduction curve as function of pore pressure obtained from Humble pilot simulation.

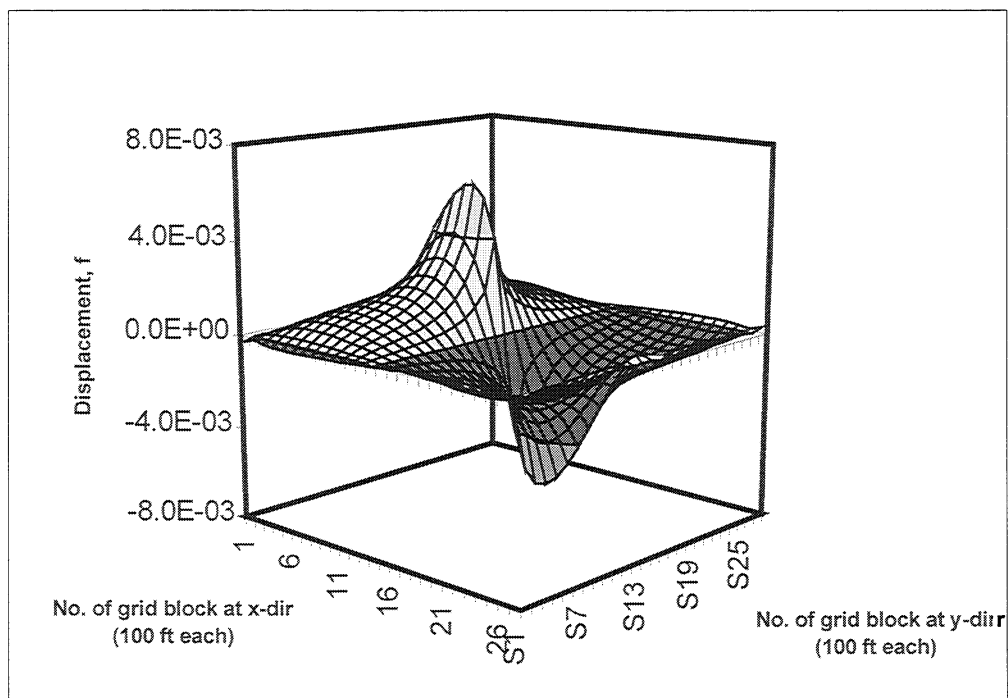


Fig. 3.3-3 Solid displacement distribution in x-direction at 20 days.

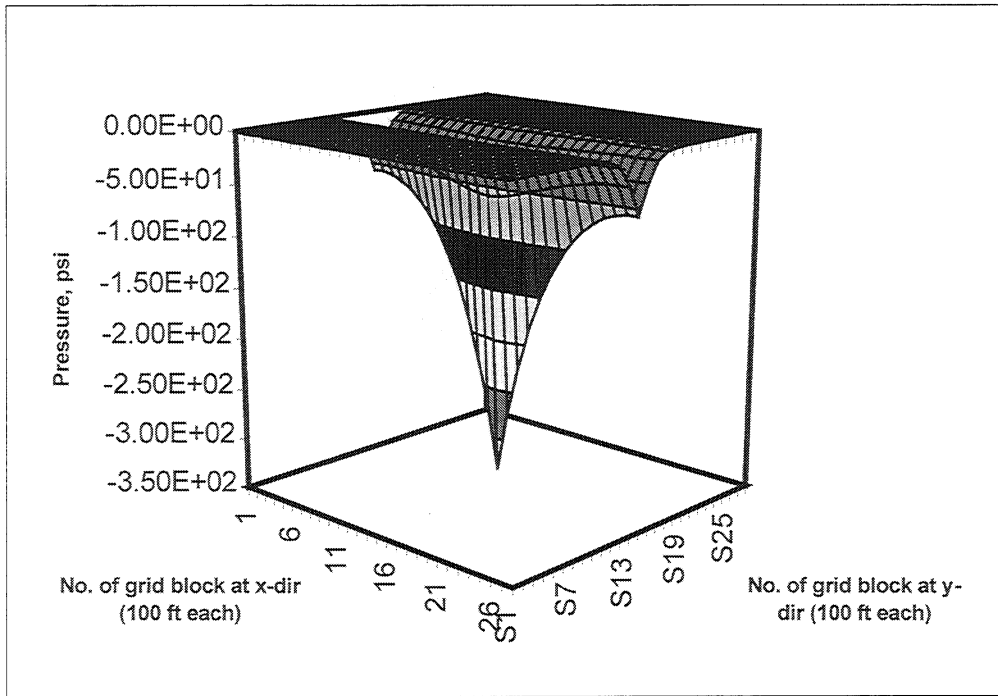


Fig. 3.3-4 Fracture pressure distribution at 20 days.

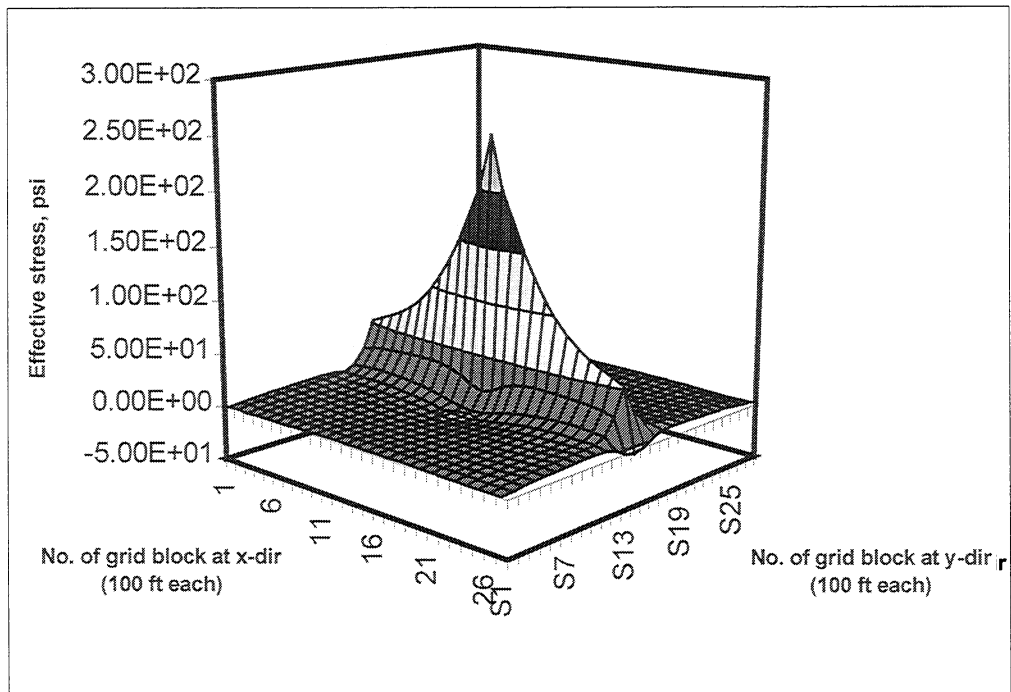


Fig. 3.3-5 Effective stress distribution in x-direction at 20 days.

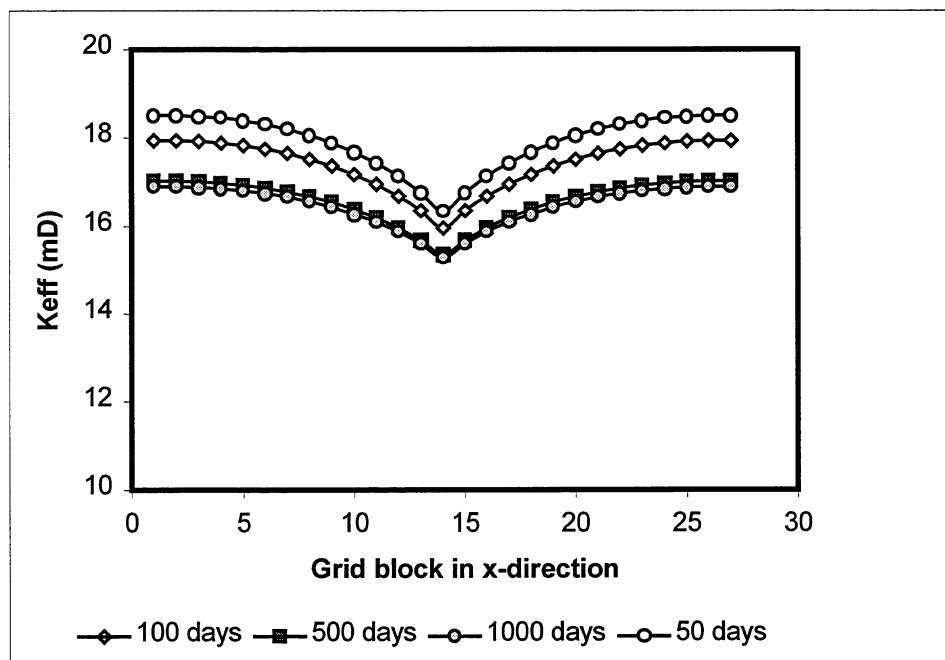


Fig. 3.3-6 Reduction of effective fracture permeability at the grid blocks in the x-direction intersect through the grid block containing the well.

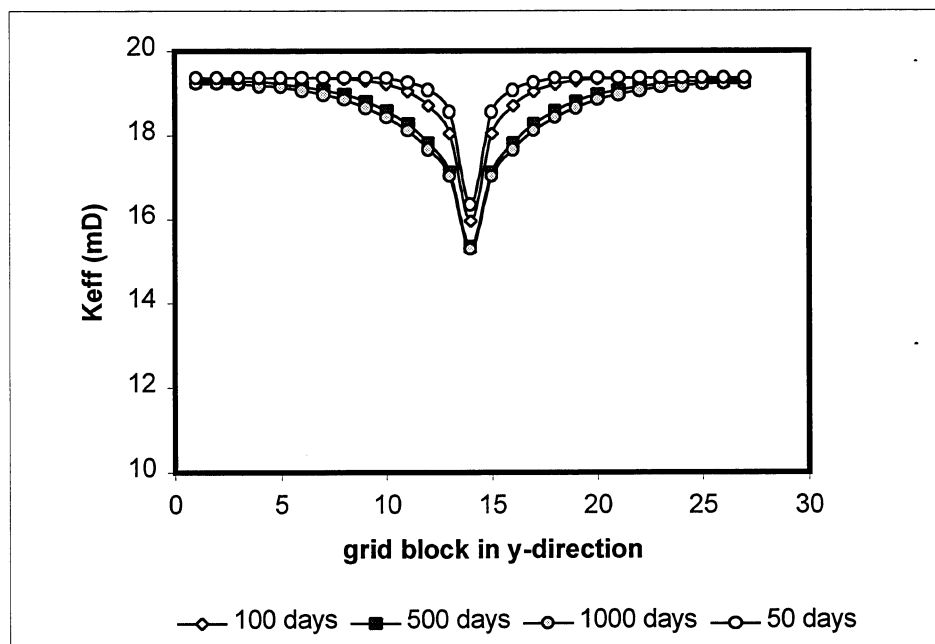


Fig. 3.3-7 Reduction of effective fracture permeability at the grid blocks in the y-direction intersect through the grid block containing the well.

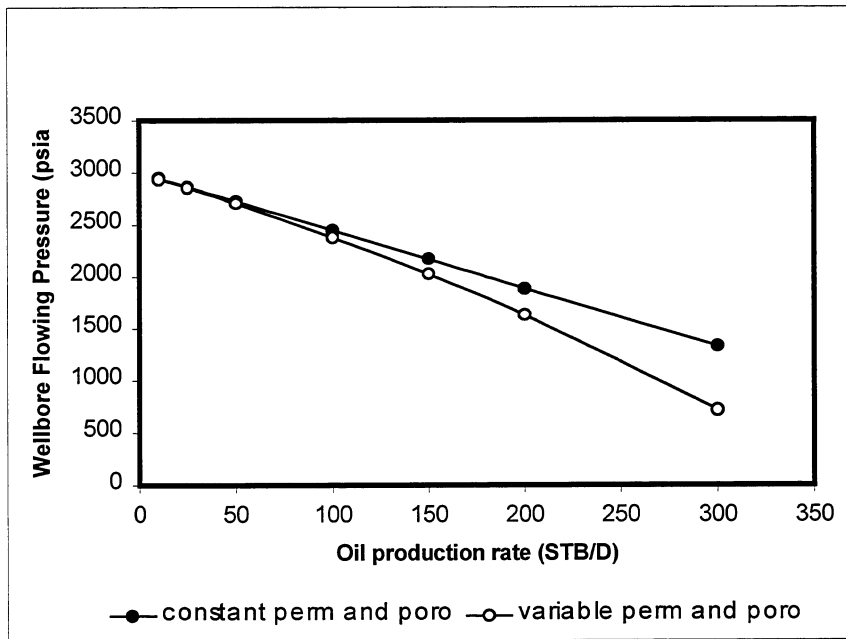


Fig. 3.3-8 Flow rate as a function of bottomhole pressure from the conventional dual-porosity simulator.

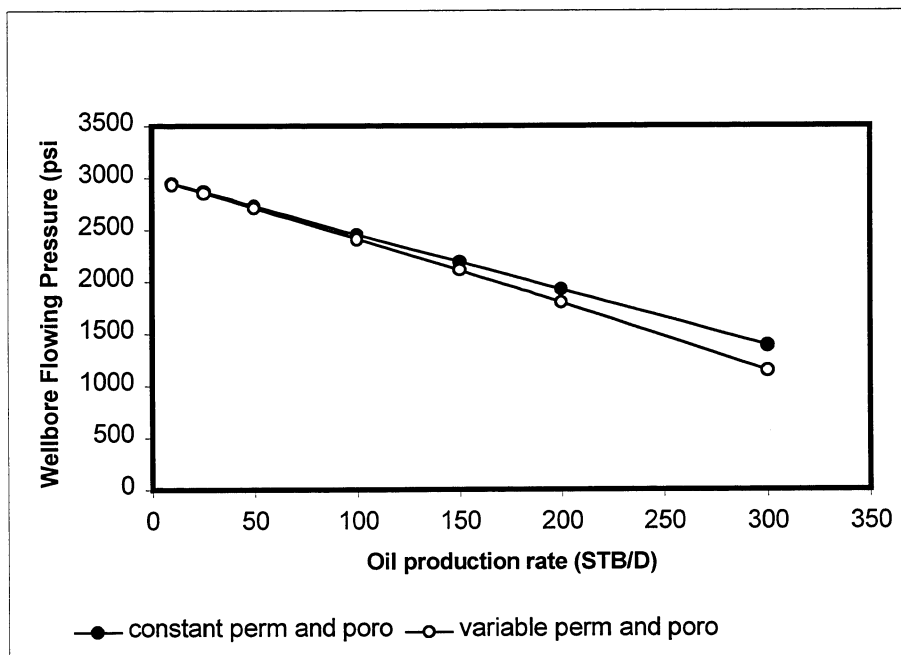


Fig. 3.3-9 Flow rate as a function of bottomhole pressure from the stress dual-porosity simulator.

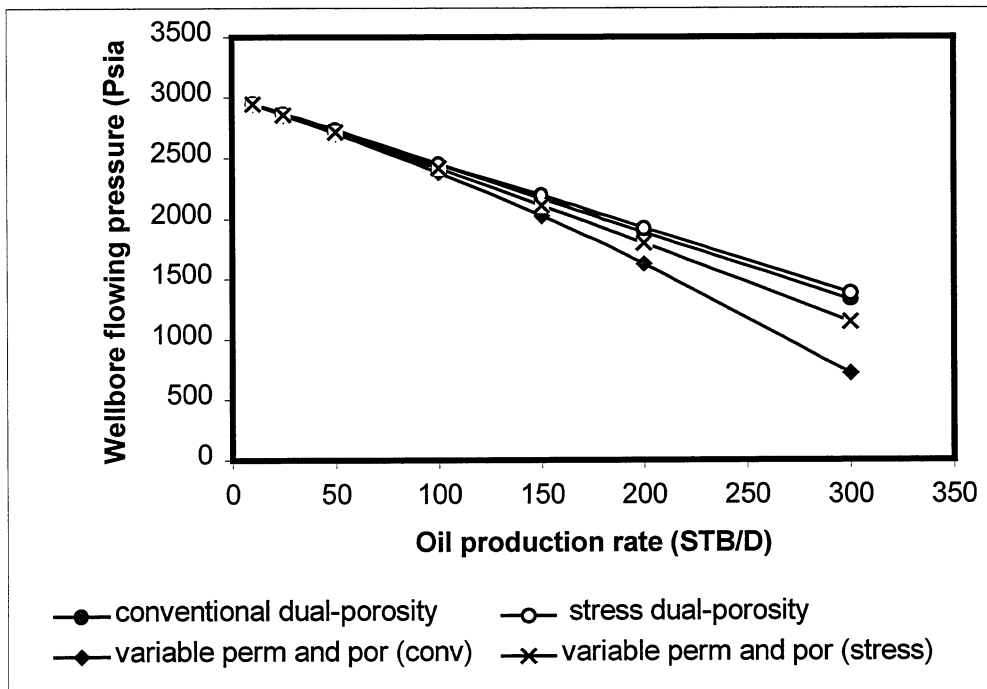


Fig. 3.3-10 Comparison of performance between conventional and stress dual-porosity simulators.

3.4 SIMULATED HORIZONTAL WELL PERFORMANCE IN THE NATURALLY FRACTURED SPRABERRY TREND AREA

During the first and second year of the project, efforts were made in numerical simulation of the Humble Waterflood Pilot was performed using commercial VIP and ECLIPSE simulators. A pilot model was developed using the three-phase, three-dimensional, dual porosity. A good quality of history match was achieved. This section presents the feasibility of using horizontal wells in this area using that pilot model. Several studies were performed to maximize the use of horizontal wells including:

- (1) The comparison of performance between horizontal and vertical wells with different average reservoir pressures.
- (2) The comparison of performance between horizontal and vertical wells with and without water injection.
- (3) The comparison of performance of using horizontal injection and vertical injection wells.
- (4) The comparison of performance of using constant and cyclic injection rates.

3.4.1 Introduction

As described in the first section of this report the Spraberry Trend area has a stratigraphy mainly composed of sandstone, shales, siltstone and limestone (Wilkinson, 1953, Warn and Sidwell, 1953, and Stanley, 1951). The mass of rock is divided into three distinct units: the Upper Spraberry, a sandy zone; the Middle Spraberry, a zone of shales and limestone; and the Lower Spraberry, a sandy zone.

The Upper Spraberry unit occurs at an average depth of 7000 ft with a gross thickness of approximately 220 ft. It is composed of six stacked units (1U-6U) (Guevara, 1988). The individual beds rarely exceed 15 ft in thickness. Reservoir characterization demonstrated that the productive oil sands in the Upper Spraberry are from two thin intervals, the 1U and 5U, respectively. The reservoir rocks in the 1U and low porosity and permeability characterize 5U. Extensive sets of interconnected vertical fractures allow oil recovery from this low permeability sandstone.

The purpose of this study is to investigate the benefit of using horizontal wells in the Spraberry Area through the application of horizontal well simulation scenarios conducted in the Humble waterflood pilot (Fig. 3.4-2). The reservoir model was developed and matched with the Humble pilot performance in the previous work by Putra, Kindem and Schechter (1996). After characterization and modeling the simulation from that pilot, several scenarios were conducted to:

- Evaluate the effects of different average reservoir pressures and the length of horizontal well sections on oil recovery.

- Compare the performance of vertical and horizontal production wells.
- Compare the performance of vertical and horizontal injection wells.
- Compare the performance of vertical and horizontal wells with and without water injection.
- Demonstrate innovative developmental and water injection methods for improving oil recovery from naturally fractured reservoirs.

These simulations require running a series of sensitivity simulations for each type of well completion, vertical and horizontal wells, and for each type of operation, natural depletion (primary recovery) and water injection (secondary recovery).

3.4.2 Horizontal Well Performance

Recent research on horizontal wells has focused increasingly on fractured reservoirs. One of the research objectives is to increase well productivity compared to that obtained with vertical wells. Due to its length, often much greater than a vertical well, a horizontal well can intercept many more fissures than a vertical well, thus obtaining higher productivity.

The basic reservoir model used in this study is identical to the Humble pilot model. The reservoir parameters for the simulation of the horizontal well in this study were obtained after history-matching the Humble waterflood pilot. The simulation scenarios were conducted to evaluate the effects of different average pressures with different lengths of horizontal well sections on oil recovery. The simulations were performed using a constant plateau rate of 100 BOPD, no water injection, and running with 500 psi BHP for 10 years. These simulations were by no means optimized, but to illustrate the potential benefits associated with horizontal wells in the Spraberry oil province. Since the average pressure is unknown, the average reservoir pressure was varied from 1000 psia to 1500 psia with different lengths of horizontal well sections. The simulation result is shown in Fig. 3.4-3.

The horizontal production well represents a significant improvement over the vertical production wells. The use of a horizontal production well could result in three to five times more cumulative oil production than use of a vertical production well. Thus, horizontal production wells could reduce the number of wells by a factor of two. In addition, the cost of a horizontal production well typically is only 1.2 to 1.5 times than that of a vertical production well (per foot drilled). The simulation results clearly indicate the benefit of using horizontal production wells in the Spraberry Trend Area.

The simulation result also suggested that maintaining or increasing the average reservoir pressure is critical. Increasing the average reservoir pressure by 250 psia would almost double the oil production rate. The pressure can be maintained or increased by injecting water perpendicular to the fracture direction (staggered line drive pattern). This pattern will also delay the water breakthrough in the producing wells.

3.4.3 The Effects of Water Injection on the Performance of Vertical and Horizontal Wells

Elkin (1963) found that overinjection might have been responsible for low recovery in the Spraberry area. He showed that the water breakthrough was characteristic of the Spraberry at the stage of depletion and at high water injection rates. Schechter *et al* (1996) also mentioned that after waterflooding was initiated in the Humble pilot test, water breakthrough occurred in most producing wells.

Several simulation cases were performed to test these hypotheses. As a base case, a vertical well with natural depletion was run followed by a case using injection wells. The water injection rate from each well varied from 100 to 1000 stbw/d. Simulations were run for 10 years with 500 psia BHP and 600 psia average reservoir pressure.

The size of the reservoir model was reduced to 40-acres compared to the 80-acre Humble pilot model, in order to accelerate the CPU running time. The grid dimension was 15 x 15 x 3 and the pattern was set up to be a staggered line drive pattern.

The effect of the vertical production well with and without the vertical injection well on the oil production rate is shown in Fig. 3.4-4. The initial oil rate of 12 bbls/day was produced with natural depletion and the average oil rate was only 8 bbls/day afterward. The water was injected 1000 stbw/d per well from four vertical injection wells. At about 1.5 years after initiation, the water started to sweep oil to the production well until the production rate peaked at 50 bopd. As water was produced, the oil rate decreased sharply to zero oil production rate by about eight years. The cumulative oil production for the injected case was approximately double that of the case without injection.

The effect of oil production using a horizontal production well with and without a vertical injection well is displayed in Fig. 3.4-5. The horizontal well section was set at a 500 ft length perpendicular to the fracture direction. Two cases were run, natural depletion (without injection wells) and waterflooding (with injection wells). In the natural depletion case, the use of a horizontal production well increased cumulative oil production four times over that predicted by the vertical production well. At the initial time, 75 bopd was produced, 6.25 times more than that produced by the vertical well. As in the case of a vertical production well, the production rate from the horizontal production well decreased as pressure decreased. However, the oil production rate declined much faster because of a higher-pressure drop than in the vertical well case.

In the waterflooding case using a horizontal well, four vertical injection wells were used. The water started sweeping oil after six months of injection and induced a production rate faster than vertical production well. This is because the horizontal production well had a larger drainage area. Production peaked at 100 bopd for about one year. The oil peak rate was also longer than that from a vertical production well because the horizontal production well sweeps the oil bank from the fracture more uniformly, causing a delay in water breakthrough. Using a horizontal production well with vertical injection wells could recover oil almost 30% over recovery obtained without injection wells.

In addition to setting the horizontal section perpendicular to the fracture direction, a case using a parallel to the fracture direction was also performed. However, the oil production rate was lower, recovering 25% less oil than in the case of the horizontal well with natural depletion (Fig. 3.4-5). The poor performance resulted because the horizontal production well did not intersect with the matrix rock, and therefore the pressure drop could not be maintained. The effect of water injection on oil rate was observed at the same time as for vertical production well because of similar distance to the vertical injection wells.

The simulation results from vertical and horizontal production wells with vertical injection wells show that it is crucial to optimize the water injection rate in order to delay water breakthrough in naturally fractured reservoirs. Two optimizations can be applied; either by reducing the injection rate or by using a cyclic waterflood. This study will be discussed later.

For the next scenarios, using horizontal injection wells compared the performances of vertical and horizontal production wells. Only two horizontal injection wells were opened. The horizontal injection wells were parallel to the fracture direction because the injection wells should push the oil from the matrix to the fractures (forced imbibition) and to the production well. Although the oil peak rates were lower in both vertical and horizontal production wells, the high production rates were maintained longer and the cumulative oil productions were higher than those obtained by using vertical injection wells (see Fig. 3.4-6). The response of water injection was delayed because both vertical and horizontal injection wells used the same water injection rate (1000 stbw/d).

Several simulations were conducted to optimize the water injection rate for both vertical and horizontal injection wells. The water injection rate for each injection well was varied from 100 stbw/d to 1000 stbw/d. The simulations were run until oil production no longer occurred and the cumulative production rate from each injection rate was recorded as shown in Figs. 3.4-7 and 3.4-8.

The constant injection rate simulation results show an optimum injection rate for each vertical injection well to produce the maximum cumulative oil production (235.751 MSTB). The horizontal production well is 200 stbw/d. Using 400-stbw/d injection rate for each horizontal injection well, the horizontal production well produced 221.048 MSTB cumulative oil production. Thus, the horizontal production well with the vertical injection well could produce 15 MSTB higher than that with horizontal injection wells. However, the injection rate from the vertical injection well was more sensitive than that from the horizontal injection well. For instance, when the high injection rate (above 500 stbw/d) was used, the cumulative oil production from the horizontal production well with horizontal injection wells was significantly higher than that with vertical injection wells.

This study has shown that using vertical injection wells with high injection rates (greater than 500 stbw/d per well) is not successful in the 40-acre Spraberry fractured reservoir.

Study results show that the optimum injection rate for a horizontal injection well is about twice that of a vertical injection well.

The difference between natural depletion and waterflooding performance, as previously discussed, led to the use of a cyclic operation. Since reservoir pressure declines rapidly due to production, water injection is required to restore the pressure and is followed by producing a well without any water injection.

This cyclic operation was performed to observe the effect on the oil production rate. Two cyclic schemes were conducted; the cyclic rate scheme of 2:2 and the cyclic rate scheme of 1:2. The cyclic rate scheme of 2:2 means two years producing without waterflood, followed by producing with a waterflood for the next two years. The results of the cyclic rate schemes were compared to constant injection rate results as shown on Figs. 3.4-7 and 3.4-8. The simulation results show that the cyclic rate scheme of 1:2 gave the highest cumulative production rate, followed by the cyclic rate scheme of 2:2 and the constant injection rate. This is because cessation of water injection permits capillary force to hold much of the water in the rock. During pressure reduction, capillary force aids in the expulsion of oil from the matrix into the fractures (A similar concept was also proposed by Elkins (1963)).

In addition, two of the four vertical injection wells were replaced with one horizontal injection well as shown in Fig. 3.4-9. The well patterns of model 2 did not show any significant improvement on oil production rate compared to model 1.

Figure 3.4-10 shows the comparison between the optimum rate from constant injection rates (250 STBW/D per well) and from the cyclic rate scheme of 1:2. The cyclic rate increased the oil production rate more than using the constant injection rate because the cyclic rate used a higher injection rate. Both schemes reached the same oil peak rate. However, the cyclic rate scheme of 1:2 produces slightly more (10 MSTB) than the constant injection rate.

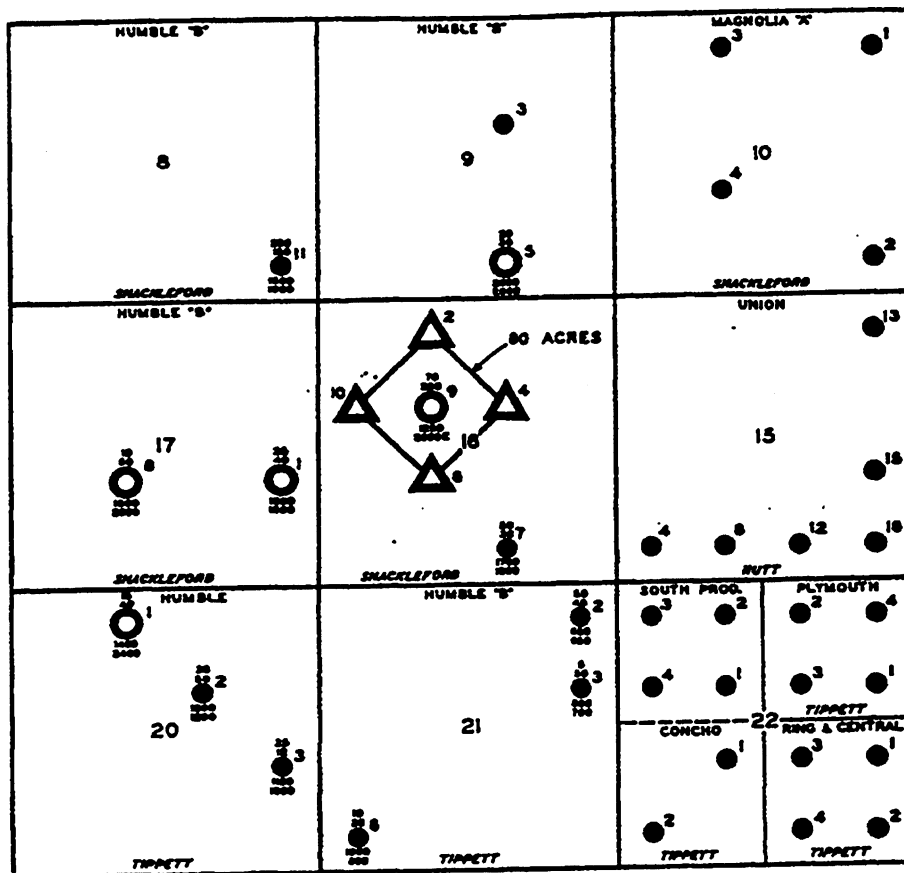
3.4.4 Conclusions

1. Use of horizontal production wells could increase cumulative oil production by three to five times compared to vertical production wells in the Spraberry formation.
2. Increasing the average reservoir pressure significantly increases the oil production rate.
3. A Horizontal production well surrounded by vertical injection wells could give higher cumulative oil production than that of horizontal injection wells if the injection rate can be optimized. However, the production rate with vertical injection wells is more sensitive than that of horizontal injection wells.
4. High water injection (greater than 500 STBW/D per well) is not successful in a 40-acre Spraberry fractured reservoir using vertical injection wells with a constant injection scheme.

5. Optimization of the injection rate is important prior to conducting waterflooding in naturally fractured reservoirs.
6. The optimum injection rate for horizontal injection wells is about twice that of vertical injection wells.
7. Use of a cyclic water flood with vertical injection wells could restore reservoir pressure and increase oil recovery in the Spraberry Trend Area.

3.4.5 References

1. Elkins, L.F.: "Cyclic Water Flooding the Spraberry Utilizes 'End Effect' to Increase Oil Production Rate," *JPT*, (May 1963).
2. Guevara, E.H.: "Geology Characterization of Permian Submarine Fan Reservoirs of the Driver Water flood Unit, Spraberry Trend, Midland Basin, Texas," Report of Investigations No. 172, Bureau of Economic Geology, The University of Texas at Austin (1988).
3. Putra, E., Kindem, E., and Schechter, D.: "Reservoir Simulation of a Water flood Pilot in the Naturally Fractured Spraberry Trend, "
4. Schechter, D.S., McDonald, P., Sheffield, T., Baker, R. "Reservoir Characterization and CO₂ Pilot Design in the Naturally Fractured Spraberry Trend Area," paper SPE presented at 1996 SPE Permian Basin Oil and Gas Recovery Conference, Midland, March 1996.
5. Stanley, T.B., et al.: "Geology Investigation of the Spraberry, Midland Basin, West Texas," Humble Oil & Refining Co.
6. Warn, G.W. and Sidwell, R.: "Petrology of The Spraberry Sands of West Texas," *J. of Sed. Pet.*, **23**, No. 2 (June 1953), 67-74.
7. Wilkinson, W.M.: "Fracturing in Spraberry Reservoir, West Texas," AAPG Bulletin, **37**, No.2, (Feb. 1953), 250-265.



HUMBLE WATER FLOOD TEST



WATER INJECTION WELL

INJECTED WATER IN PRODUCTION

- 25 PRODUCTION TEST WHEN WATER INJECTION STARTED - BOPD
- 40 PRODUCTION TEST FALL 1955 - SPRING 1956 - BOPD
- 1000 RESERVOIR PRESSURE WHEN WATER INJECTION STARTED - PSI
- 1500 RESERVOIR PRESSURE FALL 1955 - SPRING 1956 - PSI
(SONIC MEASUREMENTS)



Fig. 3.4-2 The Humble waterflood test showed that production of the center pilot well increased to over 250 bopd at the beginning of waterflooding

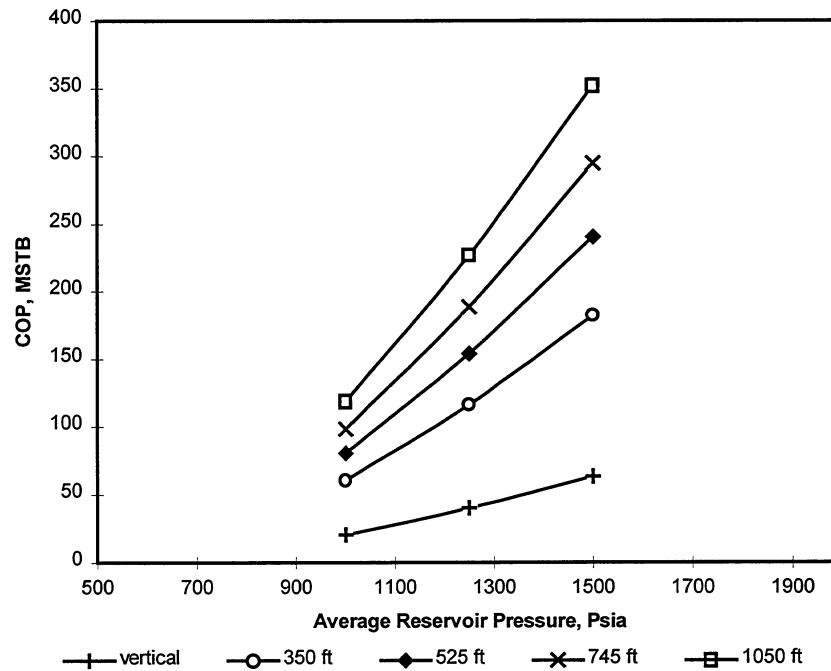


Fig. 3.4-3 Effect of average reservoir pressure on cumulative oil production (COP).

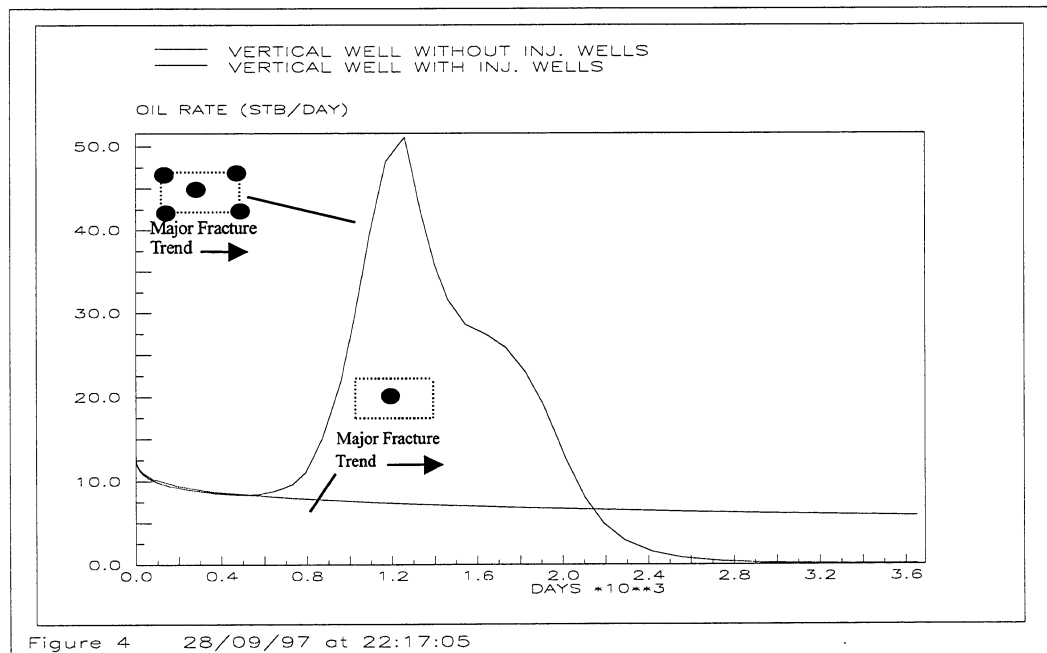


Fig. 3.4-4 The effect of a vertical production well on the oil production rate.

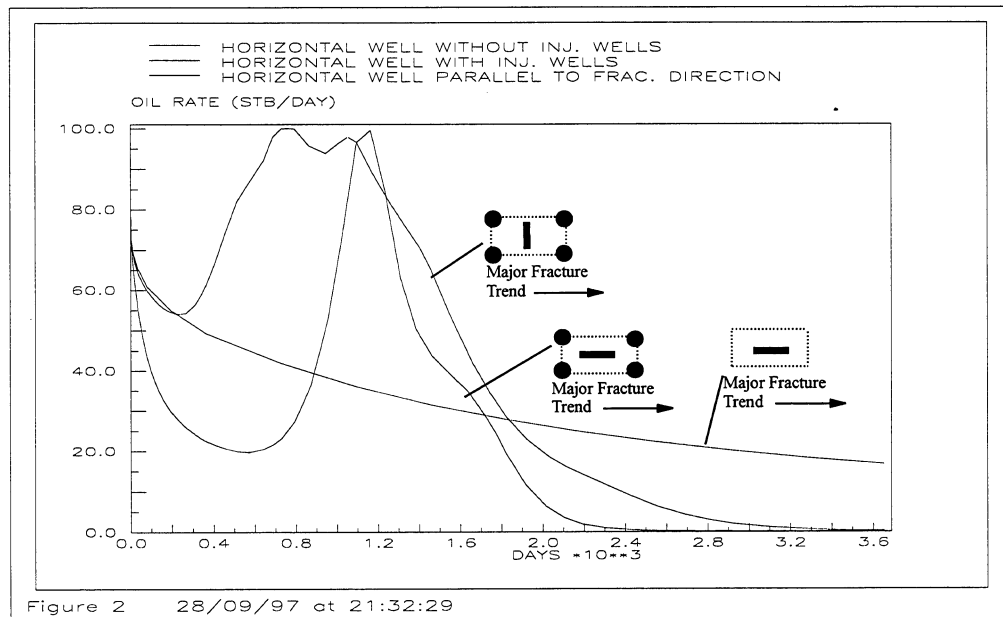


Fig. 3.4-5 The effect of a horizontal production well with vertical injection wells on the oil production rate.

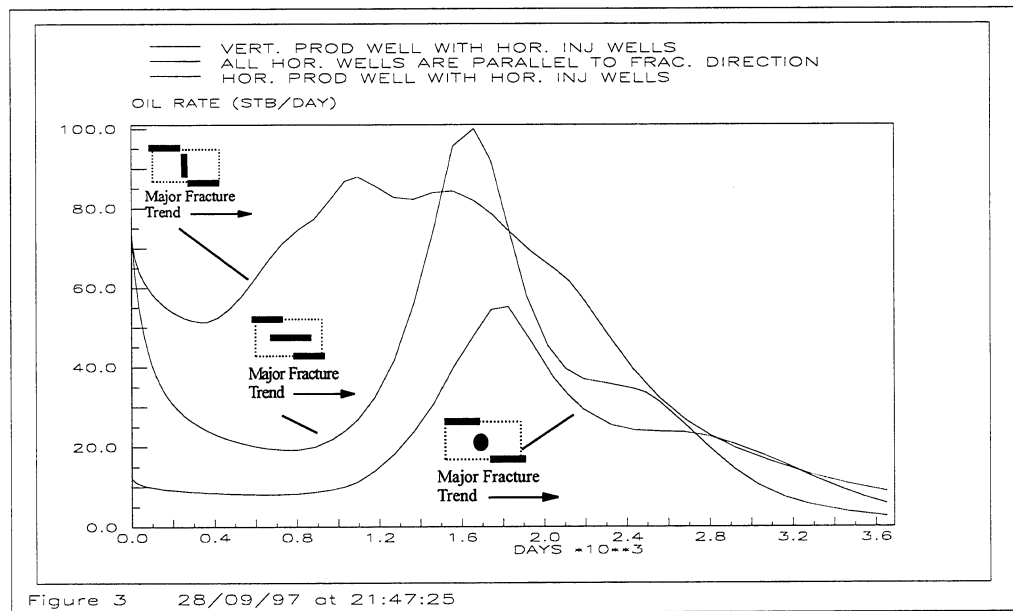


Fig. 3.4-6 The effect of vertical and horizontal production wells with horizontal injection wells on the oil production rate.

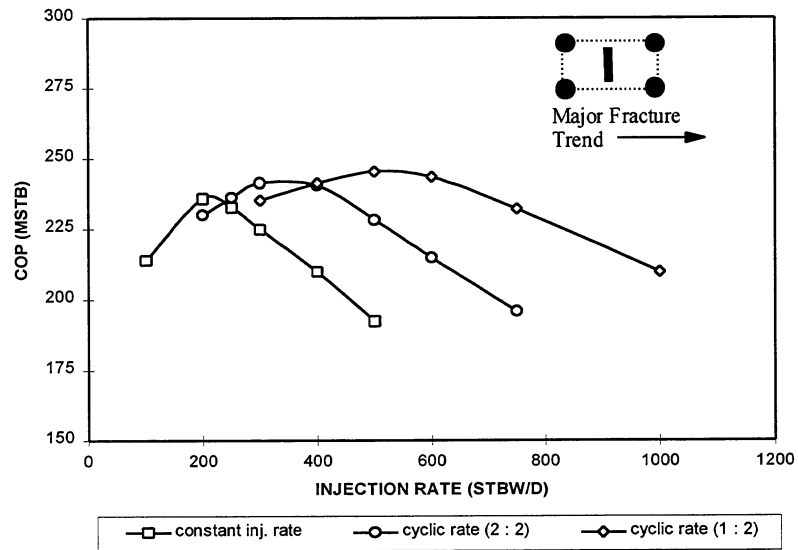


Fig. 3.4-7 The effect of a horizontal production well with vertical injection wells and different injection schemes on cumulative oil production.

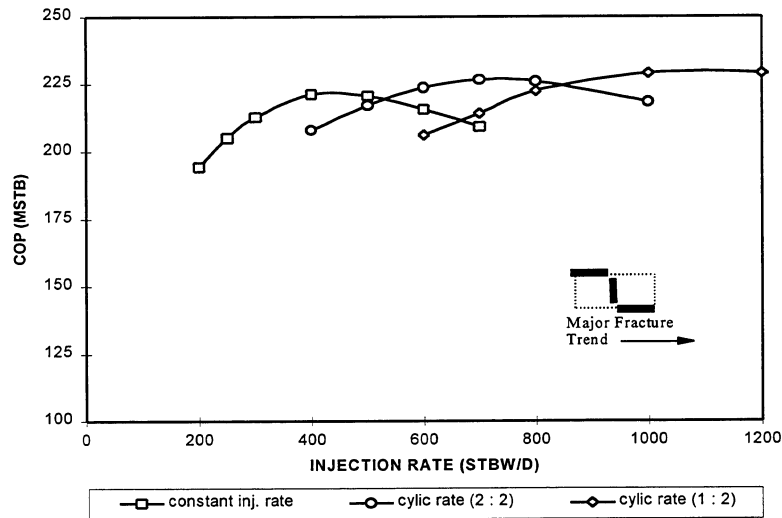


Fig. 3.4-8 The effect of a horizontal production well with horizontal injection wells and different injection schemes on cumulative oil production (note: the cumulative oil production is lower than that shown in the previous figure).

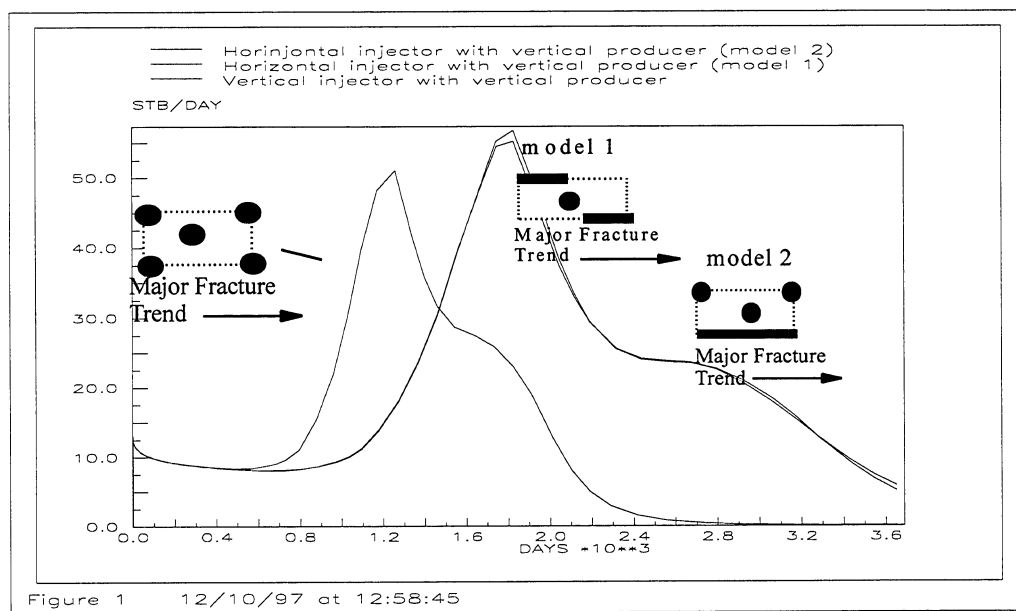


Fig. 3.4-9 The effect of a vertical production well with vertical and horizontal injection wells.

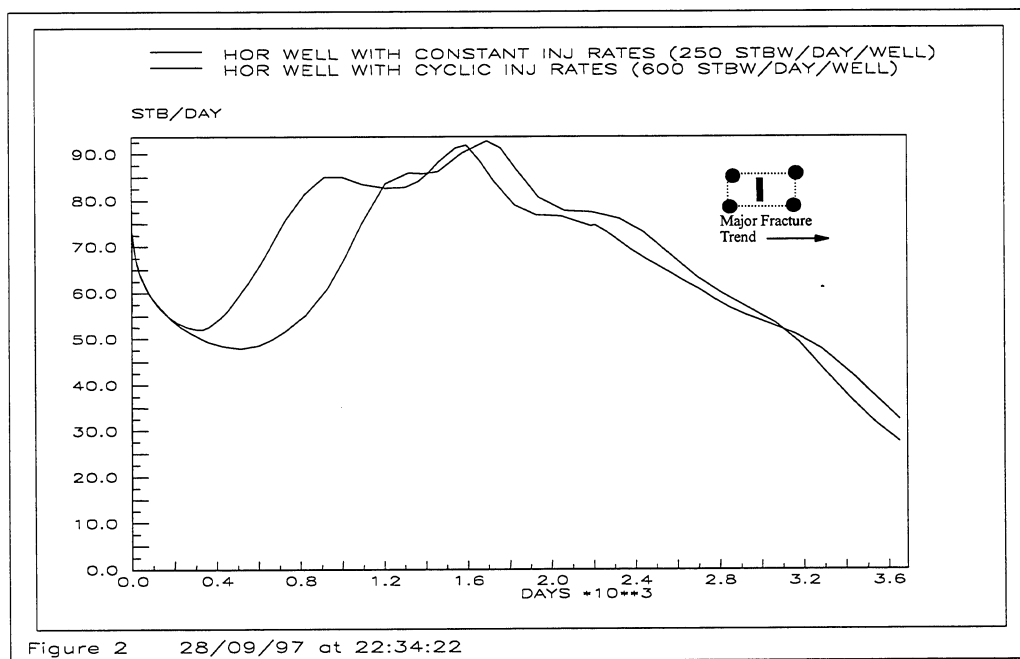


Fig. 3.4-10 The effect of a cyclic rate of 1:2 and a constant injection rate on the oil production rate

4 INVESTIGATION OF RECOVERY MECHANISMS BY CO₂ INJECTION IN FRACTURES SYSTEM

4.1 ANALYSIS OF CO₂ GRAVITY DRAINAGE

4.1.1 Introduction

During the first and second year of this project, four CO₂ gravity drainage experiments were performed using a 500 md Berea core, a 50 md Berea core, a 0.01 md reservoir core, and a 0.38 md reservoir core from the Spraberry Trend Area. Experimental details were presented in the First and Second Annual Technical Progress Report (Schechter, 1996; Schechter, 1997). Oil recovery curves are presented in Fig. 4.1-1. The effectiveness of the CO₂ gravity drainage decreases with decreasing rock permeability and increasing water saturation.

There exists an argument that matrix blocks in naturally fractured reservoirs may not be vertically continuous due to possible horizontal fractures or thin shale partings in the pay zone; and, that this matrix discontinuity may affect gravity drainage efficiency (Suffridge, 1991; Luan, 1994). To address this issue, we conducted an experiment using a stack of whole cores simulating vertically discontinuous matrix blocks during the first quarter of the third year. The core stack has an average permeability of 0.05 md and porosity of 10.7%. A water saturation of 37.6% was achieved before CO₂ gravity drainage was initiated. The results of the experiment indicate that core discontinuity did not significantly affect the efficiency of CO₂ gravity drainage, which is consistent with other investigations (Horle, 1990; Thomas, 1991; Conway, et al, 1996).

In order to optimize the CO₂ pilot design in the E.T. O'Daniel Unit of the Spraberry Trend Area, we have scaled up our experimental results from core to field scale. The scaling uses our mathematical model presented in the First Annual Technical Progress Report (Schechter, 1996). The results indicate that depending on matrix permeability, water saturation and fracture intensity, a significant amount of oil can be recovered from the pilot area by CO₂ flooding in a relatively short time period. Assuming a matrix air permeability of 0.9 md, water saturation of 0.45 and fracture spacing of 1.6 ft in the pilot area, the scaling model predicts incremental oil recovery of 10% within 2 years.

4.1.2 Laboratory Stacked Core Experiment

Core Sample. The 2.5 in. whole cores were taken from the 1U Unit of the Upper Spraberry in the horizontal E.T. O'Daniel #28. The first core is core No. 132 taken from depth 7667 to 7668 ft. The second core is core No. 142 taken from depth 7677 to 7678 ft.

The cores were cleaned. Lengths of the first and the second core are 9.750 in. and 9.875 in., respectively. The diameters of the first and the second core are 2.57 in. (6.53 cm) and 2.59 in., respectively. The porosities of the two cores are reported as 0.109 and 0.097, respectively. Their air permeabilities are 0.16 md and 0.13 md, respectively.

Brine. Synthetic Spraberry brine was used in the experiment. Density and viscosity of the brine is 1.08 g/cc and 1.18 cp under room temperature (80°F) and ambient pressure (12.6 psi), respectively.

Oil. Spraberry dead oil was used in the experiment. The composition of the oil was obtained from GC analysis. The average molecular weight of the dead oil is 342.80. Separator oil samples were tested at 100°F and 1000 psig. The density is 0.8329 g/cc and the viscosity is 2.956 cp. The minimum miscibility pressure (MMP) of the oil was measured at 1550 psig using slim tube at the reservoir temperature of 138°F. Details were presented in the First Annual Technical Progress Report (Schechter, 1996).

Procedure. The experimental procedure is schematically illustrated in Fig. 4.1-2. The unclamped core sections were placed in series and sealed in a core holder with 2,150 psig confining pressure (Fig. 4.1-2a). Brine was then injected into the cores. After brine saturation, average porosity and permeability to brine were determined to be 0.107 and 0.05 md respectively. Spraberry oil was then injected into the cores (Fig. 4.1-2b) for establishing an initial water saturation. After establishment of the initial water and oil saturations, brine was injected into the core again to reduce the oil saturation in the core (Fig. 4.1-2c). The purpose of the second water injection was to simulate increasing water saturation as waterflooding proceeds. Water injection was terminated when a water saturation of 37.7% was achieved in the core. The two core sections were then taken out from the core holder and clamped into one stack. Finally, the brine/oil-saturated core stack was placed vertically in a drainage cell and CO₂ was introduced into the drainage cell (Fig. 4.1-2.d). Cell pressure was maintained between 1,900 psia and 2,000 psia. The cell temperature was 138°F. Oil volumes recovered during the experiment were collected and recorded.

Results. Both brine and oil have been produced from the core stack. The produced oil is yellow in color. The experimental results are presented in Fig. 4.1-3. From the data shown in Fig. 4.1-3 water saturation dropped from 0.376 to 0.304, and the oil recovery reached 18.33% OOIP. The average molecular weights of the oil samples produced from the cores are listed in Table 4.1-2 .

4.1.3 Comparison and Discussion

Fig. 4.1-4 displays all of the CO₂ experiments for comparison. Excluding the Berea high permeability water-wet cores from discussion, a comparison and analysis of the continuous reservoir cores and stacked core is emphasized at this time.

From Fig. 4.1-4 the 0.38 md continuous core has a lower rate than the 0.01 md reservoir core. As stated earlier, this could be a result of the higher water saturation in the 0.38 md core. The water saturation distribution is unknown in both cores and could be more beneficial in the lower permeability cores. A possible explanation is that a higher water saturation could cause water shielding effects causing a slower response time for the more permeable core.

The previous annual report (Schechter, 1996) reported higher water production rates initially until a water saturation of approximately 0.39 was reached. Free water production was suggested as having relative permeability effects within the core. However, all of the cores tested had initial water production resulting in lower water saturations. The stacked core of 0.05 md has a slightly faster response than the 0.38 md core. Again this could be related to the water saturation distribution and/or a water shielding effect. However, the slightly faster response could be due to an effect of the horizontal fracture. The 0.05 md stacked reservoir core has a slower response time than the 0.01 md reservoir core with approximately the same water saturation. Again, water is produced resulting in a lower final water saturation.

4.1.4 Scaling of the Experimental Results

The overall goal of this project is to assess the economic feasibility of CO₂ flooding the naturally fractured Spraberry Trend Area in West Texas. This objective will be eventually accomplished by field demonstration in the 10 acre E.T. O'Daniel pilot. However, designing the CO₂ injection in the E.T. O'Daniel pilot area requires predictions of oil production rate, cumulative oil production, and oil recovery in the pilot area. The results of our CO₂ gravity drainage experiments make such predictions possible. The experimental data have been scaled up to the pilot dimensions using our newly developed mathematical model (Schechter and Guo, 1996) to forecast production performance in the pilot area.

The E.T. O'Daniel CO₂ pilot involves six water injection wells, three CO₂ injection wells (one of them may be a horizontal well), three oil production wells, and three log-observation wells. The well location (not to scale) is shown in Fig. 5. The area to be swept by CO₂ between the CO₂ injection wells and oil production wells is 1,500 ft long and 300 ft wide, comprising 10.33 acres. The current oil reserve in this area is estimated to be about 38,500 STB. Reservoir parameters used in the reserve calculations are

summarized in Table 4.1-3. The values for water and gas saturations under the current reservoir conditions are estimated based on Elkins' report (Elkins, 1996).

Assuming water saturation $S_w = 0.45$, fracture spacing 1.6 ft, and average matrix permeability 0.9 md, oil recovery, oil production rate, and cumulative oil production from the pilot are predicted and demonstrated in Fig. 4.1-6–Fig. 4.1-8, respectively. From these figures the predicted oil recovery factor is about 0.10 IOIP (oil in place at the beginning of CO₂ injection). Oil production rate will drop from 19 STB/D to 12 STB/D in two years, and cumulative oil production will reach 4,000 STB after two years of production. Obviously, the degree of heterogeneity in the fractures and matrix will determine the economics of CO₂ flooding in Spraberry. The pilot test will determine this information.

4.1.5 Current CO₂ Gravity Drainage Laboratory Experiments

Currently, we are expanding and conducting a new CO₂ gravity drainage experiment on a Spraberry core. The goal of this experiment is to investigate the effects of water imbibition followed by CO₂ gravity drainage on oil recovery under reservoir conditions.

Core Sample. The core was taken from Spraberry and is 21.75 in. (55.25 cm) in length and 3.235 in. (8.22 cm) in diameter. The bulk volume is 2929.53 cm³. The core was cleaned with chloroform, methanol and toluene injections. After the core sample was cleaned, it was dried in a temperature of 138°F for 10 days.

Brine. Synthetic Spraberry brine is used in this experiment. Density and viscosity of the brine is 1.08 g/cc and 1.18 cp under room temperature (80°F) and ambient pressure (12.6 psi), respectively.

Oil. Spraberry dead oil is used in this experiment.

Procedure. The experimental procedure is schematically illustrated in Fig. 4.1-9. The core was placed in a Hassler core holder and saturated with brine at room temperature and then at 138°F. The pore volume determined with brine was 374.0 cm³ and the porosity is 12.76%. The brine permeability was 0.259 md. Spraberry dead oil was then injected into the core at a low rate (5 cm³ per hour) at 138°F and ambient pressure. The oil saturation is 75.27% and the brine saturation, S_{wi} , is accordingly 24.73%. The core was aged for approximately 61 days. However, the core was resaturated with oil during this time to induce a final saturation of S_{oi} of 80.93% and S_{wi} of 19.07%. Prior to setup for the imbibition experiment the pressure was released to ambient and 43 cm³ oil and 8640 cm³ of gas was produced. This gives a final core oil volume of 259.6 cm³ and an oil saturation, S_{oi} , of 69.41%. Normally gas saturation is ignored and the remaining saturation is assumed to be water of 30.59%.

4.1.6 Summary

Our previous four experiments on CO₂ gravity drainage using continuous Berea and Spraberry reservoir cores indicate that rock permeability and water saturation are two major factors affecting the efficiency of oil recovery during CO₂ injection into naturally fractured systems. The results of the experiment using discontinuous Spraberry cores confirm the previous experimental results and indicate that horizontal core discontinuity may not be significant factor affecting the CO₂ gravity drainage process. However, results are inconclusive as to what degree.

Scaling of data from the CO₂ gravity drainage experiments to field pilot dimension predicts that in two years of CO₂ injection, oil recovery factor will be about 0.10 IOIP. Oil production rate will drop from 19 STB/D to 12 STB/D, and cumulative oil production will reach 4,000 STB from the 10.33 acres of area to be flooded after two years of production.

4.1.7 References

1. Conway, P.I., Damm, M., and Andersen, P.M.: "Full Field Dual Porosity Modeling of a Complex Fractured Chalk Oil Reservoir Subject to both Gas and Water Injection," paper SPE 36931 presented at the 1996 SPE European Petroleum Conference held in Milan, Italy, October 22-24
2. Elkins, L.: "Condensed Report: Spraberry CO₂-Gravity Drainage Telephone Conference Call," May 14, 1996.
3. Luan, Z.: "Some Theoretical Aspects of Gravity Drainage in Naturally Fractured Reservoirs," paper SPE 28641 presented at the 1994 Annual Technical Conference and Exhibition of SPE, New Orleans, September 25-28.
4. Horle, T.: "Laboratory Studies of Capillary Continuity in Fracture/Matrix Systems," *SPERE* (August 1990).
5. Schechter, D.S.: "Advanced Reservoir Characterization and Evaluation of CO₂ Gravity Drainage in the Naturally Fractured Spraberry Trend Area," First Annual Technical Progress Report, Contract No. DE-FC22-95BC14942, U.S. DOE, (Dec 1996).
6. Schechter, D.S.: "Advanced Reservoir Characterization and Evaluation of CO₂ Gravity Drainage in the Naturally Fractured Spraberry Trend Area," Second Annual Technical Progress Report, Contract No. DE-FC22-95BC14942, U.S. DOE, (Dec 1997).
7. Schechter, D.S. and Guo, B.: "Mathematical Modeling of Gravity Drainage After Gas Injection into Fractured Reservoirs," paper SPE 35170 presented at the 1996 SPE Improved Oil Recovery Symposium Tulsa, April 22-24, 1996.
8. Suffridge, E.E. and Renner, T.A.: "Diffusion and Gravity Drainage Tests to Support the Development of a Dual Porosity Simulator," paper presented at the 6th European IOR-Symposium, held May 21-23, 1991 in Stavanger, Norway.
9. Thomas, L.K.: "Ekofisk Nitrogen Injection," *SPFE* (June 1991).

Table 4.1-1 Physical Properties of Core Samples Used in the Experiments

Core No.	1	2	3	4	5
Core Type	Berea	Berea	Spraberry	Spraberry	Spraberry
Configuration	continuous	continuous	continuous	continuous	Stacked
Porosity, %	18.7	13	10	11.1	10.7
Permeability, md	500	50	0.01	0.38	0.057
Water Saturation, % PV	35	29.3	38.6	45	37.6
OOIP (cc)	544.5	411.1	273.8	209.3	111.0
OWIP (CC)	293.2	171.2	172.1	171.3	67
Length (cm)	55.52	55.25	55	55.245	24.77&25.08
Diameter (cm)	10.16	10.16	10.16	8.89	6.5278&6.57866.35
Oil recovery, %	42	54	30.8	24	19.1
Time of Exp. (days)	6	220	190	167	331
Vp					178

Table 4.1-2 Average Molecular Weights of the Oil Samples Produced

Oil Sample No.	Period of Sample Produced, Day	Average Molecular Weight
1	0-9	253.94
2	10-23	282.96
3	23-38	291.98
4	39-63	294.02
5	64-77	318.05
6	78-100	319.90
7	101-125	334.31
8	126-174	351.38
9	175-231	386.48
10	232-331	394.83
Dead Oil		342.8

Table 4.1-3 Calculations of Current Oil Reserves in the Area to be Swept by CO₂ in the E.T. O'Daniel CO₂ Pilot

Area to Be Swept by CO ₂	10.33 acres
Net Pay	20 ft
Bulk Volume	9x10 ⁶ ft ³
Porosity	0.1
Pore Volume	9x10 ⁴ ft ³
Water Saturation	0.45
Gas Saturation	0.25
Oil Saturation	0.30
Oil Formation Volume Factor	1.25 rb/STB
Current Oil In Place (COIP)	38,500 STB

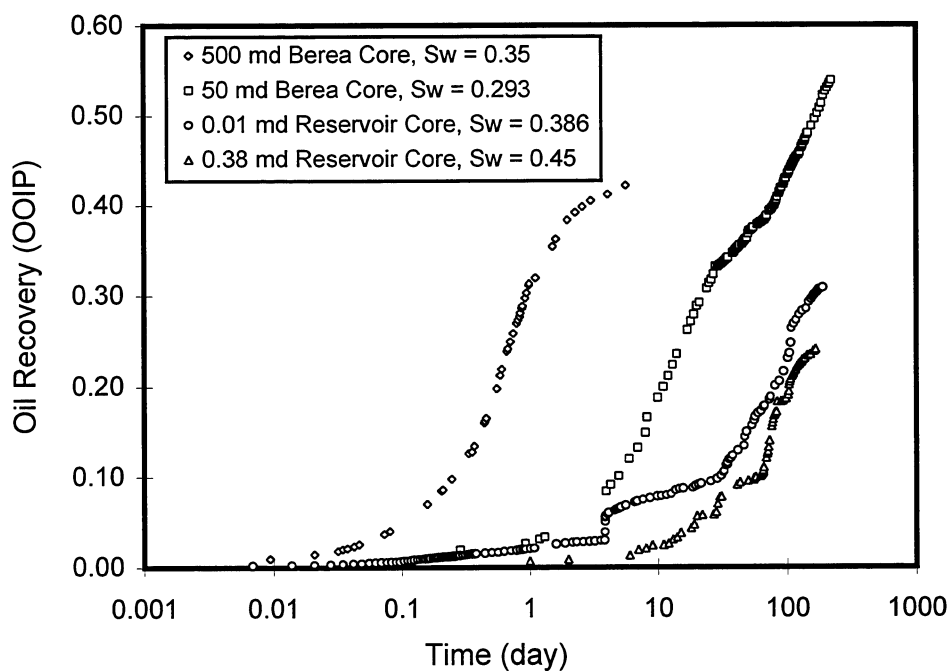


Fig. 4.1-1 Oil recovery curves obtained from four CO₂ injection experiments using continuous cores with different permeabilities and water saturations.

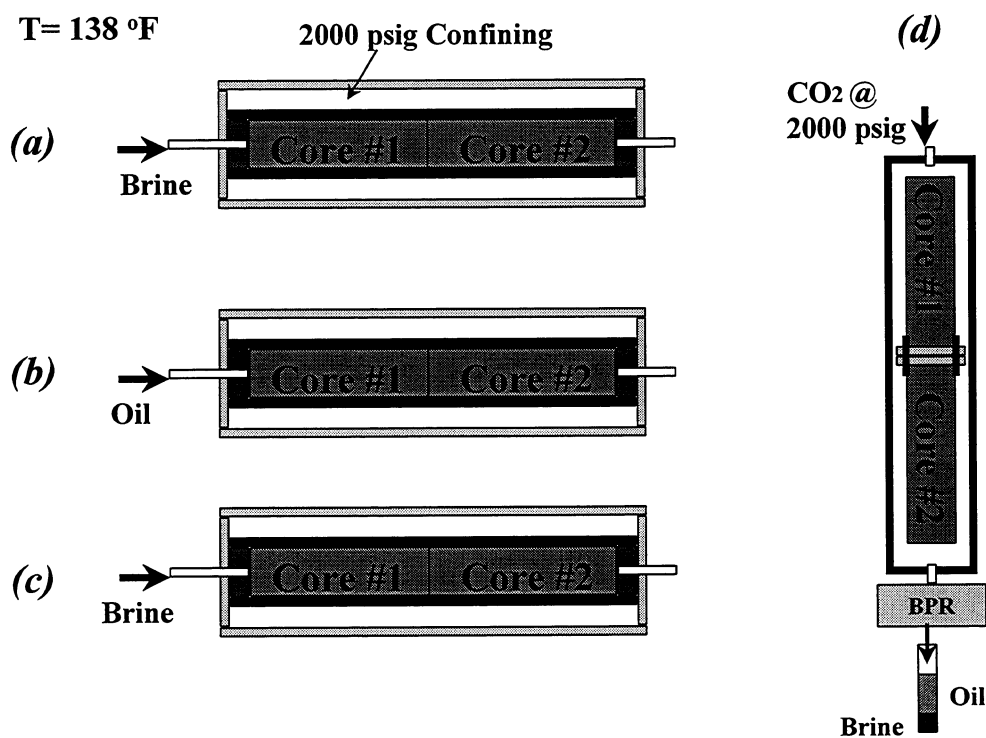


Fig. 4.1-2 - Schematic illustrating experimental procedure.

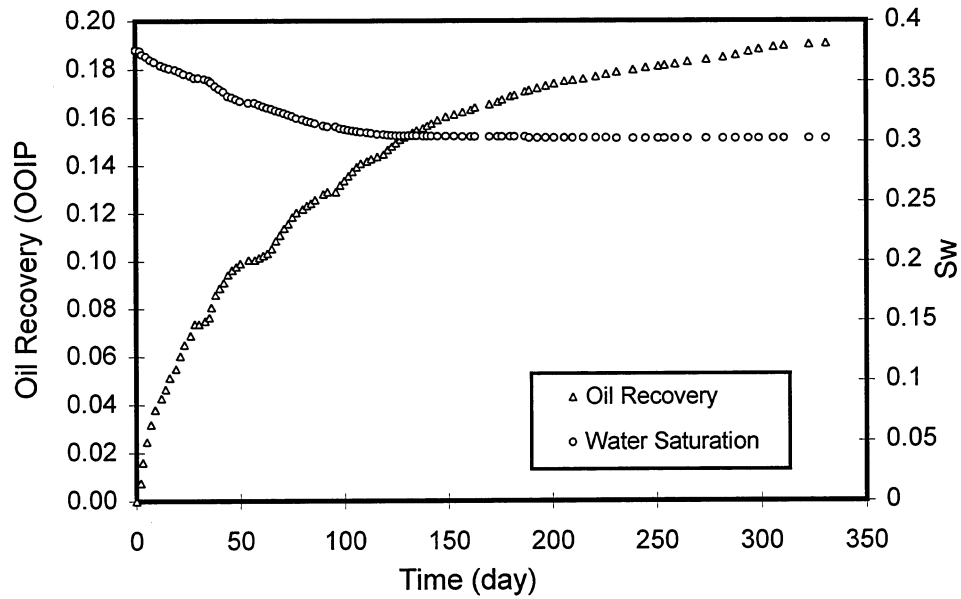


Fig. 4.1-3 Oil recovery curve obtained from a CO₂ injection experiment using a 0.05 md core stack with an initial water saturation 0.376.

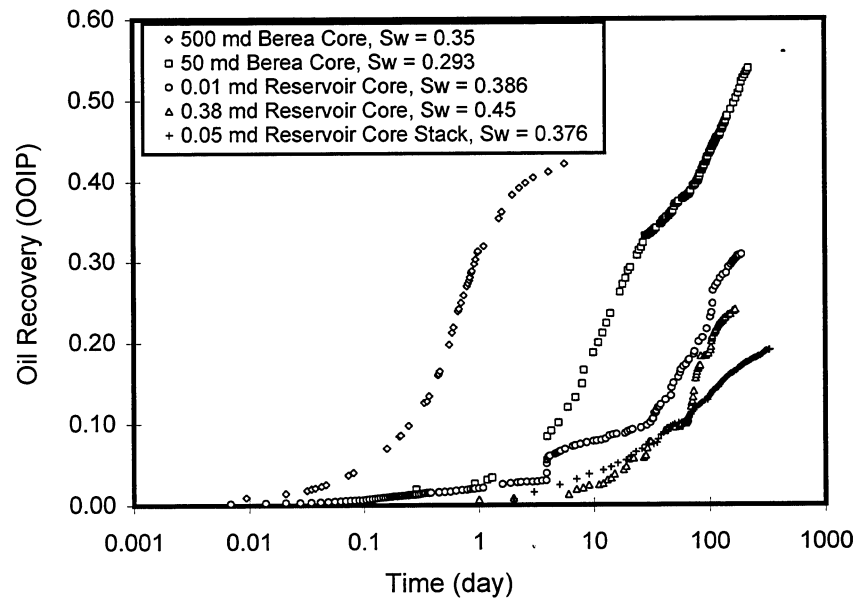


Fig. 4.1-4 Comparison of oil recovery curves obtained from five CO₂ injection experiments using cores with different permeabilities and water saturations.

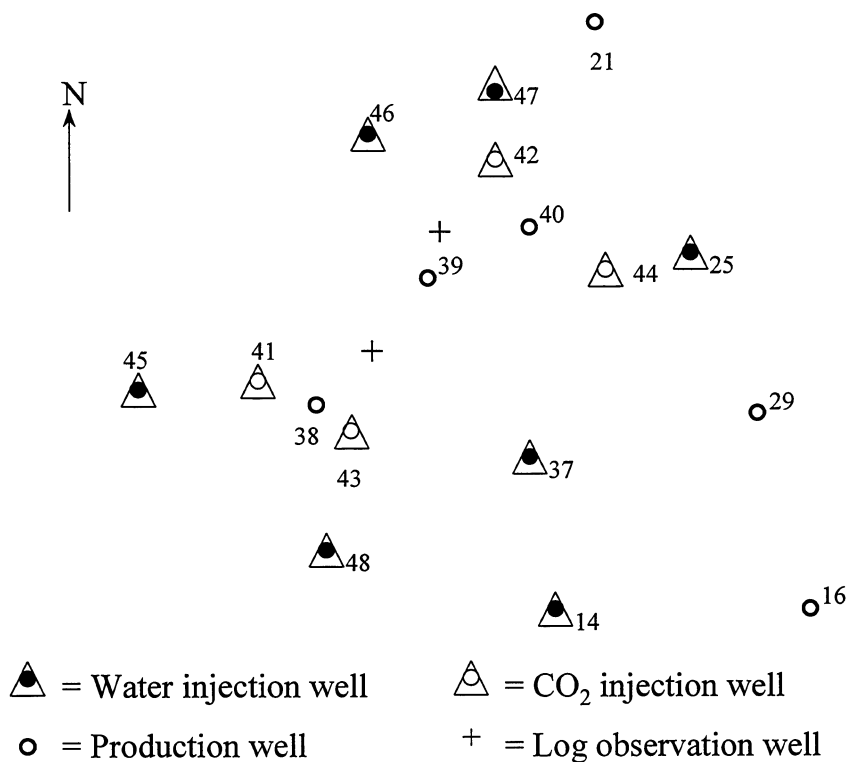


Fig. 4.1-5 Well locations in the E.T. O'Daniel CO₂ pilot (not to scale).

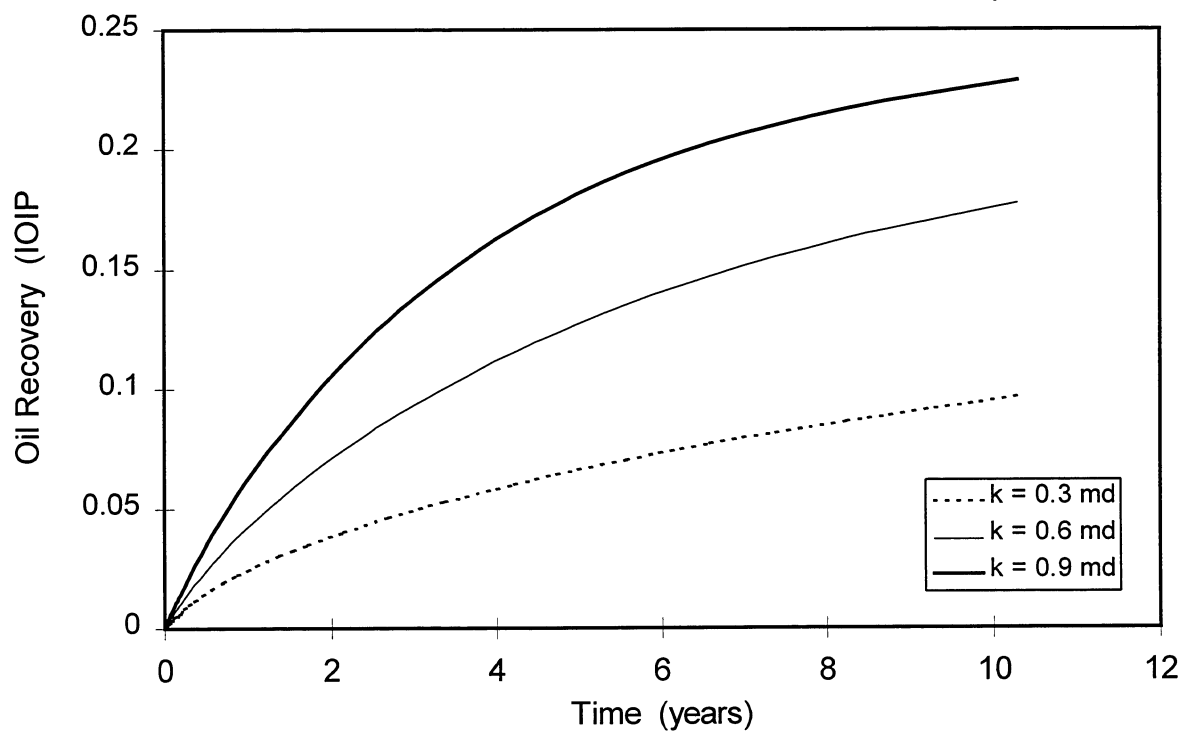


Fig. 4.1-6 Predicted oil recovery from the E.T. O'Daniel CO₂ pilot area.

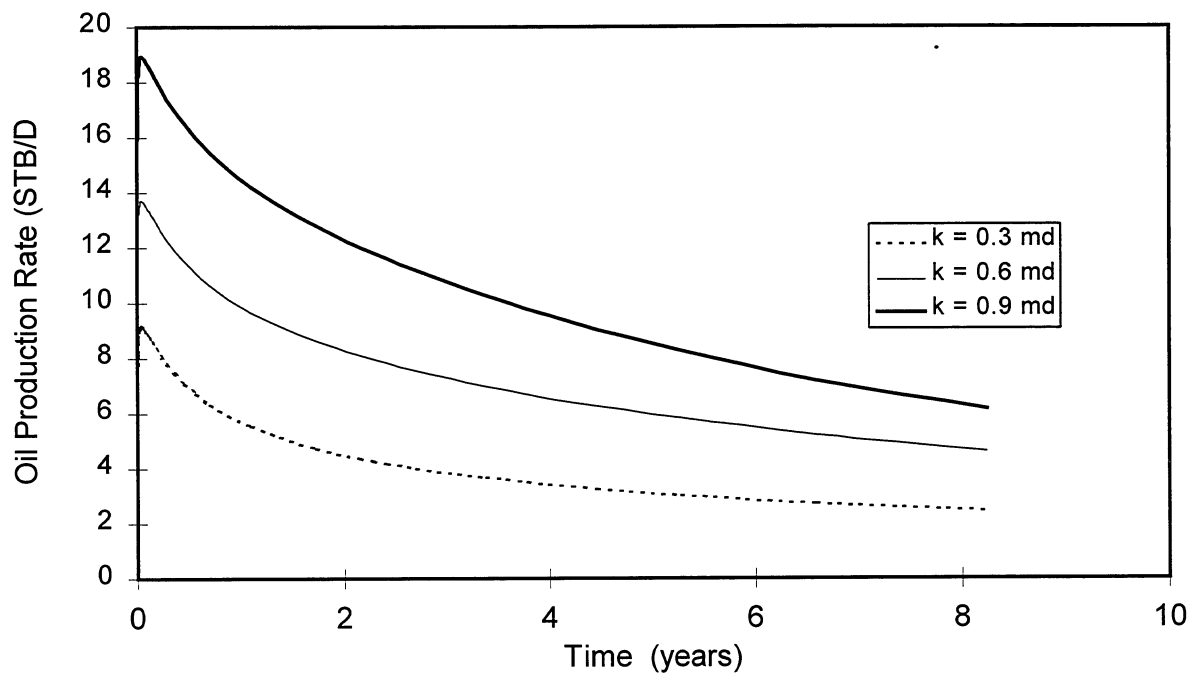


Fig. 4.1-7 Predicted oil production rate from the E.T. O'Daniel CO₂ pilot area.

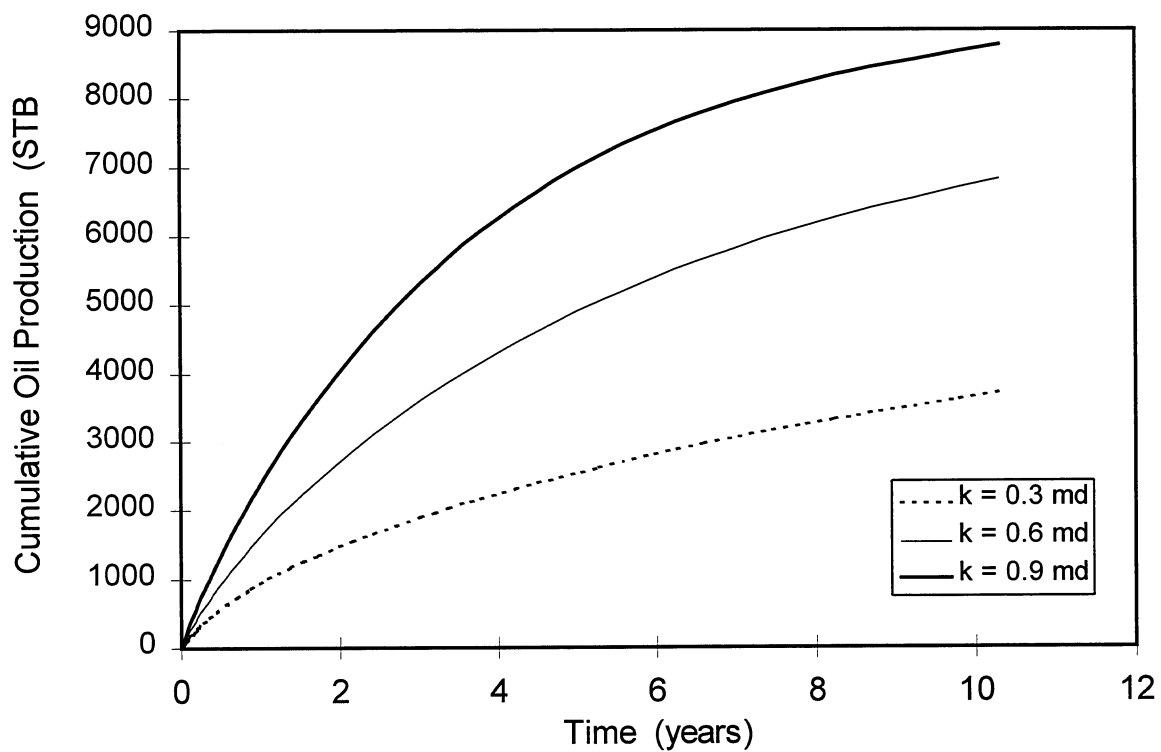


Fig. 4.1-8 Predicted cumulative oil production from the E.T. O'Daniel CO₂ pilot area.

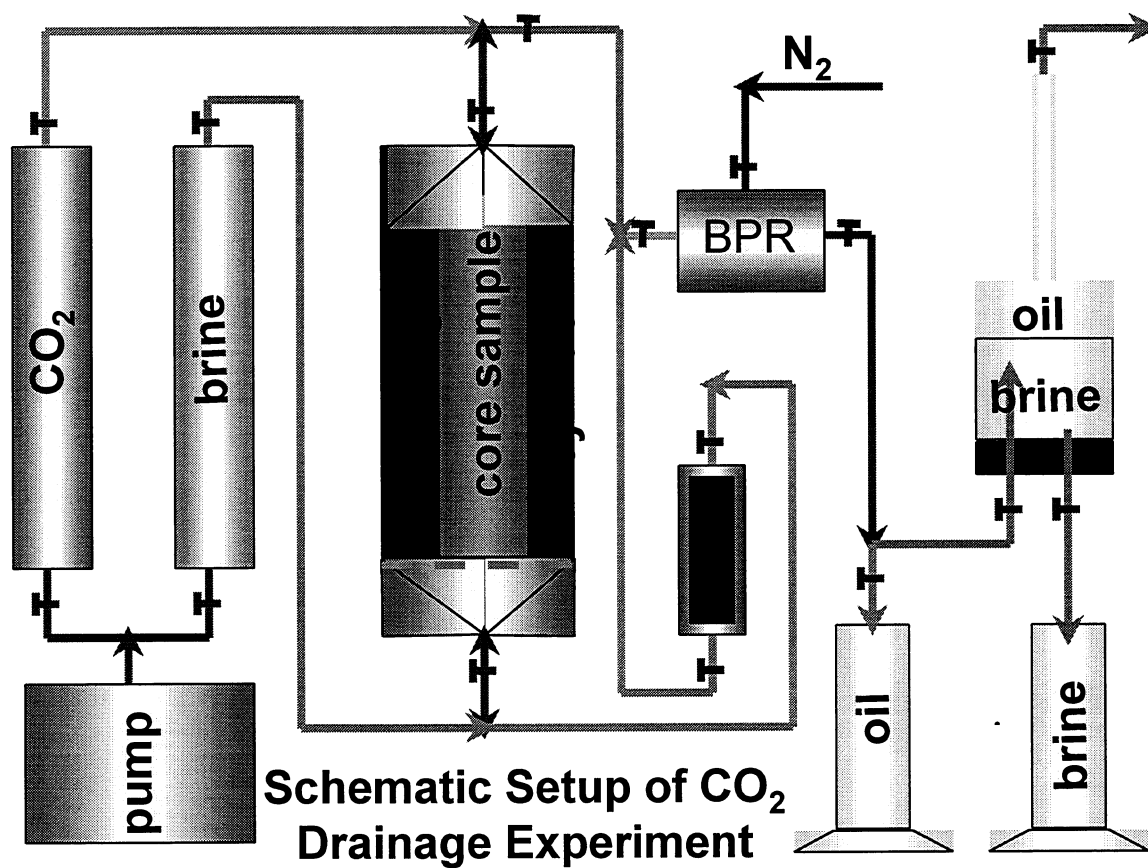


Fig. 4.1-9 Schematic of imbibition gravity drainage experiment.

5 FIELD DEMONSTRATION PROJECT

A major milestone of this project is to implement a field demonstration of the technology researched in the laboratory. A 10-ac. pilot project is being designed and implemented in the Pioneer Natural Resources' E.T. O'Daniel Unit. There will be six water injection wells surrounding four CO₂ injection wells with three producers in a line drive configuration northeast southwest. Seven producing wells will ring the pilot (see Fig. 4.1-5). The location of the CO₂ pilot has been shifted approximately 0.25 miles north of the location identified in the original submittal. The attached plat shows the modified configuration and location of each well in the pilot.

Budget Period #2 of this project commenced on 1/12/98 and comprises the following two tasks: Task #1 – Field Demonstration, and Task #2 – Associated Technology Transfer. The Field Demonstration task began in January 1998 and includes modifying the configuration of the CO₂ pilot; the drilling, logging and completion of the pilot producers, water injectors, CO₂ injectors and logging observation wells; and the construction of the water and CO₂ injection facilities.

5.1 DRILLING

The proposed design of the pilot requires drilling a total of 16 wells:

- Six water injection wells, #25, #37, #45, #46, #47 and #48;
- Four CO₂ injection wells, #41, #42, #43 and #44;
- Three producers, #38, #39 and #40;
- Two logging observation wells.

As of September 28, 1998, two water injectors, wells #47 and #48, and all three producers have been drilled, and logged. The Upper Spraberry intervals 1U and 5U have been cored in all five of these wells and reservoir data is presently being accumulated. The dual lateral horizontal core well has been completed and the core analyzed with the analysis aiding in characterizing the Spraberry Reservoir.

5.1.1 Flood Facilities

The waterflood and CO₂ injection facilities are new facilities to be built for the 10-acre demonstration pilot. Due to the position, accessibility and size of the location surrounding well #37, this site has been chosen for the water and CO₂ injection facilities. The design of the injection facility has been completed.

5.1.2 Future Plans

Wells #45 and #46 will be drilled and wells #25 and #37 will be converted from producers to water injectors in the fourth calendar quarter of 1998. This will complete

the 1998-drilling schedule. The CO₂ injection wells and the logging observation wells will be drilled in 1999. Water injection to the pilot wells is anticipated to begin before year-end 1998.

